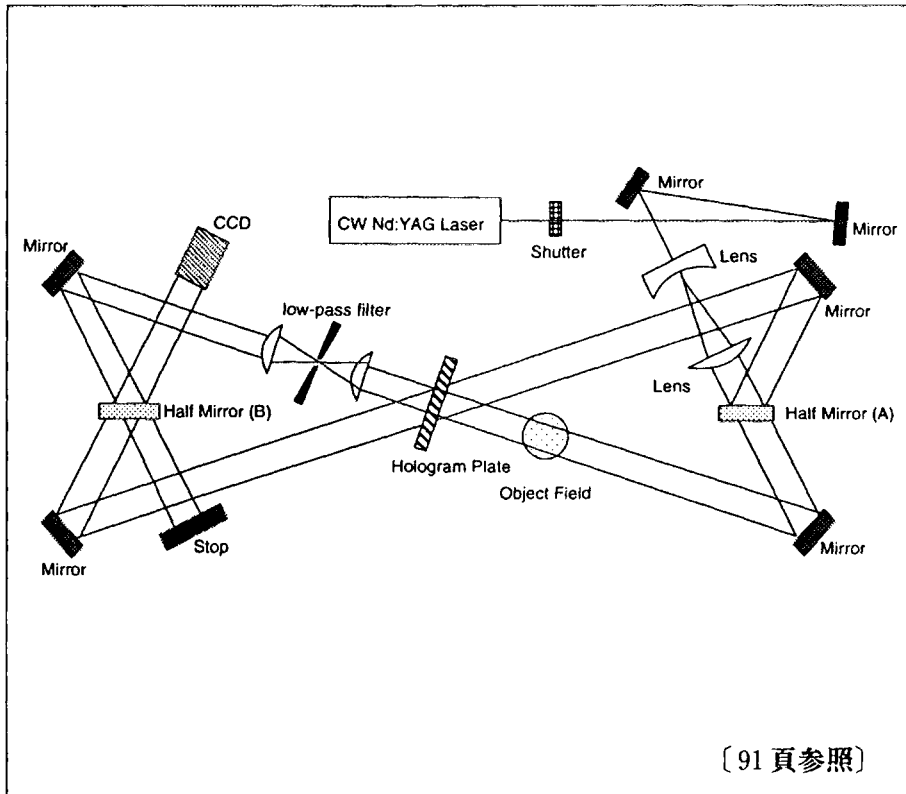




核融合炉ブランケット設計基礎実験装置

平成7年度 研究成果報告書



平成 8 年 10 月

東京大学工学部

2

Annual Report of the CTR Blanket Engineering
Research Facility in 1995

The Faculty of Engineering
The University of Tokyo,
October 1996

This is an annual report of the studies on Controlled Thermo-nuclear Reactor(CTR) Blanket Engineering which have been carried out in the Faculty of Engineering, the University of Tokyo, in FY 1995.

This research facility on the CTR Blanket Engineering is located in the Nuclear Engineering Research Laboratory, the Tokai-mura branch of the Faculty of Engineering.

For more information on this report, please contact:
Prof.Nobuyuki Inoue (Chairman of the steering committee of CTR Blanket Engineering Research Facility), Department of Quantum Engineering and System Science, the Faculty of Engineering, the University of Tokyo,
(Address) 7-3-1, Hongo, Bunkyo-ku, Tokyo 113, JAPAN.

For more information on this facility, please contact;
CTR Blanket Management staff, Nuclear Engineering Research Laboratory, the Faculty of Engineering, the University of Tokyo.
(Address) Tokai-mura, Ibaraki-prefecture 319-11, JAPAN

Contents

Preface N. Inoue (Chairman of the Steering Committee)

I. Summary of Research Progress

1. Transport of Impurity Particle at Plasma/Solid-Liquid Interface	1
2. Mechanism of Tritium Trapping and Re-emission on/from CTR Fuel Cycle Materials	4
3. Particle Dynamics in Near-Surface Region of Solid and Their Characterization	6
4. Study of First Wall Fuel Dynamics by Utilizing a Hydrogen Isotope Beam	9
5. Study on Sorption and Release of H ₂ and H ₂ O on/from Plasma/Wall Interface Based on Quantum Chemistry	13
6. Behavior of First Wall During Plasma Disruption	14
7. Application of High T _c Superconductor to Development of Fusion Reactor	15
8. Electromagnetic Nondestructive Evaluation of Fusion Reactor First Wall	19
9. Irradiation-Induced Microstructural and Mechanical Property Changes in Fusion Materials	21
10. Study on Image Analysis for First Wall	23
11. Development of Surface Characterization for Fusion Materials Using Laser Resonance Ionization Spectroscopy	25
12. Numerical Prediction of Turbulent Fluid Flow and Heat Transfer in Complex Geometry	26
13. Basic Study on a Thermoacoustic Refrigerator	29
14. Behavior of Hydrogen Isotopes on the Surface of Solid Breeding Materials	30
15. Hydrogen Absorption/Desorption Characteristics of Uranium Alloys	32
16. Physico-chemical Behavior of Liquid Breeding Materials	34
17. Irradiation Effects of Special Purpose Ceramic Materials for Fusion Reactors	37
18. Trap Mechanism of Tritium in Tritium-Materials Interactions	41

19. In-situ Observation of Cascade Damage Produced by High Energy PKA	43
20. Evaluation of Irradiation Behavior of Fusion Materials	46
21. Ion Beam Irradiation Effect on Non-Metallic Materials	48
22. The Study on Systematization of Design Technology	50
23. Engineering Design of Neutron Diagnostic Systems for Fusion Experimental Reactors	52
24. Characterization of Nuclear Fusion Radiation Field with Optical Techniques	54
25. Correction Technique of Scattering Neutron Components of FNR Images	56
26. Management Section of the CTR Blanket Engineering Research Facility	57

II. Research Reports

1	Analysis of Particle Transport in a Gas Target Divertor	61
	S.Ohtsu and S. Tanaka	
2	Sorption and Desorption of Tritiated Water Vapor on Piping Materials of Nuclear Fusion Reactor	63
	S. Tanaka and R. Ohmori	
3	Work Function Measurement of the Surface of Solid Materials by Use of High-Temperature Kelvin Probe	65
	A. Suzuki, K. Yamaguchi and M. Yamawaki	
4-1	Retention of Hydrogen Isotopes and Helium in Nickel	67
	M. Okada, R. Sato, K. Yamaguchi and M. Yamawaki	
4-2	Hydrocarbon Transport in the Laboratory Plasma(MAP)	69
	S. Matsuyama, K. Yamaguchi, S.Tanaka and M. Yamawaki	
4-3	The Rate-Limiting Process of Hydrogen Transport in Mo	71
	K. Ohkoshi, Y.Chikazawa, V. Bandourko, K. Yamaguchi and M. Yamawaki	
5	Quantum Chemical Estimation of Sorption/Desorption of H ₂ and H ₂ O(gas) at the Plasma-Wall Interface	73
	S. Nagasaki, S. Tsushima, M. Tanaka and Y. Umemura	
6	Evaporative Behavior of Carbon with MPD Arc Jet	75
	T. Sukegawa, H. Madarame and K. Okamoto	

7	Application of High Tc Superconductor to Passive Control of Plasma Position	77
	T. Uchimoto, N.Ikatsu, Y. Yoshida and K. Miya	
8	Computation of Eddy Current–Crack Interaction Based on Vector Potential Integral Formulation	81
	Y. Yoshida and K. Miya	
9	A modeling of Radiation Induced Microstructural Evolution under Applied Stress in Austenitic Alloys	83
	H.Tanigawa, A.Kohyama, Y.Katoh and Y.Kohno	
10–1	Extraction of Density Distributions and Particle Locations from Hologram Images	90
	K. Okamoto, K. Ikeda and H. Madarame	
10–2	New Tracking Algorithm for Particle Image Velocimetry	92
	K. Okamoto, Y.A. Hassan and W.D.Schmidl	
11	Development of Resonance Ionization Spectroscopy System for Fusion Material Surface Analysis	98
	T. Iguchi, Y.Satoh and M.Nakazawa	
12	Active Control of Vortex Dipoles and Heat Transfer with Wall Deformation	100
	N. Kasagi and Y. Mito	
13	Basic Study on a Thermoacoustic Refrigerator	102
	T. Saito, E. Hihara and H. Sakai	
14–1	Study on the Surface Hydroxyl Group on Solid Breeding Materials by Infrared Absorption Spectroscopy	104
	S. Tanaka and M. Taniguchi	
14–2	Study on the Surface Hydroxyl Group on Solid Breeding Materials by Ab-initio Calculations	106
	S. Tanaka and M. Taniguchi	
14–3	The Influence of Irradiation Defects on Tritium Release from Li ₂ O	108
	S. Tanaka and V. Grishmanov	
15	Study on Hydrogen Absorption/Desorption Properties of Uranium Alloys	110
	H. Ito, K. Yamaguchi and M. Yamawaki	
16–1	Compatibility of YTTRIA(Y ₂ O ₃) with Liquid Lithium	112
	T.Mitsuyama, T.Yoneoka, T.Terai and S. Tanaka	

16-2	Chemical Form of Released Tritium from Molten Li_2BeF_4 Salt Under Neutron Irradiation at Elevated Temperatures	114
	A. Suzuki, T.Terai, T. Yoneoka and S. Tanaka	
17-1	Effect of 520MeV Kr^{20+} Ion Irradiation on the Critical Current Density of Bi-2212 Single Crystals	116
	T.Terai, Y.Ito and K.Kishio	
17-2	Degradation of Insulating Ceramics due to Irradiation	118
	T. Kobayashi, T. Terai, T.Yoneoka and S. Tanaka	
18	Regrowth of Tritium Release from Tritium Contaminated Materials	120
	F. Ono, M. Yamawaki and S. Tanaka	
19	A Study of Defect Cluster Formation in Vanadium by Heavy Ion Irradiation	126
	N. Sekimura, Y.Shirao and k. Morishita	
20	Microstructural and Microchemical Evolution in Vanadium Alloys by Heavy Ion Irradiation	128
	N. Sekimura, H. Kakiuchi, Y. Shirao and T. Iwai	
21-1	Construction of Ion Beam Pulse Radiolysis System	130
	N. Chitose, Y. Katsumura, M. Domae, K. Ishigure and T. Murakami	
21-2	Changes in the Surface Electronic States of Semiconductor Fine Particles Induced by High Energy Ion Irradiation	132
	T. Yamaki, K. Asai and K. Ishigure	
22	Knowledge Model of Trainee for Training Support System of Plant Operation	134
	Y. Furuhami, K. Furuta and S. Kondo	
23	High Energy Resolution Characteristics on 14MeV Neutron Spectrometer for Fusion Experimental Reactor	136
	T. Iguchi, E.Takada and M.Nakazawa	
24	Neutron Radiation Distribution Sensor Using Flexible Plastic Scintillating Fiber Combined with the Time-of-Flight Technique	138
	E. Takada, K. Sugiyama, H.Takahashi, T. Iguchi and M. Nakazawa	

25	Correction of Fast Neutron Scattered Components from Fast Neutron Radiography Images	143
	K. Yoshii and H. Kobayashi	
III.	List of International Conferences and Workshops Sponsored and/or Supported by the Members of BLT	147
IV.	Participants List to the CTR Blanket Engineering Research Project	149

目 次

巻頭言

運営委員長 井上 信幸 (システム量子工学科)

I. 経過報告

1	プラズマ／固体・液体界面における不純物粒子の輸送挙動	1
2	核融合炉実用材料へのトリチウム付着と再放出メカニズムの解明	4
3	固体表面近傍における粒子挙動の評価法の開発に関する研究	6
4	水素同位体ビームによる第一壁燃料ダイナミックスの研究	9
5	プラズマ／壁界面における水素や水蒸気の吸着・脱離に関する 量子化学的検討	13
6	ディスラプション時の第一壁の挙動	14
7	高温超電導体の核融合炉高度化への応用	15
8	核融合炉第一壁の電磁的非破壊検査	19
9	照射による材料組織・強度特性変化の研究	21
10	第一壁の画像解析に関する研究	23
11	レーザー共鳴イオン化分光を用いた核融合炉材料界面特性の 評価手法の開発	25
12	複雑形状流路内乱流の熱・運動量輸送の数値予測	26
13	熱音響型冷凍機の基礎的研究	29
14	固体増殖材料表面における水素同位体の挙動	30
15	ウラン合金の水素同位体吸収特性	32
16	液体トリチウム増殖材料の物理化学的挙動	34
17	核融合炉用機能性セラミックス材料の放射線照射効果	37
18	トリチウム－材料相互作用におけるトラップメカニズム	41
19	イオン照射下その場観察法による高エネルギーPKAカスケード損傷 ...	43
20	核融合炉材料の照射下挙動評価に関する研究	46
21	非金属材料のイオン照射効果の研究	48
22	設計技術の体系化研究	50
23	核融合実験炉中性子計測システムの工学設計	52
24	光学的手法による核融合反応放射線場のキャラクタリゼーション	54
25	高速中性子ラジオグラフィの散乱線補正	56
26	ブランケット管理部	57

II. 研究成果報告

1	ガスダイバータにおける粒子輸送解析	61
	大津 繁樹、田中 知 (システム量子工学専攻)	
2	核融合炉実用材料へのトリチウム付着と再放出メカニズムの解明	63
	田中 知、大森ルミ (システム量子工学専攻)	
3	高温ケルビン計による固体材料表面の仕事関数測定	65
	鈴木敦士、山口憲司、山脇道夫 (原子力工学研究施設)	
4-1	ニッケル中における水素同位体およびヘリウム保持に関する研究	67
	岡田光正、佐藤力哉、山口憲司、山脇道夫 (原子力工学研究施設)	
4-2	M A P 装置による炭化水素輸送過程の研究	69
	松山征嗣、山口憲司、田中 知*、山脇道夫 (原子力工学研究施設、* システム量子工学専攻)	
4-3	M o における水素輸送の律速段階	71
	大越啓志郎、近澤佳隆、ヴァシリ・バンドゥルコ、山口憲司、 山脇道夫 (原子力工学研究施設)	
5	プラズマ/壁界面における水素や水蒸気の吸着・脱離に関する 量子化学的検討	73
	長崎晋也、津島 悟、田中将隆、梅村康洋 (システム量子工学専攻)	
6	M P D アークジェットによる黒鉛の蒸発挙動	75
	助川敏男、班目春樹、岡本孝司 (原子力工学研究施設)	
7	高温超電導体によるプラズマ位置の受動制御	77
	内一哲哉、井勝伸彦、吉田義勝、宮 健三 (原子力工学研究施設)	
8	ベクトルポテンシャル積分方程式に基づく渦電流探傷順問題の数値計算	81
	吉田義勝、宮 健三 (原子力工学研究施設)	
9	オーステナイト系合金の照射下組織発達に及ぼす外部応力効果のモデリング	83
	谷川博康、香山 晃、加藤雄大、幸野 豊 (材料学専攻)	
10-1	ホログラムからの粒子、密度情報の同時抽出	90
	岡本孝司、池田 耕、班目春樹 (原子力工学研究施設)	
10-2	粒子画像流速測定法における新粒子アルゴリズム	92
	岡本孝司、Y.A. Hassan*, W.D. Schmidl* (原子力工学研究施設、* Texas A&M University)	
11	レーザー共鳴イオン化分光を用いた核融合材料界面特性の評価手法の開発	98
	井口哲夫、佐藤 泰*、中沢正治* (原子力工学研究施設、 * システム量子工学専攻)	
12	壁面変形による渦対と熱伝達のアクティブ制御	100
	笠木伸英、三戸陽一 (機械工学専攻)	

13	熱音響型冷凍機の基礎的研究	102
	齊藤孝基、飛原英治、酒井 均 (機械工学専攻)	
14-1	赤外吸収分析による固体増殖材表面水酸基の研究	104
	田中 知、谷口正樹 (システム量子工学専攻)	
14-2	Ab-initio 計算による固体増殖材表面水酸基の研究	106
	田中 知、谷口正樹 (システム量子工学専攻)	
14-3	照射欠陥がLi ₂ Oからのトリチウム放出に及ぼす影響	108
	田中 知、Victor Grishmanov (システム量子工学専攻)	
15	ウラン合金の水素吸蔵放出特性に関する研究	110
	伊藤 洋、山口憲司、山脇道夫 (原子力工学研究施設)	
16-1	イットリア(Y ₂ O ₃)と液体リチウムとの両立性	112
	満山孝明、米岡俊明、寺井隆幸、田中 知 (システム量子工学専攻)	
16-2	高温照射下FLIBE(Li ₂ BeF ₄)からのトリチウム放出化学形	114
	鈴木晶大、寺井隆幸、米岡俊明、田中 知 (システム量子工学専攻)	
17-1	Bi-2212 単結晶の臨界電流密度に対する520MeV Kr ²⁰⁺ イオン照射 効果	116
	寺井隆幸、伊藤康行、岸尾光二* (システム量子工学専攻、 * 応用化学専攻)	
17-2	絶縁性セラミックスの放射線照射による特性劣化	118
	小林知洋、寺井隆幸、米岡俊明、田中 知 (システム量子工学専攻)	
18	トリチウム汚染材料からのトリチウム再放出	120
	小野双葉、田中 知* (原子力工学研究施設、*システム量子工学専攻)	
19	重イオン照射によるバナジウムの欠陥クラスター形成に対する カスケード損傷効果の効果	126
	関村直人、白尾泰之、森下和功* (システム量子工学専攻、*原子力工学研究施設)	
20	重イオン照射によるバナジウム合金のミクロ組織・組成変化の研究	128
	関村直人、柿内宏憲、白尾泰之、岩井岳夫* (システム量子工学専攻、*原子力研究総合センター)	
21-1	イオンビームパルスラジオリシスシステムの構築	130
	千歳範壽、勝村庸介、堂前雅史、石樽頭吉、村上健 (システム量子工学専攻)	
21-2	イオンビーム照射による半導体超微粒子の表面電子状態変化	132
	八巻徹也、浅井圭介、石樽頭吉 (システム量子工学専攻)	
22	プラント操作員訓練支援システム用学習者モデルに関する研究	134
	古濱 寛、古田一雄、近藤駿介 (システム量子工学専攻)	

23	核融合実験炉用14MeV中性子スペクトロメータの高エネルギー分解能特性の評価	136
	井口哲夫、高田英治*、中沢正治*	
	(原子力工学研究施設、*システム量子工学科)	
24	プラスチック・シンチレーティング・ファイバーによる中性子束分布センサーの開発	138
	高田英治、杉山完二郎、高橋浩之、井口哲夫*、中沢正治	
	(システム量子工学専攻、*原子力工学研究施設)	
25	FNR画像における散乱線成分の補正	143
	吉井康司、小林久夫* (原子力工学研究施設、*立教大学)	
III.	核融合炉ブランケット設計基礎実験装置ユーザーが主催または後援した国際会議、ワークショップ等一覧	147
IV.	核融合炉ブランケット設計基礎実験装置研究参加者名簿	149

はじめに

本報告書は、平成7年度に工学部核融合炉ブランケット設計基礎実験装置を用いて行われた研究成果をまとめたものである。核融合開発過程で解決すべき研究課題は、炉心プラズマ物理、核融合炉工学、核融合炉の環境・安全適合性、核融合炉の経済性、社会的受容性などの多岐にわたるが、ここでは炉工学研究や安全性研究が関わっている。

本実験装置は、1977年度に設置され、爾来18年の長きにわたり本学の炉工学研究の推進と研究者の組織化に貢献してきた。この間にも核融合研究は急速な発展を遂げ、ごく一部の例をあげれば、炉心プラズマのゼロ出力条件の達成、自発電流の観測、高効率電流駆動技術の進歩、低放射化耐熱材料開発、大型強磁場超伝導磁石の実現、大容量トリチウム処理技術の確立などがあった。また日米欧の共同により、ITERの概念設計、工学設計が進められてきたことも周知の通りである。これらの進歩には、人材養成も含めて大学の貢献するところが著しい。それも本装置による研究のように、一度交付されるとなかなか更新されない限られた予算のもとで実施された研究成果が殆どであることから、研究の進歩にあわせて必要十分な予算が手当てされていれば、その成果は如何ほどであったかと思われる。

核融合炉ブランケット設計基礎実験装置は、ここ数年来検討されてきた原子力工学研究施設の将来計画の一環として、新たな展開がはかられようとしている。研究予算も将来計画との関連課題に重点配分されてきた。したがって、この報告書に記載された研究成果もこうした条件下で得られたものである。国全体としては科学技術立国が叫ばれ、科学技術基本計画が作成されたところである。また大学の核融合研究に関しては、科学研究費補助金総合研究（A）による「大学の核融合ネットワーク構想」や学術会議核融合研究連絡委員会がまとめた「核融合炉工学における共同研究拠点の整備について」などの報告書がつぎつぎに出され、今後の研究推進に反映される予定である。本学の計画はこれらを浮力として発展を図る必要がある。関係者一同、立案した将来計画の実現に向けて邁進する決意であり、各位におかれては引き続きご協力、ご支援を仰ぐ次第である。

なお、本報告書の内容についてのご意見、ご批判をいただければ誠に有り難い。連絡は成果報告を記述している各研究者、あるいはブランケット管理部長の吉田義勝助教授か私にいただければ幸いである。

核融合炉ブランケット設計基礎実験装置
運営委員長

井上 信幸
(システム量子工学専攻)

I. 經過報告

1. プラズマ/固体・液体界面における不純物粒子の輸送挙動

Transport of Impurity Particle at Plasma/Solid-Liquid Interface

研究テーマ代表者 田中 知 (システム量子工学専攻)

1 序

核融合炉ダイバータで粒子・熱粒子束制御を行なう上では、プラズマ/固体、プラズマ/液体金属界面における不純物粒子の輸送挙動の解明することが非常に重要な課題となっている。本研究グループは、直線型プラズマ照射装置MAP (Material and Plasma) と2次元多流体プラズマ輸送コード (B2.5 コード) を用いて、実験・シミュレーションの2つの方法によって、プラズマ第一壁相互作用に関する研究を進めている。

2 研究進捗状況

Ti合金 水素プラズマ照射実験

直線型定常プラズマ発生装置 MAP による Ti合金に対するプラズマ照射実験を行い、高熱負荷にさらされた時に想定される Ti材料の振舞い (表面の変質や Ti不純物のプラズマへの挙動等) に関する知見が得られた。

分光器による Ti(I),Ti(II) のスペクトルを同定によって、Ti(I) が比較的径方向に広く分布しているのに対し、Ti(II) はプラズマ中心付近に大きい分布をもつことが観測された。また、SEMによるTi合金の表面観察からは、アーキングによるスポットが観察された。また、Tiの薄膜がMAPのプラズマ上流側の円筒状真空容器壁とターゲット後方の円筒状真空容器壁面に形成されているのが観測されたことから、Ti粒子がプラズマ流またはガス流に押されて後方に飛散していることが判明した。

定常型核融合炉ダイバータにおける粒子輸送計算

2次元多流体プラズマ輸送コード (B2.5 コード) を用いて、実際の定常トカマク型実験装置においてプラズマ-固体相互作用の数値シミュレーションを行い、ダイバータ形状による粒子輸送挙動について調べた。その結果、バッフル板・ドームをダイバータに挿入した場合、ダイバータ高温部への中性粒子の流入が増加し、ダイバータ部での中性粒子のリサイクリングを増加させることによって、中性粒子がダイバータ領域に閉じ込める効果が上がる事が判明した。

3 今後の予定

以下の事を今後の研究課題として予定としている。

1. 定常プラズマ源 (MAP) を用いて炭素系、金属 (W, Mo, Li, Li-Pb) 不純物粒子の輸送挙動 (スパッタリング、化学形変形、付着、励起を含む) を自発及びレーザ励起発光、重量変化法等による調べる。
2. ガスダイバータを模擬した実験装置をMAPに組み込み、固体壁からの反射及び荷電交換で発生する中性粒子挙動を高性能分光器によって解析する。また、ガスパフー排気のマクロマスバランスの評価とモデル計算との比較を行なう。
3. MAP実験によって得られた結果をもとにダイバータ板上でのプラズマ及び中性粒子の境界条件を同定し、トカマク型核融合炉ダイバータ領域における不純物輸送・粒子制御のシミュレーションを行う。

4 発表論文リスト

(A) 学位論文等

該当なし

(B) 国外学会誌等

- (a) S. Ohtsu, S. Tanaka and B.J. Braams
Numerical Simulation of the ITER Gaseous Divertor with the B2.5 code
Contributions to Plasma Physics. 36 (1996) 282-287.
- (b) S. Matsuyama, K. Yamaguchi, S. Tanaka and M. Yamawaki "The research on impurity atomic and transport processes in relation to the boundary plasma region",
'7th International Conference on Fusion Reactor Materials',
Obninsk, Russia, September 23-29, 1995
- (c) S. Matsuyama, K. Yamaguchi, S. Tanaka and M. Yamawaki, "
'The research on impurity atomic and transport processes in relation to the boundary plasma region",
4th Japan-Russia Workshop on Interactions of Fuel Particles with Fusion Materials (IFPFM 4),
Moscow, Russia, September 29 - 30, 1995
- (d) S. Matsuyama, K. Yamaguchi, S. Tanaka and M. Yamawaki
"The hydrocarbon transport in the laboratory plasma MAP",
'7th International Toki Conference on Plasma Physics and Controlled Nuclear Fusion',
Toki-city, Gifu-ken, Japan. November 28- December 1, 1995

- (e) S. Ohtsu and S. Tanaka
“Modeling of Impurity Behavior in Divertor Region”
4th Japan-CIS Workshop Interactions of Fuel Particle with Fusion Materials,
Moscow, Russia, September 29-30, 1995.
- (f) S. Ohtsu and S. Tanaka,
“Impurity Transport Modeling in Divertor Region”
The 3rd Sino-Japanese Symposium on Materials for Advanced Energy Systems
and Fission and Fusion Engineering,

4.1 (C) 国内学会誌等

- (a) 松山征嗣、山口憲司、田中知、山脇道夫;
「対向壁損耗再付着現象に関連した、不純物輸送過程の研究」
日本原子力学会「1995年秋の大会」,
日本原子力研究所、10月17～19日(1995)
- (b) 松山征嗣、山口憲司、田中知、山脇道夫;
「定常プラズマ発生装置による炭化水素輸送実験」
日本原子力学会「1996年春の大会」, 大阪大学, 3月26日～29日(1996)
- (c) 大津 繁樹 田中 知 B.J.Braams
「B2.5コードによるダイバータモデリング」
プラズマと壁との相互作用に関する研究会,
核融合科学研究所 1995年9月12～13日
- (d) 大津 繁樹 田中 知 B.J.Braams
「ダイバータ部での粒子排気・注入効果」
プラズマ核融合学会第12回秋期講演会 岩手大学 1995年9月25日～27日
- (e) 大津 繁樹 田中 知 B.J.Braams
「ガスダイバータ中での流れと熱輸送解析」
プラズマ核融合学会第13回年会 京都大学 1996年3月21日～23日

2. 核融合炉実用材料へのトリチウム付着と再放出メカニズムの解明

Mechanism of Tritium Trapping and Re-emission on/from CTR Fuel Cycle Materials

研究テーマ代表者 田中 知 (システム量子工学専攻)

1. 序

核融合炉材料とトリチウムの相互作用についての研究は、その多くが核融合炉第一壁、ブランケット材料、金属ベッドまたは白金パラジウム膜などとの相互作用についてのものである。しかし核融合炉システムは炉・ブランケット・燃料精製システム等で構成されており、各システム間はほとんどが配管で連結されている。その配管の全長は20mにおよぶといわれる。これだけの長さになると配管内面とトリチウムの総接触面積は非常に大きく、トリチウムが内面に付着することによる回収ロス、配管を透過しての環境中へのトリチウムの放出などは無視できない。したがって通常運転時または事故時の配管とトリチウムの挙動を知ることは、核融合炉の安全性の確立、機器の効率的な運転、トリチウムインベントリーの評価・低減につながるものである。

最近になってステンレス鋼のような配管を構成する金属の理想的な表面とトリチウムとの相互作用の研究が行われるようになってきたが、脱離量の測定から求めた付着量の評価、除染係数や活性化エネルギーの決定などを主目的としている場合が多い。実験に使われる金属表面は清浄なものの場合がほとんどで実際の使用状態とはかなり異なっていると考えられる。現時点では、実際に近い状態での配管材料とトリチウムの相互作用の研究は始まりつつある状況であり、様々な表面状態におけるデータの整備と付着・脱離メカニズムの解明が必要である。このような観点から使用状態によりちかい配管材料表面とトリチウムの相互作用を調べることを本研究の目的としている。

2. 研究進捗状況 (装置の改良等を含む)

FT-IR (Fourier transform infrared spectrophotometer) を用いて、SUS316, NiO, Cr₂O₃ の粉末に30℃で重水蒸気を付着させて、その吸着、乾燥脱離、交換反応脱離の様子を観察することができた。重水蒸気が吸着すると2100~2700cm⁻¹の付近に大きなピークが現われた。この波数は水の赤外線吸収波数の約 $1/\sqrt{2}$ に相当し、しかもその形状は幅広い。そのため重水素の換算質量を考え併せると、金属粉末表面に物理吸着している表面重水によるものであると考えている。この表面重水は303Kで脱離実験を行ったところ、Cr₂O₃とNiOの場合、乾燥脱離では7時間経過してもピークが確認できたが、水蒸気と接触させた交換反応脱離では短時間で残存が確認できなくなった。このため交換反応による脱離速度は乾燥脱離速度よりもかなり早いということがわかった。一方ステンレス鋼の場合、4時間ほど乾燥脱離を行うと70%以上除去されることがわかった。

さらにこのピークの全波数領域は、一様なスピードで吸着・脱離が起きるわけではなく、波数依存性があることがわかった。低波数 (2430cm⁻¹)、中波数 (2580cm⁻¹)、高波数 (2650cm⁻¹) の吸収率の変化を調べたところ、高波数側は吸着速度も脱離速度も遅かった。

また、試料は前処置としてArガス中で乾燥させて用いた。そこで乾燥温度(673Kあるいは303K)の違いが吸着・脱離に与える影響について調べた。高温で乾燥させた時のほうが吸着量の減少と脱離速度の低下がみられた。

一方、昇温・光励起脱離装置は雰囲気(温度、添加ガスとその分圧、照射波長)を制御できるように設計を行った。この設計に基づき組み立てと調整に取りかかった。

3. 今後の予定

平成7年度に得られた実験結果の波数依存性が表面とのどのような結合状態から生じているのかを調べるために、試料の表面状態を明らかにする必要があると考えられる。そこでXRDを用いて高温で乾燥した場合と室温乾燥のみの場合の試料の表面状態の変化の様子を観察し、表面変質と観察された違いを関係づけることができるか調査する。また、粒子径測定装置を用いて試料サイズを測定し、異なる試料どうしの吸着・脱離量を比較する。

昇温・光励起脱離装置は完成次第すぐに実験を開始し、重水の熱エネルギー吸収による活性化エネルギーその算出、光エネルギー照射による脱離エネルギーの算出、熱と光エネルギーの脱離効率の違い、両者を組み合わせてより効率的に脱離を行うことができないかを調べる。また、熱エネルギーによる脱離ピークは複数得られると期待されるが、各ピークがFT-IRで得られた波数領域のどのあたりに位置するのかを調べられないかと考えている。

平成7年度は3つの試料を中心に実験を行ったが、使用状態にあるステンレス鋼を考えたときに酸化鉄(Fe₂O₃)の影響はかなり大きく無視できないものと思われる。したがって酸化鉄の重水蒸気の吸着状態をその場観察したいが、この試料は赤外線を吸収してしまい現在の拡散反射法を用いたFT-IRでの観察は難しいことがわかった。今後は酸化鉄に対するその場観察に適した実験方法を探していく必要がある。

平成8年度はSTM(Scanning Tunneling Microscope)としても使える雰囲気制御チャンバー付AFM(Atomic Force Microscope)を設置予定である。AFMは試料表面原子と吸着原子を3次元的にその場観察することができる。しかもSTMと違いAFMは試料の導電性を必要としないため酸化物試料も観察対象になる。この装置を用いてFe₂O₃も含め各種試料表面の観察、およびできれば試料表面に吸着した重水蒸気の観察を予定している。

4. 発表論文リスト

(C) 国内学会誌等

(1) 東京大学 大森ルミ、米岡俊明、田中 知:

「ステンレス鋼材料への室温付近での重水蒸気の付着」、

日本原子力学会、大阪、3月27日、1996年

3. 固体表面近傍における粒子挙動の評価法の開発に関する研究

Particle Dynamics in Near-Surface Region of Solid and Their Characterization

研究テーマ代表者 山口 憲司 (原子力工学研究施設)

1 序

本研究は、固体表面上ならびにその近傍での粒子の挙動を、既成の分析手法を用いて評価するのみならず、新しい手法の適用の可能性についても検討するものである。特に当グループは、従来、表面分析付水素透過実験装置 (HYPA-IV) を用いて、金属における水素同位体の透過挙動と表面組成の関係を明らかにしてきた。本研究はこれを発展的に継承すべく、以下の研究項目を掲げており、最終的には、概算要求プロジェクトに貢献し得るデータの取得を目指す。

1. 固体表面の仕事関数の測定と雰囲気効果の解明:

高温ケルビン計により、金属、あるいはセラミックス材料の仕事関数を測定する。特に雰囲気の効果に着目しその影響を明らかにすることを目的とする。

2. 金属表面の酸化・偏析に関する研究:

既設のオージェ電子分光装置、2次イオン質量分析計等を用いて、金属表面での酸化や偏析に関する研究を行う。

3. 新分析手法の導入に関する検討:

他実験設備 (重照射、ライナック等) を表面近傍のバルク水素濃度の測定や吸着・脱離の研究に適用できないか検討する。

2 研究の進捗状況 (装置の改良等を含む)

初年度にあたる今年度は、主として高温ケルビン計の体系の構築を行い (英文報告書参照)、以下の研究課題に本装置を適用した。

(1) 核融合炉固体増殖材の仕事関数測定

核融合炉固体増殖材表面に及ぼすスイープガス効果や照射効果を解明することは、トリウム燃料サイクルを確立する上で非常に重要である。本研究では、仕事関数が表面状態に非常に敏感であることに着目して、スイープガスや照射による仕事関数変化を測定する手法 (高温ケルビン計) を開発し、 Li_4SiO_4 について雰囲気ガスによる仕事関数変化を測定した。金属酸化物の仕事関数を雰囲気中の酸素分圧に対してプロットした曲線の傾きは、金属不足型 (M_{a-x}O_b)、酸素過剰型 (M_aO_{b+x}) では正、酸素不足型 (M_aO_{b-x})、金属過剰型 (M_{a+x}O_b) では負となる。 Li_4SiO_4 ではその傾きが正であることがわかり、表面欠陥が金属不足型か酸素過剰型であることが明らかになった。

(2) 固体電解質の仕事関数に対する表面添加物の効果

安定化ジルコニア (ZrO_2) は、ソリッドステートの電池やセンサーに応用される固体電解質の代表的な例である。また、原子炉燃料被覆管として用いられているジルカロイの腐食によって酸化被膜が形成されるが、その酸化速度は不純物に影響される。本研究では、固体電解質および腐食の基礎的研究として、純 ZrO_2 、 $ZrO_2 + 2\%Y_2O_3$ 、 $ZrO_2 + 2\%Nb_2O_5$ について、高温ケルビン計を用いて雰囲気変化による仕事関数変化を測定した。それらの結果を相互に比較することにより、仕事関数の酸素分圧依存性が添加物の原子価に依存することを明らかにした。

3 今後の予定

高温ケルビン計については、約 1000 K までの温度で接触電位差が測定できることが確認できた。今後さらに高温での測定が可能となるべく装置の改善を行いたい。また、現在装置内の酸素ポテンシャルは露点計を用いて間接的に評価しているが、固体電解質 (ZrO_2) を用いた酸素計を導入することにより直接的に測定したい。

さらに、表面ならびにその近傍での粒子挙動を計算機によるシミュレーションで評価し、実験結果と比較、検討したい。

4 発表論文リスト

(A) 学位論文等

- (1) 鈴木 敦士, 「核融合炉固体増殖材の表面特性への雰囲気効果に関する研究」, 東京大学修士論文 (1996 年 3 月).
- (2) 清水 信行, 「量子機能性材料の表面電子特性に関する基礎研究」, 東京大学卒業論文 (1996 年 3 月).

(B) 国外学会誌等

- (1) A. Suzuki, K. Yamaguchi, M. Yamawaki and J. Nowotny, "Work function measurement of the surface of ceramic breeder under controlled atmosphere", presented at 4th Int. Workshop Ceramic Breeder Blanket Interactions, Kyoto, Japan, October 9-11 (1995).
- (2) A. Suzuki, K. Yamaguchi and M. Yamawaki, "Study on defect structure and stoichiometrically-varied surface layer formation of Li_4SiO_4 by means of work function measurement", Int. Symp. Material Chemistry in Nuclear Environment (Material Chemistry '96), Tsukuba, Japan, March 14-15 (1996).

(C) 国内学会誌等

- (1) 山脇 道夫, 鈴木 敦士, 「固体増殖材表面におけるスニープガス効果」, 弥生研究会: 第 6 回「核融合炉燃料サイクルの基礎過程」研究会, 東京, 3 月 25 日 (1996).

- (2) 鈴木 敦士, 清水 信行, 山口 憲司, 山脇 道夫, 「雰囲気制御下での Li_4SiO_4 仕事関数測定」, 日本原子力学会「1996 年春の年会」, M15, 吹田, 3 月 27～29 日 (1996).

4. 水素同位体ビームによる第一壁燃料ダイナミックスの研究

Study of First Wall Fuel Dynamics by Utilizing a Hydrogen Isotope Beam

研究テーマ代表者 山脇 道夫 (原子力工学研究施設)

1 序

本研究は、トリチウムを含む水素同位体と、第一壁の候補材料と目される各種金属ならびにセラミックス材料の間の相互作用を広範に調べることを目的としている。ここでは、単に個々の現象の解明にとどまらず、第一壁近傍における燃料・不純物の粒子ダイナミックスの評価に資するデータの取得にも重点が置かれている。

2 研究の進捗状況 (装置の改良等を含む)

(1) トリチウムビーム試験装置 (TBTS) によるプラズマ-材料相互作用 (PMI) の研究

核融合炉では D-T 反応により生じたヘリウム灰は燃料希釈と放射損失を引き起こし、点火条件の維持を困難にする。このヘリウム灰はダイバータによって排気されるが、ダイバータのヘリウム灰排気効率を向上させる方策の1つとして、ヘリウムを選択的に排気できるニッケル、バナジウム等の金属の使用が検討されている。本研究では、金属膜によるヘリウム灰排気特性に関する研究の一環として、トリチウムを含む水素同位体ビーム照射によるニッケル (Ni; 純度 99.7 %, 厚さ 0.1 mm) 中での水素同位体の保持挙動を調べた。

軽水素、重水素イオンを Ni に室温で照射した後、昇温脱離試験を行ったところ、脱離する水素同位体のピーク温度は、水素同位体の質量数が大きいものほど高くなることが分かった。トリチウム打ち込みに関しては、630 MBq のトリチウムガスを装置体系内に導入し、上述した Ni 膜に室温で照射を行った (入射エネルギー; 3 keV)。昇温脱離試験の測定結果から、Ni から脱離したトリチウムの化学形は DT と T₂ がほとんどであることがわかった。また、DT、T₂ としての脱離量は、四重極質量分析計による測定の結果、それぞれ、 2.1×10^{14} DT (0.37 MBq)、 3.4×10^{13} T₂ (0.12 MBq) であった (英文報告書参照)。

(2) 核融合プラズマ対向材における損耗・再付着現象の研究

核融合対向壁とプラズマとの相互作用により発生する不純物の挙動の研究は主プラズマへの混入阻止および対向壁の寿命という観点から非常に重要である。我々は以前に核融合の境界プラズマを模擬する定常型プラズマ発生装置 MAP (Materials And Plasma) を用いて、黒鉛、ほう素対向壁からスパッタされた炭素、ほう素不純物のプラズマ中における輸送過程の相違を明らかにするとともに、化学スパッタされた炭化水素のプラズマ中における温度分布を求めるなどのことを行ってきた (英文報告書参照)。さらに現在、ガスダイバータ等の中性原子または分子を多く含む低温高密度プラズマにおいて、水素分子と不純物分子とのエネルギー移行過程の評価を実験、計算両面から行うとともに、不純物粒子が壁に付着する過程を量子的に評価する研究を行っている。

(3) Mo における核融合炉燃料粒子輸送の律速過程

水素透過が少なく高融点金属のプラズマ対向材である Mo に関して、 D_2^+ ビーム注入による水素透過実験を行った。用いた試料は厚さ 0.1 mm、純度 99.95 % の多結晶 Mo 薄膜であり、これを超高真空容器内に設置し、3 keV D_2^+ ビームを照射した。ビーム照射中の照射側真空容器内の圧力は 1×10^{-3} Pa 台、透過側真空容器内の圧力は 1×10^{-6} Pa 台に維持された。重水素透過率を温度に対して Arrhenius プロットしたところ直線状となり、実験における最高温度 1000 K では 0.2 程度にまで達した。見かけの活性化エネルギーは 41.5 kJ/mol と算出された。透過スパイクは、900 K、800 K においてそれぞれ 2 分、30 分程度のタイムスケールで観察された。また、透過側表面に対する Ar^+ 照射によって透過速度に変化は殆んど見られなかった。これらの結果より、水素透過の律速過程は上流側は再結合律速、下流側は拡散律速と考えられる (英文報告書参照)。並行して、「その場 (*in-situ*)」オージェ電子分光法および二次イオン質量分析法によって、表面での carbide、oxide の存在、最外表面への S の偏析が観察された。

3 今後の予定

プラズマ-材料相互作用における粒子バランスの研究を、さらに「界面現象」という観点より発展させたいと考え、本テーマとは別個に新たなテーマを提案するに至った (固体表面近傍における粒子挙動の評価法の開発に関する研究: 代表; 山口 憲司)。今後も、さらに上述したような視点からのアプローチを続け、概算要求プロジェクトの推進に貢献したいと考えている。

4 発表論文リスト

(A) 学位論文等

- (1) V. V. Bandourko, "The kinetic parameters of surface processes during ion-material interaction", Thesis Dr. Eng., Univ. Tokyo, September 1995.
- (2) 佐藤 力哉, 「核融合炉材料中の水素同位体及びヘリウムの保持に関する研究」, 東京大学修士論文 (1996 年 3 月).
- (3) 近澤 佳隆: 「高 Z 高融点プラズマ対向材料における水素リサイクリング・透過挙動」, 東京大学卒業論文 (1996 年 3 月).

(B) 国外学会誌等

- (1) V. Bandourko, M. Yamawaki, K. Yamaguchi, N. Koborov, V. Kurnaev and D. Levchuk, "Simultaneous measurements of the particles reflection, reemission and permeation during low ion energy bombardment of niobium", 16th Int. Conf. Atomic Collisions in Solids, Linz, Austria, July 17-21 (1995).

- (2) V. Bandurko, K. Yamaguchi, K. Ohkoshi, M. Yamawaki, N. Koborov, V. Kurnaev and D. Levchuk, "The kinetic parameters of surface processes during ion-driven permeation through niobium membrane", presented at IUVSTA Int. Workshop Plasma Sources and Surface Interactions in Materials Processing, Fuji-Yoshida, Japan, September 20-22 (1995).
- (3) V. Bandourko, M. Yamawaki, K. Yamaguchi, V. Kurnaev, D. Levchuk and A. Pisarev, "Deuterium permeation through Nb during low energy ion irradiation at controlled surface conditions", presented at 7th Int. Conf. Fusion Reactor Materials, Obninsk, Russia, September 25-29 (1995).
- (4) S. Matsuyama, K. Yamaguchi, S. Tanaka and M. Yamawaki, "A basic study on erosion-redeposition processes in the boundary plasma region", presented at 7th Int. Conf. Fusion Reactor Material, Obninsk, Russia, September 25-29 (1995).
- (5) V. Bandurko, K. Ohkoshi, K. Yamaguchi, M. Yamawaki, N. Koborov, V. Kurnaev and D. Levchuk, "Effect of the ion-induced desorption on ion-driven deuterium permeation through niobium membrane", presented at 13th Int. Vacuum Congress, 9th Int. Conf. Solid Surfaces, Yokohama, September 25-29 (1995).
- (6) M. Yamawaki, V. Bandourko, K. Yamaguchi and K. Ohkoshi, "Permeation, trapping and reemission of deuterium implanted in Nb membrane", 4th Japan-CIS Workshop on Interactions of Fuel Particles with Fusion Reactor Materials, Obninsk, Russia, September 29-30 (1995).
- (7) K. Ohkoshi, K. Yamaguchi, V. V. Bandourko and M. Yamawaki, "Basic study on particle dynamics of fusion reactor fuel", presented at 3rd Sino-Japanese Symp. Materials for Advanced Energy Systems and Fission and Fusion Engineering, Chengdu, China, October 30 - November 3 (1995).
- (8) S. Matsuyama, K. Yamaguchi, S. Tanaka and M. Yamawaki, "Hydrocarbon transport in the laboratory plasma (MAP)", 7th Int. Toki Conf. Plasma Physics and Controlled Nuclear Fusion, Toki, Japan, November 28 - December 1 (1995).
- (9) M. Yamawaki, N. Chitose, V. Bandurko and K. Yamaguchi, "Impact of surface phenomena in metals on hydrogen isotope permeation", *Fusion Eng. Des.* 28 (1995) 125-130.
- (10) K. Yamaguchi, R. Satoh and M. Yamawaki, "Physical and chemical aspects of hydrogen transport in fusion reactor materials", *J. Grad. Sch. Fac. Eng. Univ. Tokyo (B)* 43(3) (1996) 251-281.

- (11) V. Bandurko, T. Nagasaki, K. Yamaguchi and M. Yamawaki, "Effect of surface impurities segregation and ion sputtering on ion driven deuterium permeation through copper", J. Nucl. Mater. 220-222 (1995) 904-907.

(C) 国内学会誌等

- (1) 松山 征嗣, 山口 憲司, 山脇 道夫, 「不純物輸送過程に関連した損耗再付着現象の研究」, 日本原子力学会「1995 年秋の大会」, F61, 東海, 10 月 17~20 日 (1995).
- (2) 山口 憲司, 佐藤 力哉, 山脇 道夫, 「種々の水素同位体ビームによるプラズマ対向材料との相互作用」, 日本原子力学会「1995 年秋の大会」, F63, 東海, 10 月 17~20 日 (1995).
- (3) ヴァシリ・バンドゥルコ, 大越 啓志郎, 山口 憲司, 山脇 道夫, 「重水素イオンによる Nb の透過、反射挙動」, 日本原子力学会「1995 年秋の大会」, F65, 東海, 10 月 17~20 日 (1995).
- (4) 松山 征嗣, 山口 憲司, 山脇 道夫, 「対向壁、損耗付着現象の研究」, 第 1 回核融合エネルギー連合講演会, A49, 京都, 12 月 4~5 日 (1995).
- (5) 山口 憲司, 山脇 道夫, 「水素同位体-黒鉛材料化学的相互作用」, 第 1 回核融合エネルギー連合講演会, C30, 京都, 12 月 4~5 日 (1995).
- (6) 佐藤 力哉, 山口 憲司, 山脇 道夫, 「金属中の水素の透過、保持の理論的研究」, 第 1 回核融合エネルギー連合講演会, C42, 京都, 12 月 4~5 日 (1995).
- (7) バンドゥルコ・ヴァシリ, 山口 憲司, 山脇 道夫, 「重水素ビーム-バナジウム合金の相互作用における表面過程」, 第 1 回核融合エネルギー連合講演会, C44, 京都, 12 月 4~5 日 (1995).
- (8) 大越 啓志郎, 山口 憲司, 山脇 道夫「ニオブ膜に対する燃料粒子ダイナミクスと Ar による照射効果」, 第 1 回核融合エネルギー連合講演会, C46, 京都, 12 月 4~5 日 (1995).
- (9) 松山 征嗣, 山口 憲司, 山脇 道夫, 「定常プラズマ実験装置を用いた炭化水素輸送実験」, 日本原子力学会「1996 年春の年会」, J34, 吹田, 3 月 27~29 日 (1996).
- (10) 佐藤 力哉, 岡田 光正, 山口 憲司, 山脇 道夫, 「Ni 中の水素同位体保持に対する He の影響」, 日本原子力学会「1996 年春の年会」, J43, 吹田, 3 月 27~29 日 (1996).
- (11) 大越 啓志郎, ヴァシリ バンドゥルコ, 近澤 佳隆, 山口 憲司, 山脇 道夫, 「重水素イオン照射による Mo の透過・再放出挙動」, 日本原子力学会「1996 年春の年会」, J44, 吹田, 3 月 27~29 日 (1996).

5. プラズマ/壁界面における水素や水蒸気の吸着・脱離に関する量子化学的検討 Study on Sorption and Release of H₂ and H₂O on/from Plasma/Wall Interface Based on Quantum Chemistry

研究テーマ代表者 長崎 晋也 (システム量子工学専攻)

1. 序

核融合炉の成立性を確証するためには、第一壁材料あるいはブランケット材料中における粒子輸送現象を解明する必要がある。第一壁あるいはブランケット材料中の粒子輸送に関しては、これまで数多くの実験的・理論的研究が行われてきたが、今後メカニズムにまで踏み込んで現象を理解するためには、マクロな観点からのアプローチだけではなく、材料を構成する原子・分子1個ずつと粒子1個との相互作用にまでミクロな観点から理解する必要がある。つまり、空間的にかつまた時間的にもミクロな次元の現象を理論と実験の両面から解明し、マクロ現象の理解へとつなげることが重要であると考えられる。

このような原子レベルでの相互作用を理論的に取り扱う手法に量子化学計算がある。そこで、本研究では、第一壁候補材あるいはブランケット候補材中における粒子輸送現象をミクロに解明するために、まず代表的な金属酸化物を取り上げ、その構造や電子状態が量子化学計算で予測できるかどうかを検討した。本報告書はその経過報告である。

2. 研究進捗状況

本研究では、代表的な金属酸化物であり、量子化学計算用のデータの整備されているSiO₂とAl₂O₃を取り上げ、かつある程度複雑な形状に対応し得るものかどうかを確認するためにSiO₂とAl₂O₃の層状酸化物を検討した。モデルは、半経験的分子軌道計算プログラムMOPAC (Version 6.0; J. P. S. Stewart) 上で構築し、本プログラムに含まれるPM3法を用い計算を行った。

計算の結果、これまでの実験から推測される負電荷と比較して価電子の分布が小さく、表面に出現する負電荷も計算結果を通じて小さいことがわかった。また、SiのAl置換による余剰負電荷が周辺のO原子に局在せず、周囲に大きく広がること、ならびにAlのスパークル置換による余剰負電荷が表面まで分布せずAl周辺のO原子に局在することがわかった。

3. 今後の予定

実際の第一候補材あるいはブランケット候補材を取り上げ、その構造や電子密度等を評価するとともに、輸送される粒子の電子雲との重なりがその輸送にどのような影響を及ぼすかを検討する。

4. 発表論文リスト

梅村康洋、長崎晋也、鈴木篤之、「半経験的分子軌道法による粘土鉱物構造中の電荷分布計算」、日本原子力学会 春の年会、大阪大学、大阪、平成8年3月27-29日

6. ディスラプション時の第一壁の挙動

Behavior of First Wall During Plasma Disruption

研究テーマ代表者 班目 春樹 (原子力工学研究施設)

1 序

本研究グループは、ディスラプション時の金属製第一壁熔融凝固挙動とカーボン製プラズマ対向材料の蒸発挙動に関して実験と解析を実施して来ている。本年度は後者のテーマについて集中的に研究を実施した。

2 研究進捗状況

昨年度実施したMPDアークジェットの改造によって、パルス幅を短くし、より高熱負荷を与えることができるようになった。本年度は、改良されたMPDアークジェットを用い、カーボンの蒸発挙動に関する実験を実施した。従来、実験に用いているカーボンは、蒸発量を多くするために、熱伝導率の悪いパイロ黒鉛を用いていた。本年度は、計算コードとの比較を容易にするために、通常の等方性黒鉛 (IG-110) を用い、照射実験を実施した。なお、等方性黒鉛は熱伝導率が良いため、パイロ黒鉛に比して蒸発量は数桁少くなると予想される。そこで、光学レンズを調整し、蒸発したカーボンの発光を、精度良く計測できるようにした。

改良されたMPDアークジェットにより黒鉛に熱負荷を加えると、飛散した粒子がプラズマと相互作用する事により、 C^+ 、 C^{++} などに変化する。これらの粒子の発光を分光分析により捉え、時間・空間分布を測定した。その結果、等方性黒鉛の発光分布は、従来のパイロ黒鉛の場合の発光分布と異なる事が判った。

- 照射を繰り返す事により、発光量が単調に増大する。
- パイロ黒鉛の場合よりも遅れて、大量の発光が観測される。

これらの現象は、照射による蒸発・再付着挙動や、ガスの影響によると考えられるが、その原因に関しては現在調査中である。

3 今後の予定

等方性黒鉛の発光分布に関して、パイロ黒鉛と異なる理由に関して調査を実施する。さらに、得られた実験データから、そのメカニズムを考察する。

プラズマと蒸発黒鉛との相互作用に関して、実験結果を評価するとともに、解析コードを開発する。これにより、プラズマ対向材料へのエネルギー入射にたいする蒸気雲の影響を明らかにするとともに、将来的にはプラズマとプラズマ対向材料を同時に扱う解析コードの開発を目指す。

4 発表論文リスト

(C) 国内学会誌等

1. 助川 敏雄、岡本 孝司、班目 春樹、「模擬ディスラプション時の黒鉛の蒸発挙動」、日本原子力学会春の年会予稿集、(1996)、H18.

7. 高温超電導体の核融合炉高度化への応用

Application of High Tc Superconductor to Development of Fusion Reactor

研究テーマ代表者 宮 健三 (原子力工学研究施設)

1. 序

近年、高温超電導体の開発には目覚ましいものがあり、その工学的応用は多岐に渡って考えられている。本研究では、磁気閉込め方式核融合炉に対する高温超電導体の応用を様々な面から検討する。高度な電磁場の制御が求められる核融合炉に於いて、高温超電導体の持つ様々な電気磁氣的性質を利用することはその高度化に大きく貢献するものと考えられる。本年度は、「高温超電導体によるトカマクプラズマ位置不安定性改善手法」について研究を実施した。これは高温超電導体の有する磁束ピン止め効果を利用しプラズマ電流が作る磁束を超電導体内に捕捉し、最終的にプラズマの位置を安定化させるものである。本手法の有効性の検証のために、以下に挙げるプラズマ-高温超電導連成数値解析及び高温超電導動的特性実験を行なった。

2. 研究進捗状況

平成7年度の研究テーマとその内容は以下の通りである。

(a) プラズマ-高温超電導連成数値解析

高温超電導体をトカマクプラズマに配置した場合の安定化効果を評価するために、プラズマ動的平衡計算および超電導遮蔽電流計算の連成解析を実施した。プラズマ動的平衡計算は、プラズマ、コイル群、構造物を複数のリング電流で近似する簡易計算手法を用い、高温超電導遮蔽電流計算については、臨界状態モデルに基づいて解析をおこなった。計算体系として、ITER(国際熱核融合実験炉)の概念設計を選び、そのプラズマ周辺に、Bi系高温超電導線材を配置した場合のプラズマ位置の時間発展を評価した。その結果高温超電導体を配置することにより、プラズマの寿命は msec のオーダーから min のオーダーに向上するとの結果が得られ、高温超電導体によりプラズマの位置安定性は著しく改善することが判った。

(b) 核融合炉磁場環境下における高温超電導体の動的特性解明

高温超電導体をプラズマ位置制御に応用する場合、核融合炉の磁場環境下でのプラズマと高温超電導体との相互作用の解明が必要となってくる。そこで、コイルにより、プラズマを模擬した高温超電導体の実験を実施し、非常に速い磁場変化の際に誘起される超電導遮蔽電流の支配的パラメータを調べた。コイル磁場のパルス長は、0.1 ~ 30 msec というプラズマ位置不安定性の時定数に相当する範囲を選んだ。その結果、核融合炉の磁場環境下では超電導遮蔽電流はフロー抵抗に大きく依存することが判明した。さらに超電導体のフロー抵抗

を実験的に同定することを行なった。

3. 装置の改良等

2 mF コンデンサーバンクによるパルスコイル電源を用いて、高温超電導体パルス励振装置を組み立てた。本装置は、片持ち梁に固定された超電導体、パルスコイル及び振動波形測定系 (レーザー変位計) からなる。

4. 発表論文リスト

(A) 学位論文等

- (1) 井勝伸彦：「高温超電導体によるプラズマの位置不安定性の抑制」、修士論文
- (2) 津守秀昭：「分子動力学による超電導電磁現象の数値解析」、卒業論文

(B) 国外学会誌等

- (1) T.Uchimoto, K.Miya and Y.Yoshida: Reduction of troidal ripple by using high Tc superconductors, Fusion Engrg. Design, 27 (1995) 528-535.
- (2) T.Uchimoto, Y.Yoshida and K.Miya: Application of high Tc superconductor to passive control of plasma position, Abstr. The International Symposium on Non-linear Electromagnetic Systems (1995) A-46
- (3) Y.Fukuzaki, T.Uchimoto and K.Miya: Design Study of High Tc Superconducting Tokamak, IWAM Proc. (1995) 184-187.
- (4) Y.Aizawa, N.Ikatsu, Y.Yoshida and K.Miya: Numerical simulation of halo current in tokamak devices, Digests of 4th Jpn.-Polish Jt. Semin. Electromagn. Phenom. Appl. Technol., 30-33.
- (5) Y.Luo, K.Demachi, Y.Yoshida, K.Miya and H.Higasa: Numerical analysis of the levitation force in high Tc superconducting levitation system of a flywheel, Proceeding of 8th International symposium on superconductivity (1995) (in press).
- (6) K. Demachi, Y. Yoshida, H. Asakura and K. Miya: Numerical Analysis of Magnetization Processes in Type II Superconductors based on Ginzburg-Landau Theory, IEEE Trans. Magn. (1996) to be published.
- (7) K. Demachi, H. Asakura, Y. Yoshida and K. Miya: Numerical Analysis of Type II Superconductor based on Ginzburg-Landau Theory, Interdisciplinary Applied Electromagnetics (Proc. of the 3rd Japanese-Czech-Slovak Joint Seminar on Applied Electromagnetics) (1996) to be published.

- (8) K. Demachi, Y. Yoshida, and K. Miya: Mesoscopic Analysis of Fluxoids in Type II Superconductor, Proc. 1st Int. Workshop on Advanced Mechatronics (1995) 192-196.
- (9) N. Takeda, M. Uesaka and K. Miya: Influence of Applied Magnetic Field on Shielding Current Paths in High Tc Superconductor, Cryogenics Vol. 35 (1995) 893-899
- (10) N. Takeda, Y. Yoshida, M. Uesaka and K. Miya: Numerical analysis of restoring and levitation forces in high Tc superconducting levitation system, Elsevier Studies in Applied Electromagnetics in Materials Vol. 6 (1995) 387-390
- (11) R. Shinagawa, A. Takeshita, N. Takeda, Y. Yoshida and K. Miya: Study on Superconducting Shielding Current with Anisotropy of Critical Current Density in NbTi, Proceedings of the 1st International Workshop on Advanced Mechatronics, (1995) 188-191.

(C) 国内学会誌等

- (1) 井勝伸彦、内一哲哉、宮 健三：高温超電導体によるトカマクプラズマ位置不安定性抑制日本原子力学会「1995 秋の大会」予稿集、(1995, 日本原子力学会) 56. Reduction of vertical instability in tokamak plasma by using high Tc superconductor, (Abstr. 1995 Fall Meet. Atomic Energy Soc. Jpn.).
- (2) 品川 亮介、竹下 明、武田 信和、吉田義勝、宮 健三：NbTi/Nb/Cu 多層複合材カップの磁気遮蔽効果に関する数値計算、第 54 回 1995 年度 秋期 低温工学・超電導学会 講演概要集 (54th Meeting on Cryogenics and Superconductivity) (1995, 低温工学・超電導学会) 283.
- (3) 羅 雲、出町和之、宮 健三、樋笠博正：高温超電導の磁気軸受けへの応用 (Application of HTSC in magnetic bearing)、1995 年度秋季、54th 「低温工学・超電導学会」予稿集 (Abstr. 54th Meeting on Cryogenics and Superconductivity) (1995, 低温工学会他) 250
- (4) 内一哲哉、井勝伸彦、吉田義勝、宮 健三：高温超電導体のトカマク式核融合炉への応用 (Application of high Tc superconductors to tokamak fusion reactors)、第 1 回核融合エネルギー連合講演会 予稿集 (Abstr. The First Joint Symposium on Fusion Energy) (1995, 核融合エネルギー連合講演会) 265-266.
- (5) 福崎康博、内一哲哉、宮 健三：高温超電導安定化トカマクの運転シナリオに関する研究 (Study of operating scenario of High Tc Superconducting Tokamak)、第 1 回核融合エネルギー連合講演会予稿集 (Abstr. 1995 The First Joint Symposium on Fusion Energy) (1995, 核融合エネルギー連合講演会) 267-268.
- (6) 羅 雲、内一哲哉、吉田義勝、宮 健三：高温超電導集合体のトロイダル磁場リップル値の抑制における応用 (Application of HTSC bulks in reduction of ripple of toroidal magnetic field)、日本原子力学会他「第 1 回核融合エネルギー連合講演会」予稿集 (Abstr. 1st Joint Symposium on Fusion Energy) (1995, 核融合エネルギー連合講演会) 269-270.

- (7) 出町和之、津守秀昭、宮 健三：高温超電導体 (HTSC) の核融合炉への応用 (1) – 高温超電導体の基礎特性の評価 – (– Evaluation of the basic property of the High Tc Superconductor –)、日本原子力学会「1996 春の大会」予稿集 (Abstr. 1996 Spring Meet. Atomic Energy Soc. Jpn.) (1996, 日本原子力学会) 396.
- (8) 品川 亮介、武田 信和、宮 健三：高温超電導体の核融合炉への応用 (2) – 高温超電導体の異方性の評価 – (– Assessment of Anisotropy in HTSC (High Tc Superconductor) –)、日本原子力学会「1996 春の大会」予稿集 (Abstr. 1996 Spring Meet. Atomic Energy Soc. Jpn.) (1996, 日本原子力学会) 397.
- (9) 羅 雲、出町和之、宮 健三：高温超電導体の核融合炉への応用 (3) – HTSC フライホイールの検討 – (– Study on HTSC flywheel –)、日本原子力学会「1996 春の大会」予稿集 (Abstr. 1996 Full Meet. Atomic Energy Soc. Jpn.) (1996, 日本原子力学会) 398.
- (10) 福崎康博、内一哲哉、宮 健三：高温超電導体 (HTSC) の核融合炉への応用 (4) HTSC バルク集合体によるポロイダル磁場の整形 (– Reform of poloidal field by using HTSC bulk assembly –)、日本原子力学会「1996 春の年会」予稿集 (Abstr. 1996 Spring Meet. Atomic Energy Soc. Jpn.) (1996, 日本原子力学会) 399.
- (11) 内一哲哉、宮 健三：高温超電導体 (HTSC) の核融合炉への応用 (5) –HTSC バルク集合体によるトカマクプラズマ位置不安定性抑制– (– Reduction of vertical instability in tokamak plasma by using HTSC bulk assembly –)、日本原子力学会「1996 春の年会」予稿集 (Abstr. 1996 Spring Meet. Atomic Energy Soc. Jpn.) (1996, 日本原子力学会) 400.
- (12) 井勝伸彦、内一哲哉、宮 健三：高温超電導体 (HTSC) の核融合炉への応用 (6) – 高温超電導体とプラズマ相互作用の模擬実験による検証 –、(– Verification of interaction between high Tc superconductor and plasma by mock experiment –)、日本原子力学会「1996 春の年会」予稿集 (Abstr. 1996 Spring Meet. Atomic Energy Soc. Jpn.) (1996, 日本原子力学会) 401.
- (13) 井勝伸彦、内一哲哉、宮 健三：高温超電導体によるプラズマ位置不安定性の抑制、第 5 回 MAGDA カンファレンス 予稿集 pp49-54 (1996 日本 AEM 学会). Improvement of plasma vertical instability with use of high Tc superconductor, Abstr. 5th MAGDA confence, pp49-54.
- (14) 羅 雲、出町和之、宮 健三、樋笠博正：高温超電導フライホイールにおける磁気浮上力の解析 (Numerical analysis of the magnetic force in HTSC flywheel)、AEM Soc. Jpn. 「Fifth MAGDA Conference」Proceeding (1996, 日本 AEM 学会) 60-65

8. 核融合炉第一壁の電磁的非破壊検査

Electromagnetic Nondestructive Evaluation of Fusion Reactor First Wall

研究テーマ代表者 宮 健三（原子力工学研究施設）

1. 序

本グループは、今後の核融合炉工学において重要な課題の一つとなり得る第一壁・炉内構造物の非破壊検査について、特に電磁現象を応用した手法の適用性について、研究を進めている。平成7年度には主として渦電流探傷法の高度化についての研究を実施した。また、核融合炉体系への従来の非破壊検査手法（渦電流探傷法、電位差法、超音波診断法、SQUID等）の適用性についても調査を実施した。

2. 研究進捗状況

(a) 渦電流探傷解析技術の高度化に関する研究

原子力発電プラントや航空機の検査に盛んに適用されている渦電流探傷技術の核融合炉への適用を考えた場合、検査対象である第一壁等は半空間もしくは平板等の単純な形状に近似して取り扱うことが可能である。このような幾何学形状の場合には、導体中の特異ソースの作る電磁場はダイアディックグリーン関数として求められており、これを利用した低コスト・高精度の順問題解析が可能である。従来はグリーン関数として、電気的グリーン関数を用いる手法が主流であったが、新たに、ベクトルポテンシャルのグリーン関数を用いた手法を開発した。この定式化では積分核の特異性が弱く、数値計算の際の取り扱いに自由度が大きいという利点があり、さらに、検査対象の肉厚が十分大きい場合には理論的取り扱いの発展性に富むと考えられる。モーメント法に基づく数値計算コードを開発し、測定値と比較することにより、理論の妥当性が示され、高精度・高速度の順問題解析が可能となった。

(b) 渦電流探傷プローブの最適設計に関する研究

渦電流探傷プローブとしては、自己誘導型もしくはインピーダンス型と呼ばれる単一コイルから成るプローブ以外にも、複数のコイルを組み合わせた相互誘導型プローブ、差動型プローブ等、さまざまな種類のものが考え出されている。本研究ではまず、数値計算によって、代表的なプローブの探傷性能（リフトオフ変化等の誤差要因に対する検出能）を評価した。さらに、欠陥とプローブの組み合わせを変化させた場合の渦電流パターンを綿密に検討した結果、励起磁場の欠陥に対する水平成分が大きい場合ほど、欠陥を横切ろうとする渦電流が強く、このため、欠陥による渦電流の乱れ（すなわち、プローブ測定信号の変化）が大きくなることが判明した。この事実は、プローブ設計の指針と成り得るものである。また、この事実から、渦電流による反磁場を無視した場合でも、プローブの検出能は精度良く評価できることが分かり、プローブコイルの最適設計につながる成果が得られた。

3. 装置の改良等

特になし。

4. 発表論文リスト

(A) 学位論文等：該当なし

(B) 国外学会誌等

- (1) G.Chen, Y.Yoshida, K.Miya and M.Uesaka: Application of ECT inspection to the first wall of a fusion reactor with wavelet analysis, Fusion Engrg. Design, 27 (1995) 309-316.
- (2) Z.Chen and K.Miya: Application of Wavelet Analysis in Eddy Current Problems with Current Vector Potential Method, Abstr. Int. Symp. Non-linear Electromagn. Systems, 1995, D-12.
- (3) M.Uesaka, K.Miya and A.Takahashi: Micro-ECT by flexible microloop magnetic sensor array, *ibid*, E-28.
- (4) K.Kitsuta, M.Uesaka and K.Miya: Nondestructive evaluation via magnetic property for steel components of a nuclear power plant, *ibid*, E-31.
- (5) G.Chen, Y.Yoshida and K.Miya: A data processing method for eddy current testing of steam generator tubing, *ibid*, E-33.
- (6) Z.Chen, Y.Yoshida and K.Miya: Analysis of relations between defect shapes and wavelet coefficients of ECT data, Stud.Appl. Electromagn.Mech., 8 (1996) 295-302.
- (7) K. Kitsuta, A. Gilanyi, M. Uesaka, K. Miya, K. Aoki, A. Takahashi: Flexible Microloop Magnetic Sensor Array for Intelligent Nondestructive Eddy Current Testing, Int. Symp. Microsystems, Intelligent Materials and Robots Sendai, Japan, Sep. 1995.
- (8) A.Gilanyi, M. Uesaka, K. Miya: Electromagnetic Nondestructive Evaluation for Nuclear Power Plants, 5th MAGDA Conf., 1996, 55-59.
- (9) K.Kitsuta, M.Uesaka and K.Miya: Nondestructive evaluation for steel components in nuclear engineering via magnetic property, Digests of 4th Jpn.-Polish Jt. Semin. Electromagn. Phenom. Appl. Technol., 139-142.

(C) 国内学会誌等

- (1) 陳 振茂、吉田義勝、宮 健三、黒川政秋：差動型 ECT プローブの検出性能評価日本原子力学会「1995 秋の大会」予稿集 (1995, 日本原子力学会) 211.
- (2) A. Gilanyi, Z. Chen, K. Miya: Application of Wavelet to Differential Equation with Green Function Technique, 8th JSME CMD Conference, Nagano, Nov. 1995.

9. 照射による材料組織・強度特性変化の研究

Irradiation-Induced Microstructural and Mechanical Property Changes in Fusion Materials

研究テーマ代表者 幸野 豊 (材料学専攻)

1. 序

核融合炉材料としての使用が期待されるオーステナイト鋼、フェライト鋼、TiAl 金属間化合物、各種複合材料等の幅広い材料の核融合炉照射環境での挙動に関する研究が実施されている。具体的には、照射による微細組織変化とそれにとまなう各種強度特性変化の定量的相関を明らかにするための実験的手法の設計と開発、損傷組織発達に及ぼす外部応力効果の検討、溶接部材への照射効果の検討などである。これらの研究を通じ核融合炉環境下での材料の直面する個々の問題に関し問題解決型の研究努力が進められている。

2. 研究進捗状況及び今後の予定

基本的には数年前より設定し遂行してきた研究マスタープランに従ってほぼ順調に進捗している。材料の構造及び特性変化にたいする照射効果の研究は本テーマの枠内では高エネルギー加速粒子を用いて、上記の諸材料に対して行われており、粒子線による重照射効果に加え損傷速度の効果、ヘリウム同時照射の効果、外部応力効果などの各種照射環境因子の影響について系統的に研究を行っている。これらの研究は、さらに超高压電子顕微鏡による電子線照射、原子力研究総合センターの HIT 設備での二重ビーム同時照射、JOYO、FFTF/MOTA、EBR-II などで的高速中性子照射などの結果と連携して総合的な検討を加え、照射関連の問題について多くの新しい成果を挙げつつある。さらに、このような各種照射実験による研究と並行して、数値計算実験による照射損傷基礎過程の研究を行っている。現在までに、ヘリウム同時照射照射効果、非定常照射温度履歴効果、微量添加元素の効果について照射実験から得られた結果をよくシミュレートしうる結果が得られている。現在、外部応力効果に関連する現象を中心に数値計算実験を行っているが、今後さらに、照射硬化、照射誘起析出や偏析、溶接部材への照射効果等について数値計算実験と照射実験の両面から機構論的理解を進めていく。

3. 装置開発。整備など

HIT 設備における二重ビーム同時照射実験に関連し、従来より更に高度且つ精密な照射温度計測と制御を可能にするべく、試料温度そのものをその場測定できる機構がシステムとして完成した。本システムは遠隔制御可能であり、測定精度の向上とともに実験効率の向上に大きく寄与している。さらに本システムを発展させるべく高速温度制御機構及び大容量能動加熱機構を計画し設置しようとしており温度精度面では大きな改善が計られようとしている。また、試料位置制御システムに関しても従来の機構を一新し、高速で且つ位置制御精度が一段と改良された機構に置き換えることができた。

4. 発表論文リスト

学位論文等

- (1) 坂田 祐司 : 「中性子照射によるオーステナイト鋼の照射硬化に関する研究」
修士論文、1996年3月

- (2) 笠井 康成 : 「TiAl 金属間化合物の強度特性に関する研究」
修士論文、1996年3月

学会発表など

第116回日本金属学会

- (1) 小川 正毅、坂田 祐司、幸野 豊、香山 晃、松井 秀樹、 “TiAl 金属間化合物の高速中性子照射効果”
(2) 香山 晃、R.H. Jones、佐東 信司、 “SiC/SiC 複合材料の照射下における問題”
(3) 谷川 博康、加藤 雄大、幸野 豊、香山 晃、 “fcc 金属の照射下転位ループ組織発達に及ぼす外部応力の効果”
(4) 坂田 祐司、谷川 博康、幸野 豊、香山 晃、渡辺 誠、 “Fe-Cr-Ni 合金の損傷組織の三点曲げ試験による変形組織”
(5) 幸野 豊、香山 晃、鳴井 実、朝倉 健太郎、 “中性子照射した低放射化フェライト鋼の機械的性質変化”
(6) 香山 晃、加藤 雄大、幸野 豊、D.S. Gelles、菱沼 章道、渡辺 誠、 “316 鋼溶接継手の中性子重照射損傷組織”
(7) 佐藤 通隆、浜田 賢一、佐東 信司、瀬戸 佐智生、香山 晃、 “SiC(Ti₂O₃)/SiO₂ 複合材料の微小領域での硬度評価”
(8) 渡辺 健一郎、浜田 賢一、佐東 信司、香山 晃、 “C/C 複合材料中の繊維に対する微小押し込み試験”
(9) 佐東 信司、綱川 英男、浜田 賢一、香山 晃、 “C/C 複合材料を熱処理した時の気孔の微細構造変化”
(10) 綱川 英男、浜田 賢一、佐東 信司、香山 晃、 “C/C 複合材料の熱処理による界面構造変化”

第117回日本金属学会

- (1) Y. Sakata, Y. Katoh, Y. Kohno, A. Kohyama and T. Kishi, “The Evaluation of Mechanical Properties of Irradiated Austenitic Steels by Means of Micro-indentation Technique”
(2) Y. Katoh and T. Muroga, “Theoretical Assessment of the Influence of Clustered Defect Formation on Microstructural Development”
(3) A. Kohyama and Y. Kohno, “Present Status of JLF-1 Steel for Nuclear Fusion Reactors”
(4) H. Tanigawa, Y. Katoh and A. Kohyama, “A Modeling of Radiation Induced Microstructural Evolution under Applied Stress in Austenitic Alloys”
(5) H. Serizawa, K. Watanabe, S. Sato and A. Kohyama, “Elastic FEM Analysis of Fiber Push-out Test for C/C Composites”
(6) K. Watanabe, H. Serizawa, K. Hamada, H. Tsunakawa, S. Sato, A. Kohyama and T. Kishi, “Effect of Specimen Thickness on Interfacial Sliding Strength of C/C Composite under Fiber Push-out Test”

1 0. 第一壁の画像解析に関する研究

Study on Image Analysis for First Wall

研究テーマ代表者 岡本 孝司（原子力工学研究施設）

1 序

本グループは、昨年度までの「干渉画像を用いた三次元密度分布測定」を発展させ、密度分布計測だけではなく、レーザを用いた材料のマクロな探傷解析や、熱変形解析などへの応用を考慮した、検討を実施している。画像情報は2次元の情報であり、大量の情報を容易に得る事ができる。このため、それらの情報の中から必要な情報を抽出する技術が重要である。特に、画像解析により、密度や変形量などの物理量分布を計測し、そこから環境の情報を得ようとする事が可能である。この応用研究の中から、密度の3次元場計測、流速の3次元分布計測手法、など3次元的な挙動を解析することを実施した。

2 研究進捗状況

本年度の研究テーマとその内容は以下の通りである。

三次元密度分布計測 核融合炉における真空喪失事故の評価、及び冷却材配管破断事故などの安全評価においては、事故時に発生する気体の挙動を正確に把握する必要がある。このため、実験的、解析的に気体の挙動を評価することが重要である。特に、気体の場合は温度差、密度差により非線形で複雑な挙動を示す。このような複雑な挙動を数値的にシミュレートするためには、その基礎的な挙動を実験的に把握する必要がある。

本研究においては、密度差置換流や、密度成層流などの基礎的な現象について、実験的な研究を実施した。Nd-YAG レーザを用いたホログラム装置を製作し、リアルタイムホログラム法やホログラフィックPIV法などの実験を実施できるように装置を整備した。特に、ホログラムを用いた3次元流速分布計測手法を応用し、密度分布と流速分布を同時に計測する手法に関して予備的な実験を実施した。その結果、本手法を改良する事により、高精度な流速密度同時測定法を構築できる事をしめした。

三次元動画画像解析 液体金属ブランケット内の冷却材などの流れを解明することは、核融合炉設計上重要な課題である。これらの流れは3次元的なものであり、従来の計測手法では局所的なデータしか得ることが出来なかった。しかしながら、ロボットビジョンの検討で得られた画像認識システムを用いることによって、3次元的な流れの状況を一度に取得することが可能となる。画像データは2次元情報しか持っていないため、これらを組み合わせる3次元情報を構築するためのアルゴリズムを研究する必要がある。三次元流速分布測定手法としては、本研究によって開発した流速ベクトルヒストグラム法を発展させ、簡易な装置で汎用的な三次元流速を計測することを試みている。さらに、粒子パターンの変形に対応した、全く新しい粒子画像流速測定アルゴリズムを開発し、三次元的な流動場に適用する事を試みている。

3 今後の予定

ホログラムによる3次元密度場流速場同時測定法を確立するとともに、核融合炉で想定されている真空破壊事故時の挙動を解析する。

さらに、ホログラムを熱変形のある場に適用し、温度分布(屈折率変化)と変形量の同時測定の可能性に関して検討を実施する。

4 主な発表論文リスト

(A) 学位論文等

1. 小泉 雅樹「多時刻画像を用いたバネモデル粒子追跡法の高精度化」東京大学卒業論文(1996年3月)

(B) 国外学会誌等

1. Okamoto, K., Hassan Y.A. and Schmidl, W.D., "New Tracking Algorithm for Particle Image Velocimetry," *Experiment in Fluids*, Vol.19, No.5, (1995) 342-347.
2. Okamoto, K., "Three-dimensional Particle Tracking Algorithms: Velocity Vector Histogram and Spring Model," *Proc. PIV-Fukui'95*, (1995) 21-32.
3. Okamoto, K., Schmidl, W.D. and Hassan, Y.A., "Spring model tracking algorithm for three-dimensional particle image velocimetry," *ASME FED*, Vol.209 (1995) 91-97.
4. Okamoto, K., Schmidl, W.D. and Hassan, Y.A., "Simple calibration technique using image cross-correlation for three-dimensional PIV," *ASME FED*, Vol.209 (1995) 99-106.
5. Okamoto, K., Schmidl, W.D. and Hassan, Y.A., "Least Force Technique for the Particle Tracking Algorithm," *Flow Visualization VII*, Begell House, (1995) 647-653.

(C) 国内学会誌等

1. 岡本 孝司、鶴 大悟、馮 堅、文沢 元雄、「3次元密度分布計測へのGAの応用」可視化情報学会誌、Vol.15-S1 (1995) 173-176.
2. 鶴 大悟、佐藤 泰、班目 春樹、岡本 孝司、文沢 元雄、菱田 誠、「仕切りのある開口部における密度差駆動置換流」可視化情報学会誌、Vol.15-S1 (1995) 245-248.
3. 岡本 孝司、Philip O.G., Hassan, Y.A. 「PIVによる自由液面変動と流速変動の同時計測」可視化情報学会誌、Vol.15-S1 (1995) 261-264.
4. 岡本 孝司、「バネモデル法粒子追跡アルゴリズム」可視化情報学会誌、Vol.15-S2 (1995) 193-196.
5. 岡本 孝司、Schmidl, W.D., Hassan, Y.A. 「相関法を利用した簡易3次元粒子位置計測法」可視化情報学会誌、Vol.15-S2 (1995) 197-200.
6. 鶴 大悟、佐藤 泰、班目 春樹、岡本 孝司、文沢 元雄、菱田 誠、「垂直仕切りのある矩形開口部における水-塩水置換流」、日本原子力学会秋の大会予稿集、(1995), E38.

1 1. レーザー共鳴イオン化分光を用いた核融合炉材料界面特性の評価手法の開発 Development of Surface Characterization for Fusion Materials Using Laser Resonance Ionization Spectroscopy

研究テーマ代表者 井口 哲夫 (原子力工学研究施設)

1. 序

核融合炉環境下に置かれた材料界面では、プラズマ粒子の衝撃による材料損耗、燃料粒子のリサイクリング、中性子による核変換粒子の生成と移行など、極めて複雑な粒子輸送現象が生じており、これらは材料の界面状態に大きく影響される。従来、界面特性の評価、特にイオンスパッタリングや表面粒子吸脱着の特性評価実験において、電子やイオンビームをプローブとする分析法が用いられているが、中性粒子の分析には不向きであった。この界面近傍の中性粒子分析に有効な手法として、レーザー共鳴イオン化分光法(Resonance Ionization Spectroscopy:RIS)、即ち、特定の原子・分子のエネルギー準位幅に相当する波長の光子を、単一又は複数の波長可変レーザーで生成し、同時照射することによって、その特定の原子・分子を共鳴的に選択励起かつ分離する超高感度な元素分析法の適用が考えられる。

本研究は、現在、高速中性子科学研究設備の1つとして設置・整備されつつあるRISシステムを活用して、荷電粒子や高速中性子照射下での核融合炉材料界面現象、特に中性粒子挙動のその場観測技術としての確立と応用を目的としている。

2. 研究進捗状況

今年度実施された主な研究概要は、次の通りである。

高速中性子科学研究設備のRISシステムは、3本の波長可変レーザー(モードロックTi:サファイアレーザー1基とパルスNd:YAGレーザー励起色素レーザー2基)と飛行時間型質量分析計で構成されるが、これまでに、個々の装置の立ち上げと仕様性能が確認されている。今年度は、特に、色素レーザー系1本と質量分析計のみを組み合わせて、気体試料の分析手順を確立し、Xeガス検出に基づいて、レーザー波長・出力依存性や検出限界などの基本的なシステム性能を明らかにした。また、固体試料のレーザーアブレーションによる原子蒸気化システムの導入・整備を進めている。

3. 今後の予定

本研究プロジェクトは、立ち上がったばかりであるが、研究代表者が他大学へ転任したことに伴い、とりあえず今年度を以て、終了とせざるを得ない。しかしながら、本研究の基幹設備であるRISシステムは共同利用が可能であり、今後、中沢研(工・システム量子)グループとの共同研究プロジェクトとして遂行される予定である。

4. 発表論文リスト

(A) 学位論文

- (1) 杉山完二郎、"共鳴イオン化質量分析法を用いた超高感度FPガスモニタリング", 東京大学修士論文(1995年3月)
- (2) 門藤健司、"共鳴イオン化質量分析法を用いた破損燃料検出システムの開発" 東京大学卒業論文(1996年3月)

(B) 国外学会誌等

- (1) T. Iguchi, Y. Satoh, M. Nakazawa, et al.; "Development on Failed Fuel Detection and Location System using Resonance Ionization Mass Spectrometry", submitted to J. Nucl. Sci. Technol. (1996).

(C) 国内学会誌等

- (1) 佐藤泰、井口哲夫、中沢正治他: 「共鳴イオン化質量分析法を用いた破損燃料検出システムの開発」日本原子力学会96年秋の大会(東北大学)

1 2. 複雑形状流路内乱流の熱・運動量輸送の数値予測

Numerical Prediction of Turbulent Fluid Flow and Heat Transfer in Complex Geometry

研究テーマ代表者 笠木 伸英（機械工学専攻）

1. 序

本研究グループでは、核融合炉の第一壁あるいはブランケットを始めとする各構成要素における熱流体力学の問題に注目して、特に従来にない極めて高い熱流束をいかにして安全かつ効率的に扱うかという観点から、対流冷却にかかわるいくつかの基礎的問題を取り上げて研究を続けている。これらの研究は、機械工学専攻において行なわれている。

2. 研究進捗状況

平成7年度は、前年度の水平チャンネル内の不安定成層乱流の直接数値シミュレーションをさらに発展させ、鉛直チャンネル内の共存対流乱流のシミュレーションを行った。この流れ場には、浮力が流れを加速させる併行流と、逆に流れを抑制する対向流が共存する。シミュレーションは、さらにチャンネルに回転を加えた場合についても行われ、回転熱流体機器内の2つの効果、すなわち浮力とコリオリ力、の組み合わせ効果を検討した。

乱流熱流束輸送方程式モデルに対しては、既存の座標依存形式を再構築し、複雑流路形状に対しても適用可能な座標不変モデルを提案した。その有用性は、バックステップ乱流のシミュレーションにおいて確かめられた。

時空間的な流路変形、たとえばぜん動壁や壁面変形制御アクチュエータを含む流れ場の数値シミュレーションを行い、壁面変形が流れ場に及ぼす影響、特に壁面摩擦・熱伝達に対する効果を検討した。

固気2相乱流の直接数値シミュレーションを行い、粒子運動の記述方法により、その運動・分布形態が大きく異なることを示した。粒子・流体間には、粒子運動が流れ場に影響を及ぼさないone-way couplingを仮定した。粒子に重力を考慮し、粒子・壁面間の衝突に非弾性衝突を仮定する場合に、壁面上の低速ストリーク内に粒子の分布が集中することを示した。

3. 今後の予定

来年度は、粗さを有するダクト内乱流の直接数値シミュレーションを行い、壁面粗さの抵抗・熱伝達に及ぼす効果を検討する。また、時間的に壁面の変形するダクト内乱流の直接数値シミュレーションを行い、時空間的な流路変形の乱流場に及ぼす効果を検討する。乱流モデルについては、複雑形状流路に適用できる座標不変非等方 $k-\epsilon$ モデルの開発を目指す。固液2相乱流の直接数値シミュレーションにおいては、粒子と流体の干渉を考慮するtwo-way couplingの適用を試みる。

4. 発表論文リスト

(A) 学位論文等

- (1) 西村貢、「浮力を伴う回転系乱流熱輸送の直接数値計算」、東京大学修士論文、1996年2月.
- (2) 塚原渉、「一般形状への適用を考慮した乱流熱流束のモデリング」、東京大学修士論文、1996年2月.
- (3) 水矢亨、「乱流中の固体粒子運動の直接数値シミュレーション」東京大学卒業論文、1996年2月.

(B) 国外学会誌等

- (1) Satake, S., and Kasagi, N., "Turbulence Control with a Wall-Adjacent Thin Layer of Spanwise Damping Force," 10th Symp. Turbulent Shear Flows, Penn State, Aug. 1995, Vol. 2, pp. 11.1-11.6.
- (2) Benhalilou, M., and Kasagi, N., "Prediction of the Turbulent Flow over Riblets with a Nonlinear Low-Reynolds Number k-e model," 10th Symp. Turbulent Shear Flows, Penn State, Aug. 1995, Vol. 2, pp. 14.13-14.18.
- (3) Kasagi, N., and Satake, S., "Turbulence Control with a Wall-Adjacent Thin Layer Damping Spanwise Velocity Fluctuations," Int. Sem. Turbulence Management of Mass, Heat and Momentum Transfer, Tottori University, pp. 21-33.
- (4) Benhalilou, M., and Kasagi, N., "Numerical Prediction of Turbulent Heat Transfer on a Surface with Triangular Riblets," Proc. Int. Symp. Mathematical Modelling of Turbulent Flows, University of Tokyo, Dec. 1995, Jap. Soc. Comp. Fluid Dyn., Suppl., pp. 7-12.
- (5) Shikazono, N., and Kasagi, N., "Second-Moment Closure for Turbulent Scalar Transport at Various Prandtl Numbers," submitted to Int. J. Heat Mass Transfer, 1995.
- (6) Shikazono, N., and Kasagi, N., "Second-Moment Closure for Low-Reynolds Number Sheared Turbulence and Its Application to Stably Stratified Flows," submitted to Int. J. Heat & Fluid Flow, 1995.
- (7) Nishimura, M., and Kasagi, N., "Direct Numerical Simulation of Combined Forced and Natural Turbulent Convection in a Vertical Plane Channel," EF Conference on Turbulent Heat Transfer, San Diego, March 1996.

- (8) Benhalilou, M., and Kasagi, N., "Numerical Prediction of Turbulent Heat Transfer Augmentation on a Surface with Triangular Riblets," EF Conference on Turbulent Heat Transfer, San Diego, March 1996.

(C) 国内学会誌等

- (1) 佐竹, 笠木, 「スパン方向速度に抑制を受けるチャンネル乱流の構造と熱輸送機構」, 第32回日本伝熱シンポジウム講演論文集, 1995, Vol. I, pp. 21-22.
- (2) Benhalilou, M., Kasagi, N., 「Turbulent Heat Transfer on Triangular Riblet Surface」, 第32回日本伝熱シンポジウム講演論文集, 1995, Vol. III, pp. 627-628.
- (3) 飯田, 笠木, 「不安定密度成層乱流におけるプラントル数の効果」, 第32回日本伝熱シンポジウム講演論文集, 1995, Vol. III, pp. 641-642.
- (4) 西村, 笠木, 「鉛直チャンネル内共存対流乱流の直接数値計算による解明」, 第32回日本伝熱シンポジウム講演論文集, 1995, Vol. III, pp. 643-644.
- (5) 佐竹, 笠木, 「スパン方向速度のアクティブ制御によるチャンネル乱流のDNS」, 第27回乱流シンポジウム, 日本流体力学会誌, Vol. 14 別冊, 1995, pp. 93-96.
- (6) 飯田, 長野, 笠木, 「密度成層下にあるチャンネル乱流の直接数値シミュレーション」, 第9回数値流体力学シンポジウム講演論文集, 1995, pp. 177-178.
- (7) 西村, 笠木, 「鉛直系共存対流の直接数値計算」, 第9回数値流体力学シンポジウム講演論文集, 1995, pp. 179-180.
- (8) 佐竹, 笠木, 「アクティブ制御されたチャンネル乱流の構造」, 第9回数値流体力学シンポジウム講演論文集, 1995, pp. 183-184.

1 3. 熱音響型冷凍機の基礎的研究

Basic Study on a Thermoacoustic Refrigerator

研究テーマ代表者 齊藤 孝基 (機械工学専攻)

1. 序

熱音響冷凍機とは、スピーカーなどによって共鳴が起きている管内にスタックと呼ばれる薄い板を積層したものを流体の振動方向と一致するように置くことにより、気体の圧縮・膨張に伴う温度変化を効果的に利用する冷凍機である。この冷凍機には、機械的な振動部がないために高い信頼性が得られる、フロンを全く使用しない、などの利点があるために実用化に向けてさまざまな研究がなされている。

本研究では、作動流体として大気圧の空気を用い、熱音響冷凍機に関する実験を行う。また昨年度行った伝達関数法を用いた数値計算の結果と比較をする。

2. 研究進捗状況

前年度の実験装置に対し、共鳴管開端部を損失の小さな形状に変更し、スタックとして塩化ビニルのハニカムを用いる、という改良を行った。実験では断熱の条件でスタックの位置、長さを変えて共鳴管内各部の温度を測定した。その結果、スタックの位置、長さそれぞれに対して最適な値が存在し、それが数値計算の結果とも一致することが分かった。

3. 今後の予定

今後の予定として以下のことを考えている。

1. 実験装置に熱交換器を付加し冷凍機の成績係数(COP)を求められるようにする。
2. 実験結果と数値計算の結果を定量的に比較するためには音響エネルギーを測定する事が必要であり、その方法について検討する。
3. 外部に音の漏れにくいスピーカーを用いて、電気の入力に対する冷凍機の性能の評価を行う。
4. 数値計算の方法についても改良を行う。

4. 発表論文リスト

(A) 学位論文等

- (1) 酒井 均 : 「熱音響ヒートポンプの研究」 東京大学卒業論文 (1996年3月)

(B) 国内学会誌等

- (1) 山田 豊, 飛原英治, 齋藤孝基 : 「伝達行列法による音響式冷凍機の解析」, 日本機械学会論文集 B編, 第62巻 第595号, 平成8年3月, pp1185~1192

1 4. 固体増殖材料表面における水素同位体の挙動

Behavior of Hydrogen Isotopes on the Surface of Solid Breeding Materials

研究テーマ代表者 田中 知 (システム量子工学専攻)

1. 序

固体増殖材料よりのトリチウム回収挙動について、特に表面反応と照射欠陥の効果に着目した研究を展開している。

2. 研究進捗状況

表面反応については高温かつ雰囲気制御下でLi₂O表面のO-D伸縮振動を拡散反射装置を用いる赤外吸収実験によって観察した。複数のピークが見られ、これより表面はD₂Oの吸着に対して、均質ではないことが判った。また、D₂とD₂Oの場合で観察ピークが異なる事より、表面OD存在状態の酸素ポテンシャル依存性があることが判った。また観察されたピークの表面存在状態への帰属を合理的に行なった。表面の表面存在状態を量子化学的ab-initio計算により明らかにする研究を開始し、表面酸素濃度がODの結合エネルギーに影響する事を明らかにするとともに、安定な吸着サイトの指摘を行なった。

照射欠陥の影響については原子炉、イオン、ガンマ線照射下で低温～高温での発光現象を観察し、F⁺, F⁰, エキシトンなどの挙動についての知見を得るとともに、イオン照射後加熱時の余剰発光を観察し、これがリチウムコロイドと関係している可能性を指摘した。また、トリチウム放出と欠陥との相関を明らかにする研究に着目した。

3. 今後の予定

表面でのOD存在状態については脱離種の質量分析器による分析を行ない、これと表面状態との相関を明らかにする。

照射欠陥については、トリチウム放出との関連を更に明らかにするとともに、レーザー誘起発光など、光吸収の点よりも研究を進める。

4. 発表論文リスト

(A) 学位論文等

- (1) 谷口正樹「固体増殖材料表面における水素同位体の存在状態に関する研究」、
修士論文 (平成 8 年 3 月)

(B) 国外学会誌等

- (1) Victor Grishmanov and Satoru Tanaka, "In-Situ Luminescence Observation from Li₂O under Reactor and γ ray Irradiation" 4th Japan-CIS Workshop on Interactions of Fuel Particle with Fusion Materials, Obninsk, Russia, September 29-30, 1995 (1996) 184-189.

- (2) Victor Grishmanov and Satoru Tanaka, "In-situ Luminescence Observation from Li₂O under Reactor and γ ray Irradiation", Proceedings of the Fourth International Workshop on Ceramic Breeder Blanket Interactions, October 9-11, 1995, Kyoto, Japan, pp.153-158.

(3) Masaki Taniguchi, Satoru Tanaka and Victor Grishmanov, "In-situ Observation of Surface Hydroxyl Group on Lithium Oxide and Its Comparison with ab-initio Calculation", Proceedings of the Fourth International Workshop on Ceramic Breeder Blanket Interactions, October 9-11, 1995, Kyoto, Japan, pp.298-309.

(4) Victor Grishmanov and Satoru Tanaka, "In-Situ Observation from Li₂O under Reactor and γ ray Irradiation", Third Sino-Japan Symposium on Materials for Advanced Energy Systems and Fission and Fusion Engineering, Chengdu, China, October 30 - November 3, 1995.

(5) Satoru Tanaka and Masaki taniguchi, "In-Situ Observation of Surface Hydroxyl Group on Lithium Oxide and Its Comparison with ab-initio Calculation", Third Sino-Japan Symposium on Materials for Advanced Energy Systems and Fission and Fusion Engineering, Chengdu, China, October 30 - November 3, 1995.

(6) Masaki Taniguchi, Satoru Tanaka, H. Watanabe, "In-Situ Observation of Surface Hydroxyl Group on Li₂O at High Temperature by Infrared Absorption Spectroscopy", Proceedings of the International Symposium on Material Chemistry in Nuclear Environment, March 14-15, 1996, Tsukuba, Japan, pp.429-436.

(7) Victor Grishmanov, Satoru Tanaka and Toshiaki Yoneoka, "Irradiation Defects in Li₂O", Proceedings of the International Symposium on Material Chemistry in Nuclear Environment, March 14-15, 1996, Tsukuba, Japan, pp.749-754.

(8) Masaki Taniguchi, Satoru Tanaka and Toshiaki Yoneoka, "In-situ Observation of Surface -OH and -OD on Various Lithium Ceramics", J. Nucl. Mater. 226(1995)178-184.

(9) Masaki Taniguchi, Satoru Tanaka, Victor Grishmanov, Yoshio Nose and Takayuki Terai, "In-situ Observation of Surface Hydroxyl Group on Lithium Ceramics at High Temperature by Infrared Absorption Spectroscopy", Fusion Technology 28(1995)1284-1289.

(10) Daiju Yamaki, Satoru Tanaka and Michio Yamawaki, "Modeling of Surface Reaction in Tritium Release from Lithium Ceramics and Its Comparison with Transient Experiments", Fusion Engineering and Design 28 (1995) 286-291.

(11) Satoru Tanaka, Daiju Yamaki, Michio Yamawaki, Takashi Miyamura and Ryohei Kiyose, "Luminescence Observation from Lithium Oxide under Neutron Irradiation", Fusion Eng. Des. 28 (1995) 292-298.

(12) A. R. Raffray, M. C. Billone, G. Federici and S. Tanaka, "Progress in Tritium Retention and Release Model for Ceramic Breeders", Fusion Eng. and Design 28 (1995) 240-251.

(13) Victor Grishmanov, Satoru Tanaka and Takayuki Terai, "In-Situ Luminescence Measurement at High Temperature from Li₂O under Neutron Irradiation", Journal of Nuclear Materials (in -press).

1 5. ウラン合金の水素同位体吸収特性

Hydrogen Absorption/Desorption Characteristics of Uranium Alloys

研究テーマ代表者 山脇 道夫 (原子力工学研究施設)

1 序

ウランは水素貯蔵材として非常に優れた材料であるが、水素化に伴い微粉末化するという欠点を有する。こうした問題点に対処するため、ウランを適切な添加元素によって合金化することが1つの案として有望視されている。本研究では、ウラン (U) 系あるいはウラン (U) -トリウム (Th) 系合金に対して、水素吸収ならびに放出試験を行い、以下の項目について検討し、得られた結果をもとに、各々の水素貯蔵材としての適性を総合的に評価することを目標としている。

(1) 水素吸収量、(2) 水素吸収速度、(3) 解離圧・温度・組成特性、(4) プラトー特性、(5) ヒステリシスの特徴とその起源、(6) 水素吸収に伴う反応熱、(7) 耐微粉化特性。

2 研究の進捗状況 (装置の改良等を含む)

ウランは水素同位体の貯蔵材として利用されているが、水素の吸蔵により微粉末となり、また解離圧が低いといった特性を有している。これらの特性を改善するためには他の金属との合金化が有効である。当グループでは合金の水素吸蔵特性の研究を進めており、今年度は、U と Mn の金属間化合物について水素吸蔵特性の試験を行った。その結果、金属間化合物の1つである U_6Mn については U と比較して解離圧の上昇が確認できた。さらに X 線回折を行ったところ、試料の一部では分解が見られたが、未知のピークが観測され、3 元系の水素化物生成の可能性が示唆された (英文報告書参照)。

3 今後の予定

水素の吸蔵・放出を繰り返した U_6Mn については X 線回折により UH_3 への分解が確認された。しかし、常温で一度だけ水素を吸蔵させた試料では全く異なったピークが見られ、複合水素化物の生成の可能性が示唆された。水素化による分解が起こる条件、あるいは分解過程を観察するため in-situ での X 線回折及び熱分析が必要であると考えている。

さらに、今年度までに反応温度の低下を目的に U-Mn 系の合金について水素吸蔵特性を調べてきたが、反応温度の低下は Mn の他に Fe、Ni 等が有効であると考えられている。そこで、これまでに実験結果が報告されていない U-Ni 系の合金について、種々の組成の合金を作製するとともに、その水素吸蔵特性を調べていくことにしている。

4 発表論文リスト

(A) 学位論文等

該当なし。

(B) 国外学会誌等

- (1) K. Asada, K. Ono, K. Yamaguchi, T. Yamamoto, A. Maekawa, S. Oe and M. Yamawaki, "Hydrogen absorption properties of uranium alloys", J. Alloys and Compds. 231 (1995) 780-784.

(C) 国内学会誌等

- (1) 伊藤 洋, 山口 憲司, 山本 琢也, 堀 保恵, 大江 忍, 前川 晃, 山脇 道夫, 「ウランマンガ
ン合金の水素吸蔵特性」, 日本原子力学会「1995 年秋の大会」, H29, 東海, 10 月 17
~20 日 (1995).
- (2) 伊藤 洋, 山口 憲司, 山脇 道夫, 「ウラン合金の水素同位体吸蔵放出特性」, 第 1 回核
融合エネルギー連合講演会, B78, 京都, 12 月 4~5 日 (1995).
- (3) 山脇 道夫, 伊藤 洋, 山本 琢也, 「ウランの水素吸蔵特性を利用した電力貯蔵システ
ム・劣化ウラン活用の可能性」, 原子力工業 41(8) (1995) 67-73.

1 6. 液体トリチウム増殖材料の物理化学的挙動

Physico-chemical Behavior of Liquid Breeding Materials

研究テーマ代表者 寺井 隆幸 (システム量子工学専攻)

1. 序

本研究グループは、ここ数年来、液体増殖材料の物理化学的挙動についての研究を継続して行ってきた。液体増殖材料研究においては、絶縁性、トリチウム不透過性、耐食性を併せ持つセラミックコーティングの研究開発が盛んになってきているが、昨年は、セラミックコーティング材料と金属リチウムやリチウム鉛合金との両立性についての研究と、フッ化リチウム-フッ化ベリリウム溶融塩からの中性子照射下トリチウム放出挙動に関する研究を実施した。

2. 研究進捗状況

1) セラミックコーティングの製造とその特性評価

Hot-dipping 法・拡散合金化法・高温酸化法を組み合わせた方法により、SUS 316 鋼表面にアルミナコーティングを作成し、その製造過程における金属組織の変化と電気伝導率などの物性変化を測定した。条件をいろいろに変えて試作を行った結果、十分な絶縁性を持ったセラミックコーティングを作成する方法を確立できた。また、 Al_2O_3 、 $\text{MgO-Al}_2\text{O}_3$ 、 Y_2O_3 などの焼結体・単結晶・プラズマ溶射コーティング膜試料と金属リチウムやリチウム鉛合金との両立性を 500°C で実験により明らかにするとともに、熱力学的考察をあわせて行い、その腐食メカニズムについて考察した。

2) フッ化リチウム-フッ化ベリリウム溶融塩からの中性子高温照射下トリチウム放出挙動

液体増殖材候補材料の 1 種であるフッ化リチウム-フッ化ベリリウム溶融塩(Li_2BeF_4)からのトリチウム放出挙動を明らかにするために、弥生炉に高温照射体系を構築し、中性子高温照射下におけるトリチウム放出実験を行った。その結果、トリチウム放出化学形は体系内のフッ素ポテンシャルによって大きく変化し、スイープガスに水素ガスを添加した場合のように、これが小さいときは放出化学形は主に HT であり、試料の乾燥が不十分な場合やスイープガスに純ヘリウムを用いた場合のように、これが大きい場合には放出化学形は主に TF となることが明らかになった。また、スイープガス中の水素濃度や照射温度、試料乾燥時間などをパラメータとして放出速度を測定し、トリチウムの放出メカニズムを明らかにしつつある。

3. 今後の予定

セラミックコーティングの製造方法の検討とその特性評価をさらに進める。また、 Li_2BeF_4 からのトリチウム放出実験をさらに進め、トリチウム放出メカニズムを明らかにするとともに、放出に関係する速度論的パラメータを求める。さらには、 Li_2BeF_4 からのトリチウム回収法についての検討を行う。

4. 発表論文リスト

(A) 学位論文等

- (1) 満山孝明、"核融合炉液体増殖材料と絶縁性セラミックスとの両立性"、東京大学工学部卒業論文 (1996.3).

(B) 国外学会誌等

- (1) Takayuki Terai, "Fabrication and Properties of Ceramic Coatings for Liquid Blankets", 1995 European Lithium and Pb-17Li Workshop (Nottingham, 1995.9.18-19).
- (2) T. Terai, T. Kobayashi, T. Yoneoka, H. Tanaka and S. Tanaka, "Property Change of Y_2O_3 Coating with Liquid Breeding Materials and Electron Irradiation", The 7th International Conference of Fusion Reactor Materials (Obninsk, 1995.9.25-29), N200015.
- (3) Takayuki Terai, "Tritium Release and Tritium Recovery from Li17-Pb83", The 4th Japan-CIS Workshop on Interactions of Fuel Particles with Fusion Materials (IFPFM 4) (Obninsk, 1995.9.28-30).
- (4) Takayuki Terai, "R & D on Ceramic Coating for Fusion Reactor Blankets", The 3rd Sino-Japan Symposium on Materials for Advanced Energy Systems and Fission and Fusion Engineering (Chengdu, 1995.10.29-11.3), B107.
- (5) Takayuki Terai, "Research and Development on Ceramic Coatings for Fusion reactor liquid Blankets", The International Symposium on Materials Chemistry in Nuclear Environment (MC'96) (Tsukuba, 1996.3.14-15).
- (6) Toshiaki Yoneoka, Takayuki Terai and Yoichi Takahashi, "High Temperature Liquid Metal Corrosion and High Temperature Electrical Conductivity of Y_2O_3 ", The International Symposium on Materials Chemistry in Nuclear Environment (MC'96) (Tsukuba, 1996.3.14-15).
- (7) Akihiro Suzuki, Takayuki Terai and Satoru Tanaka, "Tritium Recovery from Molten Li17-Pb83 Alloy by Permeation Window Method", The International Symposium on Materials Chemistry in Nuclear Environment (MC'96) (Tsukuba, 1996.3.14-15).
- (8) Takayuki Terai, Toshiaki Yoneoka, Hirohisa Tanaka and Satoru Tanaka, "Fabrication of Al_2O_3 Coating on Austenitic Stainless Steel Type-316", Fusion Technology 1994 (K. Herschbach et al., Elsevier, 1995), p.1329-1332.

(C) 国内学会誌等

- (1) 米岡俊明、寺井隆幸、田中知、宇津木俊彦、高橋洋一、”ブランケット構造材料 SUS316 へのアルミナコーティング”、日本原子力学会 1995 年秋の大会（東海村、1995.10.17-20）、F47.
- (2) 鈴木晶大、寺井隆幸、米岡俊明、田中裕久、田中知、”溶融 $\text{Li}_{17}\text{Pb}_{83}$ 合金からの重水素の Nb 膜透過”、日本原子力学会 1995 年秋の大会（東海村、1995.10.17-20）、F83.
- (3) 寺井隆幸、鈴木晶大、米岡俊明、田中知、河村弘、中道勝、宮島生欣、原田良夫、”液体ブランケット用セラミックコーティングの製造とその特性”、第 1 回核融合エネルギー連合講演会（京都、1995.12.4-5）、C5.
- (4) 相良明男、本島修、山西弘城、渡辺清政、今川新作、佐藤隆、室賀健夫、大藪修義、FFHR グループ、御手洗修、田中知、寺井隆幸、松井秀樹、香山晃、野田哲二、”ヘリカル型核融合炉（FFHR）のブランケット設計（2）”、第 1 回核融合エネルギー連合講演会（京都、1995.12.4-5）、D8.
- (5) 満山孝明、米岡俊明、寺井隆幸、田中知、中道勝、河村弘、宮島生欣、原田良夫、”液体リチウムとイットリアの両立性”、日本原子力学会 1996 年春の年会（大阪、1996.3.27-29）、J29.
- (6) 鈴木晶大、寺井隆幸、米岡俊明、田中知、”高温照射下 Flibe (Li_2BeF_4) からのトリチウム放出実験（TrexFlibe）（1）トリチウム放出化学形”、日本原子力学会 1996 年春の年会（大阪、1996.3.27-29）、M17.
- (7) 寺井隆幸、”トリチウムの生成と回収”、機械の研究、47, 205-207 (1995).
- (8) 寺井隆幸、”核融合研究 II”（池上英雄編、名古屋大学出版会、1995）、分担執筆.

1 7. 核融合炉用機能性セラミックス材料の放射線照射効果

Irradiation Effects of Special Purpose Ceramic Materials for Fusion Reactors

研究テーマ代表者 寺井 隆幸 (システム量子工学専攻)

1。序

核融合炉用機能性セラミックスとして高温酸化物超伝導材料と絶縁材料を取りあげ、放射線照射による超伝導特性や絶縁特性の変化について研究を行いつつある。平成7年度は高温酸化物超伝導体のうち Bi-2212 単結晶に対する各種放射線照射による臨界電流密度の変化を測定し、放射線照射により導入された照射欠陥との関連について検討した。また、La-214 単結晶や Hg 系の試料についても照射効果の研究を開始した。さらに、絶縁材料として Al_2O_3 や Y_2O_3 をとりあげ、電子線の電場下高温照射後の電気伝導率の変化を測定した。

2。研究進捗状況

1) 高温超伝導材料の放射線照射効果と照射による特性改善

高温超伝導体 (Y系、Bi系、La系、Hg系など) に対する各種放射線 (中性子、高エネルギーイオン、電子線、 γ 線) の照射効果について実験と計算機シミュレーションにより明らかにしつつある。実験により測定する項目は、臨界温度・臨界電流密度・電気伝導率・X線回折による結晶構造の変化・電子顕微鏡による照射欠陥の観察などであり、これらの特性変化と照射粒子の種類・エネルギー・フルエンスとの関係を定量的に求めることを最終目標としている。具体的には、平成7年度には、Bi-2212 単結晶に対する 480 MeV Kr イオン、240 MeV Au イオン照射における臨界電流密度の変化を測定するとともに、28 MeV 電子線照射、高速中性子照射、120 MeV O イオン照射および 5.8 GeV Pb イオン照射前後における臨界電流密度の温度と磁場に対する依存性についてのこれまでの実験結果との比較を行った。また、TEM による照射欠陥を観察した結果、最初の3つの場合には円柱状のアモルファス領域は生じていないことを確認した。さらに、La-214系や Hg系についても、重イオン照射や中性子照射を行い、臨界電流密度の増大を確認した。

現在、照射温度の効果を調べるために、Bi-2212 単結晶への中性子照射後の熱アニールによる超伝導特性と結晶構造の変化について研究を行いつつある。

2) 絶縁性セラミックス材料の放射線照射効果

核融合炉ブランケット用絶縁材やマイクロ波導入用光学窓、第一壁コーティング材などとして重要な絶縁性セラミックス材料の放射線照射効果について、各種放射線を用

いた照射実験と特性測定、および計算機シミュレーションにより明らかにすることを目標としている。平成7年度は特に、 Al_2O_3 を対象として、照射誘起電気伝導や照射誘起絶縁破壊などの電気的特性変化を測定した。その結果、 Al_2O_3 単結晶中にNiイオンを注入することによって電気抵抗率が5～6桁程度低下すること、500℃、空气中で、 $10^5 \sim 10^6 \text{ Vm}^{-1}$ の電場をかけて $2 \times 10^8 \text{ Gy}$ まで電子線照射した Al_2O_3 単結晶の電気抵抗率が、もとの試料と比べて3桁程度低下することを確認した。現在、これらの試料の欠陥構造について現在研究を進めている。

3. 今後の予定

今後はひきつづき、各種放射線（中性子、高エネルギーイオン、電子線、 γ 線）の照射効果について実験と計算機シミュレーションにより明らかにするとともに、その特性変化と照射粒子の種類・エネルギー・フルエンスとの関係を定量的に求める。特に、照射欠陥のキャラクタリゼーションに関して、TEM観察やフラックスクリープ測定によるピンニングポテンシャルの評価、照射損傷のシミュレーション計算などを行い、生成した照射欠陥の特性変化における役割について定量的に検討する。

4. 発表論文リスト

(A) 学位論文等

- (1) 高橋崇展、”電子ビーム照射によるサファイアの電気絶縁特性の変化”、東京大学工学部卒業論文(1995.3).
- (2) 伊藤康行、”放射線照射による酸化物高温超伝導体の物性変化”、東京大学大学院工学系研究科修士論文(1995.3).

(B) 国外学会誌等

- (1) Takayuki Terai, "Property Control of High Temperature Superconductors by Particle Beam Irradiation", International Summer School on High Temperature Superconductivity (Eger, 1995.7.23-8.5).
- (2) Tomohiro Kobayashi, Takayuki Terai and Satoru Tanaka, "Electrical Property of High-Fluence Nickel-Implanted Single Crystal Alumina", The 8th International Conference on Radiation Effects in Insulators (Catania, 1995.9.11-15), O-2.20.
- (3) Takayuki Terai, Tomohiro Kobayashi, Satoru Tanaka, "Anomalous Electrical resistivity of Al_2O_3 Degraded by Electron Irradiation", The 8th International Conference on Radiation Effects in Insulators (Catania, 1995.9.11-15), P-2.52.
- (4) Noriko Chikumoto, Marcin Konczykowski, Kohji Kishio, Tsuyoshi Kimura and Takayuki Terai, "Effect of Heavy ion Irradiation on the Magnetization of La214 Single Crystals", The 8th International Symposium on Superconductivity (ISS'95) (Hamamatsu, 1995.10.30-11.2).

- (5) Y. Ito, T. Terai, S. Tanaka, N. Chikumoto and K. Kishio, "Effect of 520 MeV Kr^{20+} Ion Irradiation on the Critical Current density of Bi-2212 Single Crystals", The 8th International Symposium on Superconductivity (ISS'95) (Hamamatsu, 1995.10.30-11.2).
- (6) Noriko Chikumoto, Kohji Kishio, Tsuyoshi Kimura and Takayuki Terai, "Neutron Irradiation Effect on the Secondary Peak Observed in the Magnetization Curves of La214 Single Crystals", The 8th International Symposium on Superconductivity (ISS'95) (Hamamatsu, 1995.10.30-11.2).
- (7) Takayuki Terai, Kazuyuki Kusagaya, Yasuyuki Ito, Satoru Tanaka and Noriko Chikumoto, "Radiation Defects and Flux Pinning Properties of Bi-2212 Single Crystals", The International Symposia on Advanced Materials and Technology for the 21st Century (Honolulu, 1995.12.13-15), 725.
- (8) Takayuki Terai, "Property Control of High-Tc Superconductors by Particle Beam Irradiation", Seminar on Materials and Environmental Science (Hachioji, 1996.3.11).
- (9) Takayuki Terai and Yasuyuki Ito, "Enhancement in Critical Current Density of High-Tc Superconductor $Bi_2Sr_2CaCu_2O_x$ by Particle Beam Irradiation", The International Symposium on Materials Chemistry in Nuclear Environment (MC'96) (Tsukuba, 1996.3.14-15).
- (10) Tomohiro Kobayashi and Takayuki Terai, "Electrical Property Change of Sapphire by Particle Beam Irradiation", Proceedings of the International Symposium on Material Chemistry in Nuclear Environment (MC' 96) (Tsukuba, 1996. 3. 14-15), p.787-796.
- (11) Takayuki Terai and Yasuyuki Ito, "Enhancement in Critical Current Density of High-Tc Superconductor $Bi_2Sr_2CaCu_2O_x$ by Particle Beam Irradiation", Proceedings of the International Symposium on Material Chemistry in Nuclear Environment (MC' 96) (Tsukuba, 1996. 3. 14-15), p.829-840.
- (12) Takayuki Terai, "Property Control of High Temperature Superconductors by Particle-beam Irradiation", Proceedings of the International Summer School on high Temperature Superconductivity "ISSHTS", Volume 1/A (1995), p. 71-80.
- (C) 国内学会誌等
- (1) 小林知洋、寺井隆幸、米岡俊明、田中知、"高温、高電場中で電子線照射したアルミナ単結晶の電気抵抗率"、第56回応用物理学会学術講演会(金沢、1995.8.26-29)、26pB/II6.
- (2) 小林知洋、寺井隆幸、米岡俊明、田中知、"ニッケルイオン注入したアルミナ単結晶の電気伝導"、第56回応用物理学会学術講演会(金沢、1995.8.26-29)、28pSC/III10.
- (3) 小林知洋、寺井隆幸、米岡俊明、田中知、"高温電場印加条件下で電子線照射した単結晶 Al_2O_3 (サファイヤ) の電気抵抗率"、日本原子力学会 1996 年春の年会(大阪、1996.3.27-29)、H38.
- (4) 寺井隆幸、草ヶ谷和幸、筑本知子、岸尾光二、田中知、"酸化物高温超伝導体

$\text{Bi}_2\text{Sr}_2\text{CaCu}_2\text{O}_{8+y}$ 単結晶に対する中性子照射効果”、東京大学工学部総合試験所年報、54、119-124 (1995).

- (5) 米岡俊明、寺井隆幸、田中裕久、田中知、”セラミックコーティングとリチウムの共存性”、東京大学工学部総合試験所年報、54、131-135 (1995).
- (6) 米岡俊明、寺井隆幸、高橋洋一、”極低酸素圧下におけるイットリアの高温電気伝導性”、日本金属学会誌、60、1-8 (1996).

1.8. トリチウム-材料相互作用におけるトラップメカニズム

Trap Mechanism of Tritium in Tritium-Materials Interactions

研究テーマ代表者 小野 双葉 (原子力工学研究施設)

1. 序

核融合炉燃料である水素同位体のトリチウムに対して、トリチウム取扱装置などでトリチウムガスあるいはトリチウム水蒸気の供給から回収または廃棄までの一連の操作を行うと、配管材料や測定機器の内壁などには必ずトリチウムの吸着（付着）が起こる。この際、吸着したトリチウムはガススイープあるいは真空排気などの操作では容易に脱離せず、吸着したトリチウムの一部は表面に残る。その結果材料などの汚染がもたらされる。この汚染の度合は材料の種類、表面状態および取扱い時の真空度などで大きく異なる。また、キュリーオーダー以上の取扱いにおいては、より深刻な問題になることは良く知られている。吸着トリチウムによる材料の汚染やその除染、あるいは吸着トリチウムの再放出等に関する問題は、環境安全あるいは安全取扱い上のみならず、測定精度への影響、計量管理上からも重要である。このことから、各種材料へのトリチウムの吸着・脱離について実験的研究を行ってきた。

2. 研究進捗状況

長期間、高比放射能トリチウムガスに接触したSUS,Cuおよびガラス試料について、吸着トリチウムの再放出挙動について検討した。吸着トリチウムの脱離は、ガススイープによりバックグラウンドレベルまで回収されたトリチウムは密閉容器内に保管している間に試料表面からの再放出により容器内トリチウム濃度が上昇することが確認され、定量的な評価を行った。回収されたトリチウムの化学形はほとんどが水成分であること、金属材料への吸着トリチウムは、密閉容器開封直後に高濃度のトリチウムを放出することから、その取扱いに十分な注意が必要であること、ガラス材料からは長期間にわたってトリチウムの放出が有ることなどを指摘した。

試料内部まで取り込まれたトリチウムは、ガススイープ等により一度表面から取り去っても内部からの表面へのトリチウムの拡散により試料表面のトリチウム濃度を高め、環境への再放出に関して定量的な評価が出来た。

3. 今後の予定

各種材料に吸着したトリチウムが、漏えい、透過、拡散、再放出などにより、放射能汚染源となり、環境安全および安全取扱い上、問題になる。このことから、これまで各種材料へのトリチウムの吸着・脱離挙動について、主としてイオンチェンバー・振動容量電位差計による測定データの解析等により検討してきた。これまでのトリチウムの吸着・脱離・再放出に関する研究をさらに踏み込んで各種材料へのトリチウムのトラップメカニズムを明らかにすることを目的として以下の計算・実験などを行う予定である。

(1) FT/IR(フーリエ変換赤外分光分析器)を用いて、In-situで材料へトリチウムの吸着実験およびトリチウムを吸着させた材料での深さ方向のトリチウム濃度分布を測定し、材料へのトラップメカニズムを明らかにする。

(2) 各種水素吸蔵合金等での水素の吸蔵・脱蔵に関して、文献からの熱力学的データなどにより水素吸蔵平衡圧などの計算によるシミュレーションを行い吸蔵（トラップ）特性について検討し新しい水素吸蔵材の開発を模索する。さらに高濃度トリチウム吸蔵時

の同位体効果、同位体分離・濃縮・精製の可能性について実験的に検討を試みる。

以上の検討からトラップメカニズムの基礎的データを得ることと、各種水素吸蔵用合金等でのトリチウム吸蔵・脱蔵特性等を明らかにし、高濃度トリチウムの安全取扱い上有用なデータを得るとともに、新しい水素吸蔵材料の開発につなげる事が可能と考える。

4. 発表論文リスト

(B) 国外学会誌等

- (1) F. Ono, S. Tanaka and M. Yamawaki, "Tritium sorption by cement and subsequent release", *Fusion Eng. Des.*, 28, 378-385 (1995)
- (2) F. Ono, S. Tanaka and M. Yamawaki, "Regrowth of tritium release from tritium contaminated materials", 5th Top. Meet. Tritium Technology in Fission, Fusion and Isotopic Applications, Belgilate, Italy, May 28 - June 3 (1995).
- (3) F. Ono, S. Tanaka and M. Yamawaki, "Regrowth of tritium release from tritium contaminated materials", *Fusion Technol.* 28 (1995) 1250-1255.

(C) 国内学会誌等

- (1) 小野 双葉, 田中 知, 山脇 道夫, 「トリチウム汚染材料からのトリチウムの繰り返し脱離」, 第1回核融合エネルギー連合講演会, B70, 京都, 12月4~5日 (1995).

19. イオン照射下その場観察法による高エネルギーPKAカスケード損傷 In-situ Observation of Cascade Damage Produced by High Energy PKA

研究テーマ代表者 関村 直人 (システム量子工学専攻)

1. 序

高エネルギー中性子照射された核融合炉材料の特性変化機構を定量的に明らかにし、耐照射性に優れた材料開発を行うためには、照射損傷における原子的、電子的エネルギー損失と格子欠陥の形成の基礎過程を評価することが必要である。

本研究は、特に高エネルギーのPKA（1次はじき出し原子）から始まるカスケード損傷に注目して、重イオン加速器と透過電子顕微鏡を用いた「その場観察」及び各種イオン照射をPKAエネルギーに基づいたカスケード損傷の解析のために積極的に利用し、中性子照射による材料損傷過程と動的な材料マイクロ組織変化を予測・評価するためのモデル化を行うことを目的としている。

2. 研究の進捗状況および今後の予定

(1) BCC金属におけるカスケード損傷による欠陥クラスター形成

BCC金属はFCC金属材料に比べ、カスケード損傷による直接的な欠陥クラスター形成確率が低く、PKAエネルギーに基づいて損傷形成過程を定量的に評価しようとする試みはなされてこなかった。しかしBCC金属では、電子顕微鏡では観察できない空孔集合体であるいわゆる「マイクロポイド」が形成されることが、陽電子消滅実験から明らかにされており、カスケード損傷構造が自由点欠陥の生成量とその後のマイクロ組織発達に大きく影響を及ぼすことは明確である。

ここでは、核融合炉材料として最も精力的に研究が進められながら、以上のような損傷形成基礎過程についてほとんどデータの存在しないBCC金属であるバナジウムをとり上げ、各種イオン照射によって、カスケードからの空孔クラスタリングを支配する因子を明らかにすることを目的として、400 kV重イオン加速器を用いた実験的研究を進めた。

常温でのバナジウム薄膜に対しての 1.0×10^{16} ions/m²までの200及び400 keV自己イオン(V⁺)照射では、観察可能な欠陥クラスターは形成しなかった。このために、さらに高いカスケード内欠陥密度を得ることを目的として、50~400 keVの金イオンを試料に照射した。この結果、イオンエネルギーに応じて欠陥クラスター密度が変化することが確認された。さらに、これを試料膜厚の関数として整理した結果、格子間原子が表面に逃げうる表面近傍にのみ、高密度の2~3 nmの空孔型クラスターが形成されていることが明らかにされた。また、厚い膜の中心部分には、格子欠陥型の欠陥クラスターが形成している。

空孔型の欠陥クラスター形成と損傷エネルギー付与密度との関係を整理した結果、金イオン照射による空孔型クラスター形成の臨界イオンエネルギーは120 keVであることがわかった。これは4.9 keV/nm/ionの損傷エネルギー付与に対応しており、異なる質量を持つイオン照射実験によって、この整理法が正当であるかを確認する必要がある。

(2) 今後の予定

今後は、上記のモデル化を進めるためにXe イオンなどの照射実験を進める。

さらに極低温でのイオン照射実験及び新その場観察系を利用して、極短寿命の近傍に形成されたカスケードのよる欠陥形成過程の動的観察を行う。さらにバナジウムのカスケード損傷形成過程の分子動力学計算結果との対応を明らかにしながら、核融合炉環境における中性子照射下のP K Aエネルギーに依存するカスケードモデル化を行う。

3. 発表論文リスト

(A) 学位論文など

卒業論文

公野 昇 「環境負荷を考慮した材料設計手法の研究」

森山 圭 「バーチャルエンジニアリングに関する基礎的研究」

修士論文

白尾泰之 「重イオン照射によるバナジウムカスケード損傷構造の研究」

七丈直弘 「分散協調環境に関する基礎的研究」

博士論文

陳 迎 「知的材料設計システムによる構造予測」

(B) 学会誌など

(1)E. A. Koptelov, S. Ishino, S. Iwata and N. Sekimura,

"Interstitial Cluster Formation in Metals under Intense Irradiation"

Journal of Nuclear Materials 225 (1995)38-52.

(2)K. Morishita, H. L. Heinisch, S. Ishino and N. Sekimura,

"The Correlation of Defect Distribution in Collisional Phase with Measured Cascade Collapse Probability", Nuclear Instruments and Methods in Physics Research B 102 (1995) 67-71.

(3)N. Sekimura,

"Radiation Damage in Materials -Primary Knock-on Atom Energy Analyses of Cascade Damage", Proceedings of the 1994 Symposium on Nuclear Data, Eds., M. Kawai and T. Fukahori (1995) pp.106-111.

(4)E. A. Koptelov, S. Ishino, S. Iwata and N. Sekimura,

"On Density Effects in Point Defect Solutions under Irradiation, I. Qualitative Consideration of Quasi-equilibrium States", to be published in Journal of Nuclear Materials (1996).

(5)E. A. Koptelov, S. Ishino, S. Iwata and N. Sekimura,

"On Density Effects in Point Defect Solutions under Irradiation, II. Formation of Interstitial Dislocation Loops", to be published in Journal of Nuclear Materials (1996).

(6)N. Sekimura,

"Primary Knock-on Atom Energy Dependence of Cascade Damage Formation and Interaction" to be published in Journal of Nuclear Materials (1996).

(C) 国内外学会など

- (1)佐伯 潤、関村直人、白尾泰之 「自己イオン照射による金のカスケード重畳効果の研究」 日本金属学会（東京理科大学，平成7年4月）
- (2)N. Sekimura,
"Primary Knock-on Atom Energy Dependence of Cascade Damage Formation and Interaction"
7th International Conference on Fusion Reactor Materials (Obninsk, Russia, September 1995)
- (3)関村直人、佐伯 潤、白尾泰之、岩井岳夫
「異なったエネルギーの自己イオン組合せ照射によるカスケード損傷重畳効果の評価」
日本原子力学会（日本原子力研究所，平成7年10月）
- (4)Y. Shirao, T. Iwai and N. Sekimura,
"Defect Cluster Formation in Vanadium By Heavy Ion Irradiation"
International Symposia on Advanced Materials and Technology for the 21st Century
(Hawaii, December 1995)
- (5)N. Sekimura, J. Saeki, Y. Shirao and T. Iwai,
"Cascade Damage Formation and Interactions by Heavy Ion Irradiation"
International Symposia on Advanced Materials and Technology for the 21st Century
(Hawaii, December 1995)
- (6)N. Sekimura, Y. Kanzaki, N. Ohtake, J. Saeki, Y. Shirao, S. Ishino, T. Iwata, A. Iwase and
R. Tanaka,
"High Energy Cascades as Studied by High Energy Self Ion Irradiation"
18th International Symposium on Effects of Radiation on Materials (Hyannis, June 1996)
- (7)N. Sekimura, Y. Shirao and K. Morishita,
"Defect Cluster Formation in Vanadium under Heavy Ion Irradiation"
4th Japan-China Symposium on Materials for Advanced Energy Systems and Fission and
Fusion Engineering and the 10th Japan-China Symposium of JCSTEA Series (Sapporo, 1996)

20. 核融合炉材料の照射下挙動評価に関する研究

Evaluation of Irradiation Behavior of Fusion Materials

研究テーマ代表者 関村 直人（システム量子工学専攻）

1. 序

応力変動、温度変動、中性子フラックス変動などの動的な照射条件下におかれる核融合炉材料の材料特性の変化を定量的に評価するためには、マクロな材料特性変化に重要なミクロ過程を明らかにし、材料のミクロな変化機構に基づいたモデル化を行うことが重要である。本研究では、低放射化核融合炉構造材料として研究開発が進められているバナジウム合金を取り上げ、核変換ヘリウム生成とはじき出し損傷の同時効果が、材料ミクロ組織変化とミクロ組成変化へ及ぼす影響についてを検討した。

2. 研究の進捗状況および今後の予定

(1) バナジウム合金の照射下ミクロ組織・組成変化とこれらに対するヘリウム効果

昨年度からの純バナジウム、バナジウム－クロム合金、バナジウム－鉄合金に加え、現在核融合炉構造材料として主要候補材となっているバナジウム－クロム－チタン合金に対して二重ビーム照射を含むイオン照射試験を行い、ミクロ組織変化とミクロ組成変化を電子顕微鏡とこれに附属するエネルギー分散型X線分析装置によって明らかにした。

V-5Cr-5Tiでは、600℃照射においてTiが粒界上ではなく、粒界から50-100nm離れた位置で濃度が高くなることがわかった。原子サイズ因子から考えると、Vに比べアンダーサイズな溶質原子であるTiは、格子間原子として優先的に移動して粒界近傍で欠乏することが予想されるが、実際には濃度が上昇している。これはTiが不純物の酸素と結合し、集合体を形成しているからと考えられる。

照射された材料にスエリングが生じるためには、キャビティの核生成の他に、転位組織発達による空格子点の過飽和により、空格子点密度が増加することも必要である。これまでのtritium-trick法やDHCE法などによる中性子照射研究から、Heがスエリングを増大させることがわかっている。本研究では、30dpaまでの照射量では、Ti添加は転位組織発達を抑制していることと、Heが転位組織発達を促進していることがわかった。

今後は、さらに高照射量までのデータを取得して中性子照射との比較を行い、モデル化を進めるための各種パラメータの実測を目的としたイオン照射試験を進める。

3. 重イオン加速器の状況

400 kV重イオン加速器は、定期的にメンテナンスを加えながら、継続的に運転している。また照射するイオンエネルギー（20～400 keV）及びイオン質量の2つのパラメータを広範囲に得るため、照射可能なイオン種を増やすことにも積極的に対応している。しかし、イオン源や加速管部の一部消耗品の入手が困難になってきており、代替品を採用するために加速器内主要部の大幅な手入れが必要な時期になっている。

重イオン加速器室の-30°ビームラインおよび100 kV加速器には、大きなトラブルはなかった。

4. 発表論文リスト

(A) 学位論文など

卒業論文

柿内宏憲 「二重ビーム照射によるバナジウム合金のミクロ組織組成変化に関する研究」

修士論文

植田晃一 「酸化物軟磁性材料の電子状態計算による設計」

相原 純 「ジルカロイの腐食に関する基礎的研究」

(B) 学会誌など

(1)N. Sekimura, T. Iwai and F. A. Garner,

"Influence of Boron-generated Helium on the Swelling of Neutron Irradiated V, V-5Cr and V-5Fe", to be published in Journal of Nuclear Materials (1996).

(2)F. A. Garner, L. R. Greenwood, B. A. Loomis, S. Ohnuki and N. Sekimura,

"Influence of Flux-Spectra Differences on Transmutation, Dimensional Changes and Fracture of Vanadium Alloys", to be published in Journal of Nuclear Materials (1996).

(3)T. Iwai, N. Sekimura and F. A. Garner,

"Void Swelling Behavior in Ion-irradiated Vanadium Alloys"
to be published in Journal of Nuclear Materials (1996).

(C) 国内外学会など

(1)N. Sekimura, T. Iwai and F. A. Garner,

"Influence of Boron-generated Helium on the Swelling of Neutron Irradiated V, V-5Cr and V-5Fe", 7th International Conference on Fusion Reactor Materials (Obninsk, Russia, 1995)

(2)河西 寛、鈴木雅秀 「時効したFe-0.6Cu合金の微細組織」

日本原子力学会 (日本原子力研究所, 平成7年10月)

(3)H. Kawanishi and M. Suzuki,

"Cu-precipitates in Thermally-aged and Neutron-irradiated Fe-Cu Alloys"
International Symposia on Advanced Materials and Technology for the 21st Century
(Hawaii, December 1995)

(4)J. Aihara, H. Nakamori, H. Kawanishi, Y. Arai, N. Sekimura and S. Iwata,

"Sn precipitates in Zircaloy and Zr-Sn Alloys"
International Symposia on Advanced Materials and Technology for the 21st Century (同上)

(5)岩井岳夫、関村直人、石野栞 「鉄中のイオン照射による欠陥生成に対する銅の効果」

日本原子力学会 (大阪大学, 平成8年3月)

(6)河西 寛、鈴木雅秀 「焼き入れ・時効したFe-0.6Cu合金の微細組織」

日本原子力学会 (大阪大学, 平成8年3月)

(7)N. Sekimura, Y. Arai and S. Ishino,

"Microstructural Evolution and the Effect of Helium in Dual-Ion Irradiated Titanium Alloys"
18th International Symposium on Effects of Radiation on Materials (Hyannis, June 1996)

(8)関村直人、柿内宏憲、荒井良夫、与那嶺真一、岩井岳夫、浜田省三、三輪幸夫

「バナジウム合金のイオン照射下ミクロ組織・組成変化」

第5回TIARA研究発表会 (群馬県近代美術館, 平成8年6月)

2.1. 非金属材料のイオン照射効果の研究

Ion Beam Irradiation Effect on Non-Metallic Materials

研究テーマ代表者 石樽 顕吉 (システム量子工学専攻)

1. 序

イオンビームの誘起反応の特徴を HIMAC (放医研) 施設のパルスイオンを用いたパルスラジオリシスの手法と、拡散モデルに基づく計算機シミュレーションの両面からアプローチしている。

2. 研究進捗状況

イオンビームパルスラジオリシスの装置は組上げを終了し、実験に進んでいるが、疑似信号などに悩まされていたが、これらの問題もほぼ解決の目処が付き、本実験を開始した。昨年までの最短 $50 \mu\text{s}$ のパルスから $1 \mu\text{s}$ パルスまで使用できるようになり、時間分解能を向上できた。計算機シミュレーションについては計算機コードも完成し、種々条件下での計算を進め、イオンビームのような高 LET 放射線による水溶液の照射では Primary Yield を決定できないことが明らかとなった。これは、従来の放射線反応の描像を大きく変えるものであり、実験的な検討と平行して考察を進めている。

3. 今後の予定

HIMAC のパルスラジオリシス実験と計算機シミュレーションをさらに進め、イオンビーム誘起反応の特徴を、実験、モデルの両面から掘り下げている。具体的には KSCN 水溶液照射で生成する $(\text{SCN})_2 \cdot$ ラジカルの濃度依存性を $10^{-4} - 1\text{M}$ の範囲に渡り測定を進め、電子線照射の場合との比較検討を行っている。

4. 発表論文リスト

(A) 学位論文等

(1) 堂前雅史

"Radiolysis of Aqueous Solution of Chlorate and Perchloric Acid and Modeling of Initial Processes of Water Radiolysis"、博士論文

(2) 千歳範壽

「パルスラジオリシス法と拡散モデルを用いた水溶液のイオン照射効果の研究」
修士論文

(3) 八巻徹也

「LB法を用いた低次元半導体の構築と光・放射線物性に関する研究」, 修士論文

(4) 上里彰仁

「塩素オキソ酸水溶液の放射線反応とそのシミュレーション」、卒業論文

(5) 上田清隆

「パルスラジオリシス及びレーザーフォトリシス法による塩素オキソ酸水溶液中のレドックス反応」、卒業論文

(6) 乙坂哲也

「ポリシランの構造制御と電子物性に関する研究」、卒業論文

(B) 国外学会誌等

(1) Y. Katsumura, M. Domae et al.

"Pulse Radiolysis Study on Aqueous Concentrated Solutions"

Proc. 3rd Trombay Symposium on Radiation and Photochemistry, Bombay, 1996, 1, (1996)

- (2) Y. Katsumura
"Radiation Chemistry of Nitric Acid and Nitrates"
Proc. 3rd Trombay Symposium on Radiation and Photochemistry Bombay, 1996, 369, (1996)
- (3) Y. Katsumura, T. Azuma, M. A. Quadir, A. Domazou and R. E. Bühler
"The Radical Cation (MCH⁺) of Methylcyclohexane"
J. Phys. Chem., **99**, 12814-12821 (1995)
- (4) K. Ishigure, Y. Katsumura, G. R. Sunaryo and D. Hiroishi
"Radiolysis of High Temperature Water"
Radiat. Phys. Chem., **46**, 557-560 (1995)
- (5) Yanti S. Soebianto, Isami Kusuhata, Yosuke Katsumura, Kenkichi Ishigure, Junichi Kubo, Hisaaki Kudoh, and Tadao Seguchi
"Degradation of Polypropylene under Gamma Irradiation - Protection Effect by Additives"
Polymer Degradation and Stability, **50**, 203-210 (1995)

(C) 国内学会誌等

- (1) 千歳範壽、勝村庸介、堂前雅史、貝塚洋志、広石大介、太田隆、土肥宏一、石樽顕吉、古澤孝弘、柴田裕実、吉田陽一、村上健
「HIMACのイオンビームを用いたパルスラジオリシスシステムの構築」
第38回放射線化学討論会、金沢工業大学、金沢、1995年10月15-17日
- (2) 堂前雅史、勝村庸介、石樽顕吉、V. M. Byakov
「拡張スパーモデルによる水溶液の放射線分解初期過程の研究 II - 溶質添加系への適用と溶質の分類」
第38回放射線化学討論会、金沢工業大学、金沢、1995年10月15-17日
- (3) 千歳範壽、勝村庸介、堂前雅史、石樽顕吉
「拡散モデルによる水溶液のLET効果の研究」
第38回放射線化学討論会、金沢工業大学、金沢、1995年10月15-17日
- (4) 中柴行雄、八巻徹也、安藤将人、関修平、浅井圭介、石樽顕吉、柴田裕実
「ポリシランLB膜へのイオンビーム照射による電子構造評価」、第48回コロイドおよび界面化学討論会、札幌、1995年10月12-14日
- (5) 八巻徹也、中柴行雄、安藤将人、関修平、浅井圭介、石樽顕吉、柴田裕実、田川精一
「ポリシランLB膜中における分子間相互作用」、第14回固体・表面光化学討論会、東京、1995年11月28-29日

2.2. 設計技術の体系化研究

The Study on Systematization of Design Technology

研究テーマ代表者 近藤 駿介（システム量子工学専攻）

1. 序

本研究グループは、核融合炉システムに代表される大規模システムの設計と評価のために必要な設計手法、および解析手法の開発を行なうとともに、それらを用いて核融合炉システムなどの大規模システムに係わる研究開発の方向を示して行くことをその目的としている。

2. 研究進捗状況および今後の予定

(1) D^3He 核融合炉設計

D^3He 燃料サイクルを用いたトカマク型動力炉に関してこれまで得られた知見を基に、より経済性・安全性の高い炉システムの検討がなされた。 D^3He 炉はDT炉のようにT増殖ブランケットを必要としない。また、中性子発生がDTプラズマに比べて1/50~1/60と小さくできることから、遮蔽壁に低放射化材を用いることでより安全性の高い炉システムとして成立することが明かとなった。ガス冷却・蒸気タービンシステムの熱変換効率は、改良型ランキンサイクルを採ることで、ガス出口温度700℃に対して45~50%と試算されている。固気混相流では、He冷却より高い熱伝達特性が提示されている。固気混相流をベースにした高熱負荷第一壁およびダイバータ壁冷却の可能性について予備的検討を行った。今後、さらに整合性のある高熱負荷第一壁の設計検討を予定している。

(2) 知的訓練支援システムに関する研究

プラント運転員の想定外事象対応能力の向上を目的とした訓練を、コンピュータにより支援する手法について研究を行った。まず、想定外事象対応を含むプラント運転操作に関する知識が、階層的機能と定性因果、およびそれらの間の関係によって表現できること、このような知識構造の習得が想定外事象対応能力の向上に寄与することを実験により確認した。つぎに、この知識構造表現に基づいて、規範的運転員の有する知識をモデルベースに推論する手法、ならびに訓練者の行為からその意図を推定する手法を開発した。さらに訓練支援システムのプロトタイプを用いた実験により、これらの手法の妥当性を確認した。

(3) ニューラルネットワークに関する研究

プラントパラメータの時間軌跡より生起事象を同定する手法として、適応テンプレートマッチング法を開発した。本手法は、階層型ニューラルネットワークの汎化能力を活用して、想定され

る異常過渡事象時におけるパラメータ軌跡を記憶させ、最急降下法によって実際の測定軌跡とのマッチングを行うことで事象同定を行うものである。さらに、ファジィ推論を用いて得られた結果の確信度を評価するとともに、事前に想定していない異常過渡を分離同定することが可能である。シミュレーションを用いて本手法の耐雑音性能、耐ドリフト性能を調べ、従来の階層型ニューラルネットワークを用いる手法よりもロバストであることを確認した。

3. 発表論文

(A) 学位論文等

- (1) 古濱 寛、プラント操作員訓練支援システム用学習者モデルに関する研究、博論
- (2) 近藤貴夫、計算機シミュレーションを用いたプラント異常診断の認知過程に関する研究、修論
- (3) 中西幸作、プラント操作に用いられる知識構造の可視化に関する研究、卒論

(B) 国外学会誌等

- (1) Y. Furuhashi, et al., "Identification of Causes of Human Errors in Support of the Development of Intelligent Computer-Assisted Instruction Systems for Plant Operator Training," *Reliability Eng. & System Safety*, 47, 75-84 (1995).
- (2) Y. Furuhashi, et al., "A Methodology to Represent Plant Operator's Mental Model for Training Support System," *Proc. 5th European Conf. Cognitive Science Approaches to Process Control*, 137-146, Espoo, Finland (1995).
- (3) E. Jeong, et al., "Identification of Transient in Nuclear Power Plant Using Neural Network with Implicit Time Measure," *Proc. Top. Meet. Comp.-Based Human Support Systems: Tech., Methods & Future*, 467-474, Philadelphia, US (1995).
- (4) K. Furuta, et al., "Simulation of Communication Network Experiments by Group Cognitive Model," *Proc. 6th IFAC/IFIP/IFORS/IEA Symp. on Analysis, Design and Evaluation of Man-Machine Systems*, 151-156 (1995)..
- (5) K. Furuta, et al., "Analysis of Operator's Diagnostic Behavior Using Computer Simulation," *Proc. 6th Int. Conf. on Human-Computer Interaction*, 957-962 (1995).

(C) 国内学会誌等

- (1) 古田一雄 他, 「運転員認知モデルを用いたプラント異常診断認知過程」, *日本原子力学会誌*, 38, 65-74 (1996).
- (2) 古田一雄 他, 「集団認知モデルによるコミュニケーションネットワーク実験の解析」, *Progress in Human Interface*, 4 (2), 91-98 (1995).

2.3. 核融合実験炉中性子計測システムの工学設計 Engineering Design of Neutron Diagnostic Systems for Fusion Experimental Reactors

研究テーマ代表者 井口 哲夫 (原子力工学研究施設)

1. 序

磁場閉じ込め核融合の研究は、現在、本格的な核燃焼プラズマ実験の段階を迎えつつある。例えば、1993年12月以来、米国TFTRでは、400ショット以上のDTプラズマ実験を敢行し、900MJ以上の核融合エネルギー出力の得られることが確認された。また、E.C.のJETでも、本体装置にクローズドダイバータ部を取り付け、ブレークイーブン($Q \sim 1$)の完全実証を目的とするDT実験が、1996年後半から計画されている。さらに、制御された自己点火状態($Q \sim \infty$)の物理研究および炉工学の研究を行うため、国際熱核融合実験炉(ITER)プロジェクトの工学設計活動が、現在、日・米・欧・露の4極間で、精力的に進行中である。これら核燃焼プラズマ実験の成否には、計測系の性能が大きく関与するが、中でも核反応生成物の1つである中性子をプラズマ診断・制御に利用することの有用性が早くから認識されている。

本研究では、このようなDT核燃焼プラズマの中性子計測系、特に、中性子発生プロファイル及びエネルギースペクトル計測における技術確立を目標とし、新概念の計測方式の創案と適用性評価、プロトタイプ計測系の設計・試作と性能実証、これらの結果に基づいた設計手法の確立と実機のための工学設計を行っている。

2. 研究進捗状況

今年度実施された主な研究テーマの概要は、次の通りである。

(1) 核融合実験炉用14MeV中性子スペクトロメータの開発

現在、反跳陽子マイクロコリメータ型カウンターテレスコープという新概念の14 MeV中性子スペクトロメータにつき、プロトタイプ検出器の設計・試作と14MeV加速器中性子源を用いた性能検証実験を進めているが、今年度は、特に鉛ガラス製のキャピラリープレートベースにした反跳陽子マイクロコリメータを導入して、高エネルギー分解能の実証を試みた。その結果、試作器では検出効率が十分でなく、計数統計やS/N比に難があるものの、14MeV中性子に対して、2.5%半値幅のエネルギー分解能の得られることを確認した。これらの結果をもとに、中性子遮蔽コリメータを含むITER搭載用計測システムの最終的な設計仕様を決定した。

(2) 中性子発生プロファイルモニター用指向性中性子検出器の開発

核融合実験装置における中性子発生プロファイル測定を効率的に行うために、反跳核の前方散乱性を利用した指向性中性子検出器アレイの適用性を検討しているが、今年度は、反跳陽子コリメーション型カウンターテレスコープ方式に、陽子エネルギーの減速フィルターを導入することで、さらに指向性を改善する可能性を探った。その結果、計算と実験の両面から、わずかながらも角度分解能($\sim 1^\circ$ 程度)を向上させることが実証された。また、プラスチックシンチレーティングファイバーをトーラス

系核融合実験装置のポロイダルまたはトロイダル方向に張り巡らして、ファイバー両端まで伝搬するシンチレーション光の時間差から中性子発生プロファイルを推定する手法についても実験的に検討され、有用性が確認された。

なお、本グループにて、主に維持・運用されてきた200KVコッククロフト型加速（14 MeV中性子発生装置）は、低ビーム電流運転（ $\sim 0.2\text{mA}$ ）ながら、順調に稼働している。

3. 今後の予定

本研究プロジェクトは、研究代表者が他大学へ転任したこと、及び当初予定していた研究計画のかなりの部分を達成できたことなどに鑑み、とりあえず今年度を以て、終了とする。ただし、現在でも、ブランケット棟設備を利用する必要がある幾つかの実験課題が残されており、これらは、今後完了するまで、中沢研（工・システム量子）グループの研究プロジェクトに吸収された形で、遂行される予定である。

4. 発表論文リスト

(A) 学位論文

(1) 井内悟朗、"OTDR法による放射線分布測定法に関する研究"

東京大学卒業論文（1996年3月）

(B) 国外学会誌等

- (1) T. Iguchi, E. Takada, M. Nakazawa, J. Kaneko, T. Nishitani, T. Matoba and Y. Ikeda; "Development of 14MeV Neutron Spectrometer for Fusion Experimental Reactor", Proc. 7th Int. Toki Conf. Plasma Phys. and Contl. Nucl. Fus., Toki, 1995, E7-P2-70. (to be published in Fus. Eng. Des.)
- (2) E. Takada, T. Iguchi, H. Takahashi, M. Nakazawa and Y. Ikeda; "Distributed Fusion Neutron Sensing by Plastic Scintillating Fibers", Proc. 7th Int. Toki Conf. Plasma Phys. and Contl. Nucl. Fus., Toki, 1995, E7-P2-71. (to be published in Fus. Eng. Des.)
- (3) T. Nishitani, T. Iguchi, J. Kaneko and T. Matoba; "Neutron Spectrometers for ITER", Proc. Int. WS on Diagnostics for ITER, Varenna, 1995, I-15. (to be published in EUR Document.)

(C) 国内学会誌等

- (1) 井口哲夫、大山幸夫：「中性子工学—6. 計測技術—」プラズマ・核融合学会誌, 72(1) (1996) 142-153.
- (2) 井口哲夫：「核融合研究II 核融合炉工学（池上英雄 他 編）」第2編 核融合炉ブランケット工学 3.2.2.3, 3.4.1.1, 3.4.1.2、名古屋大学出版会 (1995).
- (3) 高田英治、高橋浩之、井口哲夫、中澤正治、「中性子発生プロファイルモニタリングのための指向性高速中性子検出器の開発」、日本原子力学会 1995年秋の大会、C28 (1995).

2 4. 光学的手法による核融合反応放射線場のキャラクタリゼーション

Characterization of Nuclear Fusion Radiation Field with Optical Techniques

研究テーマ代表者 中沢 正治 (システム量子工学専攻)

1. 序

我々のグループでは、従来から光学的な放射線測定手法について研究を進め、シンチレーティングファイバーによる放射線分布測定法等の手法が核融合反応放射線場の測定に適していることを示して来た。今年度は、昨年度より実施しているプラスチックシンチレーティングファイバー (PSF) による核融合プラズマ中での中性子発生プロファイル測定法について、その適用性を検討するとともに、核融合放射線場への Optical Time Domain Reflectometry (OTDR) 法の適用性について検討した。また、プラズマ ECT (Emission Computed Tomography) への適用を念頭におき、光学的な手法による中性子指向性検出器についても検討を進めた。

2. 研究進捗状況

(1) PSF による中性子発生プロファイル測定法に関する基礎実験

PSF を核融合装置の周辺に配置し、その上での中性子束分布を測定することによってプラズマ中での中性子発生プロファイルを測定する手法について、昨年度から研究を進めて来た。今年度は実験精度をさらに高め、本手法によって円形に配置した PSF 内部での点線源の位置を知ることが十分に可能であることを示した。今後は、点線源ではなく、分布を持った線源である場合に線源分布を再構築する手法の検討等を行うことが必要である。

(2) OTDR 法の核融合反応放射線場への適用性に関する検討

中性子照射時に光ファイバー中に生じるカラーセンターをもとに、中性子束分布を測定する手法について検討を行ったが、入力パルス光の波長が $850\mu\text{m}$ と長い場合には、OTDR 法によって測定可能なだけの損失が生成されにくく、測定が困難であることが分かった。今後は、パルス光の短波長化、より中性子に敏感な光ファイバーの利用などの方策の検討が必要である。他方、ラマン OTDR を利用する光ファイバー温度分布センサーを 14MeV 中性子環境下へ適用したところ、 $1 \times 10^6 [\text{n}/\text{sec}/\text{cm}^2]$ の中性子束下では測定結果への影響は無く、十分に温度測定が可能であることが示された。今後はより高い中性子束環境下での温度測定を試み、ラマン散乱法による温度測定法の適用限界について評価する予定である。

(3) 中性子指向性検出器の開発

PSF はその形状の長尺性から、それ自体が固有の指向性を持っているが、多数本の PSF を同時に指向性検出器として用い指向性検出器を多数本併用し、これらの測定結果をアンフォーリング法で処理することにより、角度分解能を向上させる手法について検討を行った。単一の検出器では $\pm 15^\circ$ の角度分解能が、本手法の適用によって $\pm 6^\circ$ まで向上することが示された。今後は角度分解能向上可能性について実験によって実証するとともに、データ処理法についても検討を行うことが必要である。

3. 今後の予定

PSF-TOF 法によるプロファイル測定について、データ処理手法の検討を行う。OTDR 法については、パルス光の低波長化を目指して準備を進めるとともに、温度、歪み等の測定がさらに高い中性子束下で可能か否かについて検討を行う。また、指向性検出器については、シンチレータ+光電子増倍管型の S/N 比の向上を目指し、最適なシンチレータ材料を検討するとともに、多数本+アンフォールディング方式について実験によって可能性の実証を行う。

4. 発表論文リスト

(A) 学位論文

- (a) 井内悟朗 "OTDR 法による放射線分布測定法に関する研究"、東京大学卒業論文(1996年3月)

(B) 国外学会誌等

- (a) E. Takada, K. Sugiyama, H. Takahashi, T. Iguchi, M. Nakazawa:" Neutron Radiation Distribution Sensor Using Flexible Plastic Scintillating Fiber Combined with the Time-of-Flight Technique",
IEEE Trans. NS, Vol.42, No.4, pp570-574, 1995

(C) 国内学会誌等

- (a) 高田英治、高橋浩之、井口哲夫、中沢正治：「中性子発生プロファイルモニタリングのための指向性高速中性子検出器の開発」、日本原子力学会、1995年秋の大会、日本原子力研究所、10月(1995)、C28

25. 高速中性子ラジオグラフィの散乱線補正

Correction Technique of Scattering Neutron Components of FNR Images

研究テーマ代表者 吉井 康司 (原子力工学研究施設)

1. 目的

14MeV中性子発生装置、および弥生を用いて、高速中性子ラジオグラフィ撮影技術向上のための基礎研究を進めている。撮影画像を定量的に評価したところ、散乱線の影響により濃度値の笠上げがあり、像のコントラストを低下させ、画像歪みが生じていることが分かった。そこで、FNRにおける散乱中性子の影響の補正方法について検討を行うことを、本研究の目的とした。昨年度は、薄肉円板試料を被写体モデルとして、散乱線成分を計算した所、円板の半径の2倍の距離を、コンバータと被写体の間にとると、散乱線成分が無視できる程度に減衰することがわかった。今年度は、厚肉円板試料についての計算モデルを検討し、実験との相関を調べた。

2. 研究進捗状況

厚肉円板試料についての計算モデルを検討し、実験との相関を調べた結果、解析値と実験値はよい一致を示した。厚さが3 cmの試料で、試料の半径をパラメータとした場合、半径6 cm以上の試料で散乱線成分は飽和傾向を示した。また、半径が3 cmの試料で、試料の厚さをパラメータとした場合、厚さ2.5 cmにピークを持ち、厚さが増すほど散乱線成分が小さくなる結果を示した。

3. 発表論文リスト

(B) 国内学会誌等

- (1) 吉井康司、宮健三、小林久夫、”冷却型CCDカメラを用いた高速中性子ラジオグラフィ”、1995年 日本原子力学会、秋の大会、C6
- (2) 吉井康司、”東京大学高速中性子源炉「弥生」における高速中性子ラジオグラフィ撮影技術の開発”、第47回中性子ラジオグラフィ研究会、(1995-11)
- (3) 吉井康司、”弥生炉高速中性子ラジオグラフィシステムとその応用”、平成7年度科研費総合A研究会 (1996年1月9日、10日)
- (4) 吉井康司、”高速中性子ラジオグラフィ法の開発と問題点”、放射線、Vol.22, No.1, (1996), 11-18
- (5) 吉井康司、宮健三、新村信雄、唐澤裕子、”イメージングプレートを用いた高速中性子ラジオグラフィの試み”、1996年日本原子力学会 春の年会、G12

(C) 国外学会誌等

- (1) K. Yoshii and H. Kobayashi, "Correction of fast neutron scattered components from fast neutron radiograph", Proceeding of The Second International Topical Meeting on Neutron Radiography System Design and characterization, (1995), 178-183
- (2) K. Yoshii and H. Kobayashi, "Characterization of YAYOI fast neutron radiography field", *ibid*, 165-170
- (3) K. Yoneda, S. Fujine, K. Yoshii and H. Kobayashi, "Development of a Fast, Thermal Neutron, and Gamma Ray Component Discriminator", *ibid*, 152-157
- (4) T. Nakajima, M. Oda, M. Tamaki, K. Ohkubo, K. Yoshii and S. Fujine, "Fast neutron computed tomography with TV imaging at YAYOI", *ibid.*, 209-214

26. ブランケット管理部

管理部長 井口 哲夫 助教授
 総合管理室 吉井 康司 助手

(1) 平成7年度利用について

本装置は工学部内共同利用施設で、核融合ブランケット設計基礎実験装置運営委員会により運用されている。委員長は平成7年度よりシステム量子工学科の井上信幸教授が担当された。平成7年度は表1に示す25件の研究テーマが採択され研究が進められた。

(2) 実験室管理責任者について

実験室管理責任者を表2に示すように選任し、実験室の管理及び火元責任者とした。

(3) 本装置の修理整備について

表3に管理業務報告等メモを示す。

平成7年度の特記事項としては、トリチウム工学実験室用空調機給気フィルターチェンバーが腐食したのに伴う更新、及び重イオン照射実験室暗室の雨漏りに伴うブランケット棟屋上の一部防水工事である。

(4) その他

平成7年5月19日にシステム量子工学科123講義室にて、平成6年度の本装置研究成果報告会を実施する(UTNL-R-0325にて報告書を発行)。又、平成7年9月に、本装置平成6年度研究成果報告書(UTNL-R-0327)を発行する。

表2. 平成7年度核融合炉ブランケット設計基礎実験装置実験室管理責任者

実験室名称	管理責任者(正)	管理責任者(副)	管理責任者(副) (ブランケット管理部)
超電導工学実験室	班目 春樹*	岡本 孝司	吉井 康司
重イオン照射実験室	関村 直人*	河西 寛	井口 哲夫
汎用実験室	山脇 道夫*	山口 憲司	吉井 康司
トリチウム工学実験室	田中 知*	山口 憲司	井口 哲夫
核融合量子工学実験室	中沢 正治*	高橋 浩之	井口 哲夫
第一壁電磁現象実験室	宮 健三*	上坂 充	吉井 康司

(敬称略)

表1. 平成7年度核融合炉ブランケット設計基礎実験装置研究テーマ一覧

	研究テーマ名	研究テーマ代表者
1	プラズマ/固体・液体界面における不純物粒子の輸送挙動	田中 知
2	核融合炉実用材料へのトリチウム付着と再放出メカニズムの解明	田中 知
3	固体表面近傍における粒子挙動の評価法の開発に関する研究	山口 憲司
4	水素同位体ビームによる第一壁燃料ダイナミックスの研究	山脇 道夫
5	プラズマ/壁界面における水素や水蒸気の吸着・脱離に関する量子化学的検討	長崎 晋也
6	ディスラプション時の第一壁の挙動	班目 春樹
7	高温超電導体の核融合炉高度化への応用	宮 健三
8	核融合炉第一壁の電磁的非破壊検査	宮 健三
9	照射による材料組織・強度特性変化の研究	幸野 豊
10	第一壁の画像解析に関する研究	岡本 孝司
11	レーザー共鳴イオン化分光を用いた核融合炉材料界面特性の評価手法の開発	井口 哲夫
12	複雑形状流路内乱流の熱・運動量輸送の数値予測	笠木 伸英
13	熱音響型冷凍機の基礎的研究	斉藤 孝基
14	固体増殖材料表面における水素同位体の挙動	田中 知
15	ウラン合金の水素同位体吸収特性	山脇 道夫
16	液体トリチウム増殖材料の物理化学的挙動	寺井 隆幸
17	核融合炉用機能性セラミックス材料の放射線照射効果	寺井 隆幸
18	トリチウム-材料相互作用におけるトラップメカニズム	小野 双葉
19	イオン照射下その場観察法による高エネルギーPKAカスケード損傷	関村 直人
20	核融合炉材料の照射下挙動評価に関する研究	関村 直人
21	非金属材料のイオン照射効果の研究	石樽 顕吉
22	設計技術の体系化研究	近藤 駿介
23	核融合実験炉中性子計測システムの工学設計	井口 哲夫
24	光学的手法による核融合反応放射線場のキャラクタリゼーション	中沢 正治
25	高速中性子ラジオグラフィの散乱線補正	吉井 康司

表3. 平成7年度ブランケット管理部業務報告等メモ

	内 容
5月	<ul style="list-style-type: none"> ・冷房用冷却塔の清掃および点検(5/18) ・平成6年度核融合炉ブランケット設計基礎実験装置研究成果報告会(5/19) ・廊下蛍光灯器具の交換作業(5/26) ・空調機シーズンイン点検(5/30)
6月	<ul style="list-style-type: none"> ・小山評議員見学(6/2) ・冷房用冷却水ポンプ(No.1)芯ぶれ調整(6/5) ・屋上冷却塔防錆薬品容器付属部品の修理(6/6) ・一般排水槽定期清掃(6/20) ・平成7年度R I自主点検(上半期)(6/27)
7月	<ul style="list-style-type: none"> ・ディーゼル発電機点検(7/4) ・受変電設備1ヶ年点検(高圧カットアウトヒューズの交換、およびOCBオイルの交換)(7/8) ・空調機全系統のフィルターの交換(7/10) ・無停電電源装置1ヶ年点検(7/11) ・火災報知器点検(7/18) ・中性子発生装置室用空調送風機のベアリング交換(7/21) ・ブランケット棟屋上一部防水工事(重イオン照射実験室暗室雨漏り対策)(7/18) ・温水ボイラー点検(7/28) ・火災報知器誤発報(管理室区域)(7/29)
8月	<ul style="list-style-type: none"> ・重イオン照射実験室準備室ローカルエアコン設置(8/3)
9月	<ul style="list-style-type: none"> ・地下機械室入口鉄扉の修理(9/7) ・平成7年度R I自主検査(下半期)(9/27) ・地下機械室火災感知器の交換(9月28日誤発報対策)(9/29)
10月	<ul style="list-style-type: none"> ・トリチウム工学実験室用空調機外気取り入れ用フィルターチェンバーの更新(10/30)
11月	<ul style="list-style-type: none"> ・空調機シーズンオフ点検(11/9) ・重イオン照射実験室工作室の整備(不要工作機の撤去)(11/20) ・ブランケット棟屋上清掃作業(11/21)
12月	<ul style="list-style-type: none"> ・中性子発生装置遮蔽性能検査(12/1) ・R I貯留槽バルブ交換(12/1) ・ブランケット棟屋上雨水の雨樋の変更工事(12/4) ・ブランケット棟屋上一部防水工事(重イオン照射実験室暗室の雨漏りの追加対策)(12/6) ・雨宮事務局長見学(12/14) ・冷却塔補給水配管修理(凍結破損修理)(12/27)
2月	<ul style="list-style-type: none"> ・各実験準備室へのネットワークランシーバ設置終了(2/8) ・長谷川事務局長見学(2/15) ・コピー室(BLTユーザー向けワークステーション設置室)にローカルエアコン設置(2/16) ・100KeVイオン加速器および電子顕微鏡の遮蔽性能検査実施(2/16) ・火災報知器点検(2/19) ・外部評価委員見学(2/23)
3月	<ul style="list-style-type: none"> ・平成7年度R I自主検査(1ヶ年点検)(3/22)

**NEXT PAGE(S)
left BLANK**

II. 研究成果報告

ガスダイバータにおける粒子輸送解析

大津 繁樹 田中 知 (システム量子)

Analysis of Particle Transport in a Gas Target Divertor

Shigeki Ohtsu and Satoru Tanaka
(Quantum Engineering and Systems Sciences)

Abstract

2-dimensional modelling of divertor plasma was performed with three types of the divertor geometry configuration. Pumping is effective to reduce neutral recycling to core region in the configuration without baffle. In baffle configuration, a good shielding of neutrals in the divertor region can be achieved. The dome configuration reduces plasma density near the null region and flow shear near the separatrix.

1 Introduction

In the past several years, a gas target divertor has been investigated for controlling high heat flux in ITER device. [1] Several problems about gas target divertor operation are pointed out in terms of impurity seeding and recycled neutral particles. Neutral recycling to core region should be lower for optimum confinement. For preventing neutral particles from flowing into the core region, divertor is designed with a baffle plate at the divertor throat. In both problems, it is important to study the relation between divertor geometry and plasma transports.

In this study, we have modeled a gaseous divertor by using B2.5 code. As a divertor configuration, we have investigated three types of divertor geometries which includes no baffle baffle and dome. The effects of a divertor geometry on particle and heat transports are described in this paper.

2 Results and Discussions

The 2-dimensional multifid code (B2.5 code) was used for solving plasma transports (particle, momentum, energy and

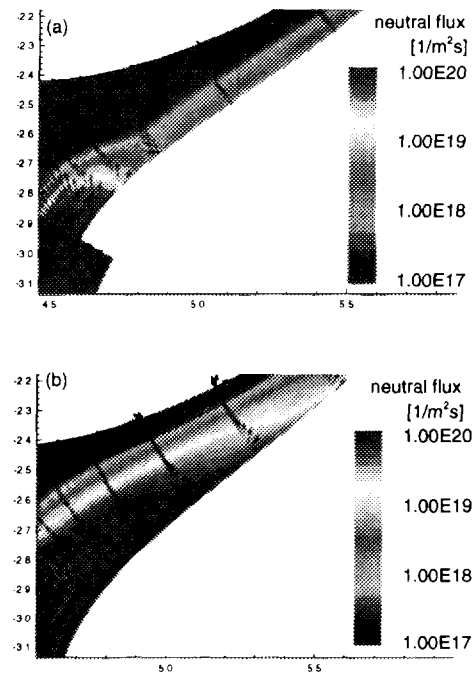


Figure 1: Vector profile and contour of neutral flux in the divertor and SOL. (a) baffle configuration (b) no baffle configuration.

charge). [2] The outer half divertor region in the geometry is considered in a single null configuration for a steady state tokamak reactor. Mesh refinement was adopted so as to become high resolution at the baffle and dome boundaries. A pumping duct is located in the lower side of the outer first wall. We considered the case where only one species, deuterium, was included. The ion and electron temperatures (T_i and T_e) at the core boundary were 250eV which corresponded to 14MW power input to SOL. The electron density was $5 \times 10^{19} \text{1/m}^3$. The boundaries in the first wall, the private flux region, and baffle side are in a condition of albedo ($=1.0$). The particle pumping was conducted in 3% of thermal flux for neutral 1% for ion except pumping parameter surveys. The neutral flux of L-shape baffle is shown in figure 1 a. It is found that the neutral flux into the core region is decreasing in order compared with that of the configuration without baffle (fig.1 b) and the baffle causes neutral preventing flows up to SOL region. As the baffle inside the sol region, the reflection at the mid plain where sol width is minimum is increased.

The dome is located in the private flux region under the null point. It is shown in figure 2 of the contour map of plasma density near the null point that plasma density has changed around the null point. High plasma density area below null point disappears and plasma density is decreasing because dome is shielding neutral flow from the private flux region into the divertor region. This can also be pointed out that less flow shear is observed near the separatri. In the ITER calculation, the backflow in the private region strongly connected to the impurity colling system and MARFE. The dome configuration can be desirable in impurity seeding since impurity localized in the lower divertor region without flowing up the private region and forming MARFE type radiation near the null point.

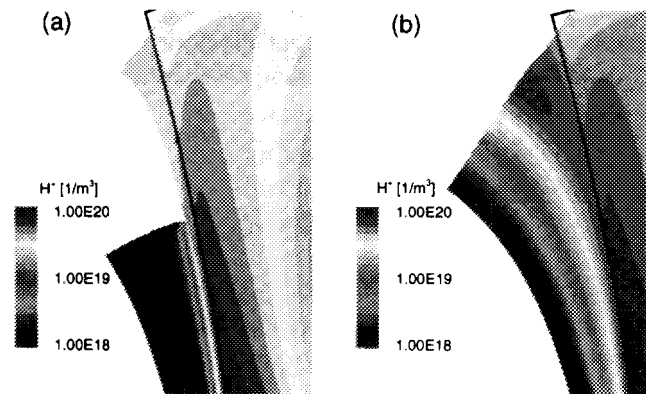


Figure 2: Hydrogen plasma density contour around the null point. (a) dome configuration (b) no dome configuration.

References

- [1] G. Janeschitz et al., J. Nucl. Mater. 220-222 (1995) 83-88.
- [2] B.J.Braams, to be published in Contrib. to Plasma Phys.

田中 知、 大森ルミ
システム量子工学専攻

Sorption and Desorption of Tritiated Water Vapor on Piping Materials of Nuclear Fusion Reactor

Satoru Tanaka and Rumi Ohmori

Department of Quantum Engineering and Systems Science

I. Abstract

Sorption and desorption of D₂O on Cr₂O₃, NiO, SS316 powders were studied at ambient temperature. When D₂O were contacted with samples after drying at 303K, broad peak was observed at 2100~2700cm⁻¹ on Cr₂O₃ and NiO. Sorption and desorption rate depended on wave numbers. Isotope exchange rate with H₂O vapor was faster than dry desorption rate. By heating pretreatment, sorption amount and desorption rate for Cr₂O₃ and NiO decreased. For SS316, broad peak was observed only after heating pretreatment at 673K.

II. Experimental

A Shimadzu FT-IR 8100 with the diffuse reflectance method was used for the measurement of infrared absorption spectra of O-D stretching vibration.

Powders of Cr₂O₃, NiO and SS316 were used. Before IR measurement, samples were dried with Ar gas at 303K or 673K. Sorption of D₂O was observed by addition of D₂O vapor at 303K. Desorption was observed by H₂O containing or dry sweep gas at 303K or by D₂O vapor containing sweep gas at various temperatures. Temperature of the sample was controlled at 303-673K.

Ar gas was used for sweep gas.

III. Results and discussion

When samples were contacted with D₂O vapor after drying at 303K or 673K, broad peak was observed at 2100~2700cm⁻¹ for Cr₂O₃ and NiO. For SS316, broad peak was observed only after heating at 673K. Infrared absorption spectra by D₂O absorbed on experimented samples are given in Fig.1. These peaks were considered to be due to O-D stretching vibration of D₂O adsorbed on the surface. The peak seemed to be composed of three components at 2430cm⁻¹(ν_1), 2580cm⁻¹(ν_2) and 2650cm⁻¹(ν_3). Multiple peaks show that surface is not homogeneous for D₂O adsorption. Broad peak indicates surface inhomogeneity and interaction through hydrogen bond.

From the desorption experiment at 303K shown in Fig.2, D₂O was not removed in seven hours under dry Ar gas but removed in a few hours under H₂O containing Ar gas. In other words, desorption rate by isotope exchange with H₂O vapor was faster than by drying. NiO had a similar tendency. However, D₂O sorbed on SS316 surface was found to be removed by more than 70% in a few hours under dry Ar gas (Fig.3).

Result of desorption by heating under 116Pa D₂O is shown in Fig.4. Peak intensity decreased with the increase of temperature for the peaks ν_1 and ν_2 , but reached a constant level for the peak ν_3 . We observed a similar tendency for NiO.

In case of Cr₂O₃ and NiO, sorption amount for the samples pretreated at 673K was about 70% of that dried at 303K. Desorption rate for the sample pretreated at 673K was slower than dried at 303K. This is considered to be caused by larger adsorption energy for the modified surface by heating pretreatment.

IV. Conclusions

Infrared absorption spectra on the surface of Cr₂O₃, NiO and SS316 were observed in-situ by FT-IR with the diffuse reflectance method. Sorption and desorption of D₂O vapor depended on the wave length of observed absorption peak. Desorption rate by isotope exchange with H₂O vapor was faster than by dry sweep gas at ambient temperature.

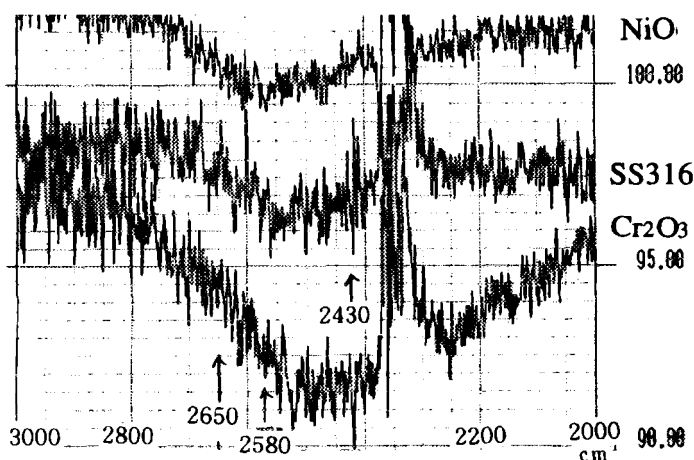


Fig.1 Infrared absorption spectra by D₂O absorbed on Cr₂O₃, NiO and SS316.

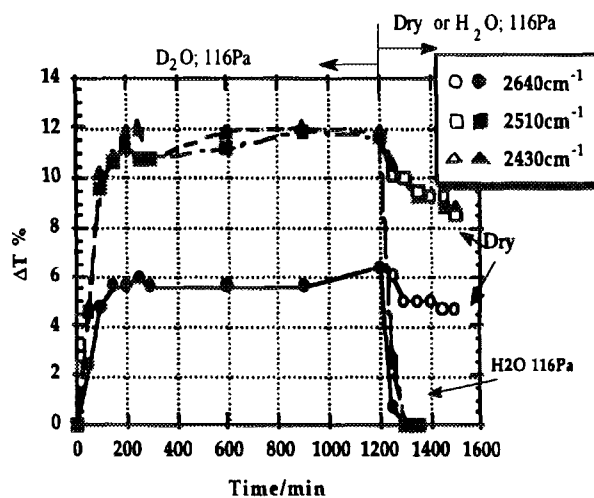


Fig.2 Sorption under 116Pa D₂O and desorption under dry sweep gas or 116Pa H₂O for Cr₂O₃. The sample was pretreated at 303K.

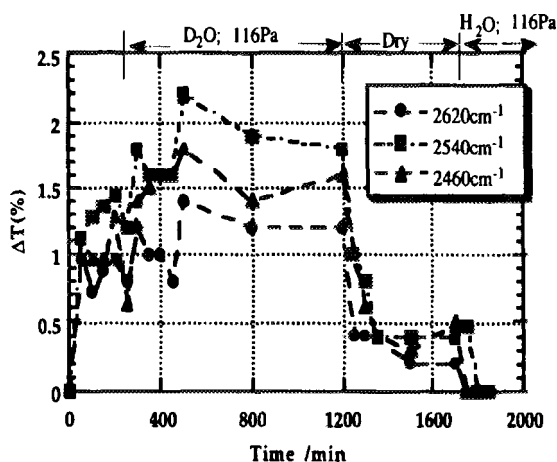


Fig.3 Sorption under 116Pa D₂O and desorption under dry sweep gas or H₂O 116Pa for SS316. The sample was pretreated at 673K.

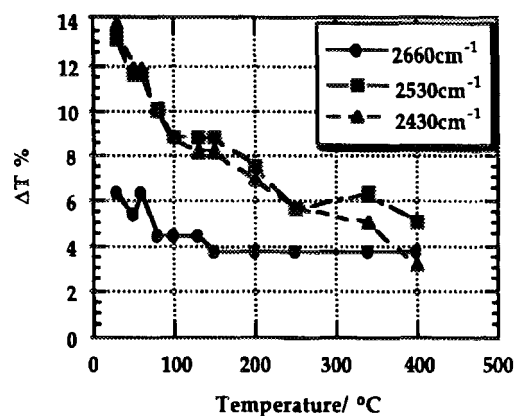


Fig.4 Desorption by heating under 116Pa D₂O for Cr₂O₃. The sample was pretreated at 303K.

高温ケルビン計による固体材料表面の仕事関数測定

鈴木 敦士、山口 憲司、山脇 道夫 (原子力工学研究施設)

WORK FUNCTION MEASUREMENT OF THE SURFACE OF SOLID MATERIALS BY USE OF HIGH-TEMPERATURE KELVIN PROBE

A. Suzuki, K. Yamaguchi and M. Yamawaki
(Nuclear Engineering Research Laboratory)

Abstract

Work function is quite sensitive to the change of surface electronic properties of solid materials. In the present study, an experimental setup is being developed, which enables to measure work function of solid materials under controlled atmosphere.

1 Introduction

Work function is quite sensitive to the change of surface electronic properties of solid materials. In this regard, work function measurement can be applied to fuel-material interaction studies related to fusion research and development where surface phenomena play a crucial role; e.g. adsorption/desorption of tritium at the surface of solid breeder materials [1], defining the role of surface impurities in hydrogen recombination process [2], etc. The present paper, to begin with, briefly reviews the basic principle of work function measurement based on contact potential difference (CPD) method. Then the outline of experimental setup is described, and the current progress and future plan are summarized.

2 Device Configuration

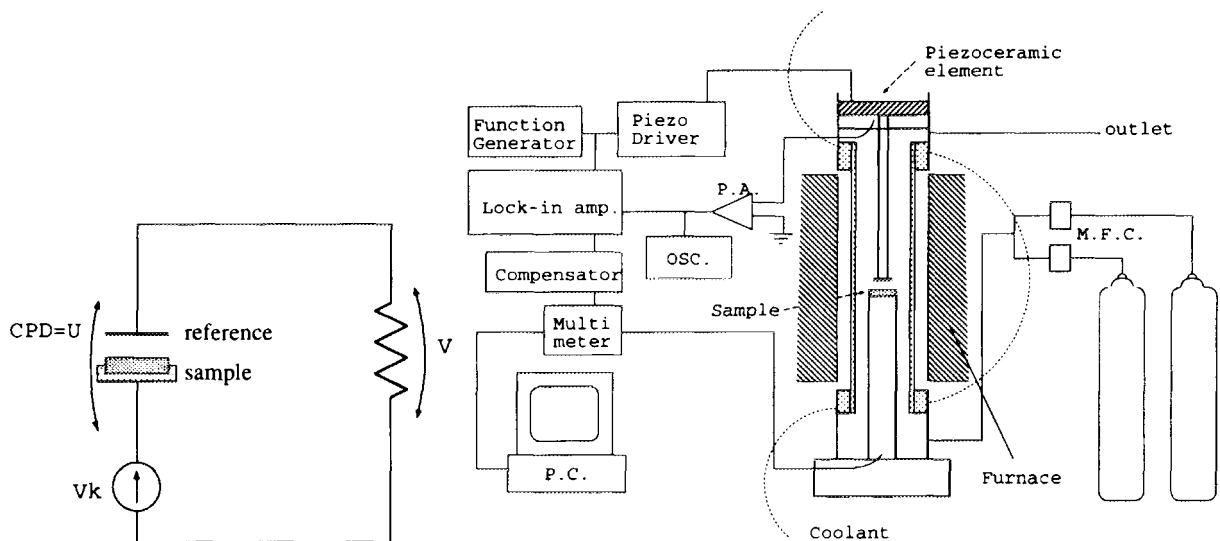


Fig.1: Principle of measuring contact potential difference (CPD) [3].

Fig.2: Schematic diagram of the Kelvin probe measurement system.

An electric circuit which is equivalent to that employed in Kelvin probe system is shown schematically in fig.1 [3]. Using the symbols defined in the figure, the following equation holds;

$$R_c \frac{d}{dt}[C(U + V_k + V)] + V = 0 , \quad (1)$$

where t is the time, R_c is the resistance, and $C = C(t)$ is the capacity between sample and reference electrodes. If one assumes

$$C(t) = C_0(1 + m \sin(\omega t)) , \quad (2)$$

where C_0 , m and ω are the constants, then the first term V_1 of $V(t)$ in Fourier expansion series becomes

$$V_1 = m\omega RC_0(V_k + U)(1 + RC_0)^{-2} , \quad (3)$$

so that $V_1 = 0$ when $U = -V_k$ [4]. Kelvin probe employs a compensation circuit which allows automatic determination of V_k . The measurement system currently under development in collaboration with Australian Nuclear Science and Technology Organisation (ANSTO) is shown in fig.2. The distance between the electrodes is periodically changed by piezoceramic driving element with a function generator. The CPD signal is first amplified by pre-amplifier (P.A.) and is further amplified by lock-in amplifier in addition to phase sensitive detection. A furnace for heating the specimen to higher temperatures (> 1000 K) is being installed. Noise from the furnace can be reduced by use of lock-in amplifier. Moreover, a personal computer (P.C.) is employed for data acquisition, while sweep gas of controlled flow rate (regulated by M.F.C. (mass flow controller)) can be admitted to the probe.

3 Current Progress and Future Plan

At present, CPD as small as 10 mV can be measured at room temperature. To date the CPD of polycrystalline Li_4SiO_4 and ZrO_2 doped with Y_2O_3 or Nb_2O_5 has been measured using Pt electrode as a reference under controlled atmosphere: i.e. equilibrium O_2 partial pressure (P_{O_2}); 10^{-35} - 10^{-13} Pa and temperature (T); 593 - 913 K for Li_4SiO_4 , and P_{O_2} ; 50 - 10^5 Pa and T ; < 913 K for doped ZrO_2 . Pellets of Li_4SiO_4 are currently under irradiation either by fast neutrons or H^+ ion beam at the University of Tokyo to investigate how the irradiations affect the value of work function.

References

- [1] The latest progress in this field can be found in Proc. Int. Workshop Ceramic Breeder Blanket Interactions, C. E. Johnson (ed.) (IEA, 1995).
- [2] M. Yamawaki, K. Yamaguchi, S. Tanaka, T. Namba, T. Kiyoshi and Y. Takahashi, J. Nucl. Mater. 162-164 (1989) 1071.
- [3] J. Nowotny, M. Sloma and W. Weppner, J. Am. Ceram. Soc. 72[4] (1989) 564.
- [4] J. R. MacDonald and D. E. Edmondson, Proc. IRE (Institute of Radio Engineers, Inc.) 19[2] (New York, 1961) pp.453-466.

ニッケル中における水素同位体およびヘリウム保持に関する研究

岡田 光正 佐藤 力哉 山口 憲司 山脇 道夫
原子力工学研究施設

Retention of hydrogen isotopes and helium in nickel

M. Okada, R. Sato, K. Yamaguchi and M. Yamawaki
Nuclear Engineering Research Laboratory

Abstract

In the present study, a thin foil of nickel was irradiated by H_2^+ , D_2^+ and He^+ to a fluence of $1.2 \sim 6.0 \times 10^{20}/m^2$ using the TBTS (Tritium Beam Test System) apparatus. The thermal desorption spectroscopy (TDS) technique was employed to evaluate the total amount of retained hydrogen isotope and helium atoms in nickel. In the spectra, two peaks appeared at $440 \sim 585K$ and $720 \sim 735K$ for helium. Hydrogen isotopes irradiation after helium preirradiation were found to enhance the helium release and to decrease the peak temperatures. Helium irradiation after hydrogen isotopes preirradiation were found to enhance the helium release, but the peak temperature showed little difference from that without preirradiation.

1. Introduction

The behavior of hydrogen isotopes and helium in the materials is one of the important factors which determine the performance of fuel plasma. And the helium ash produced by fusion reactions makes it difficult to sustain the ignition condition because of the fuel dilution and the enhancement of radiation loss. Additional pumping is necessary when the pumping efficiency in divertor region is not sufficient. In such a case, metals such as nickel and vanadium may be employed to enhance the pumping efficiency for helium ash because of their characteristic to selectively pump helium.

In the present study, we investigated the retention of helium in nickel by means of thermal desorption spectroscopy. Results are shown for thermal desorption of helium and hydrogen isotopes from nickel irradiated with helium or hydrogen isotopes ions whose dose ranging from 1.2×10^{20} to 6.0×10^{20} ions/ m^2 .

2. Experimental

The sample employed in the present study was a 0.1mm thick polycrystalline nickel foils (99.7 % in purity) and was cleansed in an ultrasonic bath with trichloroethylene. The sample was subsequently bombarded with $1.2 \times 10^{20} He^+/m^2s$ or $1.2 \times 10^{20} H_2^+(D_2^+)/m^2s$ at room temperature. The total fluences of He^+ and $H_2^+(D_2^+)$ were $1.2 \times 10^{21} He^+/m^2$ and $5.0 \times 10^{21} H_2^+(D_2^+)/m^2$, respectively.

After bombardment, the sample was irradiated with 3keV He^+ or $H_2^+(D_2^+)$ to a dose varying from $1.2 \times 10^{20}/m^2$ to $6.0 \times 10^{20}/m^2$. In order to comprehend the interactive effects between helium and hydrogen isotopes in nickel, the procedure of irradiation with He^+ and $H_2^+(D_2^+)$ was reversed. Namely, He^+ irradiation after $H_2^+(D_2^+)$ preirradiation and $H_2^+(D_2^+)$ irradiation after He^+ preirradiation were conducted and the obtained results were compared.

In the thermal desorption spectroscopy (TDS) measurement, the temperature of sample was increased to 1073K at the rate of 3K/s and the total amount of desorbed gas was measured by integrating the signal of quadrupole mass spectrometer (QMS) which had been calibrated beforehand.

3. Results and discussion

The thermal desorption spectrum measured for the sample which was irradiated with He^+ to a dose of $1.2 \times 10^{20}/\text{m}^2$ is shown in Fig.1. The total amount of helium is $1.2 \times 10^{19} \text{He}/\text{m}^2$ and the peaks of desorption are observed at 552K and 737K. Table 1 summarizes the temperature of desorption peaks obtained under various irradiation conditions.

The total amount of desorbed helium in irradiation No.2 was about $3.9 \times 10^{19} \text{He}/\text{m}^2$. However the amount of helium desorption in irradiation No.3 was not measured because the atomic weights of both helium and deuterium are ~ 4.0 and it is difficult to distinguish helium from deuterium by QMS. The temperatures of desorption peak of helium are 525K and 728K in irradiation No.2 and 502K and 722K in irradiation No.3. The hydrogen isotopes irradiation after helium preirradiation shifts the desorption peaks to lower temperature and increases the total amount of helium desorption, which implies that the apparent activation energy of He desorption is decreased due to hydrogen irradiation.

The total amounts of desorbed helium are $8.8 \times 10^{19} \text{He}/\text{m}^2$ in irradiation No.4 and $2.4 \times 10^{20} \text{He}/\text{m}^2$ in irradiation No.5. Helium is desorbed at 444K and 723K in irradiation No.4 and at 551K and 734K in irradiation No.5. The total amount of desorbed helium in the case of H_2^+ irradiation after He^+ preirradiation (No.4) was much larger than that in the case of He^+ irradiation after H_2^+ preirradiation (No.5). The shift of helium desorption peaks to lower temperature was more significant in the case of irradiation No.4 than irradiation No.5.

4. Conclusion

- Hydrogen isotopes ions irradiation to nickel after He^+ preirradiation increases the total amount of desorbed helium and decreases the apparent activation energy of helium desorption.
- The thermal desorption of helium due to He^+ irradiation after hydrogen isotopes ions preirradiation occurs almost at the same temperature as compared with that without preirradiation.
- The total amount of helium desorption in the case hydrogen isotopes ions irradiation after He^+ preirradiation is larger than that in the case of He^+ irradiation after hydrogen isotopes ions preirradiation.

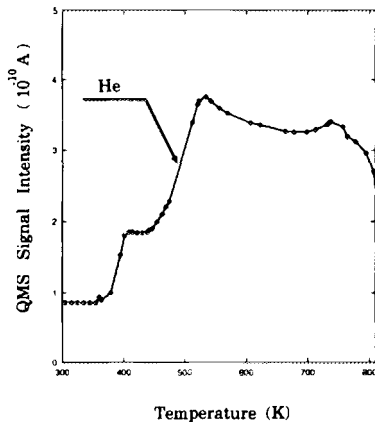


Fig. 1 Thermal desorption spectrum of He from Ni irradiated to $1.2 \times 10^{20} \text{He}^+/\text{m}^2$.

No.	Irradiation Conditions	Temperature of the lower peak [K]	Temperature of the higher peak [K]
1	$\text{He}^+ 1.2 \times 10^{20} / \text{m}^2$	552	737
2	$\text{He}^+ 1.2 \times 10^{20} / \text{m}^2$ ↓ $\text{H}_2^+ 6.0 \times 10^{20} / \text{m}^2$	525 (\ \)	718 (\ \)
3	$\text{He}^+ 1.2 \times 10^{20} / \text{m}^2$ ↓ $\text{D}_2^+ 6.0 \times 10^{20} / \text{m}^2$	502 (\ \)	722 (\ \)
4	$\text{He}^+ 6.0 \times 10^{20} / \text{m}^2$ ↓ $\text{H}_2^+ 6.0 \times 10^{20} / \text{m}^2$	444 (\ \)	723 (\ \)
5	$\text{H}_2^+ 6.0 \times 10^{20} / \text{m}^2$ ↓ $\text{He}^+ 6.0 \times 10^{20} / \text{m}^2$	551 (→)	734 (→)

Table 1 Temperature of helium desorption under various irradiation conditions.

MAP 装置による炭化水素輸送過程の研究

松山 征嗣¹ 山口 憲司¹ 田中 知² 山脇 道夫¹

1. 東京大学工学部附属原子力工学研究施設
2. 東京大学大学院工学系研究科システム量子工学専攻

HYDROCARBON TRANSPORT IN THE LABORATORY
PLASMA (MAP)S. Matsuyama¹, K. Yamaguchi¹, S. Tanaka², and M. Yamawaki¹

1. Nuclear Engineering Research Laboratory, the University of Tokyo
2. Department of Quantum Engineering and Systems Science, the University of Tokyo

Hydrocarbons are admitted in the laboratory plasma in order to investigate the transport processes of carbon - containing molecules in relation to redeposition processes in the fusion boundary plasma. When CH₄ was introduced into the plasma, CH radical band spectra were optically identified, while in the case of C₂H₂ introduction, C₂ radicals were also identified in addition to CH radicals. Excitation temperature was determined from CH and C₂ spectra band, which was observed to increase on approaching to the target.

INTRODUCTION

Carbon materials have been used as plasma facing components in major tokamaks, and will be continuously used such as in the form of carbon composites or in the form of the matrix coated by beryllium or others. However, graphites in general have several drawbacks such as high chemical sputtering rate and radiation enhanced sublimation. Therefore, the transport processes in relation to redeposition of the sputtered carbon have been investigated from the standpoint to determinate the net-erosion rate, but studies of chemical sputtered hydrocarbons have been performed less systematically, for example, the temperature of impurity molecules in the boundary region has been scarcely reported. In the present study, we have performed such experiments that the hydrocarbons (CH₄ and C₂H₂) were admitted to the laboratory plasma in order to simulate the transport processes of chemically sputtered hydrocarbon species in relation to redeposition at the target.

EXPERIMENTAL

The plasma generator 'MAP (Materials And Plasma)' has been employed in the boundary layer physics and chemistry studies involving plasma and materials. The hydrocarbons (CH₄ and C₂H₂) were vertically introduced, at 10 cm apart from the target, through a nozzle aperture into a steady - state hydrogen plasma with a ratio of C_xH_y:H₂=1:4 (40:160 in cm³/min), The total pressure in the chamber was $P=6 \times 10^{-2}$ Pa, while the magnetic field was $B = 0.02$ T. The electron temperature was about 10 eV and the electron density was about 10^{18} m⁻³. An optical measurement system with a photo multichannel analyzer (PMA) was used during these experiments to record photoemission in the plasma. The focusing lens can be driven in axial and radial directions of the plasma, so that the spatial distribution of the luminescence can be obtained.

A quantum mechanical approach was employed to calculate the emission spectra to fit the measured spectra,

$$I_{v'J'v''J''} = \frac{N_{v'J'}}{2J'+1} A_{v'v''} S_{J'J''}, \quad (1)$$

where $I_{v'J'v''J''}$ is the signal intensity of photo-emission by a molecular transition from the vibrational state v' and rotational state J' in the upper excited electronic state to v'' and rotational state J'' in the lower electronic state, $S_{J'J''}$ is the Hönl-London factor, $N_{v'J'}$ is the number of molecules in the excited - state $v'J'$, $A_{v'v''}$ is the Einstein coefficient for the transition. and $q_{v'v''}$ is the Franck - Condon factor. The value of $N_{v'J'}$ in Eq.(1) for one electronic state can be defined assuming Boltzman distribution:

$$N_{v'J'} = K g_{v'} \exp\left(\frac{-E_{v'}}{kT_{v'}}\right) g_{J'} \exp\left(\frac{-E_{J'}}{kT_{J'}}\right), \quad (2)$$

where K is constant. Furthermore, $g_{v'} = 1$ for all vibrational levels in diatomic molecules and $g_{J'} = 2J' + 1$. Substituting Eq.(2) into Eq.(1) and summing all the constant terms into K' gives

$$I_{v'J'v''J''} = K'E^3 q_{v'v''} S_{J'J''} \exp\left(\frac{-E_{v'}}{kT_{v'}}\right) \exp\left(\frac{-E_{J'}}{kT_{J'}}\right), \quad (3)$$

$$\lambda = hc/E, \quad \lambda: \text{wavelength}. \quad (4)$$

In the above equation, E is the energy difference between the initial and final states, v and J , and $q_{v'v''}$ is the Franck - Condon factor. ν_e is the electronic energy difference between the upper and lower states. The spectra fitting procedure completes by computing photo-emission intensities $I_{v'J'v''J''}$ and E and then calculating λ to obtain spectral lines with respect to emission wavelength (nm).

RESULT AND DISCUSSION

In the experiments line intensities of radicals originating from the impurities admitted from the nozzle to the H_2 plasma are optically measured in the range of 420 to 560 nm. When CH_4 was introduced, the $A^2\Delta - X^2\Pi$ band of the CH - radical was identified in the vicinity of 430 nm, while in the case of C_2H_2 introduction, not only CH - radical band but also C_2 band with large intensity were identified,

Fig.1 show the spectra calculated by a quantum mechanical approach of CH, which agree with the measured spectra. The calculated spectrum is dependent on the excitation temperature, so that the excitations temperatures in the experiments can be obtained by fitting the calculated spectra to the experimental one. Excitation temperatures, as evaluated from the curve-fitting of the optical emission spectra of CH and C_2 at selected positions along the plasma axis, are shown in **fig.2**. The excitation temperatures of CH and C_2 were found to be in the range of 3000 to 4000 K. The excitation temperatures of radicals rose gradually in the approach to the target, which seems to indicate that the radicals, by acquiring energy by collision with the plasma particles from behind, gradually enhance their energy.

SUMMARY

When CH_4 was introduced into the plasma, the $A^2\Delta - X^2\Pi$ band of the CH - radical was identified in the vicinity of 430 nm, and while in the case of C_2H_2 introduction, not only CH - radical but also large C_2 band were identified; namely, the bands of the $A^3\Pi_g - X^3\Pi_u$ - transition in the vicinity of 460 nm and 560 nm. Curve - fitting was performed on the obtained CH and C_2 spectra band, and the excitation temperature was evaluated in selected positions along the plasma axis. It is observed that the excitation temperature rose gradually along the approach to the target.

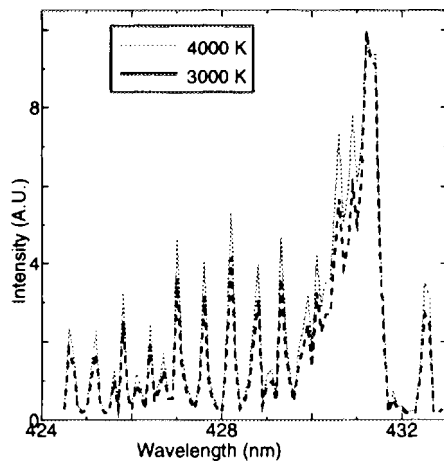


Fig.1: The fitted CH spectra according to the quantum approach.

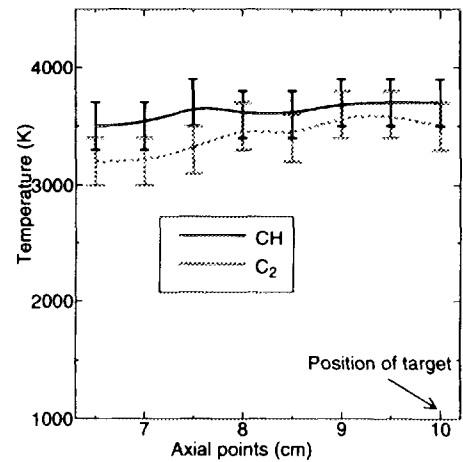


Fig.2: The axial distribution of the excited temperature of CH and C_2 .

Mo における水素輸送の律速段階

大越啓志郎、近澤佳隆、ヴァシリ・バンドゥルコ、山口憲司、山脇道夫
原子力工学研究施設

The Rate-Limiting Process of Hydrogen Transport in Mo

K. Ohkoshi, Y. Chikazawa, V. Bandourko, K. Yamaguchi and M. Yamawaki
Nuclear Engineering Research Laboratory

Abstract

Hydrogen isotope transport characteristics of Mo, whose refractory properties are considered to be suitable as plasma facing material, was investigated by applying 3 keV D_2^+ beam to the membrane specimen. The Arrhenius plot of deuterium permeation probability showed linear increase against the reciprocal temperature and its apparent activation energy was determined as 41.5 kJ/mol. The simultaneous irradiation of 3 keV Ar^+ onto backside surface of specimen had little effect on the deuterium permeation rate. According to these results, the rate-limiting process of deuterium transport in Mo was determined.

1 Introduction

It is important to understand fuel particle dynamic behavior around plasma facing materials (PFM) in a controlled thermonuclear fusion reactor in order to control the fuel burning process and ensure safety of tritium management.

Mo is a refractory metal whose melting point is 2,893 K and has small hydrogen solubility and diffusivity, which are considered to be favorable from the point of view of tritium retention and permeation.

In the present study, measurement of permeation rate and the effect of surface impurities at different temperatures were investigated employing *in-situ* AES (Auger electron spectroscopy) and SIMS (secondary ion mass spectrometry) surface analyses.

2 Experimental

The specimen was a foil of polycrystalline Mo (14mm ϕ , 0.1 mm t), which was welded on the top of a cylindrical sample holder of the experimental device (Fig.1). The specimen separates the upstream-side (irradiation-side) and downstream-side (back-side) chambers and is insulated from the vessel for measurement of the ion current of incident beam.

The beam was a molecular ion (D_2^+) beam, which was emitted from IS2 in Fig.1, and the beam energy was set at 3 keV and the flux was $3.3 \times 10^{16} D_2^+ / m^2 s$. The base pressure in the upstream-side chamber was

around $10^{-4} - 10^{-3}$ Pa and that of downstream-side was 10^{-6} Pa. The pressures were monitored by B.A. gauge during experiment, whereas the partial pressures were measured by QMS (quadrupole mass spectrometer). The AES and SIMS analyses were performed occasionally in order to check the specimen surface impurities. The specimen temperature was varied from 350 to 1000 K.

3 Results and discussion

The dependence of permeation probability due to IDP (ion-driven permeation) on the specimen temperature, T , is shown in Fig.2. The permeation probability reached ~ 0.20 at 1000 K and the apparent activation energy of permeation was determined to be 41.5 kJ/mol. During irradiation of D_2^+ beam onto the upstream-side surface of specimen, irradiation of 3 keV Ar^+ beam onto the downstream-side surface was performed. The time dependence of deuterium permeation rate after termination of Ar^+ irradiation is shown in Fig.3. Quite in contrast to Nb, where permeation probability shows drastic increase by Ar^+ irradiation [1], the change for Mo was almost negligible. The characteristics described above show that the rate-limiting process of deuterium transport in Mo is "RD" type, which means that the rate-limiting processes for the upstream-side and downstream-side of specimen are the recombination and diffusion, respectively [2].

The transient permeation behavior due to D_2^+ beam injection showed a “permeation spike”, where permeation rate increased after the start of beam irradiation and then decreased to its steady state value. It showed interesting temperature dependence that the peak of spike appeared 1 minute after the start of irradiation at 900 K, whereas it took 30-40 minutes at 800 K. This difference may be attributed to the surface impurity compositions or surface defects. The downstream-side surface impurity compositions measured by AES showed the existence of carbon and oxygen, and as shown by Fig.4, the surface concentration of sulfur rapidly increases in the temperature range 800 - 900 K. In this sense, more active control of the surface impurity compositions (i.e., the artificial change of surface impurities by means of O_2 or H_2S admission) is required.

4 Conclusion

The temperature dependence of IDP rate through Mo was measured and its apparent activation energy was determined to be 41.5 kJ/mol. The Ar^+ irradiation onto the downstream-side surface showed little effect on the permeation rate. These results indicate that the rate-limiting process for Mo is RD type. The surface impurity analysis by AES showed the existence of carbon, oxygen and sulfur. A strong dependence of permeation spike on temperature was observed. Further investigation on the effect of surface impurities on permeation is required.

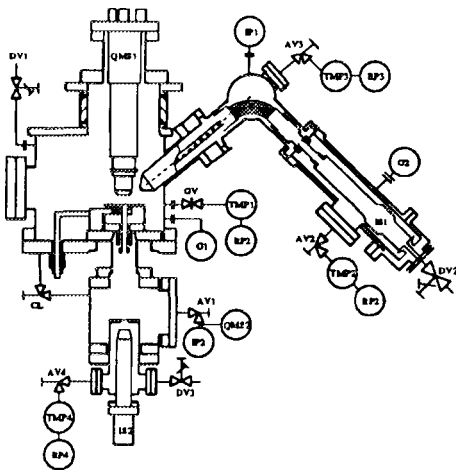


Fig.1 : Hydrogen permeation experimental device HYPA-IV.

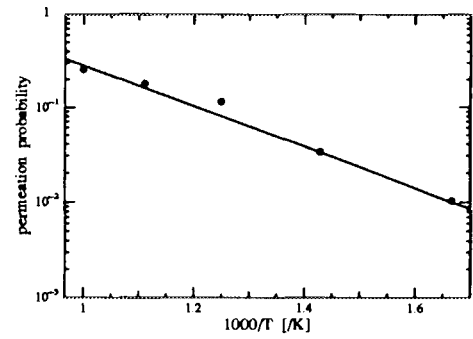


Fig.2 : Dependence of deuterium permeation probability on specimen temperature, T .

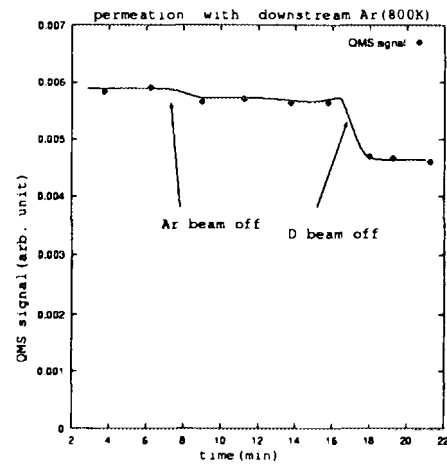


Fig.3 : Transient permeation behavior at the termination of Ar^+ irradiation.

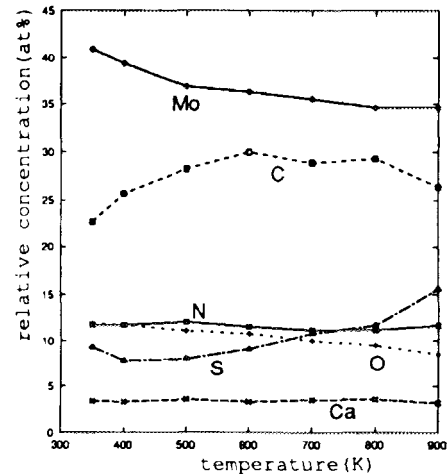


Fig.4 : Result of AES analyses at different temperatures.

References

- [1] Bandourko, V., Doctor Thesis, Faculty of Eng., Univ. of Tokyo (1995)
- [2] Doyle, B. L., J.Nucl.Mater., 111&112(1982)628-635

プラズマ／壁界面における水素や水蒸気の吸着・脱離に関する量子化学的検討
長崎晋也、津島悟、田中将隆、梅村康洋（システム量子工学専攻）

Quantum Chemical Estimation of Sorption/Desorption of H₂ and H₂O(gas)
at the Plasma-Wall Interface

S.Nagasaki, S.Tsushima, M.Tanaka, Y.Umemura (Quantum Engineering and Systems Science)

Abstract

By using MOPAC Code, we estimated the charge density of SiO₂-Al₂O₃-SiO₂ metal oxide. We could find that the such quantum chemical calculation is a fruitful tool for understanding the plasma-wall interactions from the microscopic point of view.

Introduction

In order to verify the realization of fusion reactor, it is important to elucidate the particle transport phenomena through the first wall or the blanket material. Many experimental and theoretical research works have been performed on the particle transport phenomena. It is indispensable to study the interactions between wall materials and transporting particles from the microscopic point of view for fully understanding the transport mechanism. For achieving this purpose, we take interest in the theoretical calculation based on quantum chemistry. In the present work, for the first step to make clear the microscopic interaction mechanism in the plasma-wall interface, we calculated the charge density of metal oxide and confirmed the applicability of quantum chemistry to elucidating the plasma-wall interactions.

Calculation Procedure

In the present work, we considered SiO₂-Al₂O₃-SiO₂ layer metal oxide, because the database of Si, Al, O and H are fully prepared and because the charge density of this type layer oxide has been experimentally estimated by many researchers and thus we can compare the calculated results with the experimental results. Figure 1 illustrates the ideal structure of cluster model of SiO₂-Al₂O₃-SiO₂ layer metal oxide. Si is located in the center of tetrahedra and Al of octahedra. In the present work, assuming that the lengths between Si and O and between Al and O are 11.64 Å and 1.77 Å, respectively, we developed the ideal structure of the cluster model. We set H atom in the end of the cluster. This seems that H atom is representative of the end of next cluster or is part of the OH functional group in the edge region. By using MO calculation program "MOPAC" (version 6.0; J.S.P.Stewart) with PM3 method, we calculated the charge density of the cluster in the following three cases.

- (1) charge density of ideal layer metal oxide (Fig.1),
- (2) charge density of layer metal oxide when Al atom replaces Si atom:
excessive one negative charge,
- (3) charge density of layer metal oxide when alkaline earth atom replaces Al atom: excessive one

negative charge.

Table 1 calculation results of charge density

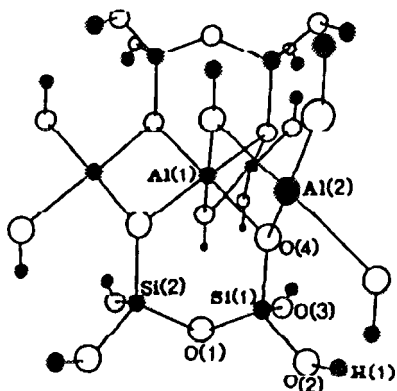


Figure 1 ideal model of layer metal oxide

Charge on atoms in each cluster model charge(electron density)				
	Original	Si(1)→Al	Al→Mg	without H(1)
Si(1)	1.29(2.71)	1.03(1.97)1)	1.87(2.13)	1.59(2.41)
Si(2)	1.28(2.72)	1.82(2.18)	1.89(2.14)	1.85(2.15)
Al(1)	0.91(2.09)	1.22(1.78)	2.00(0.00)2)	1.21(1.79)
Al(2)	0.71(2.29)	1.24(1.76)	1.28(1.72)	1.24(1.76)
O(1)	-0.61(6.61)	-0.85(6.85)	-0.93(6.93)	-0.91(6.91)
O(2)	-0.52(6.52)	-0.67(6.67)	-0.73(6.73)	-0.97(6.97)
O(3)	-0.51(6.51)	-0.66(6.66)	-0.74(6.74)	-0.71(6.71)
O(4)	-0.54(6.54)	-0.68(6.68)	-1.07(7.07)	-0.81(6.81)
H(1)	0.20(0.80)	0.20(0.80)	0.25(0.75)	-----

1)Value for Al. 2)Value for Mg.

Results and Discussion

Table 1 summarizes the calculation results. It was found that the charge profile is not changed by the replacement of central atom and the negative charge density induced in the surface is small in comparison with those experimentally expected. Furthermore, we could find that when Al atom replaces Si atom excessive negative charge can not be localized on the surrounding O atoms and expand onto the all atoms in the cluster, and that when alkaline earth atom replaces Al atom negative charge can not be distributed into the surface and be localized on O atoms surrounding Al atom. However, in fact, the negative charge is localized in the surface or on the O atom connecting too Si atom. This is considered to be because these O atoms are located on the surface and thus are negatively charged, and because the O atoms can readily become the donors of electrons. In the near future, we will estimate the structure and charge density of practical materials for the first wall and blanket material, elucidate the interactions of the material atoms with transporting particles (atoms) and understand the transport mechanism.

MPD アークジェットによる黒鉛の蒸発挙動

助川 敏男、班目 春樹、岡本 孝司 (原子力工学研究施設)

Evaporative Behavior of Carbon with MPD Arc Jet.

T. Sukegawa, H. Madarame and K. Okamoto

Abstract

Using the Magneto-Plasma-Dynamic Arc Jet (MPD Arc Jet) device, the plasma-material interaction during simulated plasma disruption was experimentally investigated. To clarify the effects of the evaporation, the isotropic graphite was used as a target. The thermal conductivity of the isotropic graphite was much higher than that of the pyrolytic graphite, resulting in smaller evaporation. The light intensity distribution during the simulated disruption for the isotropic graphite was quite different from that for the pyrolytic graphite.

Introduction

During plasma disruptions the plasma facing components will be subjected to intense heat loads for short periods of time. This phenomenon can be simulated using the MPD Arc Jet device as the heat source. In the previous studies[1], the qualitative ion distributions for the pyrolytic graphite target were evaluated. Last year, the MPD Arc Jet device had been modified to generate higher heat flux. The maximum heat flux on the specimen was about 3.6 MW/m^2 when the voltage was 400 V and the magnetic field was 0.98 T. In this study, to clarify the effects of the evaporation, the isotropic graphite (IG110) was used as a target. The thermal conductivity of the isotropic graphite was much higher than the pyrolytic graphite, resulting in smaller evaporation.

Result and Discussion

The CII line at 426.7 nm ($3d^2D-4f^2F^0$) and the CIII line at 465.2 nm ($3s^3S-3p^3P^0$) were selected for the measurements of C^+ and C^{++} ion distribution in the plasma. For the space resolved measurements, an $f = 250 \text{ mm}$ collector lens was used. The distance between the lens focal point and the specimen surface was varied to obtain the spatial distributions. For the time resolved measurements, 0.2 ~ 2 msec scan duration were used. The scan duration depended on the light intensity. In the higher intensity case, the scan duration should be shorter in order to avoid the saturation of the photo detector. Therefore, the intensity was normalized as the intensity per 1 msec.

Before the experiment, the surface of the target specimen was planed to be flat. Then the specimen was set in the MPD Arc Jet device. Figures 1 and 2 show the variation of the intensity for several serial experiments at $x = 2.5 \text{ mm}$. The distance between the measured position and specimen surface was defined as the distance x . As shown in Figs. 1 and 2, the intensity at the initial pulse (1st) was much smaller than that at the following pulses. Although the experimental conditions at 1st and 2nd pulse were the same, the results had large discrepancies. The difference was thought to be caused by the chemical effects on the surface, or the re-deposition of the evaporated graphite. However, the reason was not clarified yet.

With repeating the pulses, the intensity had a tendency to increase. This tendency was observed for every experiments with the isotropic graphite targets(IG110). While, the intensity for the pyrolytic graphite was almost constant during the serial experiments. Since the thermal conductivity of the isotropic graphite was much higher than that for the pyrolytic graphite, the amount of evaporated graphite was very few. Therefore, the surface condition might highly affect on the evaporation of the graphite. That is, when the thermal conductivity at the surface might be varied by the re-deposition or the chemical action, the evaporation rate also might be varied greatly. Then, with repeating the pulses, the evaporation rate might be varied.

In the 2nd and following pulses, there were twin peaks, 3 and 6 msec. The first peak was relatively sharp. Since the pulse duration time was about 5 msec, the second peak was observed after the heat input. The first peak was thought to be the interaction between the plasma and the evaporated graphite. However, the cause of the second peak was not clarified yet.

Figures 3 and 4 show the ion distribution of the 2nd pulse. The first peak was observed at the very small region near the surface. While the second peak was observed at all locations.

Reference

(1) H. Bolt, Y. Ooishi, M. Iida and T. Sukegawa, "Study of the Plasma-Material Interaction During Simulated Plasma Disruption", Fusion Engrg. Des. 18 (1991), pp.117-123

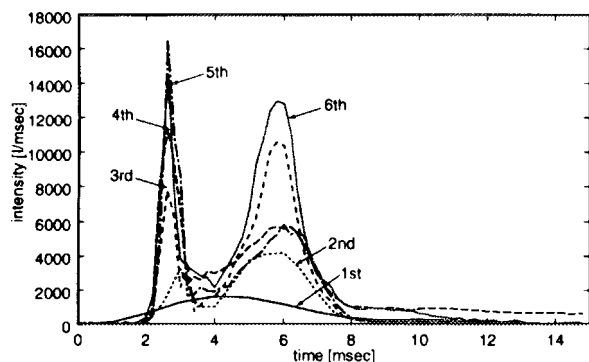


Fig.1 C⁺ ion density variation at $x = 2.5\text{mm}$

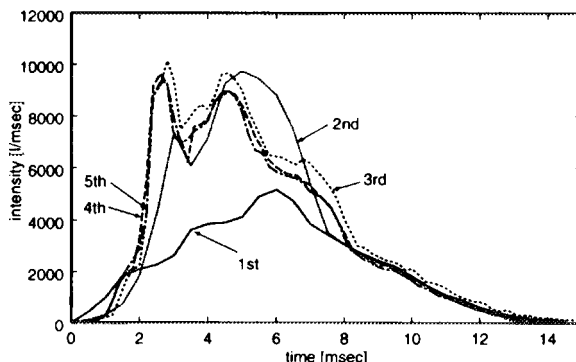


Fig.1 C⁺⁺ ion density variation at $x = 2.5\text{mm}$

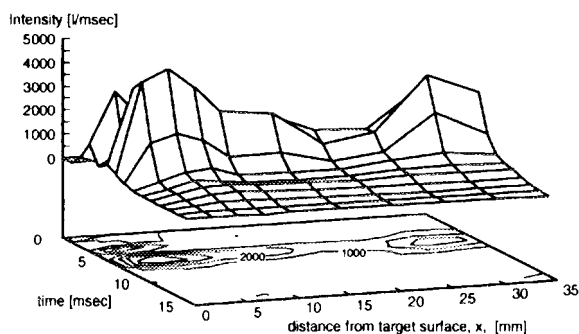


Fig.3 C⁺ ion density distribution (2nd)

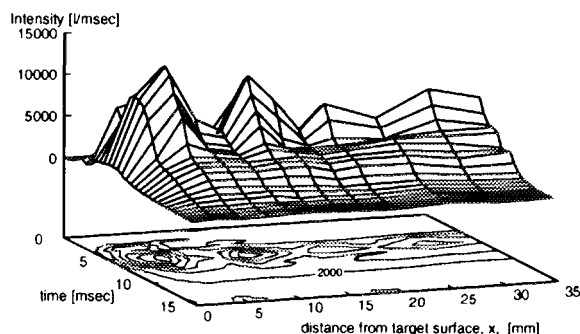


Fig.4 C⁺⁺ ion density distribution (2nd)

Application of High Tc Superconductor to Passive Control of Plasma Position

T.Uchimoto, N.Ikatsu, Y.Yoshida and K.Miya

*Nuclear Engineering Research Laboratory, The University of Tokyo
Tokai, Ibaraki 319-11, Japan*

Abstract. This paper presents a new method of plasma position control with use of high Tc superconductors (HTSC). The shielding current analysis of HTSC and MHD equilibrium analysis of tokamak plasma are coupled in order to evaluate the effect of HTSC on plasma motion and to verify the feasibility of the present method.

1 Introduction

Vertical elongations of plasma cross sections in tokamak fusion reactors are of great advantage to achieve high β values, which will lead to compact reactors. Such elongations, however, make the plasma subject to an axisymmetric MHD positional instability in the vertical direction[?]. The plasma can be stabilized to some extent by the active feedback control with Poloidal Field (PF) coils and by the eddy current induced in structures surrounding the plasma. But the above methods have their own defects, that is, the former requires greater capacity of the power source of the PF coils and the stabilizing effect of the latter decays on the order of the L/R time of the structures. Therefore, the elongation of a plasma section is restricted to a modest value in the design of recent tokamak reactors.

This paper proposes a new method to control a plasma position with use of HTSC. It is well known that the electromagnetic force due to HTSC is dynamically stable. In addition, the plasma control by HTSCs is expected to be free from the defects which the conventional controls have. Therefore, the plasma can be more stable if HTSCs are arranged around it.

The shielding current analysis of HTSCs and the MHD equilibrium analysis of tokamak plasma are coupled in order to evaluate the effect of HTSC on plasma motion. Feasibility of the proposed method is discussed in comparison with the passive control due to the eddy current induced in surrounding structures.

2 Formulations

2.1 Plasma Equilibrium Analysis

The plasma, a vacuum vessel and PF coils are simulated as ring currents using a given number N of toroidal coils, with variable sizes, positions and currents. The plasma inertia is assumed to be negligible, then the plasma equilibrium is obtained by minimizing

the free energy of the toroidal ring system. The free energy is expressed as;

$$E = U_m + U_t = \frac{1}{2} \sum_{\Phi_i = \text{const}} \Phi_i I_i + \sum_{I_j = \text{const}} \Phi_j I_j - \int_V p dV, \quad (1)$$

where U_m and U_t are the magnetic energies of the the current constant system (PF coils) and the flux constant system (plasma and vacuum vessel), respectively, Φ the magnetic flux, I the current and p the plasma pressure. The flux change of plasma and vacuum vessel is calculated as;

$$\Phi_k(t) = \Phi_k(0) - \int_0^t R_k(t') I_k(t') dt', \quad (2)$$

where R_k and I_k is the electric resistance and the current of the k -th ring, respectively.

2.2 Shielding Current Analysis of HTSC

Shielding current of HTSC is evaluated based on the critical state model by applying the magnetic vector potential method[?]. The governing equations in axisymmetric problems can be expressed as follows;

$$\frac{1}{\mu_0} (\nabla^2 - \frac{1}{r^2}) A_{sc} = -J \quad (3)$$

$$E = -(\frac{\partial A_{sc}}{\partial t} + \frac{\partial A_{ex}}{\partial t}), \quad (4)$$

where J is the superconducting current density, E the electric field, A_{sc} the magnetic vector potential due to the superconductor and A_{ex} the externally applied magnetic vector potential. In the superconductor region, the constitutive relation between J and E can be expressed as follows based on the critical state model[?]:

$$\mathbf{J} = J_c \frac{\mathbf{E}}{|\mathbf{E}|} \quad \text{if } \mathbf{E} \neq 0, \quad \frac{\partial \mathbf{J}}{\partial t} = 0 \quad \text{if } \mathbf{E} = 0, \quad (5)$$

where J_c is the critical current density. As the dependence of J_c on the magnetic flux density, $|\mathbf{B}|$, Yasukochi model[?], $J_c(|\mathbf{B}|) = J_{co} \sqrt{|\mathbf{B}|}$, is adopted.

3 Numerical Results

The stabilizing effect by HTSCs is examined in the configuration of the conceptual design of the International Thermonuclear Experimental Reactor (ITER/CDA). Its cross section and the arrangement of HTSCs are shown in Fig. 1. The plasma cross section is elongated and then it is magnetohydrodynamically unstable.

The stability condition in a shell-free plasma of major radius R_p is given by[?];

$$n = -\frac{R_p}{B_z^{ex}} \frac{\partial B_z^{ex}}{\partial R_p} > 0, \quad (6)$$

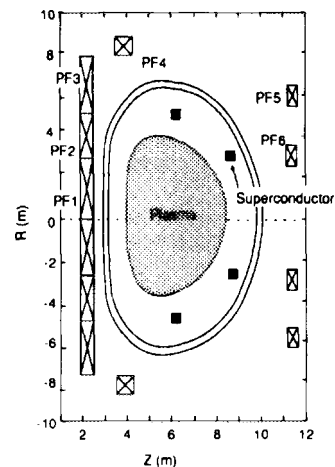


Fig. 1. Poloidal section of ITER/CDA

where B_z^{ex} is the vertical component of the externally applied magnetic field and n is called the decay index. The decay index of the conceptual design of ITER is -1.0 .

HTSCs are assumed to be silver-sheathed Bi-based high Tc superconducting cable and arranged in the form of axisymmetric toroidal coils. The cross section of each HTSC coil is 0.4 m in width and 0.4 m in height. Four HTSC coils are arranged as shown in Fig. 1. The critical current density at 1 T, J_{co} , is chosen to be the realistic value of $1.0 \times 10^8 \text{ A/m}^2$ in the calculation.

3.1 Stabilizing Effect of Vacuum Vessel

The MHD theory for a shell-free tokamak predicts that the growth rate of the vertical instability is of the order of micro-second. However, due to the presence of a conducting shell, it is reduced to the order of the L/R time of the shell[?]. Fig. 2 shows the time evolution of the plasma vertical position, where the stabilizing effect of a vacuum vessel is taken into account. The growth rate of the plasma vertical displacement is about 8 ms. it roughly agrees with The L/R time of the vacuum vessel.

Fig. 3 shows the change of plasma magnetic surface in the vertical motion. The plasma touches the wall in 120 ms, which shows the limit of the stabilization by the vacuum vessel.

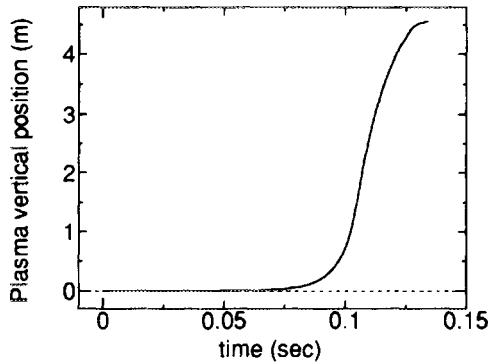


Fig. 2. Time evolution of plasma vertical position, where the stabilizing effect of a vacuum vessel is taken into account

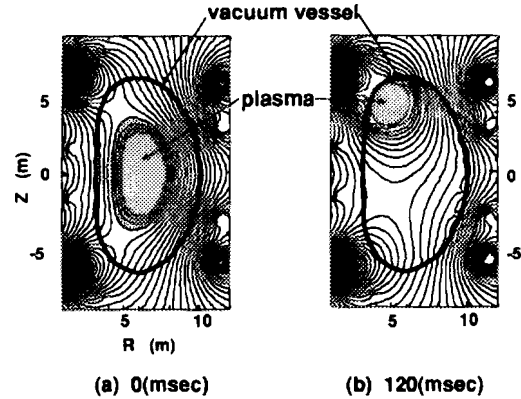


Fig. 3. Change of plasma magnetic surface in the vertical motion

3.2 Stabilizing Effect of HTSC

In the following, only the stabilizing effect of the HTSCs is taken into consideration. Fig. 4 shows the change of the magnetic energy as a function of the vertical displacement of the plasma. The decay index, n , is -1.0 in this case. In the absence of HTSCs, there is no stable region. On the contrary, if the HTSCs are introduced, the stable region exists in the neighborhood of the equilibrium point. Fig. 5 shows the relation between the decay index and the depth of magnetic energy well in the stable region. The depth of energy well decreases when the decay index is reduced, that is, the degree of the instability increases. When the decay index is reduced to be -1.6 , the well depth becomes almost zero. The HTSCs could stabilize the plasma whose decay index is up to -1.6 . Therefore, it is concluded that higher elongated plasma can be stable if the HTSC is arranged around the plasma.

The time evolutions of the plasma vertical position are calculated in the case of $n = -1.0$. In the absence of disturbance field, the plasma position is fixed near the initial equilibrium point as shown in Fig. 6, whereas the plasma with a shell moves in

the time scale of 8 ms (see Fig. 2). This shows the feasibility of position control of plasma by HTSCs. The various magnitude of disturbance field, B_d , is exerted in 1 s by changing the current of PF 4. When 10 or 50 G of B_d is exerted, the plasma remains staying near the initial equilibrium point. However, the plasma position jumps upward and moves toward the vessel wall gradually after 100 G of B_d is exerted. It can be said that the stabilization by HTSCs could withstand a disturbance to significant degree.

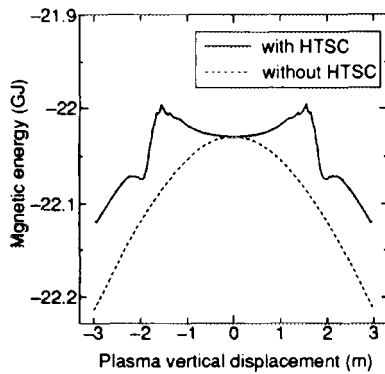


Fig. 4. Change of magnetic energy as a function of vertical displacement of plasma

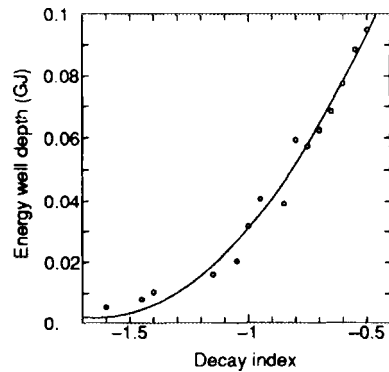


Fig. 5. Relation between decay index and depth of energy well

4 Conclusion

The new method of plasma position control with use of the HTSCs is proposed. The time evolution of the tokamak plasma equilibrium with the HTSCs is computed with the consideration of the coupling between the plasma equilibrium analysis and the HTSC shielding current analysis. The result of the calculation verifies the possibility of the proposed method.

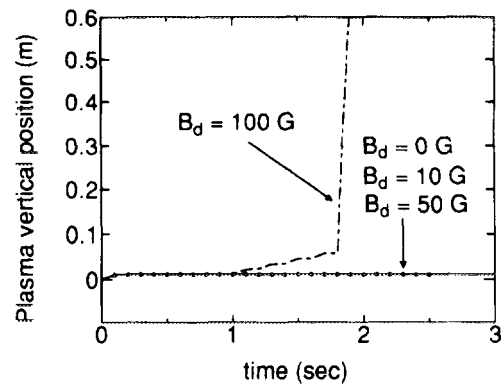


Fig. 6. Time evolution of plasma position, where the stabilizing effect of HTSCs is taken into account

5 Acknowledgement

This work was partly supported by a grant-in-aid for scientific research from the Japanese Ministry of Education, Science, Sports and Culture.

References

- [1] S.Yoshikawa, Phys. Fluids **7** (1964) 278.
- [2] N.Takeda et al., Cryogenics **34** (1994) 745.
- [3] T. Sugiura et al., Int. J. Appl. Electromagn. in Mater. **2**(1991)183.
- [4] K. Yasukochi, et al., J. Phys, Soc. Jpn. **19** (1964) 1649.
- [5] A. Fukuyama, et al., Jpn. J. Appl. Phys. **14** (1975) 871.

ベクトルポテンシャル積分方程式に基づく渦電流探傷順問題の数値計算

吉田義勝、宮健三（原子力工学研究施設）

Computation of eddy current - crack interaction based on
vector potential integral formulation

Y. Yoshida and K. Miya

Abstract This paper describes a new solution of a forward problem in eddy current testing, which is based on the vector potential integral formulation. By introducing a vector potential dyadic Green's function, a conventional electric field integral equation can be transformed to a vector potential integral equation, where the kernel has weak singularity of $1/R$ while the kernel in the electric field equation is hyper-singular. The validation of the proposed theory has been done by comparing the numerically predicted results with measured ones.

1. INTRODUCTION

Among the numerical methods for the forward problem in the eddy current testing (ECT), the volume integral approach using the electric dyadic Green's function is considered as an attractive and useful way because of its less requirement of computational resources. For this reason, the electric field integral equation (EFIE) were used by many researchers so far (e.g. see [1]).

In this paper, an alternative formulation using a vector potential dyadic Green's function is proposed. This vector potential formulation has an advantage that the Green's kernel has weak singularity of $1/R$ while the kernel in the EFIE is hypersingular.

The vector potential formulation is applied to the computation of the ECT probe responses due to an ideal crack in conducting half-space. Except for the crack region, the host conductor is assumed to be homogeneous and its conductivity is denoted as σ_0 . The crack surface is assumed to be perpendicular to the air-conductor interface. This is a good approximation of real cracks in most cases.

2. THEORY

According to the conventional electric field integral formulation, the scattered electric field due to defects in the host conductor is written

$$\mathbf{E}^s(\mathbf{r}) = i\omega\mu_0 \int_V \mathcal{G}_E(\mathbf{r}, \mathbf{r}') \cdot \mathbf{P}(\mathbf{r}') d^3\mathbf{r}'. \quad (1)$$

By introducing a vector potential dyadic Green's function \mathcal{G}_A defined by

$$\mathcal{G}_E(\mathbf{r}, \mathbf{r}') = \frac{1}{k^2} \nabla \times \nabla \times \mathcal{G}_A(\mathbf{r}, \mathbf{r}'), \quad (2)$$

(1) can be rewritten as

$$\mathbf{E}^s(\mathbf{r}) = \frac{1}{\sigma_0} \nabla \times \nabla \times \int_V \mathcal{G}_A(\mathbf{r}, \mathbf{r}') \cdot \mathbf{P}(\mathbf{r}') d^3\mathbf{r}'. \quad (3)$$

(3) leads to the following integral representation of the total field:

$$\mathbf{E}(\mathbf{r}) = \mathbf{E}^i(\mathbf{r}) + \frac{1}{\sigma_0} \nabla \times \nabla \times \int_V \mathcal{G}_A(\mathbf{r}, \mathbf{r}') \cdot \mathbf{P}(\mathbf{r}') d^3 \mathbf{r}'. \quad (4)$$

In the limit as the field point approaching to the crack face, we have

$$\left\{ \nabla_t^2 \mathbf{n} - \frac{\partial}{\partial n} \nabla_t \right\} \cdot \int_V \mathcal{G}_A(\mathbf{r}^\pm, \mathbf{r}') \cdot \mathbf{P}(\mathbf{r}') d^3 \mathbf{r}' = J_n^i(\mathbf{r}^\pm), \quad (5)$$

where $J_n^i = \sigma_0 \mathbf{E}^i \cdot \mathbf{n}$. Operating the inverse of ∇_t^2 and applying the ideal crack model [1] yield

$$\mu_0 \int_S G(\mathbf{r}^\pm, \mathbf{r}') p(\mathbf{r}') d^2 \mathbf{r}' + \psi(\mathbf{r}^\pm) = -A^{(i)}(\mathbf{r}^\pm), \quad (6)$$

where $A^{(i)} = -\mu_0 \nabla_t^{-2} J_n^i$, and $\nabla_t^2 \psi = 0$. The Green's function is given by

$$G(\mathbf{r}, \mathbf{r}') = \left\{ \mathbf{n} - \nabla_t^{-2} \frac{\partial}{\partial n} \nabla_t \right\} \cdot \mathcal{G}_A(\mathbf{r}, \mathbf{r}') \cdot \mathbf{n}. \quad (7)$$

The above integral equation is discretized by the method of moments utilizing the boundary conditions: $p = 0$ at buried edge, and $\mathbf{n}' \cdot \nabla_t p = 0$ at conductor surface, \mathbf{n}' being the unit vector normal to the conductor surface.

3. RESULTS

Numerically predicted probe responses are compared with measurement performed by Burke [2]. Figs. 1 and 2 show the impedance change due to a rectangular surface breaking crack in half-space conductor as a function of eddy current probe location. A very good agreement assures the validity of the proposed theory.

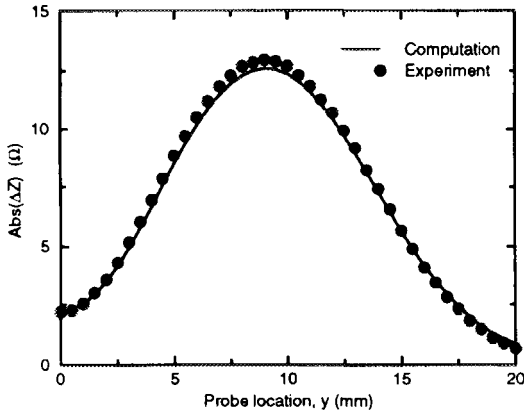


Fig. 1 Absolute value of impedance change

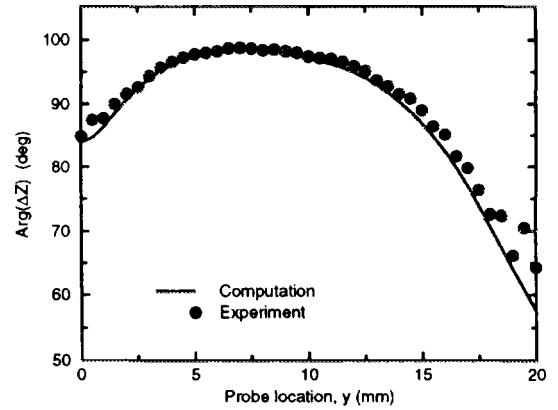


Fig. 2 Phase of impedance change

References

- [1] J.R.Bowler: J. Appl. Phys. 75 (1994) 8128-8137.
- [2] S.K.Burke: J. Nondestruct. Eval., 7 (1988) 35-41.

A modeling of radiation induced microstructural evolution under applied stress in austenitic alloys

Hiroyasu Tanigawa, Akira Kohyama, Yutai Katoh[†] and Yutaka Kohno^{††}

Institute of Advanced Energy, Kyoto University, Gokasho, Uji, Kyoto 611, Japan

† National Institute for Fusion Science, Nagoya, Aichi 464-01, Japan

†† Department of Materials Science, University of Tokyo, Hongo, Bunkyo, Tokyo 113, Japan

Abstract

Effects of applied stress on interstitial type Frank loop evolution at early stages of irradiation were investigated by both numerical calculation and irradiation experiments. In the experimental part of this work, microstructural inspection has been made by transmission electron microscopy with a special emphasis on Frank loops and perfect loops on every $\{111\}$ plane. The results of the TEM observation revealed that Frank loop concentration on a $\{111\}$ plane increased as the resolved normal stress to a $\{111\}$ plane increased and that small perfect loops were more likely produced on $\{111\}$ planes where larger resolved shear stress was applied. The model of a stress effect on Frank loop unfaulting was provided, which is triggered by nucleation of a Shockley partial dislocation loop in a Frank loop, was proposed. The results of the numerical calculation was successful to predict the strong dependence of Frank loop concentration on the resolved normal stress to $\{111\}$ plane, which was the characteristic feature seen in the irradiation experiments.

1. Introduction

There have been many attempts to model irradiation creep but the basic processes underlying those models have not been understood or proved sufficiently. The most experimental results used to make those models were obtained under insufficient conditions in controlling applied stresses and many irradiation parameters.

In our previous work [1], the EAST(External applied stress in tension) apparatus was developed to improve accuracy of ion irradiation experiments with external stresses. The ion irradiation experiments under applied stress by the EAST apparatus revealed the clear effect of applied stress on Frank loop evolution in Fe-Cr-Ni ternary alloy. It was found that Frank loop nucleation on $\{111\}$ planes became larger with increasing magnitude of resolved normal stress to the corresponding $\{111\}$ plane. A numerical calculation, based on the mechanistic model, was also carried out by integrating rate equations which describe the behavior of point defects, defect clusters, Frank loops and network dislocations. The SIPN (Stress Induced Preferential Nucleation) model was discussed to understand the applied stress effect on Frank loop nucleation. The formation probability of a tri-interstitials on a specific $\{111\}$ plane denoted by the suffix k [2] is given as:

$$P_k^{nuc} = \frac{\exp(3\Omega\sigma_k^n/k_B T)}{\sum_j \exp(3\Omega\sigma_j^n/k_B T)}$$

, where Ω is atomic volume, σ_k^n is the magnitude of resolved normal stress to $\{111\}$ plane, k_B is Boltzmann constant, and T is absolute temperature.

In fig.1 both results from the numerical calculation and from the experiments were plotted, where the external stress conditions was 35 MPa in the direction of $[\bar{1}11]$. The stress effect index on Frank loop number density, in the figure, is defined as :

$$\left(\begin{array}{l} \text{Stress effect index} \\ \text{on Frank loop number density} \end{array} \right) = \frac{N_k^{f1}(\sigma_{app} = X \text{ MPa})}{N_{(111)}^{f1}(\sigma_{app} = 0 \text{ MPa})}$$

, where $N_k^{fl}(\sigma_{app}=X \text{ MPa})$ is Frank loop number density on a particular $\{111\}$ plane denoted by k under the external applied stress of X MPa.

The predicted value of stress effect index on Frank loop number density by the numerical calculation showed positive dependence to resolved normal stress, but the quantitative difference between the computational result and the ion irradiation experimental result was quite large. This result might require the further improvement of the model to predict the effects of applied stress on Frank loop evolution.

In this work, re-analysis of previous work is carried out to improve the model emphasizing the Frank loop unfauling process. In the latter part of this paper, first we will show the results of TEM observation analyzing perfect loops, and then will propose a stress effect model on Frank loop unfauling. And the calculation results and discussion will be presented in the last part of this paper.

2. Experimentals

2.1 Experimental procedure [1]

The material used in this study was Fe-15Cr-20Ni ternary alloy. The 4 MeV nickel ion irradiation was carried out at the HIT facility (High-fluence Irradiation Test facility), the University of Tokyo, and external stress was applied by the EAST apparatus.

The displacement damage, the nominal damage rate and the irradiation temperature applied were 1 dpa, 2×10^{-3} dpa/s and 673 K, respectively. The applied stress condition was 35 MPa. The microstructure of the irradiated specimens was examined with a JEM-200CX transmission electron microscope (TEM). The range for TEM inspection was determined to be 500 to 600 nm in depth from the irradiated surface, where both displacement damage gradient and deposited nickel concentration are fairly small.

2.2 Results of the TEM observation on perfect loops

The TEM observation with the special emphasis on perfect loops was performed to the TEM specimens used in the previous work [1]. Series of TEM dark field images were taken in order to clearly present Frank loops and unfauled perfect loops, separately (fig.2). From these images, the perfect loop size distributions on each $\{111\}$ plane were obtained (fig.3). For the case of $\sigma_{||} = 12 \text{ MPa}$, many small perfect loops on the $\{111\}$ planes were observed, where resolved shear stress were being applied. Whereas, for the case of $\sigma_{||} = 36 \text{ MPa}$, the population of the small loops was quite small, where no resolved shear stress was being applied, compared with the former case. This result suggested a mechanism that resolved shear stress assisted Frank loop unfauling. This mechanism has been recognized to be an important process to understand the microstructural evolution in irradiation creep. This will be discussed in the following section.

3. Computational study

3.1 A modeling of stress effect on Frank loop unfauling

Figure 4 provides the two representative mechanisms of Frank loop unfauling; (a) unfauling process triggered by the nucleation of a Shockley partial dislocation loop (Shockley loop) inside a Frank loop, and (b) unfauling process triggered by the reaction with gliding (or climbing) network dislocation [3,4]. C.H. Henager Jr.[5] proposed the model of internal stress assisted Frank loop unfauling to calculate the creep strain. He calculated an activation barrier for the unfauling process of a Frank loop by the nucleation of a Shockley loop, depending on stacking fault energy and shear stress applied in the direction of the Burgers vector of Shockley loop. This model is based on the model of the activation energy for the unfauling of vacancy-type loops in quenched metals, proposed by Saada [6].

In the following model, the Frank loop unfauling by the nucleation and growth of a Shockley loop was included as one of the important mechanism to understand the stress effect. Hereafter, this model is called as "SIPU (Stress Induced Preferential Unfauling) model". The Frank loop unfauling by the reaction with network dislocations ((b) in fig.4) was recognized to be another important process in microstructural evolution under irradiation with applied stress. But, at present, the model does not care for the mechanism including the stress effect.

3.2 SIPU model description

The process of Frank loop unfauling by the nucleation and growth of a Shockley partial loop can be represented by following Burgers vector reaction:

$$\frac{a}{3}\langle 111 \rangle + \frac{a}{6}\langle 11\bar{2} \rangle = \frac{a}{2}\langle 110 \rangle$$

We can estimate the total energy of a Frank loop with a Shockley loop inside, by considering those line tension and the stacking fault energy [5]. The energy of the Frank loop system with resolved shear stress τ , to $\{111\}$ plane in the direction of $\langle 112 \rangle$ is given approximately by:

$$W(r) = W_0 \left[\frac{2r}{b_0} \ln\left(\frac{r}{b_0}\right) - \frac{r^2 \gamma}{b_0^2 \gamma_c} + \frac{\gamma}{\gamma_c} - \frac{r^2 \tau_s b_s}{b_0^2 \gamma} \right] \quad [A]$$

with:

$$W_0 = \pi b_0^2 \gamma_c$$

and:

$$\gamma_c = \frac{Gb_s^2}{4\pi b_0}$$

, where r is Shockley loop radius, b_s is the Burgers vector of Shockley partial dislocation, $\bar{b}_s = a/6 \langle 112 \rangle$. G is Young modulus, γ is stacking fault energy and b_0 is the core radius of Shockley loop, $b_0 \cong 2b_s$. The shear stress effect term is negative because it acts to allow the shear stresses to do work and lowers the energy of the system.

The maximum value of $W(r)$ on a $\{111\}$ plane denoted by k : W_k^{\max} , is acquired at the critical Shockley loop radius: r_c . This value defines the activation energy of Shockley loop nucleation, i.e. the activation energy of Frank loop unfaulting. Here, the assumptions are (1) the formation energy of Shockley loop nucleus is negligible and (2) the nucleated Shockley loop grows monotonically. and the probability of Frank loop unfaulting yields to:

$$P_k^{unf} = \exp\left(-\frac{\Delta W_k}{k_B T}\right) \quad [B]$$

with:

$$\Delta W_k = W_k^{\max} - W_k^0$$

, where W_k^0 is $W(b_0)$ on a $\{111\}$ plane denoted by k .

These unfaulting probabilities are included to the Frank loop growth term in the rate equation model of microstructural evolution under applied stress.

The rate equation model for the microstructural evolution under irradiation has been developed by Stoller and Odette [7] and by the present authors [8,9]. As the one extension of the model, it has been improved to be able to predict microstructural evolution under applied stress [1]. In the model, Frank loop growth rate equations were given for each $\{111\}$ plane separately, considering the stress effects on the Frank loop nucleation and growth. In this study, the stress effect on the Frank loop unfaulting has been taken into account.

The evolution of the Frank loops on each $\{111\}$ plane denoted by the suffix k is given by the following equation :

$$\begin{aligned} \frac{dN_k(i)}{dt} = & -R_k(i)N_k(i)(1 - P_k^{unf}) - N_k(i)P_k^{unf} \\ & + R_k(i-1)N_k(i-1) \times (1 - P_k^{unf}) \times (1 - P_{ND}^{unf}) \quad (\text{If } R_k(i-1) > 0) \\ & - R_k(i+1)N_k(i+1) \times (1 - P_k^{unf}) \quad (\text{If } R_k(i+1) < 0) \end{aligned}$$

, where $N_k(i)$ is the number of Frank loops in a given size class with radius r_i , and $R_k(i)$ is the transfer rate between size classes given by:

$$\frac{1}{R_k(i)} = \int_{r_i}^{r_{i+1}} \left\{ \frac{dr_k(i)}{dt} \right\}^{-1} dr_i$$

and:

$$\frac{dr_k(i)}{dt} = \frac{2\pi}{b^1 \ln(r_0/r_c)} \left[z_i^1(i)D_i C_i - z_v^1(i)D_v C_v \right]$$

where b^1 is Burgers vector of Frank loop, r_0 is the mean dislocation spacing, $(\pi\rho_n)^{-1/2}$, r_c is the core radius of Frank loop. $2b^1$, $z_x^1(i)$ is Frank loop/interstitial ($x=i$) or vacancy ($x=v$) bias in a given size class [10], D_x is the diffusivity of point defect x , and C_x is the concentration of point defect x . P_{ND}^{unf} is the possibility that Frank loop unfaults upon contacting network dislocation while it is growing[7]. Unfaulted loops are counted as the part of network dislocations.

Rate equations for the concentrations of self-interstitial atoms and interstitial clusters in this model were noted in previous work, considering the stress effect on clustering coefficients [1].

These rate equations are integrated using LSODE (Livermore Solver for Ordinary Differential Equations) [11].

4. Result and Discussion

The parameters used in this study are listed in table 1. The resolved shear stress conditions yield to the magnitude shown in fig.5, under the external applied stress conditions of 35 MPa in the direction of $[\bar{1}11]$. From fig.5, it is understood that the maximum resolved shear stress in the direction of $\langle 112 \rangle$ are 34 MPa on (111) , $(1\bar{1}1)$ and $(11\bar{1})$ planes, and 0 MPa on $(\bar{1}11)$ plane. In both resolved shear stress condition, the total energy of Frank loop system, which was calculated by equation [A], increases until Shockley loop radius reaches the critical radius (about 0.7nm), and then decreases monotonically (fig.6). The difference of the activation energy for Frank loop unfauling is 0.04 eV, but by equation [B], the unfauling possibility for $\{111\}$ planes except $(\bar{1}11)$:0.011 is double to the value for $(\bar{1}11)$ plane:0.006.

The results of the numerical calculation showed almost the same dependence of Frank loop concentration on the resolved normal stress to $\{111\}$ planes, which was seen in the irradiation experiments (fig. 7). This result means that the SIPU model successfully describes the resolved normal stress dependence of stress effect index on Frank loop number density.

But the calculation result suggests that the number density of Frank loop do not increase compared to the unstressed condition; on the other hand, the experimental result is increased. This conflict might indicate that there should be more significant applied stress effects on point defect clustering process than the current model, e.g. stress effect on clustering coefficient, or stress effect of cascade production rate.

5. Summary

- (1) The model of the applied stress effect on Frank loop nucleation (SIPN model) could not predict the positive dependence of the Frank loop concentration on the resolved normal stress to $\{111\}$ planes
- (2) The TEM observation revealed that small perfect loops were more likely produced on $\{111\}$ planes when larger resolved shear stress was applied.
- (3) The model of the applied stress effect on Frank loop unfauling (SIPU model), which was triggered by nucleation and growth of a Shockley partial dislocation loop, was provided.
- (4) The numerical calculation was successful to predict the strong dependence of Frank loop concentration on the resolved normal stress to $\{111\}$ plane.
- (5) The SIPU model could not predict the increase of Frank loop concentration, and possibilities of the stress effect were suggested.

REFERENCES

- [1] H.Tanigawa and A.Kohyama, Proceeding of the 3rd Sino-Japanese Symp. on Materials for Advanced Energy Systems and Fission and Fusion Engineering, Oct. 1995, Chengdu, China
- [2] R.V. Hesketh, Phil. Mag. 7 (1962) 1417
- [3] J.L. Strudel and J. Washburn, Phil. Mag. 9 (1964) 491
- [4] A.J.E. Foreman and J.V. Sharp, Phil. Mag. 19 (1968) 931
- [5] C.H.Henager, Jr., "Low dose irradiation creep of pure nickel", Ph.D. dissertation, Univ. of Washington (1983)
- [6] G.V. Saada, J. Phys. Soc. Japan 18, Suppl. III (1963) 41
- [7] R.E. Stoller and G.R. Odette, ASTM STP-955 (1987) 371
- [8] Y. Katoh, R.E. Stoller, Y. Kohno and A. Kohyama, J. Nucl. Mater. 210 (1994) 290
- [9] Y. Katoh, R.E. Stoller and A. Kohyama, J. Nucl. Mater. 212-215 (1994) 179
- [10] W.G. Wolfer and M. Ashkin, J. Appl. Phys. 46 (1975) 548
- [11] A.C. Hindmarsh, LSODE: Livermore Solver for Ordinary Differential Equations, Lawrence Livermore National Laboratory (1980)

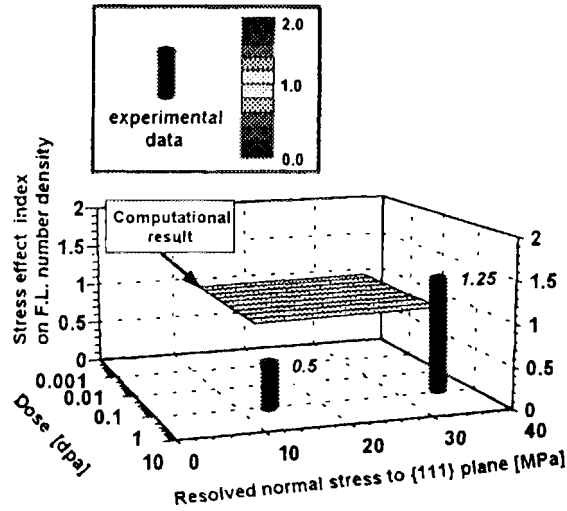


Fig.1 The calculated and the experimental results of the resolved normal stress dependence of stress effect index on Frank loop number density to every {111} plane.

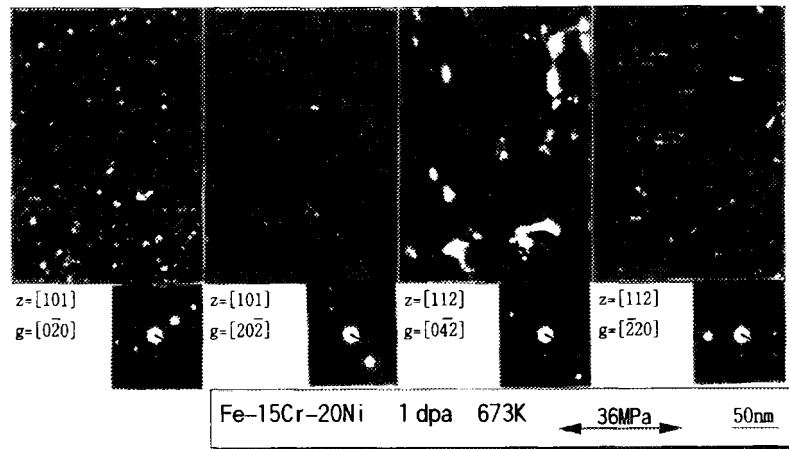


Fig.2 Series of TEM dark field images for perfect loop analysis. The applied stress condition is 36 MPa on the direction of $[\bar{1}11]$

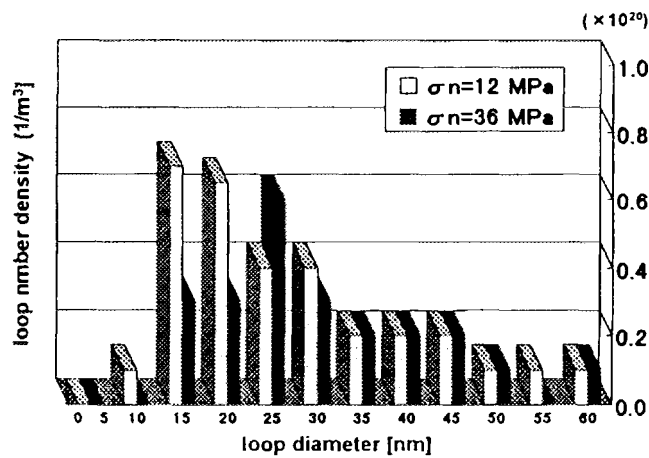


Fig.3 Perfect loop size distribution on each {111} plane. σ_n means resolved normal stress being applied to a {111} plane.

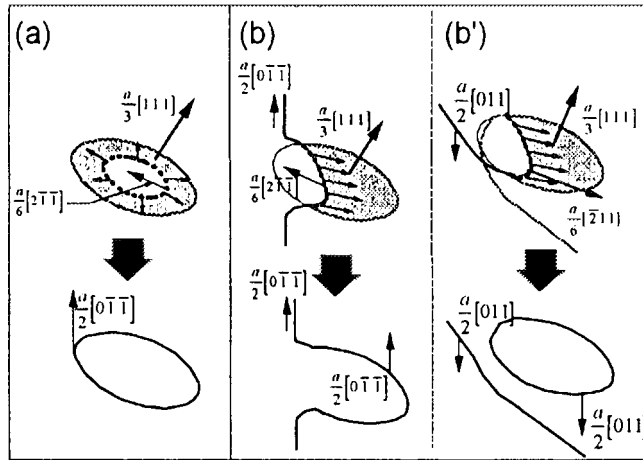


Fig.4 Schematic drawings of Frank loop unfaulting processes triggered by (a) the nucleation of a Shockley partial loop and (b),(b') the reaction with a network dislocation.

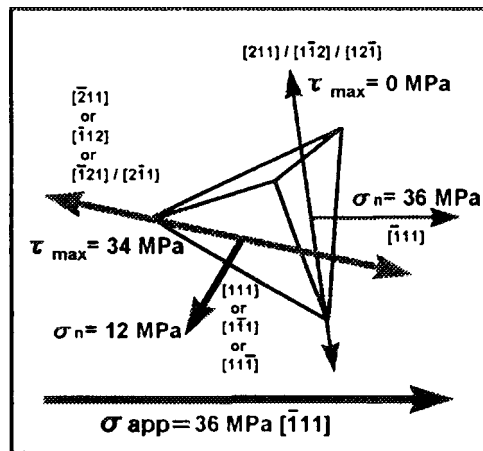


Fig.5 Schematic drawing of resolved stresses to {111} planes. The surfaces of tetrahedron indicate {111} planes.

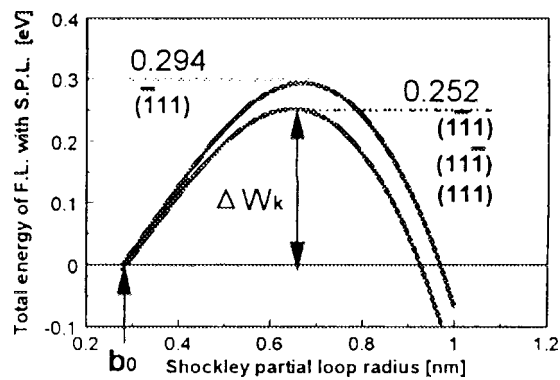


Fig.6 Total energy of Frank loop system on each {111} planes versus Shockley partial loop radius.

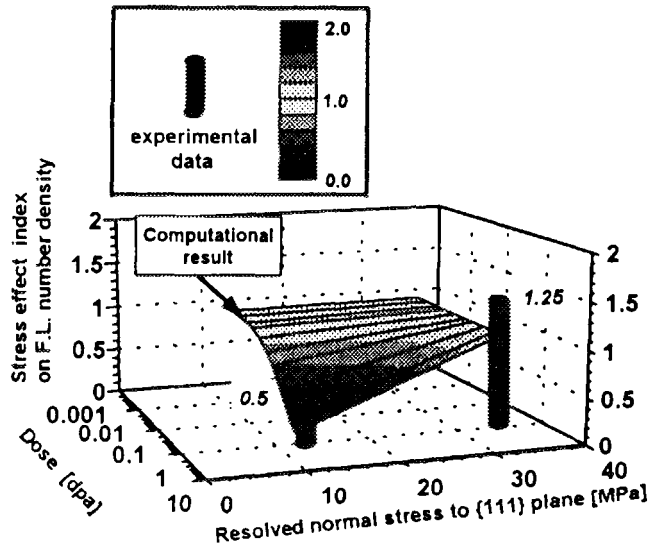


Fig.7 The calculated result of the resolved normal stress dependence of stress effect index on Frank loop number density on every {111} plane. The column suggest the experimental result for comparison.

Table 1 The calculation parameters

Lattice parameter	a_0	3.58×10^{-10} m
Vacancy migration energy	E_v^m	1.4 eV
Vacancy formation energy	E_v^f	1.5 eV
Interstitial migration energy	E_i^m	0.85 eV
Interstitial formation energy	E_i^f	5.0 eV
Vacancy vibration frequency	V_v	$5.0 \times 10^{22} \text{s}^{-1}$
Interstitial vibration frequency	V_i	$5.0 \times 10^{23} \text{s}^{-1}$
Initial dislocation network density	ρ_n	$1 \times 10^{12} \text{m}^{-2}$
Stacking fault energy	γ	0.31 J/m ²
Young modulus	G	64.9 GJ/m ³

ホログラムからの粒子、密度情報の同時抽出

岡本 孝司、池田 耕、班目 春樹 (原子力工学研究施設)

Extraction of density distributions and particle locations from hologram images

K. Okamoto, K. Ikeda and H. Madarame

Abstract

In this study, the simultaneous measurement technique for three-dimensional density and three-dimensional velocity distributions was evaluated. The Holographic Particle Image Velocimetry (HPIV) was the technique to record the three-dimensional position of the tracer particle on the hologram. When there were density distributions in the interrogation region, the plane optical wave may be modulated because of the difference of the refraction indices. Then, both of the plane wave modulated by density and the spherical wave by particle scatter were interfered with the reference beam, being recorded on the hologram. With reconstructing the hologram, the both of the modulated plane wave and spherical wave were reconstructed. Since the plane wave and spherical wave had low and high frequency, respectively, the two information could be separated using low-pass and high-pass filter. In the experiment, a jet of carbon-dioxide into air with mist were measured. Both mist particle position and the fringe shift caused by the density distribution were well observed, showing the effectiveness of the proposed technique.

Introduction

When a Loss of Vacuum event (LOVA) would occur in the fusion reactor, air may flow into the vacuum vessel, resulting in the buoyancy driven exchange flow between heated light air and heavy air. The study on the buoyancy driven flow is very important for the accidental analysis of the Fusion Reactor. However it is very difficult to measure the transient three-dimensional field. The three-dimensional velocity distributions are measured by the Holographic Particle Image Velocimetry (HPIV). (Barnhart et al., 1994, Applied Optics, 33) The three-dimensional density distributions are measured by the holographic interferometer with computer tomography technique. (Mezkirch, 1974, Flow Visualization, Academic Press). Since both technique uses the holographic technique, the three-dimensional velocity and density distribution might be measured simultaneously. Yano (1983, Flow Visualization III) proposed a simultaneous measurement technique for two-dimensional density and velocity distributions, using triple exposure hologram. However, there are very few studies on the simultaneous measurement of the three-dimensional density and velocity distributions. In this study, to confirm the feasibility of the three-dimensional technique, the three-dimensional particle position and variation of fringes caused by the density distribution were extracted from the Hologram images.

Results and Discussion

In order to investigate the feasibility of the simultaneous measurement technique for three-dimensional density distributions and three-dimensional velocity distribution, the heavy gas jet with small particles was measured. As experimental fluid, carbon-dioxide and air were used. In a carbon-dioxide jet into air, mist of water were introduced as tracer particles.

Figure 1 shows the schematic view of the experimental setup. As an illumination, 100mW CW diode excited Nd:YAG Laser ($\lambda = 532\text{nm}$) was used. The expanded laser beam separated into object beam and reference beam by the half mirror (A). On the holographic plate, the hologram of the particle and density distributions were recorded.

Figures 2(a) and (b) show the reconstructed images of particle and density, respectively. Using the high-pass filter, the background noise of the plane wave could be clearly cut, causing the particle image to be sharp(Fig. 2(a)). This image was taken by the CCD camera. With shifting the CCD camera location, the three-dimensional particle positions can be reconstructed. In Fig. 2(b), the fringe pattern for the jet flow was clearly observed. From the hologram, the density information could be clearly extracted. With taking the holograms from several directional view, the three-dimensional density distributions could be reconstructed using computer tomography.

The information of the density distribution and the particle positions could be reconstructed from one hologram. Therefore, the feasibility of the simultaneously measurement technique for the density and velocity was demonstrated. However, the image still had lots of noises as shown in Fig. 2. Further improvement of the technique should be needed.

Conclusion

The feasibility of the holographic technique for the simultaneously measurement of three-dimensional particle position and three-dimensional density distributions were demonstrated. The particle position and density information could be clearly reconstructed from the hologram, using high-pass or low-pass filter with relay lens.

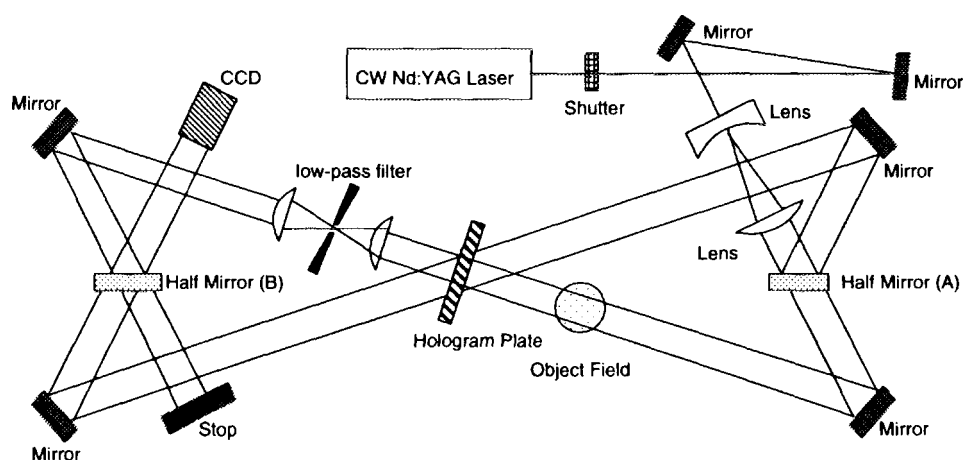


Figure 1. Schematic view of the experimental setup

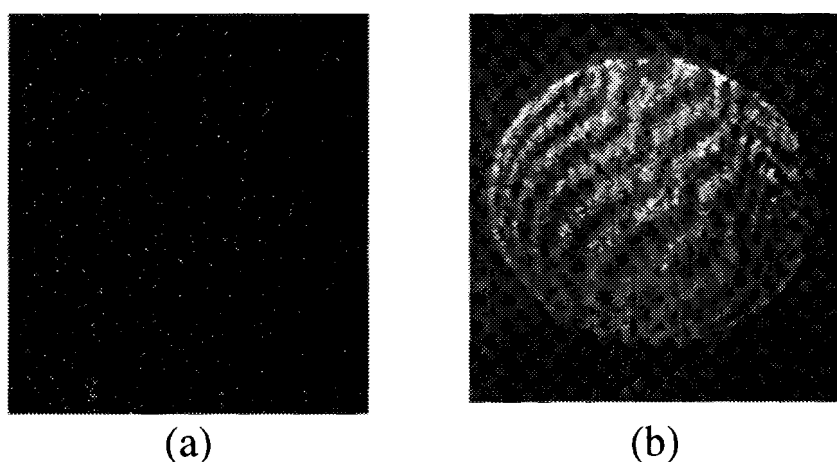


Figure 2. Reconstructed image for particle position (a) and density (b) measurement

New tracking algorithm for particle image velocimetry

K. Okamoto, Y. A. Hassan, W. D. Schmidl

342

Abstract The cross correlation tracking technique is widely used to analyze image data, in Particle Image Velocimetry (PIV). The technique assumes that the fluid motion, within small regions of the flow field, is parallel over short time intervals. However, actual flow fields may have some distorted motion, such as rotation, shear and expansion. Therefore, if the distortion of the flow field is not negligible, the fluid motion can not be tracked well using the cross correlation technique.

In this study, a new algorithm for particle tracking, called the Spring Model technique, has been proposed. The algorithm can be applied to flow fields which exhibit characteristics such as rotation, shear and expansion.

The algorithm is based on pattern matching of particle clusters between the first and second image. A particle cluster is composed of particles which are assumed to be connected by invisible elastic springs. Depending on the deformation of the cluster pattern (i.e., the particle positions), the invisible springs have some forces. The smallest force pattern in the second image is the most probable pattern match to the correspondent original pattern in the first image. Therefore, by finding the best matches, particle movements can be tracked between the two images. Three-dimensional flow fields can also be reconstructed with this technique.

The effectiveness of the Spring Model technique was verified with synthetic data from both a two-dimensional flow and three-dimensional flow. It showed a high degree of accuracy, even for the three-dimensional calculation. The experimental data from a vortex flow field in a cylinder wake was also measured by the Spring model technique.

1

Introduction

Particle Image Velocimetry (PIV) is a superior measurement technique for studying fluid flows. It offers many advantages over other conventional velocimetries, such as laser doppler anemometry and hot-wire anemometry. The primary advantage is the ability to capture spatial velocity distributions simultaneously and noninvasively.

The fluid flow is visualized by seeding with small particle tracers. Then the flow visualization images are analyzed to obtain the velocity distribution of the flow. Many algorithms for analyzing the images have been proposed. These include the cross correlation technique [1, 2, 3] and particle tracking technique [4].

In the cross correlation technique, the flow in a small sub-region is considered to have a similar vector. The sub-regions of the first and second image are denoted as $f_{(x,y)}$ and $g_{(x+p,y+q)}$, respectively. The relationship between f and g is assumed to be,

$$f_{(x,y)} = g_{(x-ut, y-vt)} \quad (1)$$

where (u, v) is a velocity. The cross correlation coefficient between f and g is

$$R_{(p,q)} = \frac{\int (f_{(x,y)} - \bar{f})(g_{(x+p,y+q)} - \bar{g}) dV}{\sqrt{\int (f - \bar{f})^2 dV} \sqrt{\int (g - \bar{g})^2 dV}} \quad (2)$$

where \bar{f} is denoted as an averaged value of f . Then, the velocity, $(u, v) = (p/\Delta t, q/\Delta t)$, can be calculated from the displacement, (p, q) , which has the highest cross correlation coefficient, R .

Although the cross correlation technique has many advantages, it also have several weak points. For example, it requires a lot of calculation time. It is also difficult to implement for three-dimensional measurements, since the technique is based on two-dimensional images.

Several studies have been carried out to improve the original cross correlation technique. Uemura et al. [3] proposed a binary cross correlation technique. The visualized image is digitized into a binary image. Then, the calculation of the cross correlation was modified into a very simple form resulting in a very fast calculation time.

Kaga et al. [5] proposed a pattern tracking algorithm. In this algorithm, to reduce the calculation time, the candidates with lower cross correlation coefficients were successively abandoned. Using this algorithm, the calculation speed was 100 times faster than that of the original cross correlation technique.

Okamoto et al. [6] proposed a Velocity Vector Histogram technique, in which the vector histogram was used instead of the cross correlation. Since the information of the particle location was used directly, this technique can easily be applied to three-dimensional measurements.

In the original and improved cross correlation techniques, the motion of the particles is assumed to be parallel as shown

Received: 7 September 1994/Accepted: 25 May 1995

K. Okamoto, Y.A. Hassan, W.D. Schmidl
Department of Nuclear Engineering
Texas A&M University
College Station, TX 77843 USA

Correspondence to: K. Okamoto

in Eq. (1). However, in a real flow field, there are other kinds of motion. These include rotation, shear and expansion. Therefore, if the other motions are not negligible, the cross correlation technique can not track the flow.

In this study, a new technique for particle tracking is proposed. It is based on a pattern matching technique which can accept rotation, shear and expansion. A highly accurate velocity distribution can be reconstructed in a short calculation time. This technique can be easily extended for three-dimension measurements.

2

Algorithm

Many pattern matching algorithms have been proposed which accept a large deformation of the pattern [7]. In Particle Image Velocimetry, a small particle cluster is considered to be an object. The clusters are matched in consecutive images. In this study, the deformation of the particle cluster is assumed to be small, resulting in a simpler algorithm.

2.1

Spring model

Typical patterns, for a particle cluster in two consecutive images, are illustrated in Fig. 1. In the second image, the pattern changes with a small rotation and shear. In this case, the cross correlation factor between the two images is very small, since there is no overlapping of the particles between the images, except for the center particle. Therefore, using conventional cross correlation techniques, the correct result can not be obtained. However, humans can easily identify that both cluster patterns are similar.

The evaluated particle P is called the target. The cluster is constructed with several particles which are located around the target P . In this study, the particles in the cluster are assumed to be connected by invisible elastic springs as shown in Fig. 2. Each particle in the cluster is connected by a spring from target P . These particles are also connected to their neighbors as shown in Fig. 2. The determination of their neighbors are based on the location. In the first image, all the springs are in the base condition (i.e., springs have no force).

In the second image, the cluster of particles is shifted by rotation and shear. According to the changes of shape, every invisible spring holds some forces.

$$E_i = k_i |\vec{r}'_i - \vec{r}_i| \quad (3)$$

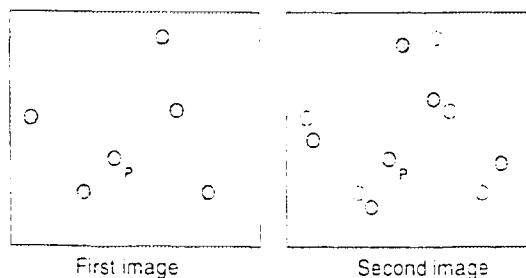


Fig. 1. Schematic of particle displacement in two images

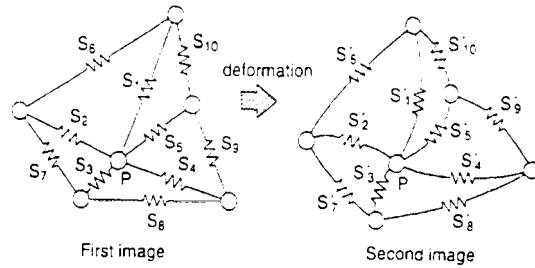


Fig. 2. Spring model

where k is a spring factor, \vec{r} and \vec{r}' are the relative vectors of the springs in the first and second image, respectively. The average force for the invisible springs is,

$$E = \frac{1}{N} \sum_i^N E_i \quad (4)$$

When there is no rotation, shear or expansion, the average force is zero (i.e., $\vec{r} = \vec{r}'$). When there is a small rotation, shear or expansion, the average force has a small value, because of the small deformations of the springs. If the target particle in the first and second image do not correspond, the average force will be very large, since the particle cluster shape will probably be very different. Therefore, pattern matching can be conducted by considering the spring force.

For a target particle cluster in the first image, the correspondent cluster in the second image is searched. The average spring force of a cluster in the second image is calculated with Eq. (4). However, for the cluster, several combinations of the springs might be considerable, since the shifting of the cluster pattern is not known. Therefore, the smallest force in these combinations is thought to be an average spring force for that cluster. Then, the average spring forces for every possible cluster in the second image are calculated. The cluster with the smallest force in the second image is considered to correspond to the cluster in the first image.

In this model, even when rotation, shear and expansion are applied to the flow, the particles can be correctly tracked. For example, in Fig. 1, the invisible spring force is not zero, but it is very small, since the deformation caused by rotation and shear is not very large. Therefore, the particle cluster can be easily tracked correctly between the images.

2.2

Spring parameter

2.2.1 Spring factor

In the spring model, there is one unknown parameter, k , the spring factor. In a particle cluster, particles which are closer to the target particle should have a greater influence on the pattern matching than particle which are father away. This is because particles which are closer together will have a greater probability of moving together. This weighting is implemented through a spring factor. Therefore, the spring factor of a closer

particle will be greater than that of a farther particle. The following spring factor is used in this study.

$$k_i = a \frac{1}{|\bar{s}_i|} \quad (5)$$

where a is a constant. In this study a is set to unity. By substituting Eq. (5) into Eq. (3), the force of the invisible spring is,

$$E_i = \frac{|\bar{s}'_i - \bar{s}_i|}{|\bar{s}_i|} \quad (6)$$

In this model, noise in the image may result in erroneous particle positions which lead to larger spring forces. To reduce noise effects, the maximum force, E_i , is limited to 1.

2.2.2

Appearing or disappearing particle

Particles appearing in the second image but not the first (or the reverse) result from image noise and the movement of particles in and out of the illuminated area. The effects of these particles on particle tracking should be taken into account.

Appearing and/or disappearing particles are considered to be a generated or broken spring in this study. The generated or broken spring is assumed to cost a force of 0.3. The force plays a role of penalty for the matching.

Even though the appearing and disappearing particle exist in the cluster, the corresponding particle cluster should have a low force for the correct matching. Therefore, the penalty should be small. On the other hand, if the penalty is very small, the cluster with very few particles always has a low force, resulting in the mismatching. In this study, the penalty is empirically assumed to be 0.3 from the results of several numerical simulations.

2.3

Pair selection

The above procedure for finding corresponding pairs is repeated for all of the particles in the first image. In this stage, erroneous pairs may be included. The cleaning procedure is carried out by using information about the spring force.

Since the cluster pair matching is based on the first image, there may be several possible candidates for each cluster in the second image, as shown in Fig. 3. The cluster pairs are sorted by information about the spring force. Then the lowest spring force cluster pairs are selected. In Fig. 3 thick line pairs are considered to be correct.

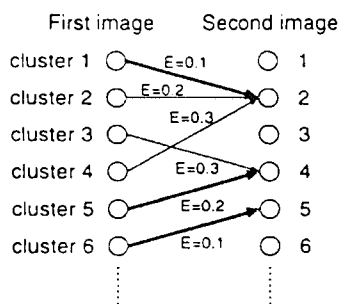


Fig. 3. Particle cluster matching between two images

Finally, the corresponding pairs of clusters are converted into the velocity field.

2.4

Three-dimensional measurement

In the three-dimensional measurement, the particle positions in the three-dimensional flow field should be known. To obtain the three-dimensional positions, several techniques [6, 8] were proposed. In this study, the particle positions are assumed to be obtained by one of these techniques. Once the three-dimensional particle positions are known, the Spring Model procedure can be applied to obtain the three-dimensional velocity field. Particles in the three-dimensional particle cluster are considered to be connected to each other by the invisible springs. The invisible spring force is calculated using the information about particle positions in the second image. The least force particle cluster in the second image is corresponded to the cluster in the first image. Then the three-dimensional velocity distributions can be obtained with the Spring Model technique.

3

Verification

In order to verify the Spring Model technique, velocity distributions were reconstructed from synthetic particle data.

Two-dimensional and three-dimensional flow fields were calculated by a numerical simulation code. Using the simulated flow, the movement of the particles was calculated. Then, the flow was reconstructed from the particle information, using the Spring Model technique. To compare the results, the flow was also reconstructed using a cross correlation technique [2], with the same particle information.

There are a few cross correlation technique which can be applied to a three-dimensional flow field. Hassan et al. [2] proposed a cross correlation technique based on the particle location, which can be applied to two and three-dimensional flows. In this study, the Spring Model technique was compared with the cross-correlation technique.

3.1

Two dimensional flow

Figure 4 shows the simulated two-dimensional laminar flow field calculated by a Finite Element Method (FEM) code. The

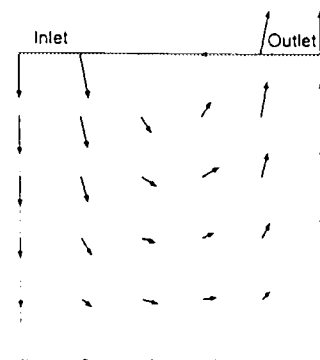


Fig. 4. Reference two-dimensional flow

inlet and outlet are located at the top. Five hundred particles were inserted into the flow field. The images of the first and second frame are shown in Fig. 5. The size of the images is 200×200 pixels. Humans can easily identify the corresponding particles, e.g., A-A' and B-B'.

Using the two images, the velocity field was reconstructed with the Spring Model and cross correlation [2] techniques. Figures 6 and 7 show the results of the reconstructed flow field.

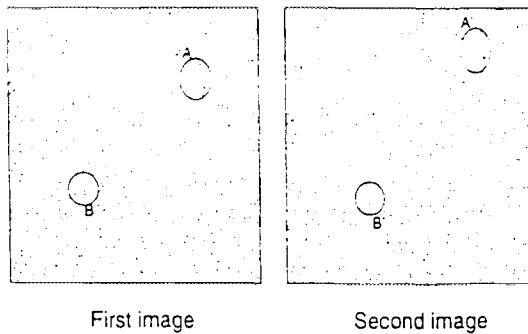


Fig. 5. Example of the synthetic images

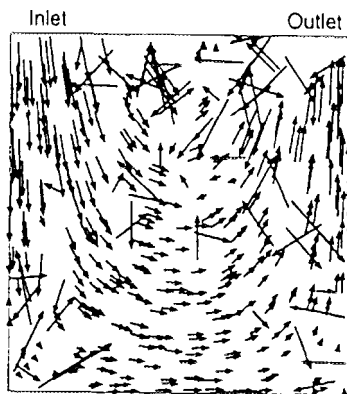


Fig. 6. Two-dimensional velocity distributions reconstructed by cross correlation

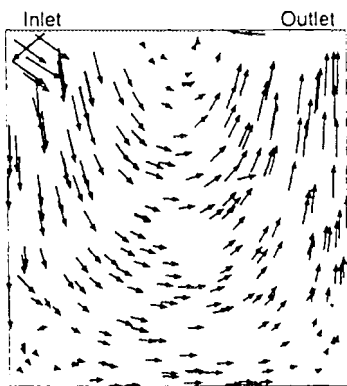


Fig. 7. Two-dimensional velocity distributions reconstructed by spring model

The cross correlation technique results had a low degree of accuracy because of the rotation and shear. Only the region where the movement was almost parallel was correctly reconstructed.

Table 1 shows the number of reconstructed vectors. 482 vectors should have been calculated, since 18 of the 500 inserted particles flowed out through the outlet. However, using the cross correlation technique, only 64% of the vectors were found. The ratio of erroneous vectors to calculated vectors was 23%.

On the other hand, the spring model technique could reconstruct the flow field with a good degree of accuracy. Even in region A of Fig. 5, where rotation and shear highly distorted the particle patterns, the velocity vectors were correctly reconstructed. In this simulation, 87% of the vectors could be correctly obtained by the spring model. The ratio of erroneous vectors was only 9%. So, the spring model is superior for measuring a flow field with rotation and shear motion.

3.2

Appearing and disappearing particle

The velocity field was again reconstructed with some appearing and disappearing (A&D) particles.

For the same particle data in the previous section, 20 particles were randomly vanished in an image, which simulates the A&D particles. Therefore, the number of particles to be tracked was 442, i.e., $482 - 2 \times 20$. Table 1 shows the results of the reconstructed vectors.

For the Spring Model, the difference of the correct vector number without A&D and with A&D was 41, which was almost the same with the number of the appearing and disappearing particles, i.e. 40. The number of erroneous vectors with A&D was also similar to that without A&D. Therefore, the appearing and disappearing particle did not affect on the yield for the Spring Model technique.

However, for the cross correlation technique, the number of correct vectors reduced dramatically. The appearing and disappearing particles lead to mismatching, resulting in the large number of erroneous vectors.

The effects of the appearing and disappearing particles were correctly taken into account in the Spring Model. The Spring Model was found to be effective for the flow field with the appearing and disappearing particles.

3.3

Three dimensional flow

Figure 8 shows the simulated three-dimensional flow field calculated by the FEM code. The inlet and outlet were located

Table 1. Results of reconstructed vectors

Dimension of flow field	2D		2D with A&D***		3D	
	CC*	SM**	CC*	SM**	CC*	SM**
Correct Vectors	[A] 309	417	91	376	260	387
Erroneous Vectors	[B] 89	40	188	38	89	59
Particle to be tracked	[C] 482		442		484	
Yield	[A/C] 64%	87%	21%	85%	54%	80%
Error ratio	[B/(A-B)] 23%	9%	68%	9%	26%	13%

*Cross Correlation technique [2]

**Spring Model technique

***Appearing and Disappearing particles

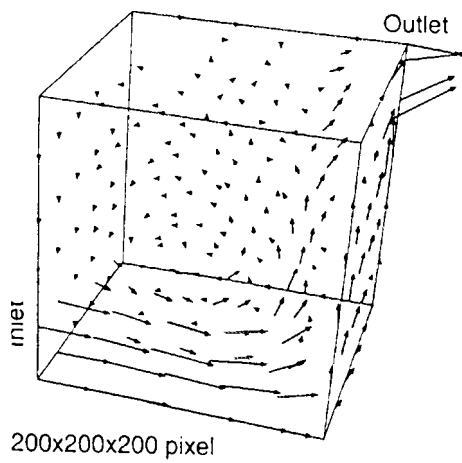


Fig. 8. Reference three-dimensional flow

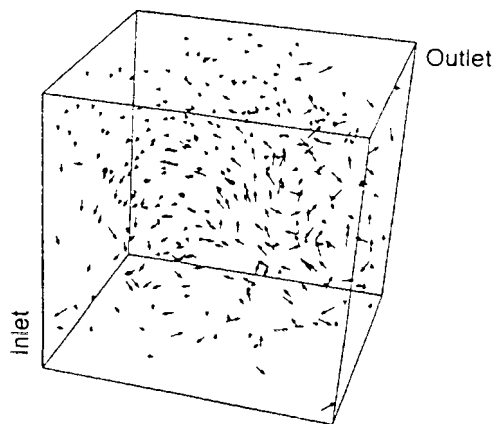


Fig. 9. Three-dimensional velocity distributions reconstructed by cross correlation

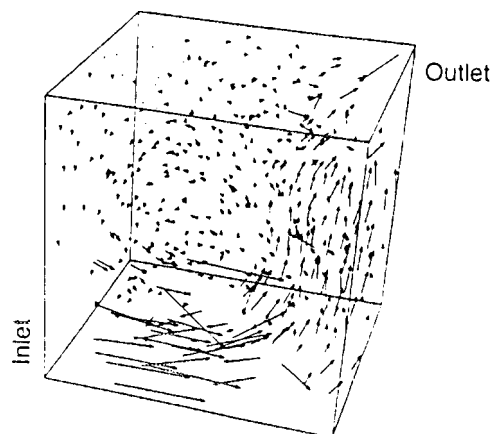


Fig. 10. Three-dimensional velocity distributions reconstructed by spring model

at the left bottom corner and right top corner respectively. The size of the cubic was $200 \times 200 \times 200$ pixels, and the inlet Reynolds number is 4000. A large three-dimensional circulation and shear flow were observed.

Five hundred particles were inserted into the flow field. Using the information about the particles, the three-dimensional velocity distributions were reconstructed by the cross correlation technique [2] and the Spring Model technique. The results are shown in Figs. 9 and 10.

In this case, the maximum particle displacement was about 100 pixels, which was about half of the length of the cubic. With the cross correlation technique, the small velocity field could be correctly reconstructed. However, the fast velocity region with large shear could not be measured. Table 1 shows the number of reconstructed vectors. Only 54% of the vectors were calculated. On the other hand, using the spring model, about 80% of the 500 velocity vectors were correctly reconstructed, even in the large displacement region. The ratios of the erroneous vectors were 26% and 13% in the cross correlation and spring model respectively. So, the spring model was found to reconstruct the three-dimensional flow field highly accurately.

In the above simulations, the yield and erroneous factors for the cross correlation technique were not good because of the long displacement of particles and rotations. If the displacement is small enough, i.e., if the time interval between the images is short enough, the cross correlation technique can reconstruct the flow field perfectly. The Spring Model technique is superior for the measurement with the large displacement and/or the rotation fields.

4

Experimental application

The Spring model technique was applied to a two dimensional flow field with a vortex. Figure 11 shows the schematic of the test section. The measurement system was the same as that of Hassan et al. [2]. The wake of the cylinder was visualized by a laser light sheet. Fluorescent seeds, 0.03 mm in diameter, were injected into the liquid phase. In the wake of the cylinder, a large vortex was periodically generated. Since the average velocity was 0.1 m/s and the cylinder diameter was 8 mm, the Reynolds number was about 800. The visualized image was digitized into a 640×480 pixel image every 53.8 msec.

Using the cross correlation and Spring Model techniques, the velocity distributions were calculated from the visualized images. In the calculation, about 500 particles in the whole images were processed and about 300 vectors were reconstructed for both methods. The yields were almost the same for both methods, since the flow was almost parallel except the wake field.

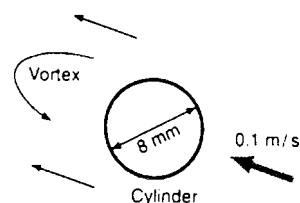


Fig. 11. Schematic of the test section

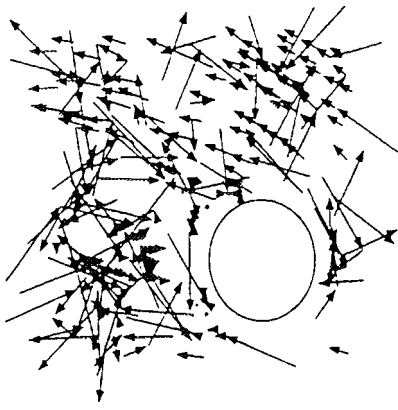


Fig. 12. Velocity distributions of a cylinder wake reconstructed by cross correlation

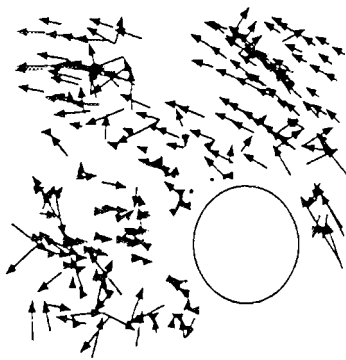


Fig. 13. Velocity distributions of a cylinder wake reconstructed by spring model

Figures 12 and 13 show the velocity distributions in the wake field reconstructed by the cross correlation and Spring Model technique, respectively. In the wake of the cylinder, large shear and rotating motion exist. Therefore, with the cross correlation technique, the wake field could not be tracked. It could only reconstruct the region where the flow was almost parallel.

On the other hand, the wake field was reconstructed by the Spring Model technique as shown in Fig. 13. Even though there was large shear and/or vortex in the flow, the spring model could reconstruct the velocity field with a high degree of accuracy. However, the results contained some errors. So some improvement of the Spring Model technique is still needed.

The calculation time for the reconstruction by the Spring Model was about 15 seconds using a Hewlett-Packard model 9000/720. It was much faster than that by the cross correlation technique, since the cross correlation technique took more than 3000 seconds using the same computer.

5

Conclusion

A new tracking algorithm for Particle Image Velocimetry has been proposed, which can be applied to a flow field with rotation, shear and expansion.

Corresponding patterns of particle clusters in the first and second image are composed. In the first image, the particles of the particle cluster are assumed to be connected by invisible elastic springs. In the second image, according to the pattern changes of the particle cluster, the invisible springs have some forces. The smallest force pattern in the second image corresponds to the original pattern in first image. Using this information, the particle movement can be tracked. This technique can be applied to flows with rotation, shear and expansion. A three-dimensional flow field can also be reconstructed with this technique.

The effectiveness of this technique was verified with synthetic data from two-dimensional and three-dimensional flows. The results showed a high degree of accuracy. The vortex flow field of a cylinder wake was also measured by the technique and resulted in a high degree of effectiveness.

References

1. Adrian RJ (1991) Particle-imaging techniques for experimental fluid mechanics. *Ann Rev Fluid Mech* 23: 261
2. Hassan YA; Blanchat TK; Seeley Jr CH; Cnaan RE (1992) Simultaneous velocity measurements of both components of a two-phase flow using particle image velocimetry. *Int J Multiphase Flow* 8: 371
3. Uemura T; Yamamoto F (1989) A High Speed Algorithm of Image Analysis for Real Time Measurement of Two Dimensional Velocity Distributions. *ASME FED-85: 129*
4. Nishino K; Kasagi N; Hirata M (1989) Three-dimensional particle tracking velocimetry based on automated digital image processing. *Trans ASME J Fluid Eng* 111: 384
5. Kaga A; Inoue Y; Yamaguchi K (1991) Application of a Fast Algorithm for Pattern Tracking on Airflow Measurements. *Flow Visualization VI, Springer-Verlag, 853*
6. Okamoto K; Madarame H; Shioya R (1991) Measurement of Velocity Distribution in a Tank by Velocity Vector Histogram. *ASME, FLUCOME'91, 601*
7. Tang YY; Suen CY (1994) New Algorithms for Fixed and Elastic Geometric Transformation Models. *IEEE Trans Image Processing* 34: 355
8. Yamamoto F; Uemura T; Iguchi M; Ohta J; Wada A; Mori K (1993) 3D PTV based on binary image correlation method and its application to a mixing flow with a bubbling jet. *Comput Meth Exp Meas* 229

レーザー共鳴イオン化分光を用いた核融合材料界面特性の評価手法の開発
井口哲夫（原子力工学研究施設）、佐藤 泰、中沢正治（システム量子工学専攻）

Development of Resonance Ionization Spectroscopy System
for Fusion Material Surface Analysis

T. Iguchi¹, Y. Satoh² and M. Nakazawa²

1 Nuclear Engineering Research Laboratory

2 Dept. of Quantum Engineering and Systems Science

Abstract

A Resonance Ionization Spectroscopy(RIS) system is now under development aiming at in-situ observation and analysis neutral particles emitted from fusion material surfaces under irradiation of charged particles and neutrons. The basic performance of the RIS system was checked through a preliminary experiment on Xe atom detection.

1. Introduction

Under nuclear fusion reactor environments, complicated particle transport phenomena occur through sputtering and erosion of plasma facing materials, recycling of fuel particles, nuclear transmutation and damage of materials by neutron irradiation, etc. These phenomena strongly depend on the surface condition of materials, and so far some beam probes of electrons and ions such as EPMA, AES, SIMS, etc., have been preferably used for the surface characterization of fusion materials. The charged particle beam probes, however, are not suitable for the analysis of neutral particles which are dominantly transported in the processes of sputtering, absorption and desorption through the surface of fusion materials. As one of the most promising technique to analyze neutral particles emitted from material surfaces, Resonance Ionization Spectroscopy(RIS) is available, in which wavelength-tunable lasers are used to efficiently and selectively ionize atoms of a specific analyte element. In this study, we are aiming to establish an in-situ observation technique and its application for neutral particle analysis on fusion material surfaces under irradiation of charged particles and neutrons. Here are reported on an outline of the RIS system and the preliminary results on the system performance, in particular on the efficiency and selectivity through Xenon gas detection.

2. RIS system and preliminary experiment

The RIS system used in this study is one of the main equipments being developed at the Fast Neutron Science Facility in NERL, the University of Tokyo. Fig. 1 shows an experimental arrangement for the basic performance check, which consists of one tunable laser, a pulsed Nd:YAG laser (Quanta-Ray, GCR-190-10) pumping dye laser (Lambda Physik, Scanmate-1E-UV) system and a time-of-flight reflectron type mass spectrometer with a field-free drift region approximately 90cm long and a pair of chevron-mounted microchannel plate ion detectors. As a test sample, Xe atoms of natural abundance were analyzed where a resonance ionization process utilizing a two-photon excitation of its $5p^56p[5/2]_2$ level (256.02 nm) followed by one-photon ionization at the same wavelength from the excited state was employed. This experimental simplicity is good for the RIS on dynamic process of neutral particles emitted from the material surface, but must be counterbalanced by the fact that the high-intensity light necessary for the two-photon transition with a low probability can cause nonlinear processes such as multiphoton ionization leading to interferences by other species.

3. Results and discussion

Fig.2 shows an example of the time-of-flight mass spectra of Xe atoms of natural abundance obtained from the preliminary experiments. The experimental ratios of isotopic abundance agreed well with the reference data in the concentration below 10^{16} atoms/m³. The good selectivity of Xe atoms was also confirmed through the laser wavelength scanning. The detection limit was estimated around 56 atoms per a sensitive volume along the laser path from the ¹²⁴Xe (natural isotopic abundance of 0.096%) peak counts and the MCP noise level. The detection efficiency was also determined as ~ 0.12 through the ¹²⁹Xe peak counting. At present, the laser power is 0.7 mJ/pulse at maximum corresponding to $\sim 8 \times 10^8$ W/cm² and not so high that the resonant ionization probability is saturated. By increasing the laser power, therefore, the detection limit or efficiency will be further improved.

As the next step experiment for the solid surface analysis, the pulsed ablation laser to atomize the sample will be introduced into the present system, being synchronized with the RIS laser.

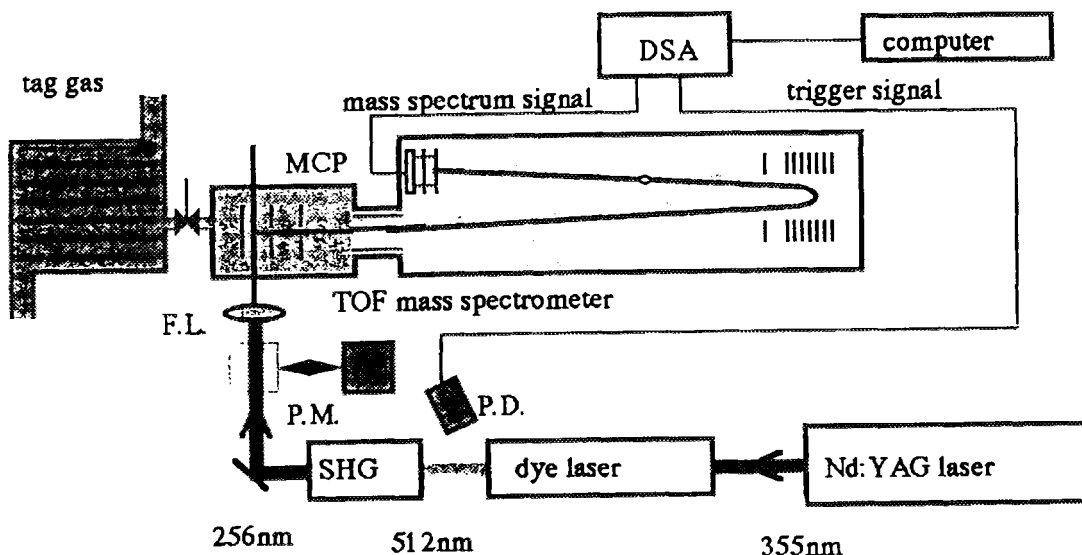


Fig. 1 Experimental arrangement of RIS for Xe atom detection

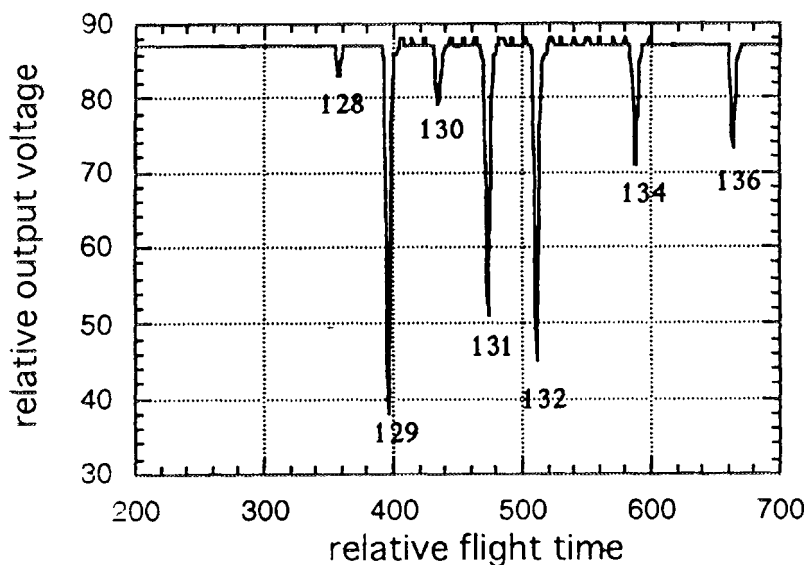


Fig. 2 An example of the time-of-flight mass spectra of Xe atoms of natural abundance

Active control of vortex dipoles and heat transfer with wall deformation

N. Kasagi and Y. Mito

Department of Mechanical Engineering

Abstract

Active control of vortex dipoles and heat transfer is studied by performing numerical simulations. Wall deformation is chosen for control. A two-dimensional flow model is constructed with a vortex dipole and a Couette flow by replacing a longitudinal vortex and a wall-sheared flow in wall turbulence. Simple feedback control laws are tested in this study, which sense a velocity component, v or w , near a wall and produce a discrete wall-velocity normal to the unactuated wall multiplied by a constant under constraint of a constant cross-sectional area. Drag reduction is achieved, 12 % at the maximum for a v -sensing law and 6 % for a w -sensing law, for the modeled flow field. The variations of the phenomena which lead to drag reduction are discussed by comparing flow fields and wall shapes of drag reducing cases.

1 Introduction

For control of turbulence transport phenomena, various devices have been developed in passive and active means: riblets and LEBU (large-eddy-break-up) devices for passive ones and polymer additions, blowing & suction and wall oscillations for active ones. Feedback control can achieve higher performance with the feedback of the information of the flow field especially when the flow field is spatiotemporally changeable. Wall deformation is chosen for an actuator of the feedback control in this study.

Turbulence drag reduction can be achieved by attenuating turbulence coherent structures, such as longitudinal vortices and sweeps, and reducing Reynolds stresses. To simplify the phenomena and extract the effect of the wall deformation on the longitudinal vortical component, a two-dimensional flow model is proposed by replacing quasi-streamwise vortical structures and a wall-sheared flow in wall turbulence by a vortex dipole and a Couette flow and assuming a uniform flow field in the streamwise direction. Active control with wall deformation is tested for the drag reduction problem of the flow model. Simple control laws are devised which sense a velocity component, v for v -sensing laws or w for w -sensing laws and calculate wall velocity multiplied by a constant under constraint of a constant cross-sectional area. The objectives of this study are to discuss the applicability of the active control with wall deformation and to obtain a generalized concept for control of skin-friction and heat transfer.

2 Numerical Procedure

An incompressible flow and a passive scalar are assumed for fluid and temperature respectively. The governing equations are the Navier-Stokes equations, the continuity equation and the energy equation. All equations are expressed in general coordinates because a boundary-fitted coordinate system is used. The computational grid is calculated at every time step, that is, at every wall deformation. For the temporal discretization, a four-step fractional-step method is used for the velocity field and a Crank-Nicolson method is used for the temperature field. For the spatial discretization, a discrete second-order difference method is used.

A flow function of a vortex dipole is given by $\psi = U^* a J_1(kr/a) \sin \theta$ ($r \leq a$, $k = 3.83$), which is a imaginary one induced in the cylinder in the uniform inviscid flow. The governing parameters for the vortex dipole are decided based on the observation of direct numerical simulations for turbulent channel flows and turbulent boundary layers. All parameters are nondimensionalized by wall units

of the initial Couette flow. The vortex diameter and the vortex height are set to be 25 and 30 ν/u_τ , respectively from the most frequent values. The vortex circulations are set to be 60 and 500 ν from the most frequent value and the maximum class value respectively. Prandtl number is set to be unity.

For active control laws with wall deformation, v -sensing laws and w -sensing laws are used. The v -sensing law and the w -sensing law are expressed by $v_w^{n+1} = C_v v_s^n$ and $v_w^{n+1} = C_w (|w_s^n| - \overline{|w_s^n|})$ respectively under constraint of a constant cross-sectional area, where $C_v, C_w = \text{const.}$ and v_w^{n+1}, v_s^n and w_s^n are wall deformation velocity at t^{n+1} , sensed v and w components at t^n respectively. The sensors are located very close to the wall in this study. For v -sensing laws, the wall actuation promotes the fluid motion when $C_v > 0$ and the wall actuation bumps the fluid motion when $C_v < 0$. For w -sensing laws, $C_w > 0$ is only assumed. The wall velocity becomes positive when the magnitude of the spanwise wall shear stress becomes large and negative when the magnitude of the spanwise wall shear stress becomes small.

3 Results and Discussion

The v -sensing laws of $C_v > 0$ are effective on drag reduction of the flow model for the whole range of the longitudinal vortex circulation. The w -sensing laws of $C_w > 0$ are effective on drag reduction for the vortex dipoles of high circulation. In these drag reducing cases, sweep positions ($v < 0$ regions) correspond to valleys of wall shapes. By taking this mode, local skin-friction can be reduced at valleys. This contributes to the drag reduction in spite of the existence of the high shear regions at crests of both sides of the valley. For the v -sensing laws of $C_v < 0$, this is not the case.

The behavior of the heat transfer almost agrees with the behavior of the skin friction at the present Prandtl number ($\text{Pr}=1$).

References

1. Mito, Y. and Kasagi, N., 1996, Numerical simulation of a flexible channel flow, The 73rd JSME Spring Annual Meeting, Narashino, April, vol. 3, pp. 349-350.
2. Mito, Y. and Kasagi, N., 1996, Active control of vortex dipoles and heat transfer with wall deformation, 33rd National Heat Transfer Symposium of Japan, Niigata, May, vol. 2, pp. 393-394.

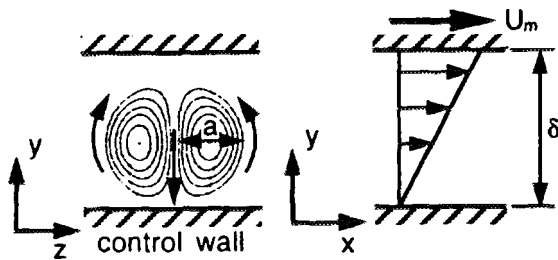


Fig. 1 Initial flow geometry

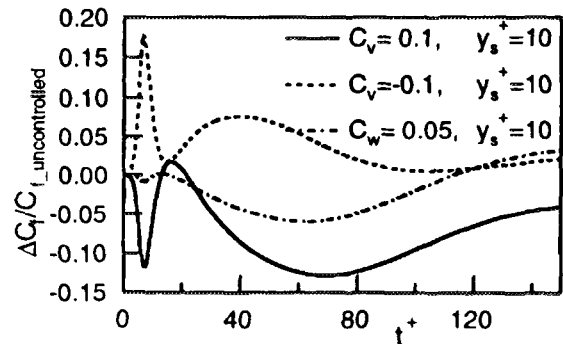


Fig. 2 Friction coefficients ($\text{Re}_\tau = 500$)

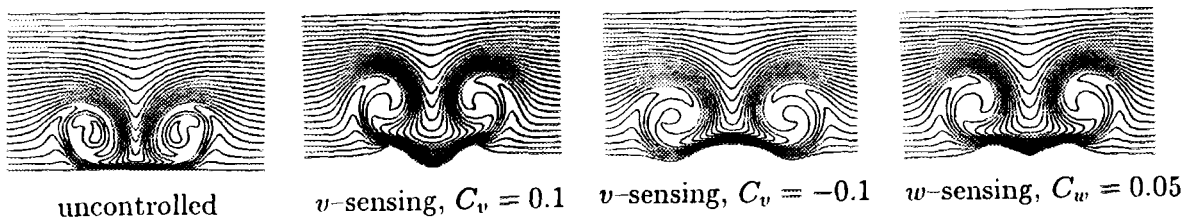


Fig. 3 Streamwise velocity ($\text{Re}_\tau = 500, y_s^+ = 10, t^+ = 53$)

熱音響型冷凍機の基礎的研究

斎藤孝基, 飛原英治, 酒井均 (機械工学科)

Basic Study on a Thermoacoustic Refrigerator

T.Saito, E.Hihara, H.Sakai

Department of Mechanical Engineering

Abstract

The thermoacoustic refrigerator consists of a speaker, a tube resonator and a stack of thin plates aligned parallel to the tube axis. As the gas oscillates along the stack, heat pumping effect occurs by heat exchange between the gas and the stack. In this study, The axial temperature distribution was measured in the resonance tube in order to understand the thermoacoustic effect and to compare with the numerical simulation performed last year.

1. Introduction

A thermoacoustic refrigerator used in this study is schematically shown in Fig.1. Acoustic oscillation is excited by the speaker which connected with the resonance tube by the tank. The speaker-side end of the resonator is designed to reduce the loss of acoustic energy. When the speaker drives the acoustic oscillation at the wavelength about four times as long as the length of the resonator, the gas inside the resonator oscillates with a velocity antinode at the speaker-side end and a pressure antinode at the closed end. A stack of thin, well-spaced plates is installed in the resonator. By the acoustic pressure, a parcel of the gas near the plate moves toward the closed end and is adiabatically compressed. At this time the gas temperature is higher than the stack, so the gas at a few penetration depth from the stack rejects heat to the stack. Similarly, when the gas is at the side of the speaker, the parcel of the gas absorbs heat from the stack. This is because adiabatic expansion has brought its temperature below the stack. Thus, the parcel of the gas transports a little heat from the speaker-side to the closed side during each cycle of the acoustic wave. As a result, a temperature gradient is made along the stack.

2. Experiment

In the experimental apparatus, a loud speaker was used, and the tank and the resonance tube were made of acrylic resin. The resonance tube was 500mm in length, and its cross section is 50mm in width and 60mm in height. A honey comb, which is made of vinyl chloride, was used as a stack. Temperature was monitored by thermocouples at each position of the resonator.

With this experimental apparatus we made two experiments. The first experiment was performed by changing the position of the stack. In this experiment, the length of the stack was fixed at 100mm. The second experiment was performed by changing the length of the stack, fixing the center position of the stack. In each case, temperature was measured at both ends of the stack at 10W, 20W

and 30W of electrical input to the speaker.

3. Result

Figure 2 shows the result of the first experiment. In this figure, the x-axis represents the position of the stack and the y-axis represents temperature change. The temperature difference has a maximum when the position of the stack is 150mm. The result of the second experiment is shown in Figs.3 and 4. Figure 3 shows the effect of the length of the stack on the temperature change. Figure 4 represents temperature difference between the hot end and the cold end. According to Fig.4, we can see the maximum temperature difference when the stack is 120mm long.

These two experiments qualitatively agree with the numerical simulation performed last year.

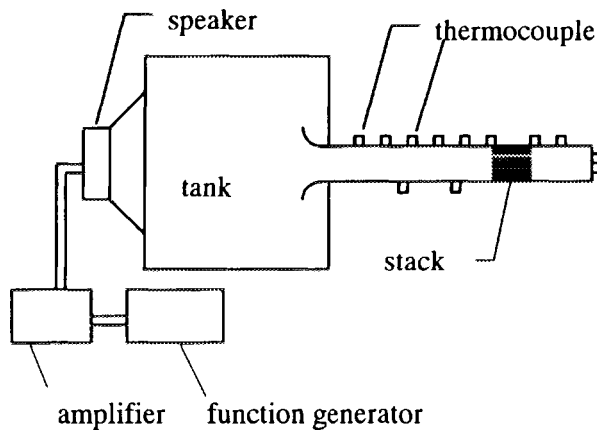


Fig.1 Experimental apparatus

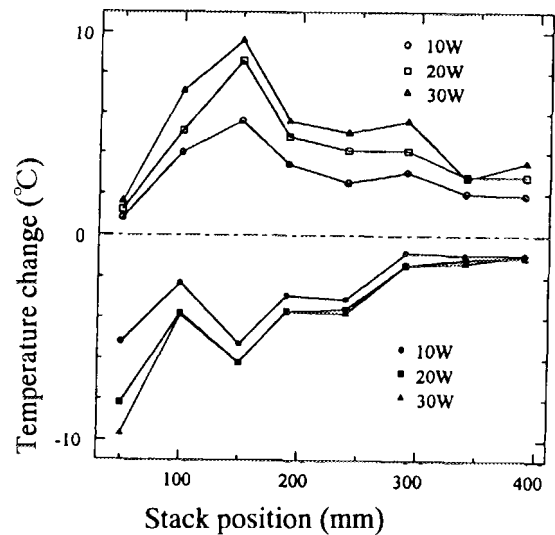


Fig.2 Effect of stack position

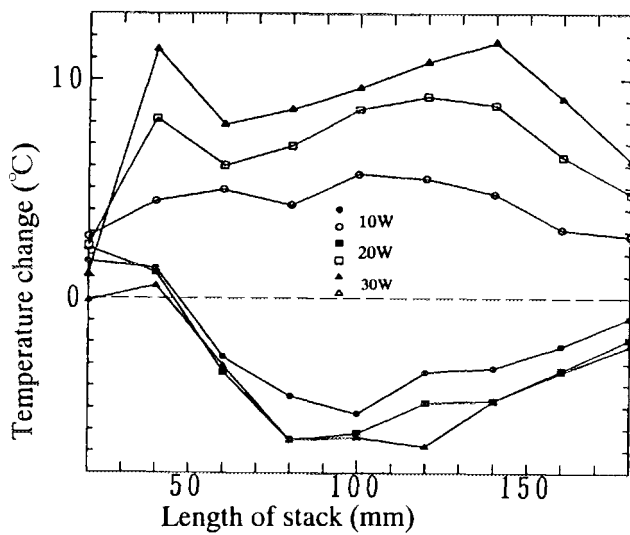


Fig.3 Effect of stack length

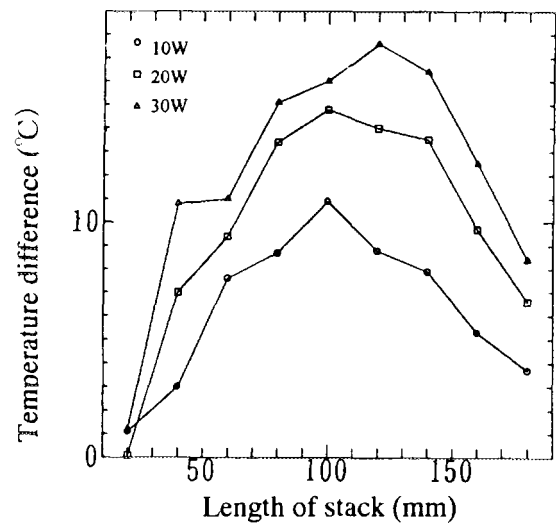


Fig.4 Effect of stack length

Study on the surface hydroxyl group on solid breeding materials by infrared absorption spectroscopy

Satoru Tanaka and Masaki Taniguchi

Department of Quantum Engineering and Systems Science

Abstract

Hydroxyl groups on the surface of Li_2O were studied by using a diffuse reflectance method with Fourier transform infrared absorption spectroscopy at high temperature up to 973K under controlled D_2O or D_2 partial pressure. It was found that hydroxyl groups could exist on Li_2O surface up to 973K under Ar atmosphere. Under D_2O containing atmosphere, only the sharp peak at 2520cm^{-1} was observed at 973K in the O-D stretching vibration region. Below 973K, multiple peaks due to the surface -OD were observed and they showed different behavior with temperature or atmosphere. Multiple peaks mean that surface is not homogeneous for D_2O adsorption. Assignment of the observed peaks to the surface bonding structure was also discussed.

I. Introduction

On the surface of Li_2O , tritium is considered to exist as a hydroxyl group of -OT. Tritium is released by recombination of surface -OT. It means that the reaction rate is influenced by the bonding strength of -OT to the surface. Therefore it is strongly required to understand the nature of surface -OT at high temperature and under the controlled atmosphere expected in the fusion reactor blanket. In-situ infrared absorption spectroscopy, which observes the O-D stretching vibration of surface hydroxyl group of -OD at high temperature under controlled atmosphere, was found to be a powerful method for this purpose because the vibration frequency is affected by the bonding strength of -OD to the surface.

II. Experimental

Infrared absorption spectra were recorded using a Shimadzu FT-IR 8100 with a resolution of 2cm^{-1} . In order to observe the absorption spectra of powder samples, the diffuse reflectance method was used. The temperature of the sample was controlled from room temperature to 1073K by the heater attached under the sample holder. The atmosphere in the chamber was controlled by the sweep gas of dry Ar, Ar + D_2O (1~400Pa) or Ar + D_2 (0~1.0 %). At the downstream the water vapor pressure was checked by a dew point meter.

III. Results and discussions

Fig.1 shows the change of absorption spectra of Li_2O at various temperatures. Before measurements, Li_2O sample was exposed to 300Pa D_2O atmosphere at 833K for 8 hours and then, the sample was dried under Ar atmosphere and the temperature was increased slowly up to 973K. The spectra was measured after at least 12 hours at each temperature. Several peaks were observed in the O-D stretching vibration region ($3200 - 2200\text{cm}^{-1}$). At 833K, broad bands attributed to -OD were observed at $3100 - 2800\text{cm}^{-1}$ and $2700 - 2400\text{cm}^{-1}$. Intensities of these bands decreased with increasing the temperature, and they disappeared by drying at 973K for more than 12 hours under dry Ar atmosphere. This means considerable amount of -ODs could exist below 973K under Ar atmosphere and these -ODs desorbed through recombination reaction above 973K. These peaks also disappeared at 833K when the sample was exposed to 3400Pa H_2 containing atmosphere for more than 24 hours. Dissociative adsorption of H_2 is considered to enhance the desorption of -OD as HDO.

We also observed the absorption spectra of Li_2O under D_2O vapor at various temperatures. Multiple peaks were observed and they showed different dependence on temperature and D_2O vapor pressure. Fig.2 shows the typical absorption spectra of Li_2O under D_2O atmosphere at 833K. Under a low D_2O vapor pressure, only the peaks at 2520cm^{-1} and 2490cm^{-1} were observed. These peaks became larger with increasing D_2O vapor pressure up to 76Pa and peak intensity at 2520cm^{-1} was saturated above 76Pa. Peaks at 2660cm^{-1} and 2620cm^{-1} appeared only under higher D_2O vapor pressure. These peaks could not be observed under low D_2O pressure below 76Pa, but in the region of higher D_2O pressure

above 157Pa, these peaks appears and increased in intensities with increasing D₂O vapor pressure. These facts indicate that surface is not homogeneous for D₂O adsorption and there exists multiple adsorption sites for -OD.

The observed peaks at various temperatures and their tentative assignments are summarized in Table.1

References

1. S.Tanaka, M.Taniguchi, M.Nakatani, D.Yamaki and M.Yamawaki, *J. Nucl. Mater.*, **218**,335 (1995).
2. M.Taniguchi, S.Tanaka, Y.Nose, *Fusion Technology*, **28**,1284 (1995).
3. M.Taniguchi, S.Tanaka and T.Yoneoka, *J.Nucl.Mater.*, **226**, 178(1995).

Table 1: Tentative assignment of observed peaks to the surface nature

observed peaks	surface nature
2900cm ⁻¹	many O ²⁻ exist around the -OD, on irreversibly stabilized or modified surface by heat treatment at 973K
2748cm ⁻¹ , 2717cm ⁻¹	"isolated" deutroxyl groups with several adjacent O ²⁻
2660cm ⁻¹	deutroxyl group with several adjacent -OD
2540cm ⁻¹	deutroxyl groups with small number of O ²⁻
2490cm ⁻¹	in the neighbor
2520cm ⁻¹	adsorbed on a most active site

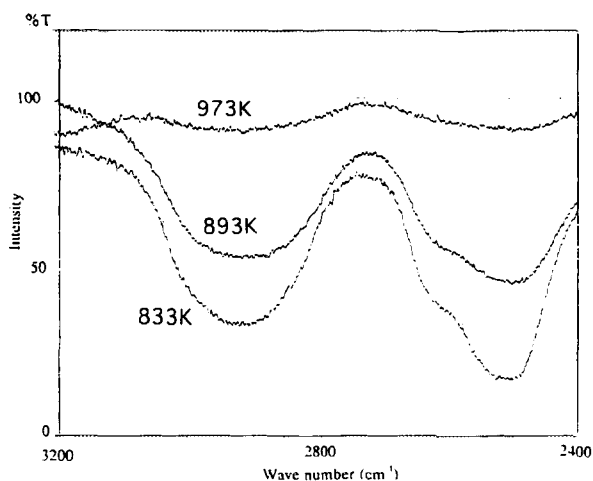


Figure 1: Absorption spectra of Li₂O during drying up to 973K

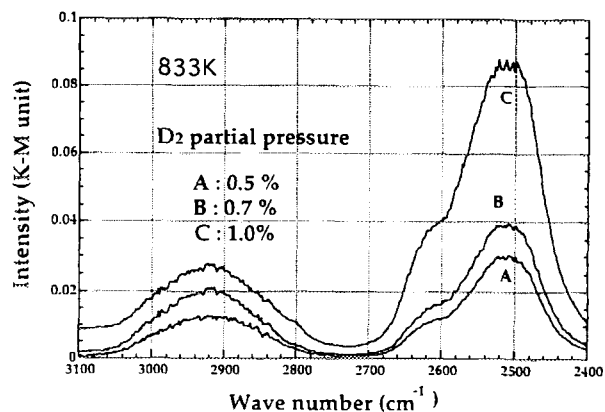


Figure 2: Absorption spectra of Li₂O under D₂O vapor at 833K

Ab-initio 計算による固体増殖材表面水酸基の研究

田中 知, 谷口正樹 (システム量子工学科)

Study on the surface hydroxyl group on solid breeding materials
by ab-initio calculations

Satoru Tanaka and Masaki Taniguchi

Department of Quantum Engineering and Systems Science

Abstract

The nature of -OH on the surface of Li_2O was analyzed with the ab-initio quantum chemical calculation technique. Calculation results showed that the stretching vibration of O-H is affected by the chemical species around the -OH.

I. Introduction

On the surface of Li_2O , tritium is considered to exist as a hydroxyl group of -OT. Tritium is released by recombination of surface -OT. It means that the reaction rate is influenced by the bonding strength of -OT to the surface. Therefore it is strongly required to understand the nature of surface -OT. For this purpose, we observed the hydroxyl group on the surface of various lithium ceramics by using the diffuse-reflectance FT-IR. However, some of the results were difficult to be explained only by the experimental technique. For example, effect of the O^{2-} around the -OH, interaction between the Li^+ and the -OH, edge and corner in the crystal, rampling and relaxation of the surface, and so on. Therefore, we are now trying to apply the quantum chemical calculation technique to clarify these problems. But in the present stage, most of these subjects contain problems to be solved. In the previous paper, we will show the preliminary results which we have performed using the quantum chemical calculation approach.

II. Calculation Method

To treat the adsorption phenomenon on the surface of the crystal, we have utilized the CRYSTAL92, the ab-initio Hartree-Fock crystalline orbital LCAO SCF program. In this calculation code, crystalline orbital is expressed as the linear combination of atomic orbital and no other adjustable parameters are needed. The basis set used in this work was the optimized one by Dovesi et al. for bulk Li_2O . This basis set is triple zeta quality for the oxygen and includes the polarization function for the lithium atom. It is reported that lattice constant, elastic constant and some other properties for bulk Li_2O calculated by using this basis set were in good agreement with experimental value.

III. Application of ab-initio calculations to the analysis of -OH on Li_2O (110) surface

Slabs consisting of atomic layers parallel to the Li_2O surface have been considered in order to deal with the surface adsorbate. To evaluate the effect of the interaction between O^{2-} and OH^- , we considered four types of geometry, which differ in the configuration of O^{2-} ion around the OH^- as shown in fig.1. Under these geometries, we searched for the equilibrium O-H bonding length of OH. Total energy of the system was calculated as a function of O-H distance (d). Results for all the geometries are summarized in table 1. Bonding length tends to become shorter (bonding strength becomes stronger) with increasing the number of O^{2-} around the OH. This tendency is in good agreement with Peri's explanation mentioned above. However, when the number of O^{2-} is four, the bonding strength became the longest. Such a structure as too many O^{2-} s existing closely in the neighbor is considered to be not stable.

We also analyzed the -OH on Li_2O (110) surface at various coverages. For this purpose, we considered three types of configuration as shown in fig.2. In the geometry A, 100 % of the sites is covered with hydroxyl group. Each hydroxyl group has four neighboring -OHs. In the geometry B, 50 % of the site is covered with hydroxyl group and another site is occupied by the oxygen ion. Each hydroxyl group has two oxygen ions and two hydroxyl groups in the neighbor. And in the geometry C, 25 % of the site is covered with hydroxyl group. Each hydroxyl group has two neighboring oxygen ions and two oxygen vacancies. To describe 25 % coverage, Supercell method was adopted.

For these configurations, the equilibrium O-H bonding length was calculated by the same method as mentioned in the previous section. The results of the calculation were 0.99 Å for the geometry A (100 % coverage), 0.96 Å for B (50 %), and 0.95 Å for C (25 %).

Bonding strength of O-H became weaker with increasing the coverage from 50 % to 100 %. This is considered to be by the reason that interaction between the two adjacent hydroxyl groups for the

geometry A is larger than that for the geometry B. In the case of the geometry A, such an interaction as hydroxyl bonding might occur.

Bonding strength of O–H did not change so much when the coverage changed from 25 % to 50 %. The distance of the two adjacent hydroxyl groups in the geometry B is considered to be long enough not to interact with each other. Note that the distance between the two adjacent hydroxyl groups for the geometry B is longer than that for the geometry A.

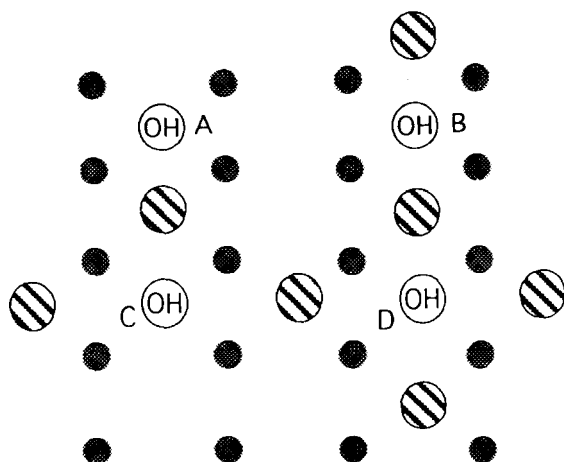


Figure.1 Geometry for the calculation

Table 1: The equilibrium bonding length of O-H

	number of O ²⁻	O-H length
A	1	0.980 Å
B	2	0.955 Å
C	3	0.950 Å
D	4	1.00 Å

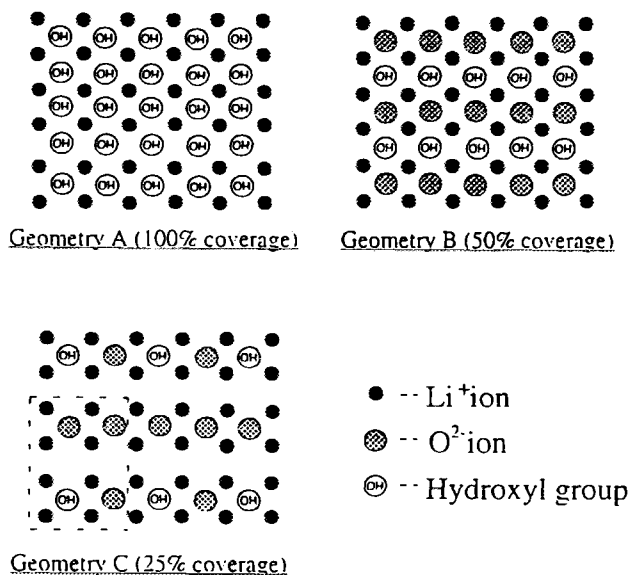


Figure.2 : Geometry for the calculation

The influence of irradiation defects on tritium release from Li_2O

Satoru Tanaka and Victor Grishmanov

During reactor irradiation of Li_2O defects are introduced by neutrons, triton and helium ions produced by ${}^6\text{Li}(n, \alpha){}^3\text{H}$ reactions and γ -rays. Simultaneous measurements of luminescence emission and tritium release were performed under various conditions (temperature, sweep gas chemical composition) for Li_2O single crystal and polycrystal in order to elucidate possible influence of defects on tritium release.

1. Introduction

There are a number of papers carrying information of tritium release retardation from Li_2O [1, 2, 3]. During the temperature transient 530-640 °C, it was observed a negative peak [3]. There are two hypothesizes for this phenomenon: first, variation of desorption activation energy with surface coverage of sample, and second, trapping of tritium by irradiation defects (or change the tritium form) in the bulk of specimen.

During the reactor irradiation the luminescence spectrum of Li_2O was found to be consisted of five emission bands at 305, 340, 375, 430 and 510 nm [4]. The 305 nm band is attributed to self-trapped exciton luminescence. The 340, 375, 430 bands are assigned to F^0 , F^+ , F_2 centers luminescence emission, respectively. The emission at 510 nm was assigned to F_2 center luminescence affected by surface OH^- group. F -centers are the subject of interest because their possible interaction with tritium. This can cause an influence on tritium release processes.

2. Experimental

Lithium oxide single crystal (or polycrystal, TD=80%) was used for investigation. Samples were irradiated by a research reactor "YAYOI" at the University of Tokyo with flux of thermal neutron up to 10^9 neutron/cm²·s, using a sweep gas of various chemical compositions (N_2 , $\text{N}_2 + 1.07\%\text{H}_2$). The luminescence from the sample was guided through

a quartz lens and an optical fiber to a monochromator, and then was measured by a photon-counting system. Released tritium was detected using the ionization chamber. The experimental facility is shown in Fig.1.

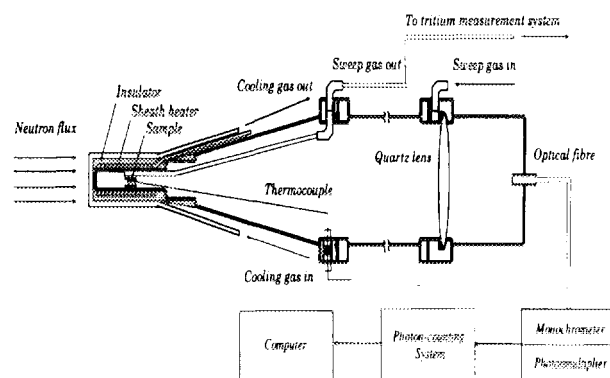


Figure 1: Facility for simultaneous measurement of luminescence and tritium release under reactor irradiation.

3. Results and discussion

The phenomenon of an excess luminescence in Li_2O at 340 nm under He^+ ion irradiation during increasing of temperature (200-500 °C) was reported [5]. Similar experiment was conducted in order to have more detail information about this phenomenon. When the temperature was reached 320-330 °C the excess of luminescence was observed with the maximum at 350 °C. It was found out that only for the emission at 340 nm (F^0 center) the phenomenon of the excess luminescence is peculiarly. By such experiment was shown that the value of the excess of luminescence

emission is dependent on irradiation time before a temperature increase. It was not observed the excess of luminescence emission in the case of temperature increase without irradiation. These results indicate that during the temperature increase a generation of F^0 centers proceeds and following excitation-relaxation process of them cause the excess of luminescence.

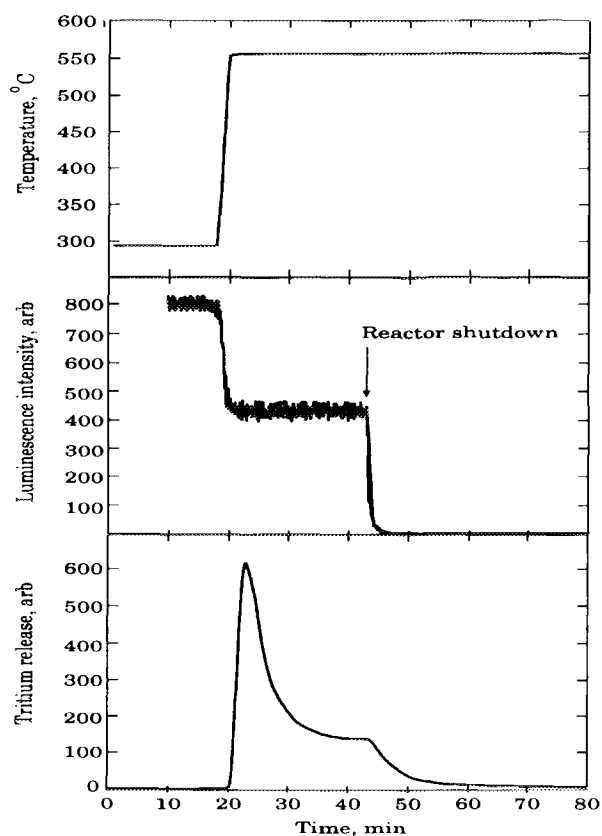


Figure 2: Simultaneous measurement of luminescence at 340 nm and tritium release during the temperature transient 295-560 °C.

According to mentioned above results, simultaneous measurement of luminescence emission and tritium release was performed for Li_2O under reactor irradiation. Unfortunately, there was not observed neither the tritium retardation nor the luminescence excess (Fig.2). It can be explain by a lower absorbed dose by the sample under reactor irradiation in comparison with ion beam irradiation.

Another set of experiments was focused on luminescence spectrum dependence on sweep gas chemical composition. The polycrystal of Li_2O was used. The design of experiment was

as following: the sample was kept at 600 °C in atmosphere of $N_2 + 1\%H_2$ for 20 hours, then temperature was decreased and spectra were taken at various temperatures. Afterwards the sweep gas was changed to N_2 and specimen was kept at 600 °C for 20 hour. The same operations were performed one more time.

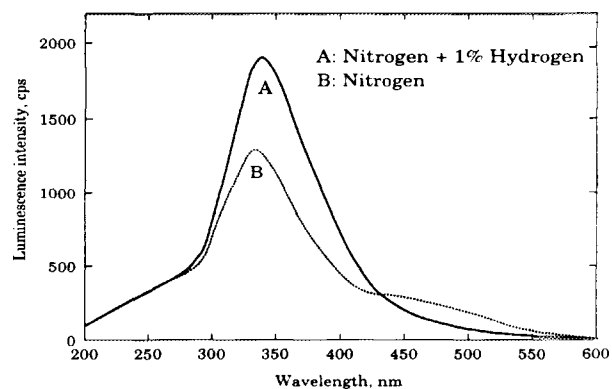


Figure 3: The dependence of luminescence spectrum on sweep gas chemical composition at 210 °C.

From the luminescence spectra at Fig.3 it is clear that sweep gas chemical composition play a significant role in a surface process. The addition of hydrogen increases luminescence intensity at 300-400 nm and causes disappearing of 510 nm peak (F_2 center luminescence affected by OH^- group).

It is concluded that simultaneous measurement of luminescence and tritium should be conducted at high irradiation dose, in order to create a high concentration of defects in Li_2O . In this case it can be expected the distinguish interaction of tritium with irradiation defects and as a consequence a change of tritium release parameters.

References

- [1] J.M.Miller et al., Fusion Technol. **14** (1988) 649.
- [2] S.Tanaka et al., Proc.of Workshop on CBBI. Paris, September 22-24, 1993 (CEA, Paris, 1994)
- [3] O.D.Slagle et al., J. Nucl. Mater. **219** (1995) 265.
- [4] Grishmanov et al., submitted to J. Nucl. Mater.
- [5] Y.Asaoka et al., Fusion Technol. **21** (1992) 1944.

ウラン合金の水素吸蔵放出特性に関する研究

伊藤 洋、山口憲司、山脇道夫（原子力工学研究施設）

STUDY ON HYDROGEN ABSORPTION/DESORPTION
PROPERTIES OF URANIUM ALLOYS.H. Ito, K. Yamaguchi and M. Yamawaki
(Nuclear Engineering Research Laboratory)

Abstract

Hydrogen absorption/desorption properties of two U-Mn intermetallic compounds, U_6Mn and UMn_2 , were investigated. U_6Mn absorbed hydrogen and the hydrogen desorption pressure of U_6Mn obtained from this experiment was higher than that of U, which was considered to be the effect of alloying, whereas UMn_2 was not observed to absorb hydrogen up to 50 atm at room temperature.

1. Introduction

Uranium has good hydrogen storage property with low hydrogen desorption pressure; i.e. high hydrogen desorption temperature, and many alloys were investigated for various utilization. In order to increase the hydrogen desorption pressure, it is suggested that alloying of metals which have high hydrogen absorption properties with those with poor absorption properties is promising. For this reason, we prepared two uranium-manganese intermetallic compounds and investigated hydrogen absorption-desorption properties.

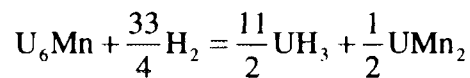
2. Experimental

In the U-Mn phase diagram, two intermetallic phases, U_6Mn and UMn_2 , have been identified. These compounds were prepared by arc melting in an argon atmosphere using high purity metals. The specimens were annealed in silica tubes under reduced pressure. After annealing (around one day at 1000 K) the specimens were cooled slowly. A small fraction of each sample was used for the hydrogen absorption/desorption measurements. Each sample was first pre-activated in hydrogen gas of about 1 atm and in the temperature range 300 - 873 K, and subjected to several hydriding-dehydriding cycles before the P-C-T readings were taken. The isotherms were measured in desorption; i.e., by extraction of hydrogen in small decrements from an initially saturated sample, and determination of the H_2 pressure above the sample after equilibrium had been established. The temperatures were chosen at 573K and 673K. In UMn_2 , another experiment was carried out in room temperature and in the pressure of about 50 atm because hydrogen absorption was not seen at 1 atm. A small fraction of each sample before and after hydriding was used for X-ray diffraction examinations in order to identify the phases.

3. Results and Discussion

3.1. U₆Mn

The pressure-composition isotherms of the U₆Mn-H system is shown in Fig.1 , and that of the U-H system is shown in Fig.2 for comparison. In the case of U₆Mn the compound U₆MnH_{16.5} was obtained. The amount of the absorbed hydrogen per g·mol of U was slightly decreased compared to UH₃. The desorption pressures of U₆Mn-H system were higher than those of U-H system when they are compared at the same temperature. The isotherms of U₆Mn-H system were similar to U-H system for H/M up to 2.5, but when the value of H/M is larger than that, the characteristics of isotherms were clearly different from those of U-H system. The X-ray diffraction pattern shown in Fig. 3 revealed decomposition from U₆Mn to UH₃ and UMn₂ upon hydrogenation. The reaction formula is considered to be as follows;



A similar trend was reported in U₆Fe-H system [1].

3.2. UMn₂

No evidence of hydrogen absorption was observed for the Mn-rich compounds UMn₂, whereas a considerable absorption was obtained for U₆Mn already at room temperature at a relatively low pressure of 1 atm.

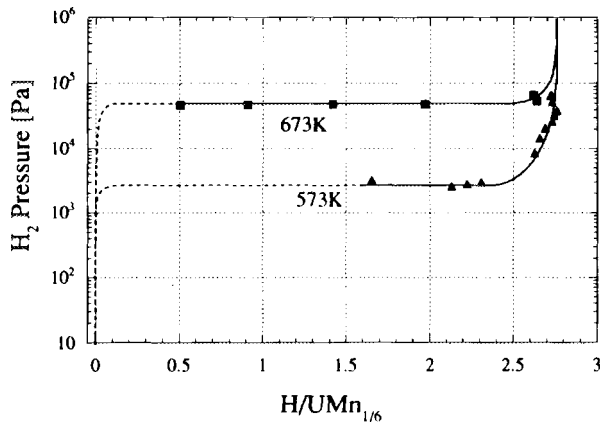


Fig. 1. Desorption isotherms of U₆Mn

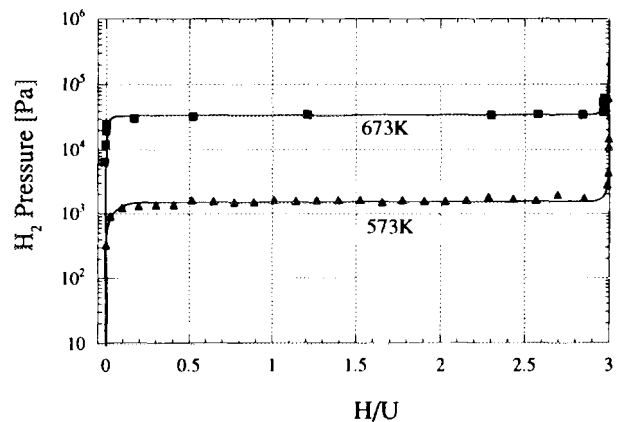


Fig. 2. Desorption isotherms of U

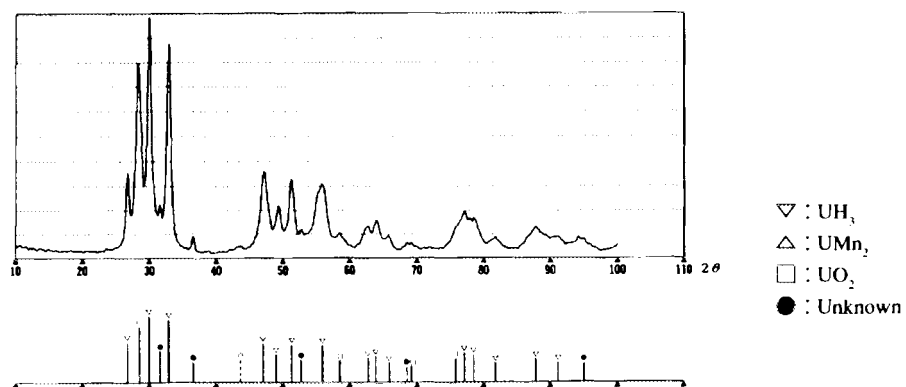


Fig. 3. XRD pattern of U₆MnH_{16.8}

Reference

1 T. Yamamoto, Dr. Thesis, Univ. of Tokyo (1989).

COMPATIBILITY OF YTTRIA (Y_2O_3) WITH LIQUID LITHIUM

T.Mitsuyama, T.Yoneoka, T.Terai, S.Tanaka

(Department of Quantum Engineering and Systems Science)

ABSTRACT

Compatibility of Y_2O_3 sintered specimens with liquid lithium was tested at 773K. No configuration change was observed with a slight increase of thickness for 1419 hr. Lithium-yttrium complex oxide ($LiYO_2$) was formed on the surface, and the inner part changed to gray or black nonstoichiometric Y_2O_{3-x} with lower electrical resistivity. It is concluded that Y_2O_3 has a possibility as a ceramic coating material for liquid blankets if it can be made into a dense coating on the surface of piping materials.

1. Introduction

Liquid blanket concepts are promising ones to realize a DEMO fusion blanket system, because it has advantages such as continuous replacement of breeder for reprocessing, no radiation damage for breeders, simpler blanket structure and better thermal transfer than solid blanket concepts. On the other hand, they have critical issues; (1) large MHD pressure drop requires large pump power, in particular in self-cooling concepts, (2) liquid breeders have a high chemical reactivity including low compatibility with structural materials, and (3) large amount of tritium may leak to environment due to permeation through structural materials in case of Li17-Pb83 blanket concept. In order to solve these critical issues, ceramic coatings on the surface of structural materials are proposed. The coating should have high electrical resistivity, high corrosion resistivity, low tritium permeability and high thermomechanical integrity.

It is well known that yttria (Y_2O_3) has remarkably large chemical stability, high resistivity and high compatibility with lithium. Nevertheless few systematic studies have been carried out on the material. In this paper, we report some experimental results on the compatibility of the Y_2O_3 sintered material with liquid lithium at 773K.

2. Experimental

The Y_2O_3 specimens were immersed in stagnant molten lithium metal at 773K for 72h, 232hr, 636hr and 1419hr under Ar atmosphere, as shown in Fig. 1. After prescribed time passed, specimens were taken out, and immersed in water for 12h and in ethanol in 1 min followed by drying. The specimens thus treated were investigated by ceramography, XRD, the dimensional change measurement and the electrical resistivity measurement.

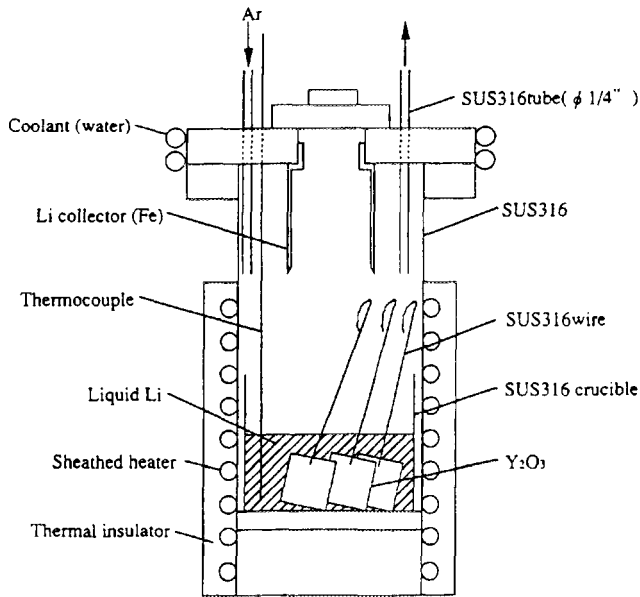


Fig.1 Sample holder

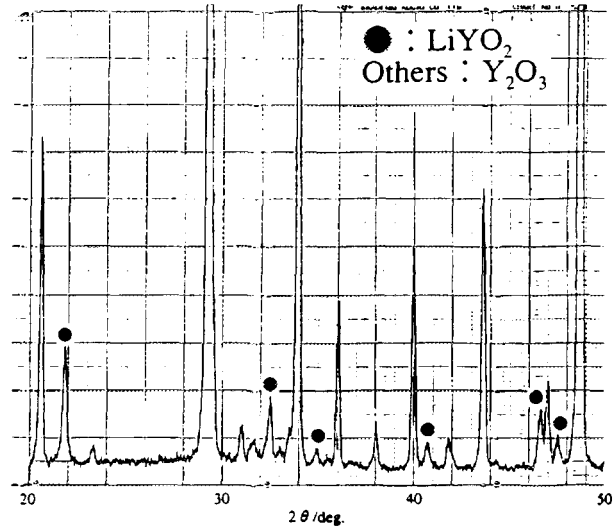


Fig.2 Typical XRD pattern

3. Result and Discussion

No significant configuration change such as fragmentation of the specimens and crack formation in the specimens were observed after the experimental treatment though the thickness of the specimens increased a little (less than 1%). The color of the specimens changed from the initial color (white) to black or gray due to the treatment. The color was getting darker and darker with dipping time and with distance from the surface of the specimens.

A typical XRD pattern for the surface of the specimen after the treatment is shown in Fig.2. Not only Y_2O_3 but also a complex oxide ($LiYO_2$) was observed. The compound increased in amount with dipping time in lithium.

Electrical resistivity determined by Cole-Cole plot in impedance measurement at room temperature decreased with dipping time. Although it decreased to the order of $10^7 \Omega m$ from the initial value of undetectable level (larger than $10^{11} \Omega m$) for 1419hr, the final value satisfies the design criterion for ITER ($>0.1 \Omega m^2/1 \mu m$). It is known that Y_2O_3 is reduced in severe reduction condition at high temperature to form Y_2O_{3-x} , which is gray or black and electronically conductive. From these facts, it is concluded that most of the internal part of the specimens changed to the nonstoichiometric phase. This means the diffusion coefficient of oxygen ion in Y_2O_3 is very large even at 773K.

高温照射下FLIBE(Li₂BeF₄)からのトリチウム放出化学形

鈴木晶大、寺井隆幸、米岡俊明、田中知 (システム量子工学科)

Chemical form of released tritium from molten Li₂BeF₄ salt under neutron irradiation at elevated temperatures

A. Suzuki, T. Terai, T. Yoneoka and S. Tanaka (Dept. Quantum Eng. & Systems Sci.)

ABSTRACT

Chemical forms of released tritium from FLIBE (the 2:1 mixture of LiF and BeF₂) by in-pile tritium release experiment were HT and TF and their proportion depended on the chemical composition of purge gas and the dehumidification time of specimen at high temperatures. The chemical form of tritium was determined by the thermodynamic equilibrium of the isotopic exchange reaction ($T^+ + H_2 \rightarrow H^+ + HT$).

INTRODUCTION

The 2:1 molten mixture of lithium fluoride and beryllium fluoride (2LiF-BeF₂ denoted as FLIBE) is considered to be a potential liquid tritium breeding material for fusion reactors, because of no irradiation damage, high chemical stability, possible use as a coolant and low electric conductivity to reduce MHD pressure drop. Critical issues in liquid blanket systems using FLIBE are corrosive behavior of TF generated by the nuclear reaction of LiF with neutron, and possible tritium permeation through structural materials from FLIBE or gas phase containing tritium. To reduce tritium permeation through structural wall and to recover tritium effectively, it is very important to clarify chemical form of released tritium from the FLIBE under neutron irradiation at elevated temperatures. In this report we have carried out some experiments to investigate chemical form of released tritium for the estimation of tritium recovery and tritium permeation.

EXPERIMENTAL

The in-situ tritium release experiment was performed using the apparatus shown in Fig.1, which consisted of a purge gas supply system, an in-reactor component, two sets of tritium monitoring system and a tritium recovery system. The in-reactor component was placed in an irradiation position of the fast neutron source reactor "YAYOI" of the University of Tokyo with the neutron flux of 10^8 - 10^9 n/cm²s. The tritium released from the specimen as HT or TF was swept by making purge gas (He+H₂) flowing over the specimen with the rate of about 100 cm³/s to the monitoring systems. The tritium-containing purge gas was divided in two lines: one has an aluminum reduction bed to convert the condensable species (TF) to non-condensable species (HT) and the other has a molecular sieve bed to capture the condensable species (TF). Thus the ionization chamber A monitored the concentration of all the released tritium species (HT and TF) and the chamber B monitored only the concentration of HT. The in-reactor component was composed of a sample container, a sheathed heater, a thermal insulator, a thermocouple and an Al₂O₃ crucible, as shown in

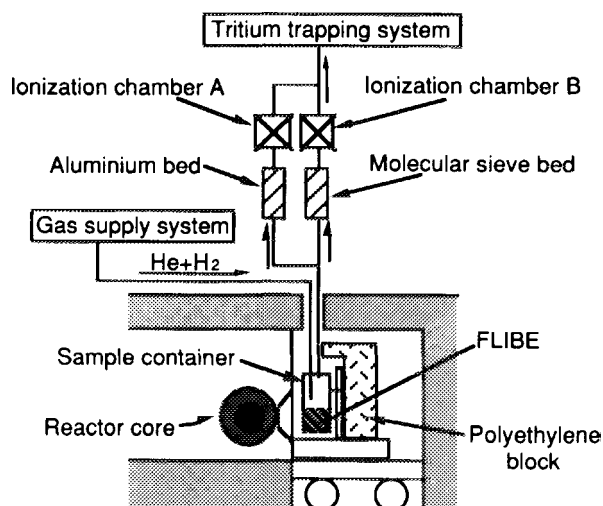


Fig.1 Apparatus for in-pile tritium release experiment.

Fig.2. The sample container was made of Monel metal (Ni70%-Cu30%), which has high tolerance for fluoric acid at high temperatures, and the tube used at room temperature was made of Teflon to avoid the change of tritium chemical form. About 200g of FLIBE was heated up to 600°C in the Al₂O₃ crucible (44mm in inner diameter, 200mm in inner depth and 5mm in thickness) installed in the sample container. It was considered FLIBE reacts with water as (BeF₂+H₂O → 2HF + BeO) at high temperature to generate HF, which increases F-potential in the system, because the sample had absorbed a small amount of water. So the dehumidification time of FLIBE is an important parameter which influences F-potential in the system.

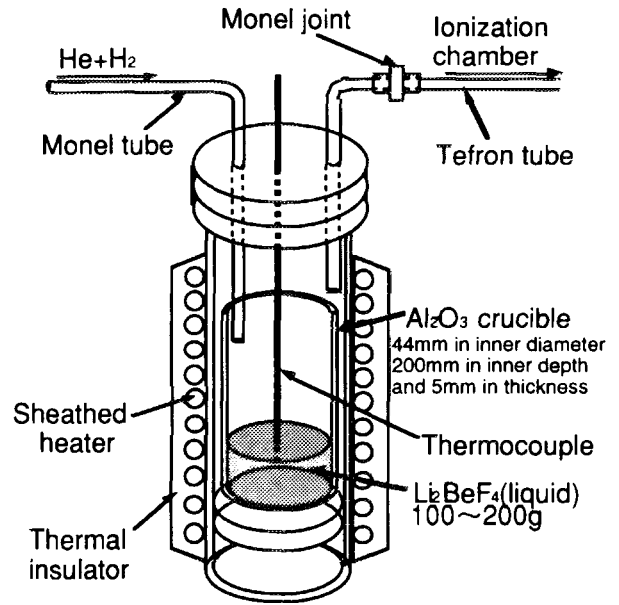


Fig.2 Cross section of Monel (Ni70%-Cu30%) sample container.

RESULTS AND DISCUSSION

Chemical form of released tritium was investigated with changing purge gas composition, dehumidification time and sample container and tubing materials. In case of H₂ purge gas and He+1%H₂ purge gas at 873K, HT was the main chemical form, while the main chemical form of released tritium after short dehumidification time (3-5 days) with He purge gas at 873K was mainly TF. After long dehumidification time with He purge gas, however, the main chemical form of released tritium changed to HT.

Table 1 Summary of chemical forms

dehumidification time	purge gas composition		
	H ₂	He +1%H ₂	He
3-5 days	mainly HT (+TF)	mainly HT (+TF)	TF
24-26 days	HT	mainly HT (+TF)	mainly HT (+TF)

A trace of hydrogen existed in the experimental system even in case of pure He purge gas as an impurity in the He purge gas and in the specimen. Probably, hydrogen was larger in concentration than the generated tritium in this experiment, because the tritium generation rate was very small. Table 1 shows the summary of the chemical forms of released tritium. The chemical forms of released tritium from FLIBE were HT and TF, depending on purge gas composition and dehumidification time of the specimen. TF was released only in case of low H concentration (He purge gas) and high F-potential (short dehumidification time) in the system. From these facts, tritium generated as T⁺ in FLIBE was released by way of two routes ; (1) direct release to purge gas as TF and

(2) release to purge gas after converted to HT by the isotopic exchange reaction (T⁺ + H₂ → HT + H⁺). The chemical form of tritium was determined by the activity of H₂ and H⁺ (F-potential) in FLIBE, and the thermodynamic equilibrium of the isotopic exchange reaction could be controlled by the H₂ concentration and HF concentration in the system, as shown in Fig. 3.

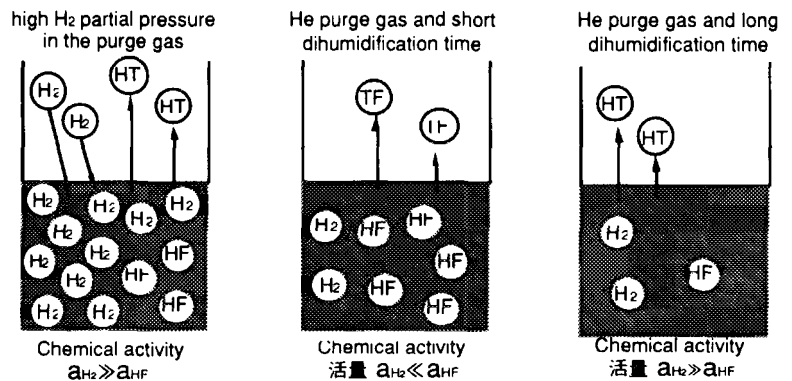
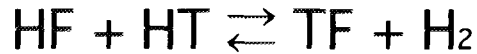


Fig.3 Mechanism of chemical form change of tritium

Bi-2212 単結晶の臨界電流密度に対する 520 MeV Kr²⁰⁺イオン照射効果

Effect of 520MeV Kr²⁰⁺ Ion Irradiation on the Critical Current Density of Bi-2212 Single Crystals

寺井隆幸、伊藤康行、岸尾光二* (システム量子工学科、応用化学科*)

Takayuki TERAJ, Yasuyuki ITO and Kouji KISHIO*

Department of Quantum Engineering and Systems Science, Department of Applied Chemistry*

ABSTRACT

Change in magnetic properties of Bi₂Sr₂CaCu₂O_{8+y} (Bi-2212) single crystals due to Kr²⁰⁺ ion irradiation is reported, focused on critical current density and irreversibility magnetic field. The Bi-2212 single crystal specimens (3x3x0.3mm³) were prepared by the floating zone method. Each specimen was irradiated with 520MeV Kr²⁰⁺ ions of 10¹⁰-10¹¹ cm⁻² in the fluence. Magnetic hysteresis was measured at 4.2K-60K with a vibrating sample magnetometer before and after irradiation. Very large enhancement was observed in critical current density and irreversibility magnetic field above 20K.

Particle-beam irradiation is one of the most promising methods to introduce strong pinning centers into High-Tc superconductors. It has been reported that the critical current density (J_c) is enhanced by the irradiation of high-energy particles such as ions, neutrons and electrons^{[1]-[3]}. In particular, high energy heavy ions are expected to produce columnar defects of a diameter close to the coherence length, which give a very large pinning force for vortices parallel to defects. In order to realize a particle-beam irradiation technique as a method for J_c enhancement, many different conditions such as the kind, the energy and the fluence of particles should be examined. We have been studying magnetic property change due to irradiation with several kinds of particles such as ions, neutrons and electrons on Bi₂Sr₂CaCu₂O_{8+y} (Bi-2212) single crystal. In this paper, we show experimental results below 60K on the critical current density (J_c) of Bi-2212 single crystal irradiated with 520MeV Kr²⁰⁺ ions.

The Bi-2212 single crystal specimens used were prepared by the floating-zone method (FZ). Their size was 2mmx2mmx50-80μm. The specimens were irradiated with 520MeV Kr²⁰⁺ ion beam parallel to the c-axis with an AVF cyclotron at JAERI, Takasaki. The fluences were 1x10¹⁰, 5x10¹⁰ and 1x10¹¹ cm⁻² corresponding to the matching field of 0.2T, 1T and 2T, respectively. Magnetization curves of the specimens before and after irradiation were measured with a vibrating sample magnetometer at 4.3K, 20K, 40K and 60K as a function of applied magnetic field up to 7.5T parallel to the c-axis with the sweep rate of 1mT·s⁻¹ to 20mT·s⁻¹. The critical current density was calculated from the magnetization hysteresis using the modified Bean's model.

The magnetic field dependence of critical current density (J_c) calculated from the magnetic hysteresis is shown in Fig. 1. Figure 2 shows the fluence dependence of J_c in typical conditions of temperature and magnetic field. The critical current density increased due to the irradiation all over the range of temperature and magnetic field investigated except 4.3K. At the temperature of 4.3K, J_c decreased with fluence. Above 40K, on the other hand, the J_c took a maximum value at the fluence of 1.0x10¹⁰ cm⁻² or 5.0x10¹⁰ cm⁻². The enhancement ratio of J_c mainly depended on temperature and it was larger at the relatively high temperatures of 40 and 60K. The little change in the low temperature of 4.3K means that a kind of defects existing in the specimen before irradiation can act as effective pinning centers even after irradiation at such a low temperature. On the other hand, the very large increase in the relatively high temperatures of 20, 40 and 60K indicates that contribution of radiation-induced defects is dominant after irradiation. Figure 3 shows the irreversibility field, where J_c disappears, increased with fluence at 40K and 60K.

REFERENCES

- [1] K. Kusagaya et al., Proc of ISS'93, 555-558 (1994).
- [2] W. Gerhäuser et al., Physica C 185-189, 2339-2340 (1991).
- [3] B. Chenevier, Jpn. J. Appl. Phys. 31, L777-L779 (1992).

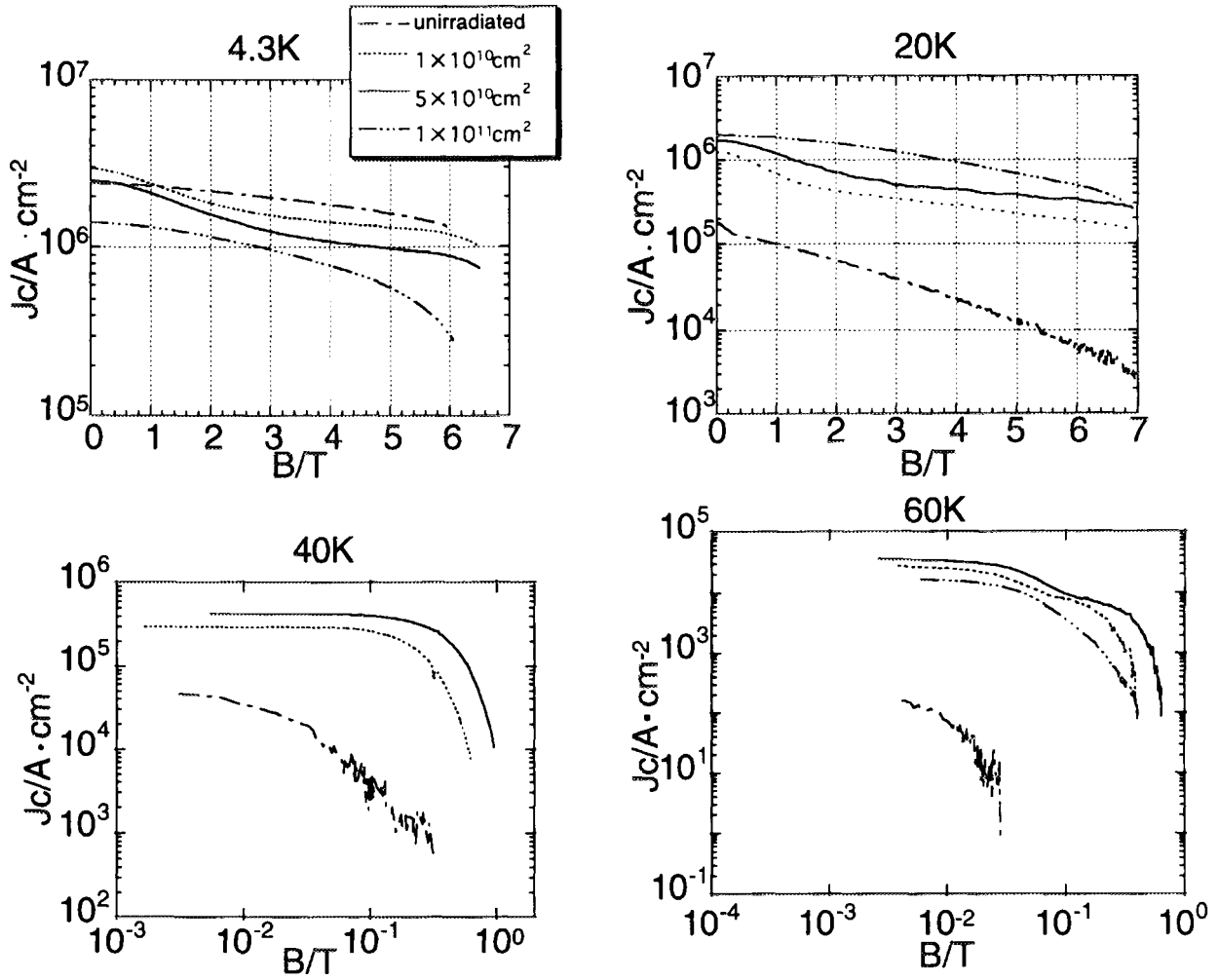


Fig. 1 Magnetic field dependence of J_c on Bi-2212 single crystals irradiated with 520MeV Kr ions.

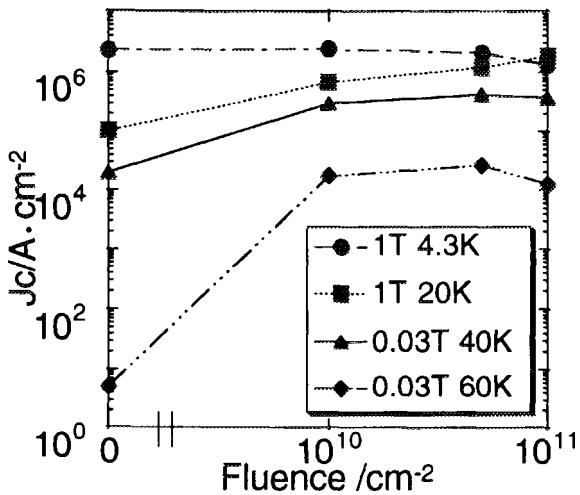


Fig. 2 Dependence of 520MeV Kr ion fluence on J_c of Bi-2212 single crystals.

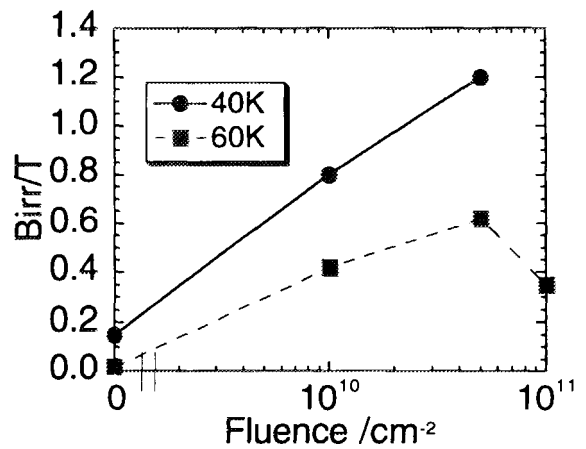


Fig. 3 Dependence of 520MeV Kr ion fluence on irreversibility field of Bi-2212 single crystals

絶縁性セラミックスの放射線照射による特性劣化

小林知洋 寺井隆幸 米岡俊明 田中知 (工学部システム量子工学科)

Degradation of insulating ceramics due to irradiation

Tomohiro KOBAYASHI, Takayuki TERAJ, Toshiaki YONEOKA and Satoru TANAKA

Department of Quantum Engineering & Systems Science

ABSTRACT

Radiation-induced electrical degradation was investigated on single crystal alumina under 2.2 MeV electron irradiation with a dose rate of 5.7×10^5 Gy/s and an electrical field of 1.6×10^5 V/m at 773 K. After irradiation, electrical resistivity both on the surface and in the bulk decreased in the temperature range of 300 to 773 K. Substantial resistivity decreased from the initial value due to the irradiation, the degradation ratio was much smaller than the case of poly-crystalline specimens. On the other hands, surface resistivity decreased with increasing temperature for measurement with an abrupt change by 4 orders of magnitude around 600 K, and it showed thermal hysteresis.

1. Introduction

Alumina is widely utilized as an insulating ceramic material because of its high physicochemical stability and quite high electrical resistivity, and it has also a potential to be utilized in systems with high energy density such as fusion reactor systems. In this case, property change under irradiation is very important. In fusion reactor systems, insulating ceramics are utilized under complex condition of electric field (10^2 - 10^7 V/m), irradiation (10 - 10^3 Gy/s) and high temperatures (350 - 800 K). In such conditions, radiation-induced electrical degradation (RIED) becomes a problem. Though several groups have been investigating this phenomenon using several kinds of irradiation such as electron, neutron and high-energy ion beams for Al_2O_3 pol crystalline specimens, it has not been clarified whether it is a bulk phenomenon or a surface phenomenon. In this study, we measured the electrical resistivity change after electron irradiation at an elevated temperature with an electrical field, in particular, not for polycrystalline specimen but for single crystal specimen of Al_2O_3 .

2. Experimental

The specimen was a disk (10 mm in diameter and 0.5 mm in thickness) of single crystal Al_2O_3 in the optical grade. The face of the crystal disk was (11 $\bar{2}$ 0) plane. It was irradiated with a 2.2 MeV electron beam from a Dynamitron accelerator of the University of Tokyo at 773 K in air with an applied electric field. The current density was $1.8 \mu\text{A}/\text{cm}^2$ at the specimen. The absorption dose rate was calculated to be 5.7×10^3 Gy/s. The specimen was attached to the surface of a heater drum with silver paste and aluminum was deposited on both sides of the surface as electrodes. The temperature of the specimen observed with the thermocouple was elevated by 30 - 40 K during electron irradiation. The applied voltage was 80 V DC and the electric field was 1.6×10^5 V/m. Irradiation was carried out for three times and the integrated absorption dose was 2.9×10^8 Gy.

The resistivity was determined by measuring current under an applied voltage by two methods; (a) direct measurement for current with a vibrating reed capacitor type ammeter and (b) measurement for voltage drop in a standard resistance. In the measurement, separation of the measured current into substantial current and surface current is very important. The former is smaller by 4 - 6 orders of magnitude than the latter, and it cannot be measured by the usual method. In this study, thus, a substantial current was measured using a guard ring system.

Because the substantial resistivity of alumina is very large at room temperature, a vibrating reed capacitor type ammeter was used for the measurement of a current to 1×10^{-14} A. In the measurement at elevated temperatures, on the other hand, a normal voltmeter was utilized, because the current was too large for the vibration reed capacitor type ammeter, which cannot respond to an abrupt change of current. In this case, the noise level in substantial current measurement was so large that the detection limit of the current was 10^{-8} - 10^{-9} A. On the other hand, surface current was

measured by the normal method. Before measurement, the specimens were cleaned with an ultrasonic cleansing machine to avoid the effects of surface contamination and adsorbed species.

3. Results and discussion

3.1 Substantial resistivity

The resistivity obtained from the results in the substantial current measurement is shown in Fig.1. For an unirradiated specimen, substantial current could be measured at room temperature using a vibrating reed capacitor type ammeter, while at elevated temperature, the current could not be measured because of large noise. The value of resistivity at room temperature decreased by 2 - 3 orders of magnitude due to the irradiation. The substantial resistivity after irradiation decreased to the level of $10^4 \Omega\text{m}$ with increasing temperature to 773 K.

This result is quite different from that of polycrystalline Al_2O_3 specimen reported by Hodgson. He claimed that a very large reduction in resistivity of more than 5 orders of magnitude was observed even at elevated temperatures. This discrepancy may derive from the existence of grain boundaries, which may play an important role for electron conduction with structural change due to the irradiation.

3.2 Surface resistance

In actual condition for utilization, the surface conduction is more important than the substantial conduction because the former is much larger in current than the latter. One of the results of the measurement is shown in Fig.2. When the specimen was warmed with a rate of 3 K/min, in a narrow temperature region, the resistance decreased abruptly by 4 orders of magnitude. This occurred around 600 K and the beginning point was different in each measurement. After the decrease, resistance was almost independent of temperature. In this temperature region, current was in fluctuation with 10 % changes in long periods and 30 % changes in short periods. In cooling at a rate of 2 K/min, the resistivity increased also abruptly as indicated with a dashed line in Fig.2. This temperature always tended to be lower by 50 - 80 K than that in warming. This temperature difference is larger than that expected from the system between warming and cooling.

These thermal hysteresis may be a characteristic phenomenon in the surface conduction of single crystal specimens, whose surface is very different from that of polycrystalline specimens in structure. The mechanism of this anomalous behavior is not clear, but it may come from a kind of feedback effect. If the resistivity of a part of the surface decreases with temperature, an excess current flows at the region. As a result, local heating occurs and it decreases the resistivity. In this mechanism, some conduction paths are finally formed on the surface, and a steady current comes to flow. Because this behavior was not observed for an unirradiated specimen, surface contamination such as diffusion of electrode material enhanced by irradiation at high temperature may be the cause.

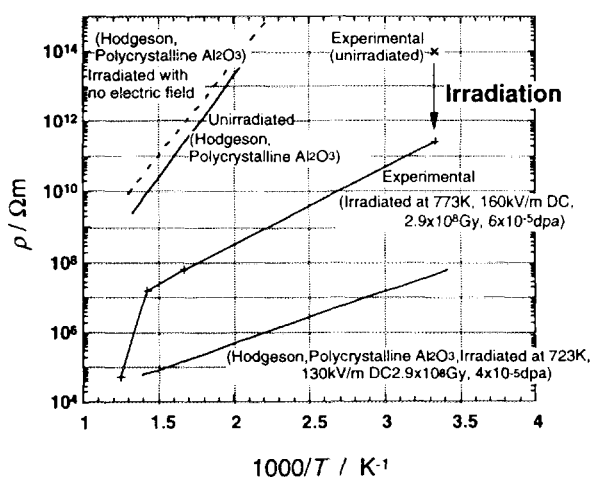


Fig.1 Temperature dependence of substantial resistivity of electron-irradiated and unirradiated specimens of Al_2O_3 .

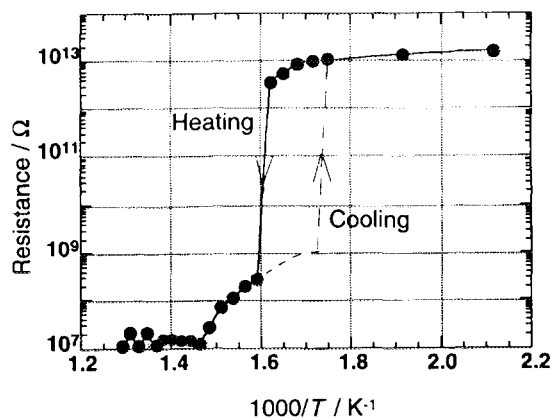


Fig.2 Temperature dependence of surface resistance of 2.2 MeV electron irradiated specimen of single crystal Al_2O_3 with a dose of $5.7 \times 10^8 \text{ Gy/s}$ at 773 K.

Futaba Ono , Michio Yamawaki
 University of Tokyo,
 2-22,Shirakata-Shirane,
 Tokai-mura,Ibaraki,
 319-11, Japan
 +81-292-87-8432

Satoru Tanaka
 University of Tokyo,
 7-3-1,Hongo,
 Bunkyo-ku, Tokyo,
 113, Japan
 +81-3-3812-2111(ext 6968)

ABSTRACT

Regrowth in tritium desorption from type 316 stainless steel, copper and borosilicate glass was studied. It was found that the tritium, which was penetrated into materials by long term contact, could not be easily desorbed by a stream of nitrogen gas (dry, wet or 10 % H₂) at room temperature.

The ratio of the tritium amount desorbed from surface by each purging to the tritium concentration in the gaseous phase under the sorption /desorption equilibrium on the surface was found to be constant through the repeated desorption. The amount of tritium desorbed by each gas purging was found to decrease by repeated desorption.

I. INTRODUCTION

Elemental tritium (T₂) at high concentration may be present in tritium extraction plants, plasma burning experiments and tritium - handling facilities. Knowledge on tritium release and retention in materials after exposure to T₂ enables the procedures for clean up and handling of contaminated surfaces and materials. In a tritium removal system for glove box, experimental room, and in a large scale reactor hall, the so-called soaking effect is a matter of problem, which is sorption of tritium gas or tritiated water vapor by various materials and subsequent reemission from them. In simulating a detritiation system or estimating a required detritiation time, database on tritium sorption and

desorption on and from various materials is essential ^{1,2}. Limited studies have been reported on tritium sorption and desorption on construction materials ³, paints ⁴, cement ⁵ and surface of a glove box ⁶.

Furthermore, stainless steel, copper and glass pipes are often used as the piping materials of experimental apparatus. If these materials are exposed for a long time to a highly concentrated tritium, tritium is sorbed by the materials and becomes difficult to be desorbed, removed or decontaminated. It is well known that the tritium contamination on the surface of materials increases in a certain period after decontaminated by the swipe or gas purging methods. HT can be converted to the radiologically much more hazardous tritium oxide (HTO) ⁷, during this process. It is also pointed out that uptake of tritium occurs through skin by contacting with tritium-contaminated surfaces ^{8,9}. Thus, the regrowth phenomenon is very important for safety handling and containment of tritium.

In the present paper, the regrowth phenomena of tritium from stainless steel, copper and glass, which were contacted with tritium gas for about one and half year were studied. The effect of the sweep-gas chemical composition on desorption and decrease in surface tritium concentration by repeated desorption was also studied.

II. EXPERIMENTAL

Type 316 stainless steel, copper, and borosilicate glass in the shape of pipes (~30 cm² in surface area) had been

exposed to the tritiated gas ($\sim 1.1 \times 10^7$ Bq/cm³) for about one and half year in the contact vessel made of glass at room temperature. The tritium contaminated specimens were put in the reaction vessel (~ 23 cm³ in volume) made of stainless steel. They were stored at room temperature. The sample were swept by purging gas (dry, wet and N₂ + H₂ (10%)) for about 2 hours at prescribed intervals. The tritium concentration in the swept gas was measured by an ionization chamber (100 cm³) + vibrating reed electrometer.

The holding period between the two desorption processes were about a few days at initial runs and two to three weeks after about ten runs. Flow rate of the purging gas was 100 cm³/min. Repeated desorption was conducted about 15 times and total period for them was about five months.

III. EXPERIMENTAL RESULTS AND DISCUSSION

A. Regrowth phenomena

An example of the repeated desorption is shown in Fig. 1. The tritium concentration in the purge gas is plotted against the elapsed time for the each repeated desorption. As shown in this figure, the initial tritium concentration for the each repeated desorption is higher than the final tritium concentration in the previous run. This shows the regrowth of tritium between the two desorption runs.

B. Evaluation

of the apparent desorption rate constant

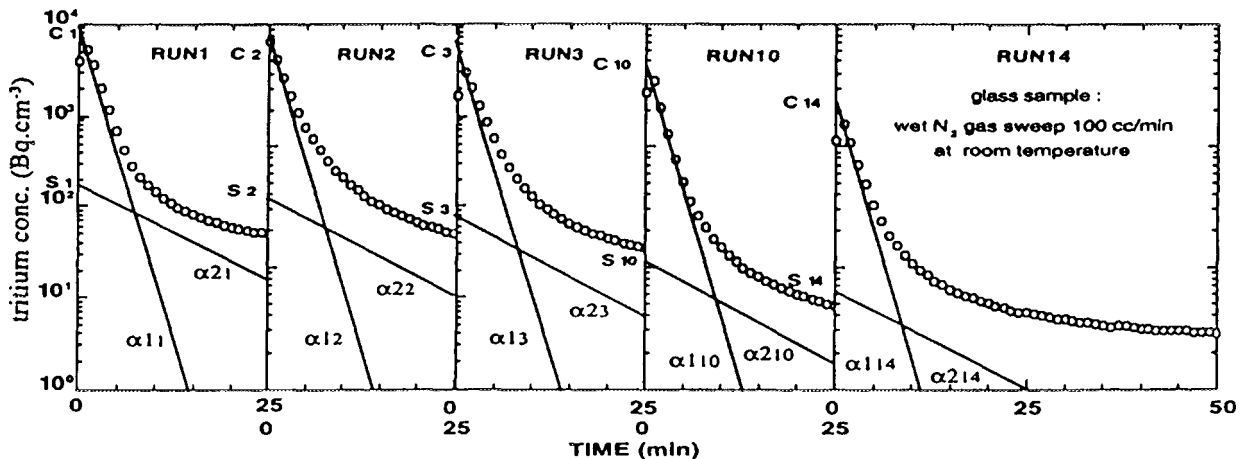


Fig. 1 Regrowth of tritium activity by repeated desorption

An example of tritium concentration in the purge gas for one desorption run is shown in Fig. 2.

The decay of tritium concentration Tn in the purge gas can be expressed by three components,

$$T_n = C_n e^{-\alpha_1 t} + S_n e^{-\alpha_2 t} + X_n e^{-\alpha_3 t} \quad \text{----- (1)}$$

at t=0, Tn = Cn + Sn + Xn.

The first term corresponds to the exhaust of tritium in the chamber by gas purging because alpha1 was found to be independent of materials and can be expressed by the flow rate and the chamber volume. The second term is considered to be the tritium desorbed from the surface of sample and the third term tritium diffused out of the bulk to the surface during this desorbing process.

In Fig. 2, the intercepts at the Y axis indicate the initial concentrations Cn, Sn and Xn for each component.

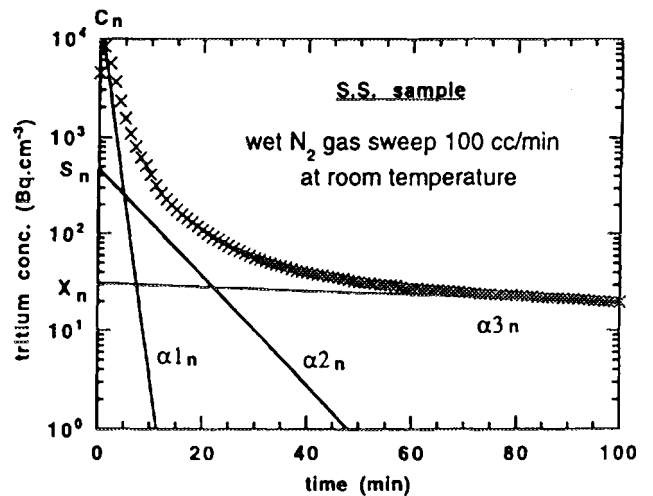


Fig. 2 An example of tritium activity in the purge gas during desorption for stainless steel.

Slopes, α_2 and α_3 , are the apparent desorption rate coefficients for the second and the third component, respectively. C_n is considered to be the equilibrium tritium concentration in the gas phase contacting with tritium contaminated materials. S_n is considered to be the tritium amount desorbed from the surface by each purging process. By using the surface area of the sample, the volume of the chamber and the purge-gas flow rate, equilibrium concentration on the surface can be calculated from S_n .

Fig. 3 shows elapsed time dependence of the apparent desorption coefficients α_2 and α_3 . α_1 is also plotted for comparison. The values of α_2 were found to be constant through the repeated desorption. This means that the tritium desorption rate is independent of the desorption run number, or the desorption mechanism does not vary from desorption to desorption. Some scatter was found for α_3 , this was considered to be caused by low concentration and the influence of desorbing period.

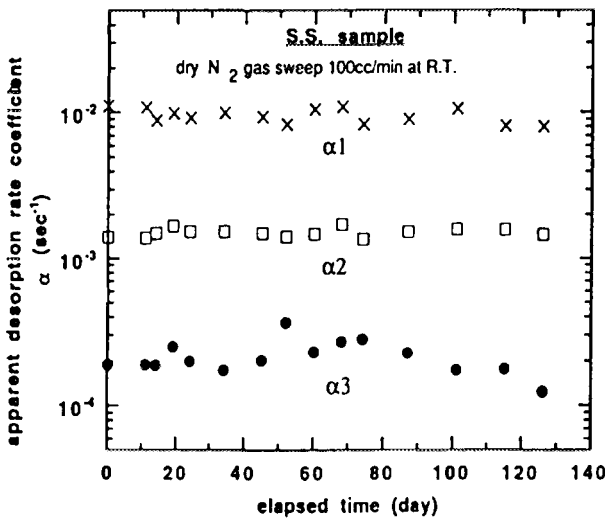


Fig. 3 Elapsed time dependence of apparent desorption coefficient

Fig.4 shows the apparent desorption rate coefficients for the materials and the purge-gas tested. The values of the coefficients were evaluated by averaging the desorption rate coefficients of all the desorption runs. It was found that α_2 for the wet sweep gas was larger than the other sweep gas. This indicates the effect of exchange reaction with H_2O .

C. Evaluation of the equilibrium sorption coefficient

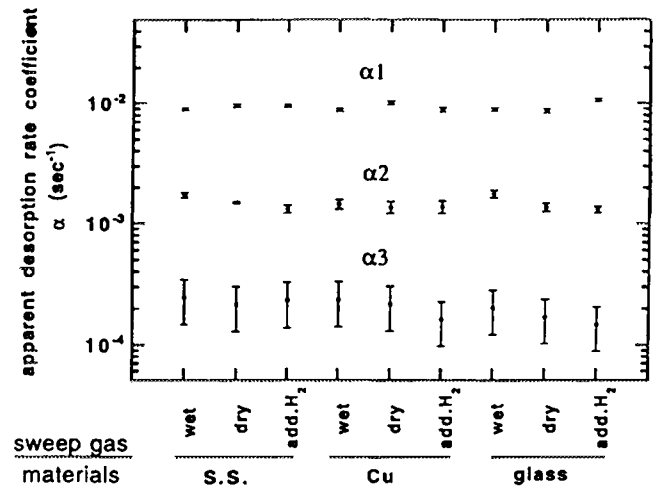


Fig. 4 Sweep gas and material dependence of apparent desorption rate coefficient.

As explained before, S_n is the amount of surface tritium desorbed by the n -th gas purging and C_n is the equilibrium tritium concentration in the gaseous phase. Moreover, S_n is considered to be proportional to the equilibrium amount of tritium sorbed on the surface. Therefore the ratio S_n/C_n is considered to be proportional to the equilibrium sorption coefficient. In this paper, this ratio was named as the apparent sorption coefficient.

Figure 5 shows a typical plot of the dependence of the apparent sorption coefficient on the sampling period, the time between the two succeeding purging runs. This figure indicates that the tritium concentration between the gas phase

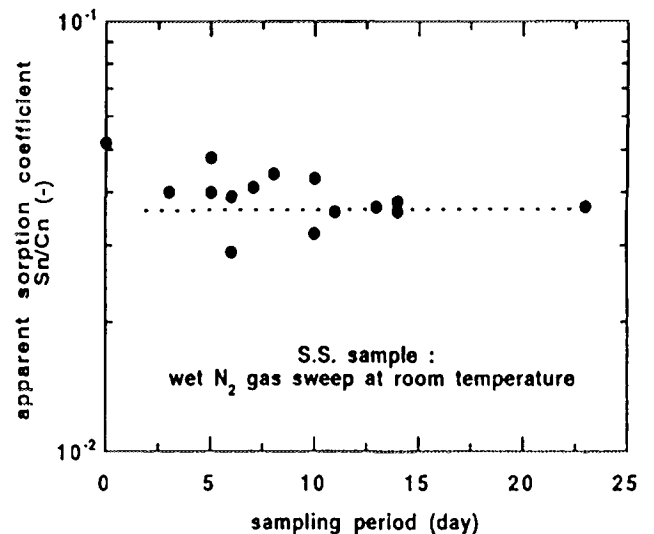


Fig. 5 Sampling period dependence of apparent sorption coefficient.

and the specimen surface becomes equilibrium after a holding period of a few days. The averaged apparent sorption coefficient for the all materials and the purge - gas tested are shown in Fig. 6. In the case of glass, it was found that the

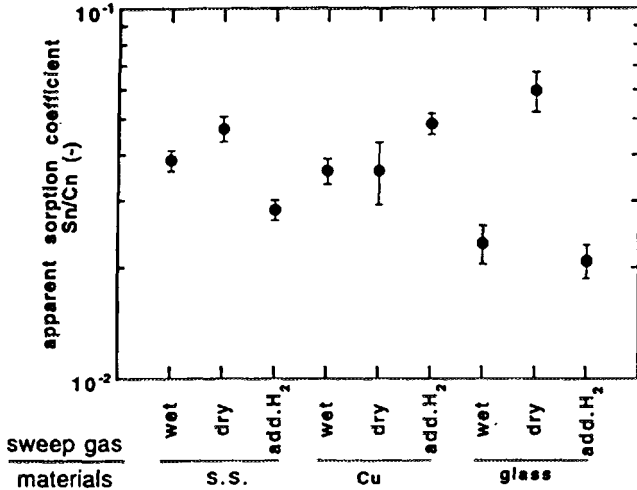


Fig. 6 Averaged apparent sorption coefficient for S.S. Cu and glass

effect of the sweep gas chemical composition is larger than the other materials. The sorption coefficients in glass and S.S. for dry sweep gas were found to be larger than those for the other gases. Surface of stainless steel and glass is considered to be oxide such as Cr₂O₃ or SiO₂. Tritium release is considered to be enhanced by exchange reactions with H₂O or H₂ on the surface, such as



This enhanced desorption from the surface to the gas phase causes lower sorption coefficient.

On the other hand, surface of copper is considered to be clean or oxide layer is thin.

D. Decrease of the tritium amount desorbed by repeated purging

Figure 7 shows the plotting of the desorbed tritium amount Sn by each purging against the run number. At the beginning to run number of about ten, linear relationship was observed. The holding period between the two desorption processes was a few days at the initial runs to about ten and two or three weeks after this. During the desorption processes, tritium is considered to migrate from the bulk to the surface. Therefore desorbed tritium per holding time, Sn/day, (D) is

considered to be more appropriate than Sn. Figure 8- 10,

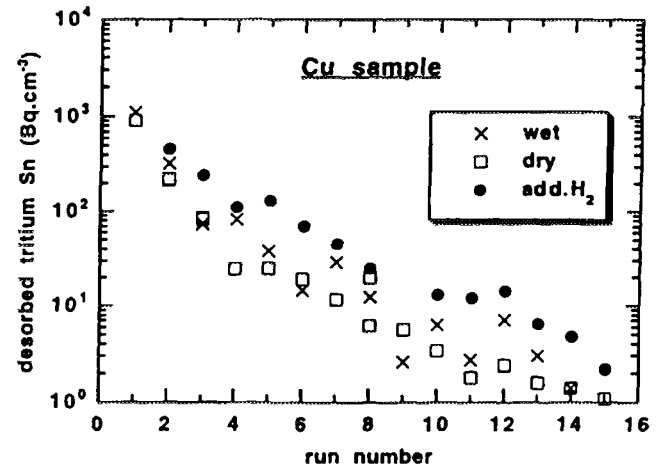


Fig.7 Run number dependence of desorbed tritium amount by repeated desorption for copper

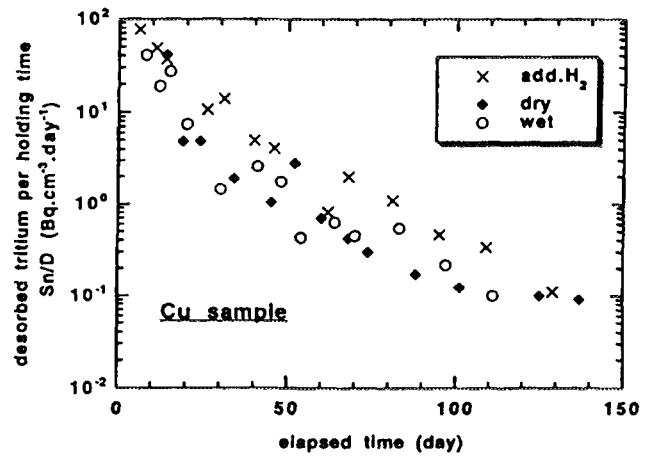


Fig. 8 Elapsed time dependence of desorbed tritium amount per holding time by repeated desorption for Cu

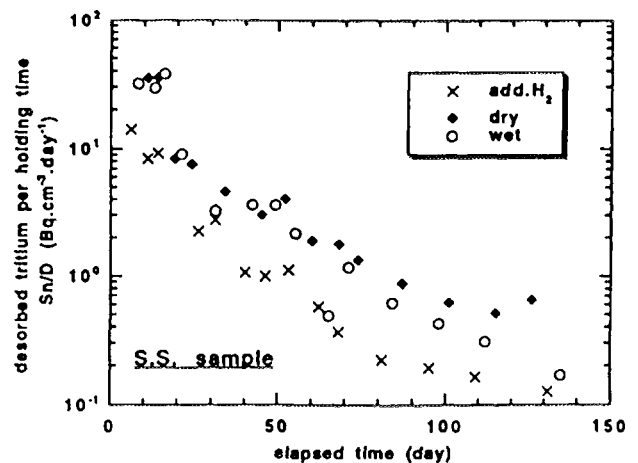


Fig. 9 Elapsed time dependence of desorbed tritium amount per holding time by repeated desorption for S.S.

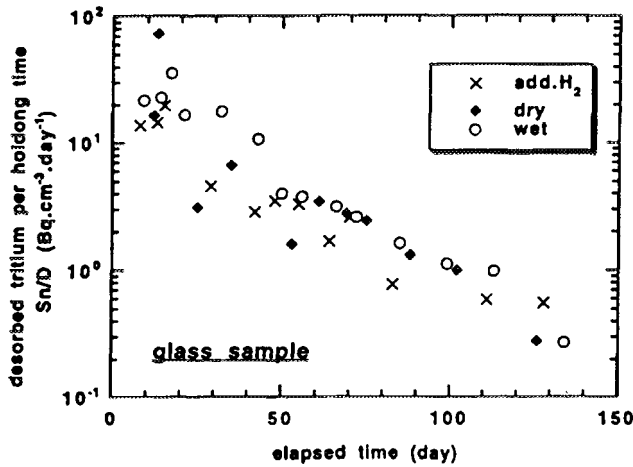


Fig. 10 Elapsed time dependence of desorbed tritium amount per holding time by repeated desorption for glass

show the S_n/D against the elapsed time from the beginning of first desorption. Linear relationship was found in a wider range than in Fig.7. From the linear relationship $\log S_n = a - bn$, where n is the desorption run number, in the period of about 10 -100 days, the slope b was calculated. Table 1 shows the evaluated slopes for the tested materials and the sweep gas.

The slope for glass was found to be smallest. In the same material, the slope for the wet sweep gas was found to be largest. The slope is considered to be affected by the tritium migration velocity from the inner part or bulk to the surface. In the previous experiment ¹², it was found that tritium penetrates deeper in glass than in S.S. and copper. In all

Table 1 Value of the slope b in the fitting of $\log S_n = a - b \cdot n$

N_2 sweep gas	glass	S.S.	Cu
	(elapsed time:day ⁻¹)		
add.H ₂	0.0303	0.0399	0.0509
dry	0.0352	0.0363	0.0449
wet	0.0394	0.0442	0.0537

materials, tritium was found to penetrate more than 25 μm . But the concentration at the few μm depth from the surface was

found to be about three orders of magnitude smaller than that at the surface for glass. But for copper it was about six orders of magnitude and for stainless steel about four orders of magnitude. Slower tritium diffusion in glass is also considered to be one of the reasons.

Fig. 8,9 shows that the decreasing rates become smaller in the longer elapsed time than 100 days. This is considered to show the different tritium migration or trapping mechanism.

IV. CONCLUSIONS

Tritium regrowth phenomena were studied by repeated desorption by gas purging. Following conclusions were obtained by these studies.

(1) For the materials contacted with high - concentration of tritium for a long period, tritium regrowth was found in a short time after desorption by gas purging.

(2) It was proved that apparent desorption rate coefficient for each desorption process is constant through out the repeated desorption and is susceptible to the component of the sweep gas. Wet gas sweeping hastened the desorption rate by exchange reaction.

(3) From the estimated equilibrium tritium concentration in the atmosphere and the tritium desorbed from the surface for each desorption process, the equilibrium sorption coefficient was evaluated. It was found that this coefficient became constant if the holding time between the two desorption processes was longer than a few days. Equilibrium sorption coefficient for 10% H₂ added N₂ is the smallest on glass and stainless steel samples but the largest in the case of copper sample.

(4) The tritium amount S_n desorbed by each purging was found to decrease by repeated desorption. The relation of $\log S_n = a - bn$ was obtained at the beginning, where n is the desorption run number. The magnitudes of the decreasing rate (b) was in the order of $\text{Cu} > \text{S.S.} > \text{glass}$.

REFERENCES

1. S. Tanaka, F. Ono, T. Masegi and Y. Takahashi, "Simulation of Soaking Effect in Air Detritiation System," *Fusion Eng. Design.*, 7, 353 (1989).

2. R. G. Clemmer, R. H. Land, V. A. Maroni and J. M. Mintz, "Simulation of Large Scale Air Detritiation Operations by Computer Modeling and Bench-Scale Experimentation," *Proc. Seventh IEEE Symp. Eng. Prob., Fusion Res.*, p.1653 (1982).
3. F. Ono, S. Tanaka and M. Yamawaki, "Sorption and Desorption of Tritiated Water on Paints," *Fusion Technol.*, **21** (2) 827 (1992).
4. R. S. Dickson and J. M. Miller, "Sorption of Tritium and Tritiated Water on Construction Materials," *Fusion Technol.*, **21** (2) 850 (1992).
5. F. Ono, S. Tanaka and M. Yamawaki, "Tritium Sorption by Cement and Subsequent Release," *Fusion Eng. and Design*, **28**, 378 (1995).
6. F. Ono, S. Tanaka and M. Yamawaki, "Sorption of Tritiated Water on Organic Materials and Subsequent Desorption," *Fusion Technol.*, **21**, 1964 (1992).
7. C. J. Sienkiewicz, "Tritium Surface Concentration," *Fusion Technol.*, **8**, 2444 (1985).
8. R. A. Surette and R. G. C. McElroy, "Regrowth, Retention and Evolution of Tritium from Stainless Steel," *Fusion Technol.*, **14**, 1141 (1988).
9. J. R. Johnson and B. F. Peterman, "Metabolism of Tritium Uptake due to Handling of Metal Surfaces Exposed to Tritiated Hydrogen Gas," *CFFTP-G-87026/AECL-9518* (1987).
10. M. Saeki and T. Hirabayashi, "Sorption Mechanism of Tritium on the Surface of Borosilicate Glass," *Radiochim. Acta.*, **35**, 233 (1984).
11. T. Hirabayashi, M. Saeki and E. Tachikawa, "Sorption and Desorption of Tritium on the Surface of Type 316 Stainless Steel," *Int. Symp. on Fusion Reactor Blanket and Fuel Cycle Technol.*, Oct. 27-29, 1986, University of Tokyo, Tokaimura, Japan.
12. F. Ono, "Experimental research on sorption/desorption for safety handling of tritium," *Doctoral thesis*, University of Tokyo, 1994.

重イオン照射によるバナジウムの欠陥クラスター形成に対する
カスケード損傷効果の効果

関村 直人、白尾 泰之（システム量子工学専攻）
森下 和功（原子力工学研究施設）

A Study of Defect Cluster Formation in Vanadium by Heavy Ion Irradiation

Naoto SEKIMURA, Yasuyuki SHIRAO and Kazunori MORISHITA

Formation of defect clusters in thin foils of vanadium was investigated by heavy ion irradiation. In the very thin region of the specimens less than 20 nm, vacancy clusters were formed under gold ion irradiation, while very few clusters were detected in the specimens irradiated with 200 and 400 keV self-ions up to 1×10^{16} ions/m². The density of vacancy clusters were found to be strongly dependent on ion energy. Only above the critical value of kinetic energy transfer density in vanadium, vacancy clusters are considered to be formed in the cascade damage from which interstitials can escape to the specimen surface in the very thin region.

1. Introduction

In BCC metals, cascade damage results in very low density of defect clusters in irradiated specimens compared with FCC metals [1]. Vanadium alloys are attractive candidate materials for fusion structural materials because of their excellent low induced activities in addition to mechanical properties at elevated temperatures. The effect of helium on irradiation behavior of vanadium alloys has been extensively studied for example by DHCE (Dynamic Helium Charging Experiments) and tritium trick techniques. However, very limited data are available for fundamental defect production behavior in vanadium. Recently molecular dynamic simulation of cascade damage from high energy PKA (Primary Knock-on Atom) has successfully demonstrated that defect production behavior in vanadium [2].

In the present study, thin foils of pure vanadium were irradiated with self-ions and heavy ions to investigate defect cluster formation by cascade damage to understand correlation rules for vacancy clustering.

2. Experimental

Thin foils of 99.9% pure vanadium were annealed at 1173 K for 1 hr in high vacuum followed by furnace cooling. These specimens were electro-polished to get thin foils for TEM observation. They were irradiated with 200 and 400 keV self-ions (V⁺) up to 1.0×10^{16} ions/m² at room temperature. This foil samples were also irradiated with heavier ions (50 - 400 keV Au⁺, 1×10^{16} ions/m²) at room temperature.

Irradiated specimens were observed by TEM operated at 200 kV.

3. Results and Discussion

Very few clusters were detected in the specimens irradiated with 200 and 400 keV self-ions up to 1×10^{16} ions/m². However, gold ion irradiation produced visible defect clusters in thin foils of vanadium. The density of vacancy clusters were found to be strongly dependent on ion energy. Figure 1 shows specimen thickness dependence of areal density of observed clusters. Density of

observed cluster images was found to decrease with thickness. In the thicker region of the specimens, interstitial clusters are formed, considering the depth distribution of displacement damage deposition by gold ions. However, in the very thin region of the specimens less than 20 nm, vacancy clusters were formed under gold ion irradiation.

Figure 2 shows cluster density per damage energy by gold ion irradiation. In very thin region of the specimens, cluster density was found to increase linearly with deposited energy.

From these results, vacancy clusters are considered to be formed in the cascade damage from which interstitials can escape to the specimen surface in the very thin region, only above the critical value of kinetic energy transfer density in vanadium,

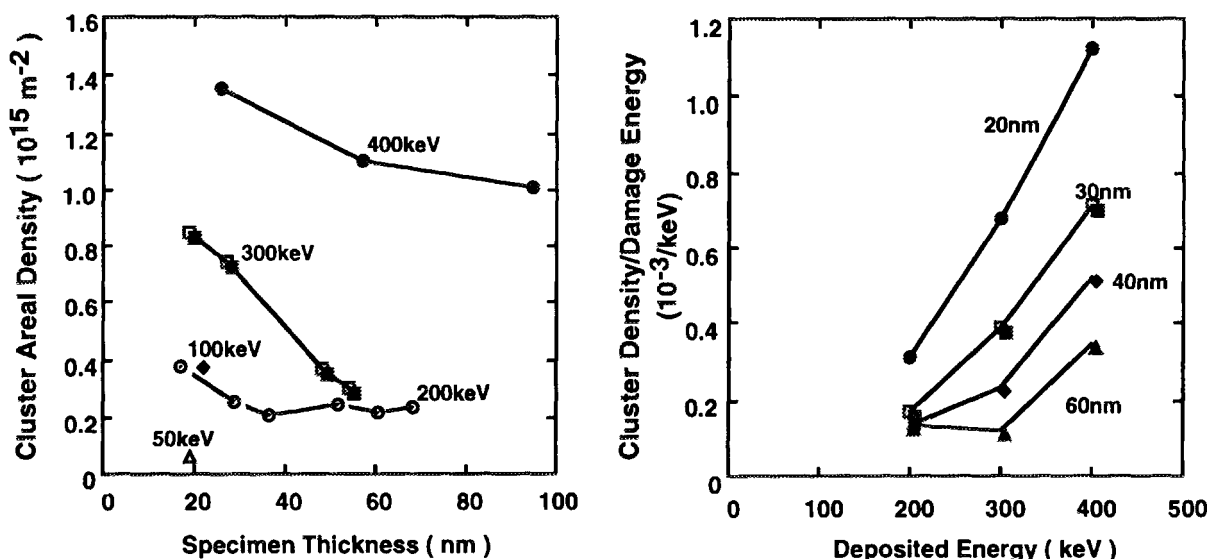


Figure 1 Thickness dependence of observed defect cluster density in thin foils of vanadium irradiated with 50 - 400 keV gold ions to 1.0×10^{16} ions/m².

Figure 2 Ion energy dependence of defect cluster density per damage energy in thin foils of vanadium irradiated with 50 - 400 keV gold ions to 1.0×10^{16} ions/m².

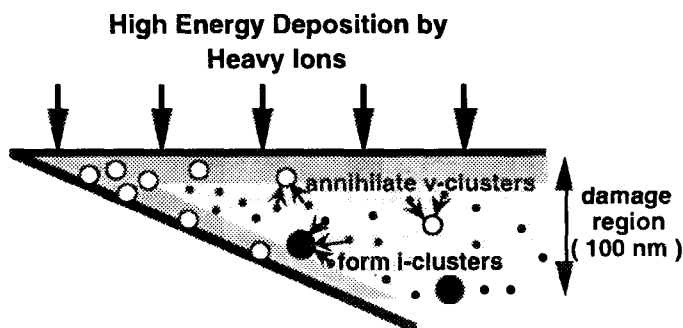


Figure 3 Schematic representation of defect cluster formation in thin foils of vanadium irradiated with gold ions

4. Reference

- [1] N. Sekimura, Y. Kanzaki, S. Okada, T. Masuda and S. Ishino, J. Nucl. Mater. 212-215 (1994) 160-163.
- [2] K. Morishita and T. Diaz de la Rubia, to be published.

重イオン照射によるバナジウム合金のミクロ組織・組成変化の研究

関村 直人、柿内 宏憲、白尾 泰之（システム量子工学専攻）
岩井 岳夫（原子力研究総合センター）

Microstructural and Microchemical Evolution in Vanadium Alloys by Heavy Ion Irradiation

Naoto SEKIMURA, Hironori KAKIUCHI, Yasuyuki SHIRAO and Takeo IWAI

Microstructural and microchemical evolution in vanadium alloys were investigated using heavy ion irradiation. No cavities were observed in V-5Cr-5Ti alloys irradiated to 30 dpa at 520 and 600°C. Energy dispersive X-ray spectroscopy analyses showed that Ti peaks around grain boundaries. Segregation of Cr atoms was not clearly detected. Co-implanted helium was also found to enhance dislocation evolution in V-5Cr-5Ti. High density of matrix cavities were observed in V-5Fe alloys irradiated with dual ions, whereas cavities were formed only around grain boundaries in single ion irradiated V-5Fe.

1. Introduction

Vanadium alloys are attractive candidates for fusion blanket structural materials because of their high temperature mechanical properties and low induced radioactivities after neutron irradiation. However, it was recently shown that moderate additions of undersized solutes such as Fe, Cr and Si can induce swelling rates that are much higher than those observed in fcc alloys [1-3]. Fe additions in particular appear to induce large swelling without any indication of saturation occurring. The origin of this behavior and its relationship to other fusion-relevant irradiation variables are not yet known in detail.

In this study, microstructural and microchemical changes in V-5Cr-5Ti, V-5Cr and V-5Fe alloys under ion irradiation were examined focusing mainly on the effect of He generation on swelling and microstructural evolution.

2. Experimental

V-5Cr, V-5Cr and V-5Fe alloys were prepared by arc-melting in an inert gas atmosphere and annealing at 1000°C for 3.6 ks in high vacuum, followed by rapid cooling. They were irradiated with 4 MeV Ni³⁺ ions to 30 dpa at the damage peak depth with simultaneous implantation of helium by 400 keV He⁺ ions at He(appm)/dpa ratio of 5. Irradiation temperatures were 520 and 600°C. Irradiated surface of the specimens were removed by electropolishing and back-thinned to perforation to observed damage peak depth region by TEM (Transmission Electron Microscope). Microchemical distributions of irradiated specimens were also measured by EDS (Energy Dispersive X-ray Spectroscopy).

3. Results and discussion

Cavities were formed in irradiated V-5Fe at all the irradiation conditions. Cavities grow larger at 600°C. Co-implanted helium was found to affect distributions of cavities in this alloy. Cavities were uniformly distributed in the matrix in the dual beam irradiated specimens, whereas single beam irradiation produces high density of cavities near the grain boundaries.

No cavity formation was detected in V-5Cr-5Ti irradiated only with Ni ions at 520 and 600°C. At 600°C, high density of V₂C precipitates were observed in the matrix of V-5Cr-5Ti and defect free

zone was observed near the grain boundaries. Figure 1 shows measured microchemical evolution in V-5Cr-5Ti irradiated with Ni ions at 600°C. Ti atoms has their peaks at 50-100nm from the grain boundaries. These are considered to come from the binding of Ti atoms with O (oxygen) atoms which are the major interstitial impurities in vanadium alloys. No segregation of Cr atoms were observed whereas Cr is undersized solute in vanadium alloys. At 520°C, no distinct segregation of solute atoms were detected.

Helium atoms produced by transmutation reactions in vanadium alloys under fusion conditions can enhance swelling as studied by tritium-trick method and DHCE (Dynamic Helium Charging Experiments). In this study, helium is also found to increase dislocation density of irradiated V-5Cr-5Ti alloys. Table 1 compares measured dislocation density in V-5Cr-5Ti irradiated with dual ions and single ions at 520 and 600°C to 30 dpa. It was also found that Ti addition to V-5Cr reduces dislocation evolution.

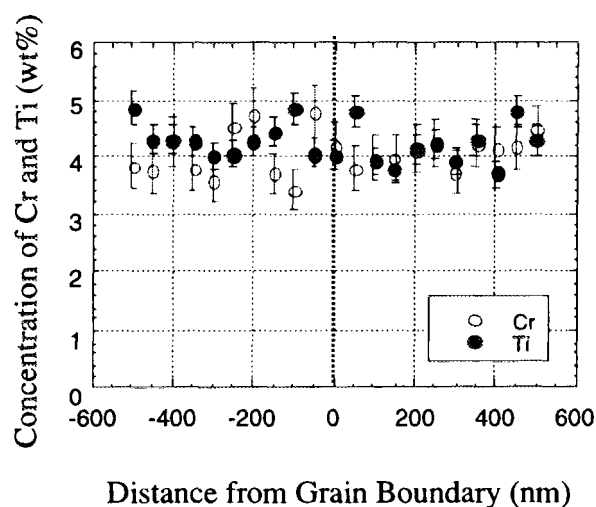


Figure 1 Solute Distributions in V-5Cr-5Ti irradiated with Ni ions at 600°C to 30 dpa.

Table 1 Dislocation Density in V alloys irradiated with Heavy Ions to 30 dpa (m⁻²).

Irradiation Temp.	520°C	600°C
V-5Cr-5Ti single beam	1.8×10^{15}	1.7×10^{15}
V-5Cr-5Ti dual beam	2.1×10^{15}	2.0×10^{15}
V-5Cr dual beam	/	2.4×10^{15}

References

- [1] H. Matsui, D. S. Gelles and Y. Kohno, Proceedings 15th ASTM International Conference on Effects of Radiation in Materials, ASTM STP 1125 (1992) 928.
- [2] H. Nakajima, S. Yoshida, Y. Kohno and H. Matsui, J. Nucl. Mater. 191-194 (1992) 952.
- [3] F. A. Garner, D. S. Gelles, H. Takahashi, S. Ohnuki, H. Kinoshita and B. A. Loomis, J. Nucl. Mater. 191-194 (1992) 948.

イオンビームパルスラジオリシスシステムの構築

千歳範壽 勝村庸介 堂前雅史 石樽顕吉 村上健
(システム量子工学科)

Construction of Ion Beam Pulse Radiolysis System

N. Chitose, Y. Katsumura, M. Domae, K. Ishigure and T. Murakami
Department of Quantum Engineering and Systems Science

Abstract An ion beam pulse radiolysis system has been constructed at HIMAC facility. Ion beam of 24 MeV He^{2+} with the duration longer than 1 μs is available for irradiation. Three kinds of aqueous solutions, $(\text{C}_6\text{H}_5)_2\text{CO}$, NaHCO_3 and KSCN , were irradiated and the absorption signals were observed.

Introduction

It is widely recognized that the radiolysis of aqueous solution is a basic subject not only in radiation chemistry but in the many other fields in technology, biology and medicine. A number of studies have been carried out by electron beam pulse radiolysis, and the process of the water radiolysis with low LET radiation is well known. Recently the use of high LET radiations for cancer therapy has aroused the interest in LET effect. In the present research, a system of ion beam pulse radiolysis has been constructed at HIMAC (Heavy Ion Medical Accelerator in Chiba) facility, and the species produced in the radiolysis of aqueous solution were observed.

Experimental

The irradiation chamber as shown in Fig. 1 is set up on one of the beam lines. Helium ions (24 MeV) pass through the window of 10 μm harvar foil, and reach the sample. The beams are chopped and the duration is adjusted from 1 to 100 μs . As the penetration range of 24 MeV He^{2+} ion is short ($\sim 500 \mu\text{m}$ in water), the solution is directly contacted with the window. The window is supported by the stainless steel plate with mesh to prevent the bending. Only ion particles which pass through the mesh reach the sample. The shape of the plate is also shown in the figure.

The yields of products are measured by the absorption method. Laser light, 633 nm line of He-Ne laser or 488 nm line of Ar ion laser, is used as the analyzing light. The light passes through the sample cell in parallel to the surface of the window, and goes along the line of the holes of the stainless mesh, giving the optical path of 5 mm. It is necessary to measure the signals as a function of the distance from the window in order to determine the yields as a function of LET. So, the analyzing light is expanded by a cylindrical convex mirror after passing through the cell, and cut by the slit. In the present experiment the area within 100 μm from the window is normally measured.

Fig. 2(a) shows the trigger system. The trigger pulses of the accelerator are put into the digital delay generator to trigger the shutter and the digitizer synchronously. The beam current is picked up at the end

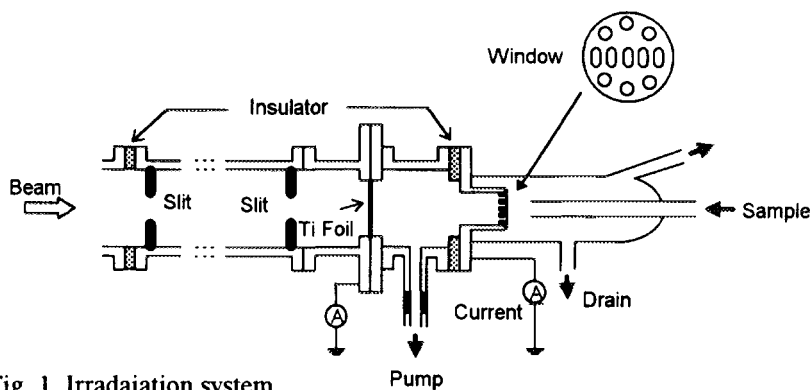


Fig. 1. Irradiation system.

of the vacuum duct and measured by the current integrator or by the digitizer. The beam current and the output of the photodiode can be recorded in the digitizer simultaneously, and it can be used to adjust the trigger delay. Typical trace of the digitizer is shown in Fig. 2(b). The absorbed dose is calculated by the beam current and LET.

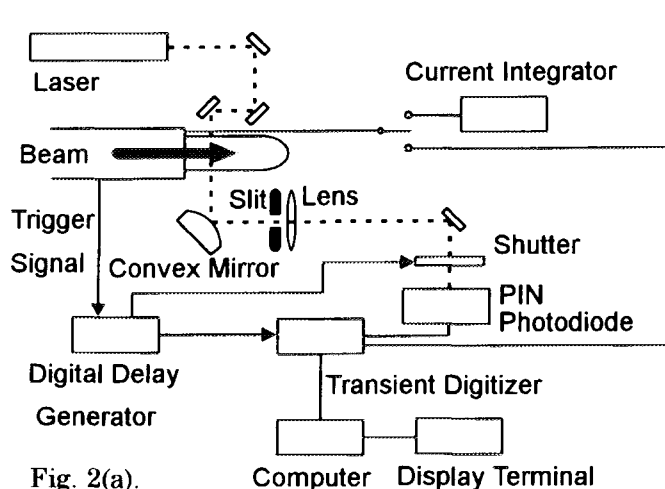


Fig. 2(a).

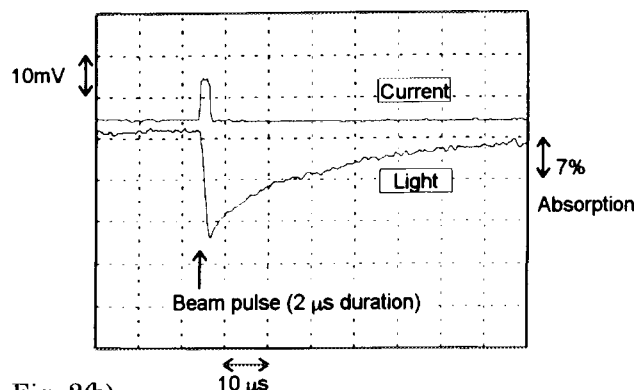


Fig. 2(b).

Fig. 2(a) Trigger system. (b) Typical optical absorption signal and beam current signal.

Results

Three kinds of aqueous solutions, benzophenone, NaHCO_3 and KSCN , were irradiated to test the system and absorption signals corresponding to $(\text{C}_6\text{H}_5)_2\text{CO}^-$, CO_3^- and $(\text{SCN})_2^-$ respectively were observed. The identification of the signals was confined by the effect of scavenger and the saturated gas. Fig. 3 shows the timeprofiles of the absorbance observed at 488 nm in the irradiation of 10^{-2} M KSCN solution. Pulses of $10 \mu\text{s}$ were used and the absorbed dose was approximately 50 Gy per pulse. The solution was saturated with nitrous oxide (curve (a)), or with air (curve (b)). The signal was fairly small in the solution containing 0.2 M ethanol saturated with air (curve (c)). Thiocyanate anion reacts with OH and produces $(\text{SCN})_2^-$, which has an absorption peak around 475 nm. As ethanol is a scavenger of OH , the observed signal is identified to be the absorption due to $(\text{SCN})_2^-$. In the presence of N_2O , e_{aq}^- is converted to OH . The ratio of the yield in the N_2O saturated solution to that in the air saturated solution was studied, and the value of two has been reported in the irradiation with electron beam. In this experiment, the ratio of the yield at the maximum is less than 2. Though the maximum yields can not be compared because of the decay taking place during the pulse, the ratio is considered to depend on LET.

Different signals were also observed under a certain condition. These signals have similarity, but they were proved not to be the absorption due to the species. The real origin of the signals is not known. One explanation may be that it is caused by a change of refractive index of water due to the temperature rise by the irradiation. These signals interfere with the measurement, but they can be reduced by adjustment of the optical alignment.

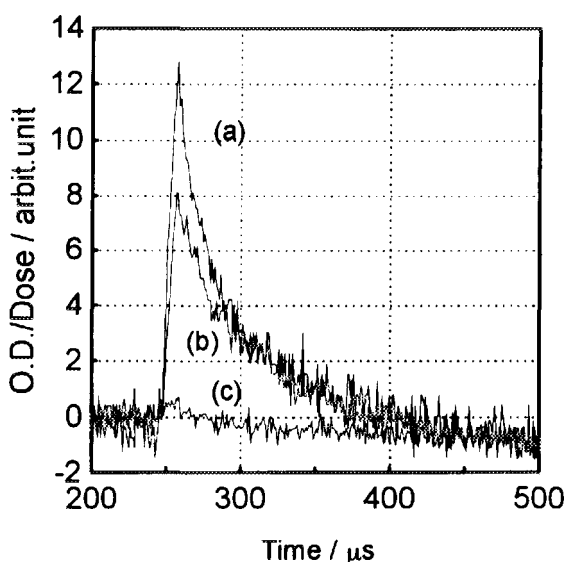


Fig. 3. Timeprofiles of the absorbance observed at 488 nm in the irradiation of 10^{-2} M KSCN solution with $10 \mu\text{s}$ pulse.

イオンビーム照射による半導体超微粒子の表面電子状態変化

八巻 徹也・浅井 圭介・石樽 顕吉 (システム量子工学専攻)

CHANGES IN THE SURFACE ELECTRONIC STATES OF SEMICONDUCTOR FINE PARTICLES INDUCED BY HIGH ENERGY ION IRRADIATIONTetsuya YAMAKI, Keisuke ASAI and Kenkichi ISHIGURE
(Department of Quantum Engineering and Systems Science)**Abstract**

We performed steady-state and time-resolved measurements of the ion-induced emission and photoluminescence (PL) on semiconductor fine particles prepared by Langmuir-Blodgett (LB) methods. We found that the proton irradiation would establish surface passivation of the particles. The carrier recombination dynamics and the post-irradiation processes at the particle surface were discussed as to each emission band.

Introduction

Currently there is considerable interest in nanosized semiconductor particles offering optical properties which are applicable to nonlinear optical devices [1]. One promising approach to synthesizing well-defined particles involves their formation in LB films [2]. LB films have an advantage in that particles can be coated onto a substrate for incorporation into a device. In such fine particles, a large percentage of the atoms exist on the surface, where dangling bonds or other defects produce traps for electrons and holes. Therefore, it has been important to study particle-surface states which have great influence on the electronic properties of the particles. In this study, CdS (cadmium sulfide) fine particles were prepared in LB films. And then we examined the changes in the electronic states induced by high energy ion irradiation, which is known to be useful for surface modification of bulk materials.

Experimental

CdS particles were synthesized through the infusion of H₂S onto cadmium arachidate ((C₁₉H₃₉COO)₂Cd) LB films deposited on Si substrates [2]. On those samples, we observed steady-state spectra and time-resolved profiles of the emission induced by 1 MeV H⁺ bombardment and then measured PL after the irradiation.

Results and Discussion

Fig. 1 shows typical steady-state spectra of ion-induced emission from CdS fine particles [3,6]. Various emission bands (420-460 nm (R), 500-510 nm (P) and 560-610 nm (Q)) attributed to the excitonic state and different defects in the band gap were observed at the initial irradiation stage (a). As the dose increased, the emissions via the trapping sites decreased in intensity and the band-edge emission developed as shown in (b). This indicates that the ion irradiation would remove almost all the trapping

sites in the band gap.

Ion-induced emission decay curves of CdS fine particles, monitored at 430 nm (R), 510 nm (P) and 600 nm (Q) are illustrated in Fig. 2 [5,6]. The 430-nm emission (R), the band-edge emission, showed a single-exponential decay. In contrast to this, the decay curves of the low-energy emissions (P) and (Q) showed a multi-exponential shape which is probably due to the wide distribution of radiative states in the band gap. These decays could be explained by the model based on a donor-acceptor recombination.

The PL spectra [4,6] taken after the irradiation drastically changed in the course of the surface processes, such as stabilization and formation of trapping sites, which might be occurring under the photooxidizing conditions. In addition, it was suggested that new defect sites originating from sulfur vacancies would generate in the presence of both sulfur-related defects and Cd atoms.

References

- [1] R. K. Jain and R. C. Lind, *J. Opt. Soc. Am.*, **73**, 647 (1983).
- [2] N. A. Kotov, F. C. Meldrum, C. Wu and J. H. Fendler, *J. Phys. Chem.*, **98**, 2735 (1994).
- [3] K. Asai, K. Ishigure and S. Shibata, *J. Lumin.*, **215**, 63 (1995).
- [4] K. Asai, T. Yamaki, K. Ishigure and S. Shibata, *Thin Solid Films*, in press.
- [5] K. Asai, T. Yamaki, S. Seki, K. Ishigure and S. Shibata, *Thin Solid Films*, in press.
- [6] T. Yamaki, K. Asai, K. Ishigure and S. Shibata, *Proc. of the 7th International Symposium on Advanced Nuclear Energy Research*, to be published.

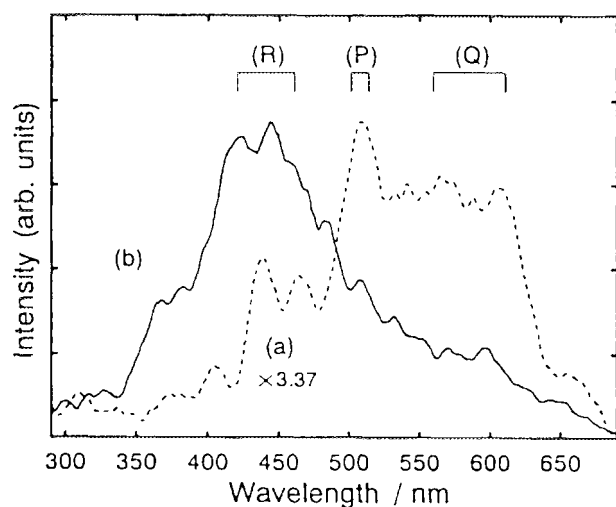


Fig.1. Steady-state spectra of ion-induced emission from CdS fine particles. The spectra were obtained at the initial irradiation stage (a) and after high-dose irradiation (b).

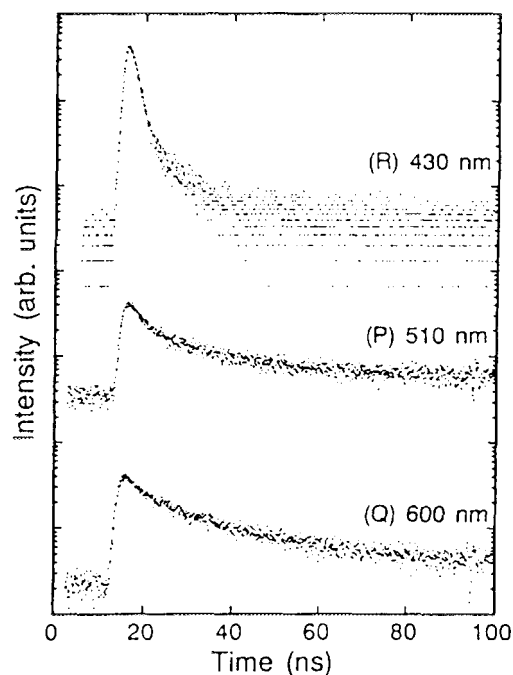


Fig.2. Ion-induced emission decay for CdS fine particles, monitored at 430 nm (R), 510 nm (P) and 600 nm (Q).

プラント操作員訓練支援システム用学習者モデルに関する研究
古濱 寛、古田一雄、近藤駿介 (システム量子工学科)

Knowledge Model of Trainee
for Training Support System of Plant Operation
Y. Furuhashi, K. Furuta, and S. Kondo

Abstract: We have already proposed a knowledge model of a trainee, which model consists of two layers: hierarchical function and qualitative structure. We developed a method to generate normative operator knowledge based on this knowledge model structure, and to identify trainee's intention by means of truth maintenance. The methods were tested by cognitive experiment using a prototype of training support system.

1. Introduction

The role of human operators are changing from prescribed rule-based behavior to unprescribed knowledge-based behavior, as automation based on modern technologies has been introduced. Since a good method of operator training for knowledge-based behavior, however, has not yet been established enough, we are trying to build an architecture of training support system which can support trainees to acquire a proper knowledge so that they can behave appropriately even in unanticipated situations. We have already proposed a knowledge representation of a trainee and showed its usefulness [1]. In this paper we will discuss a method to construct the knowledge model a trainee on the proposed representation, and describe the training support system architecture based on this method.

2. Knowledge Model of Trainee and Its Identification

Trainee's knowledge is represented as graphs in two layers: the function hierarchy layer and the qualitative causality layer. A link between two nodes in this representation can be thought of as an atom of trainee's knowledge. Each knowledge atom can take one of three states, "in", "out" or "unknown", which stands for the possessional state of knowledge by a trainee. A set of such knowledge atoms can be the knowledge model of a trainee. A trajectory containing more than one knowledge atom is called a path, and nodes connected with a path are reachable. If two nodes at the both ends of a knowledge atom in the function hierarchy layer are reachable through any path in the qualitative causality layer, such a path is the justification of the knowledge atom.

Identification of the knowledge model of a trainee is performed by truth maintenance as follows. When a trainee takes an operation A, its goal X, related to A in the function hierarchy layer, is selected, and then it is tried to identify the justification path of the knowledge atom (X-A). If the other operation B is required further to justify the identified justification path, the following default rule is created, and the state of knowledge atom (X-A) is set "in".

$$\frac{(X-A):(X-B)}{X \leftarrow A \wedge B}$$

If a trainee fails to attain the goal X though he/she has performed the operation A, the state

of knowledge atom (X-B) is changed to “out”. If it becomes clear that the aim of having done A is not to achieve X, the state of knowledge atom (X-B) is changed to “unknown”. The consistency of the knowledge model is maintained by altering either the states of knowledge atoms or default rules in a similar manner.

3. Training Support System

The architecture of the training support system developed based on the method described so far is illustrated in the figure below. The domain knowledge base contains a plant model and definitions of unit operations. The knowledge compiler constructs a normative knowledge model of an operator, and this normative model comes to be the initial framework and the final goal of the knowledge model of a trainee. The model manager watches response of a trainee and modifies the knowledge model by the truth maintenance explained above. At the same time it judges the appropriateness of trainee’s response. The dialogue manager generates queries to a trainee and the correct answers to them.

This system has been implemented on an EWS using the G2 knowledge shell as well as the Prolog language. The target plant assumed in a test consists of a few tanks, valves and pipes. An experiment was performed using a task of filling up a tank with liquid by valve operation. The states identified for knowledge atoms in the knowledge model were verified against interviews to the subjects after experimental sessions, and it was shown that the identification was appropriate in most cases.

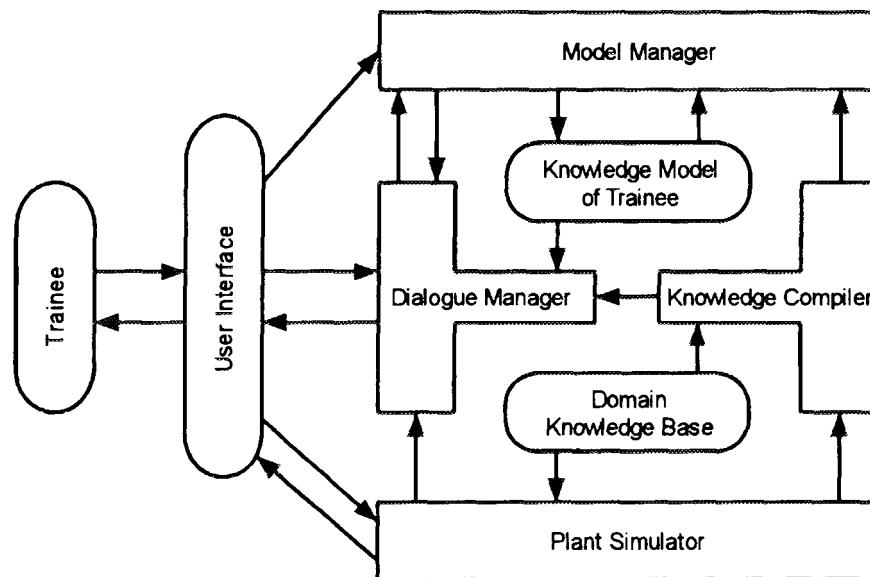


Figure: Architecture of training support system.

核融合実験炉用14MeV中性子スペクトロメータの高エネルギー分解能特性の評価
井口哲夫（原子力工学研究施設）、高田英治、中沢正治（システム量子工学専攻）

High Energy Resolution Characteristics on 14MeV Neutron Spectrometer for Fusion Experimental Reactor

T. Iguchi¹, E. Takada² and M. Nakazawa²

1 Nuclear Engineering Research Laboratory

2 Dept. of Quantum Engineering and Systems Science

Abstract

A 14MeV neutron spectrometer suitable for an ITER-like fusion experimental reactor is now under development on the basis of a recoil proton counter telescope principle in oblique scattering geometry. To verify its high energy resolution characteristics, preliminary experiments are made for a prototypical detector system. The comparison results show reasonably good agreement and demonstrate the possibility of energy resolution of 2.5 % in full width at half maximum for 14MeV neutron spectrometry.

1. Introduction

High energy resolution neutron spectrometry in DT plasma experiments is expected to derive many useful plasma parameters such as ion temperature (or ion velocity distribution), ion density, beam-plasma interactions etc. We are now developing one promising candidate of 14MeV neutron spectrometers suitable for an ITER-like fusion experimental reactor, which is based on a detection principle of recoil proton counter telescope in oblique scattering geometry[1]. Here are described the results and discussion on the preliminary experiments for a prototypical detector system to verify its high energy resolution characteristics using a 14MeV neutron generator.

2. Preliminary experiments

To verify high energy resolution characteristics on our detector concept, we have made a prototypical detector system and measured the detector response i.e. recoil proton spectrum to 14MeV neutrons at FNS (Fusion Neutronics Source) Facility in JAERI. The detector consists of 10 μ m thick polyethylene film(a radiator) placed in parallel to the incident neutron beam, three Si-SSDs with a 2000 mm² sensitive area and 500mm thick depletion layer as the recoil proton detectors and the recoil proton collimators made of a 10mm thick lead glass plate with the holes of 200 μ m diameter and 620 μ m pitch tilted 30 degree to the plate surface, inserted between the radiator and Si-SSDs, and was operated in the air.

The detector unit was placed at a distance of about 1.0 m from the 14MeV neutron source target in the direction of 100 degree to the beam line, which ensures almost monochromatic energy of 14.1 MeV for incident neutrons to the radiator. A slit neutron collimator, of which thickness is not so sufficient to shield 14MeV neutrons, was also placed to mitigate the direct incidence of 14MeV neutrons to the Si-SSDs. The pulse

signals from three Si-SSDs were summed up and fed into a pulse height analyzer after the gain adjustment using an ^{241}Am α source. To obtain recoil proton spectra originating from the radiator, subtraction of the normalized pulse height data was made between the measurements with and without the radiator.

3. Results and discussion

Fig.1 shows preliminary comparison between the measured and calculated recoil proton spectra. The response calculation based on Monte Carlo technique simulates the scattering and transmission of recoil protons inside the collimating plate as well as the energy loss of recoil protons inside the radiator and the solid angle of recoil proton incidence to the Si-SSDs through the collimator. The calculated result seems to be in reasonably good agreement with the measured data, which gives energy resolution of 2.5 % in FWHM and detection efficiency of 2×10^{-7} counts/(neutron/cm²), although they may have a large uncertainty around 20% because of poor counting statistics of recoil protons and imperfection of background subtraction.

4. Conclusion

Through the preliminary experiments for a prototypical detector system, we have demonstrated the possibility of high energy resolution characteristics of our detector concept in 14MeV neutron spectrometry which will be required at an ITER-like fusion experimental reactor. Reasonable agreement obtained between the measured and calculated detector responses is also expected to give the validity of the design results specified for an actual system installed into the fusion device.

Reference

- [1] T. Iguchi et al., Conceptual design of neutron diagnostic systems for fusion experimental reactor, *Fus. Eng. Des.* 28 (1995) 689-698.

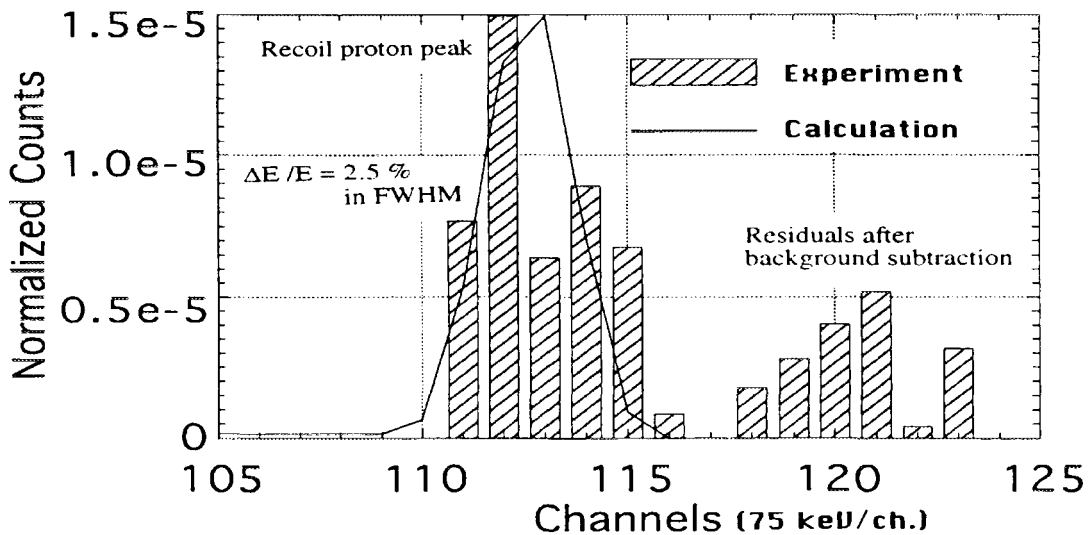


Fig.1 Comparison between measured and calculated recoil proton spectra to 14MeV neutrons

Neutron Radiation Distribution Sensor Using Flexible Plastic Scintillating Fiber Combined with the Time-of-Flight Technique

E. Takada, K. Sugiyama, H. Takahashi, T. Iguchi, M. Nakazawa

Department of Quantum Engineering and Systems Science, Faculty of Engineering, University of Tokyo

Abstract

As a promising neutron radiation distribution sensor, a long fiber system has been made using two silica fibers connected to both ends of the plastic scintillating fiber (PSF). Its basic properties were investigated to detect the position of neutron incidence with the time-of-flight (TOF) method. From the experimental results for the fission neutron source, the two linear relations were confirmed (1) between the incident position of the neutrons and the time difference and (2) between the neutron flux level and the counting rate. The spatial resolution and the counting efficiency of this system were about 60 cm (FWHM) and about 1.0×10^{-4} [counts/incident neutron] respectively using 1 mm diameter fiber of 100 m length. A neutron dose distribution measured by this system was compared with the mapping result using a conventional neutron Sievert(Sv) counter. After some correction for the spatial resolution by an unfolding method, both results showed good agreement.

I. INTRODUCTION

Scintillating optical fibers have recently been developed as a new radiation sensor and some techniques have been proposed for measuring neutron distribution with glass scintillating fiber by photonic attenuation [1] or by imaging techniques [2]. We proposed a technique to apply the time-of-flight (TOF) method to the signals from PSF ends and it has been shown that this system can measure the radiation distribution along the fiber length [3]. But, owing to a small attenuation length of PSF, the measurable length by these methods were limited to below 10 m. On the other hand, in order to elongate the signal transportation length, coupling of clear normal fibers to the ends of PSF has been tried [4]. In the present study, we thought of connecting normal fiber optics to both ends of PSF and applying TOF method to each PSF+normal fiber system as shown in Fig. 1, where the radiation distribution along its total length, L , can be measured at one time.

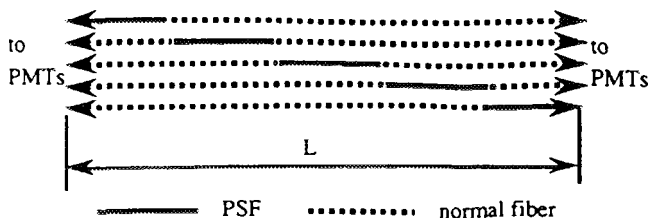


Fig. 1 Schematic view of the long range radiation distribution monitor, where TOF method is applied to each PSF+normal fiber system.

In addition to the merits of optical fibers, this system is advantageous in the possibilities (1) of very flexible sensing of radiation distribution and (2) of continuous measurement for a long distance. So, it can be applied to nuclear power plants, where unusual radiation peaks should surely be detected around the reactor vessel and along very long pipes, etc.

II. MEASURING SYSTEM

The measuring system and the properties of the PSF (BICRON BCF-20, 2.5-m long) are shown in Fig. 2 and Table 1, respectively. The number of scintillation photons produced by one incident neutron depends on the position where (n,p) scattering occurs and the emitting angle of the proton. When the neutron energy is 1 MeV, the maximum number of photons is evaluated about 1,500 and about 3.44 % of these are trapped and transmit to the ends of the PSF. The $1/e$ attenuation length of the PSF is about 3.5 m and it is much shorter than that of normal fiber optics for the same wavelength, which is generally several hundred meters. Therefore, when the PSF is 2.5-m long and the neutron of 1 MeV is incident at the middle of the PSF, the maximum number of photons that enter the Photomultiplier Tubes (PMTs) is expected about 36.

In our system, the scintillation photons that entered the PMTs (HAMAMATSU R1635-02) were converted and multiplied into voltage signal and, then, its output signal was multiplied again by the fast voltage-sensitive Pre-Amplifiers (ORTEC VT-120). The time difference between the two signals from the Pre-Amplifiers was detected through Constant Fraction Discriminators (CFDs : ORTEC 583) and a Time-to-Amplitude Converter (TAC : ORTEC 567). The risetime and gain of the PMTs were about 0.8 nsec and 8×10^5 , respectively, and the risetime of the Pre-Amplifiers was less than 1 nsec. Considering that the time walk of the CFDs was < 75 psec and the time resolution of the TAC was < 10 psec, this system was expected to detect the arrival time difference with high resolution of 1 - 2 nsec or less.

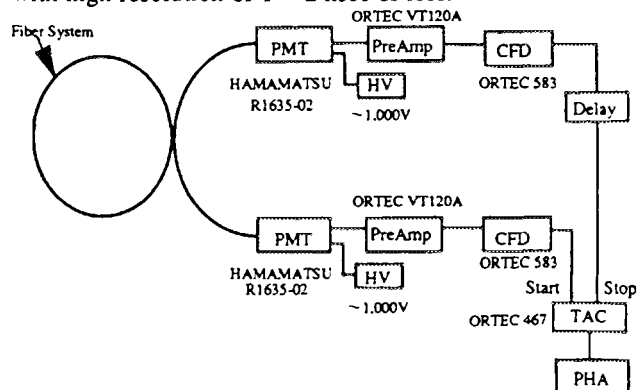


Fig. 2 Measuring system for TOF method.

Table 1 Properties of BICRON-20[4]

Items	Properties
Refractive Index of the Core	1.60
Core Diameter	1.0 mm
Numerical Aperture	0.58
Trapping Efficiency	3.44 % (min)
Peak Emission Wavelength	492 nm
Decay Time of Scintillation Photons	2.7 nsec
1/e attenuation length	> 3.5 m

III. RESPONSE OF THE TOF SYSTEM WITHOUT NORMAL FIBER OPTICS TO FAST NEUTRONS

Experimental setup for measuring the response function of this system is shown in Fig.3. PSF (2.5-m long) was placed in the fast neutron beam (5-cm diameter) extracted from the fast neutron source reactor : YAYOI (University of Tokyo), with its peak energy at 1 to 2 MeV. PSF was connected directly to the PMTs.

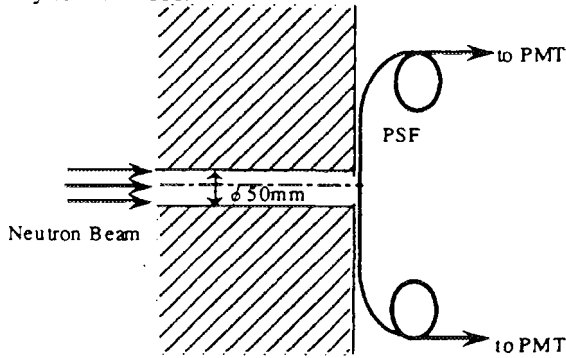


Fig.3 Experimental Setup

The measured profile is shown in Fig. 4, where the neutron beam was incident on the middle of PSF, with the PMT gain : 6×10^5 and the discrimination level of CFD : 0.8 V. From the fast neutron flux and the measured peak area, the average counting efficiency was evaluated to be 1.3×10^{-4} [counts/incident neutron into PSF core]. The spatial resolution was about 16 cm (FWHM) with the above experimental parameters.

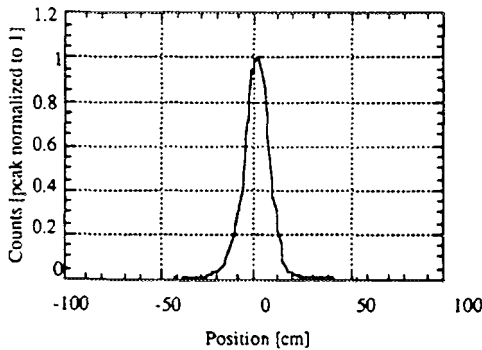


Fig. 4 Measured profile without normal fiber optics.

IV. LONG DISTANCE SIGNAL TRANSPORTATION WITH CONVENTIONAL FIBER OPTICS

For extending the length, normal fiber optics with low attenuation (20 dB/km at wavelength around 500 nm) were connected at each end of the PSF. Main properties of the fiber are tabulated in Table 2.

Its core region was made mainly of silica glass and its core diameter was 1 mm, being the same as that of PSF. Because of its large diameter and refraction rate distribution of step-index type, mode dispersion in the photonic transmission is thought to be fairly large. Measurements were performed by placing the PSF in the fast neutron beam from YAYOI and fiber optics.

Table 2 Properties of the normal fiber optics that were used

Items	Properties
Type of the distribution of refractive index	Step Index
Refractive Index of the Core	1.462
Core Diameter	1.0 mm
Numerical Aperture	0.20
1/e attenuation length at wavelength of about 500nm	220 m

A. Efficiency and Spatial Resolution

Measured profile is shown in Fig. 5, where the neutron beam was incident on the middle of the PSF. Main photonic losses in this system from the scintillating point to one PMT are evaluated as follows:(1) 1.5 dB loss in the PSF (1.25 m), (2) 10 dB loss at the FC connector mainly due to the difference of Numerical Aperture (NA) between PSF and normal fiber and (3) 1 dB loss in the normal fiber (50 m). Because of these, the counting rate was low compared to the case without normal fibers. The counting efficiency for the incident neutron into the PSF core was about 3×10^{-4} [counts/neutron] with the discrimination level set at 0.15 [V]. Compared to the case without normal fiber optics, the profile became broader and the spatial resolution was about 60 cm (FWHM).

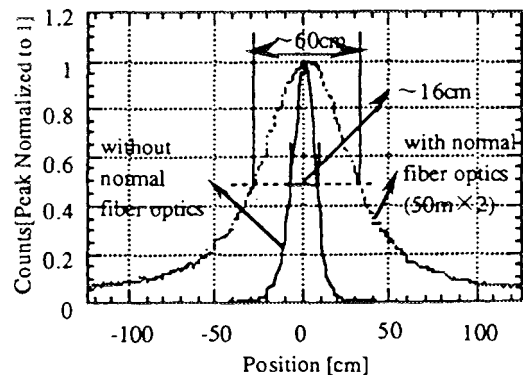


Fig. 5 Measured profile with and without normal fiber optics (The discrimination level was 0.8 V in the case of without normal fiber optics and 0.15 V with them. PMT gain was about 6×10^5 in both cases).

In order to improve the spatial resolution of the long fiber system, we tried raising the discrimination level to 0.3 V, of which the measured result is shown in Fig. 6. With the discrimination level of 0.3 V, the spatial resolution became about 50 cm and was not much improved. The counting efficiency was reduced to 4×10^{-5} [counts/incident neutron] which was about 1/8 of that in the 0.15 V case. From the physical process included in this system, the following factors are mainly considered to affect the response profile : (1) time distribution of scintillation process, (2) time resolution of signal processing and (3) time dispersion in the fiber system. In our system, the effect of (1) is estimated to be about 1 - 2 nsec, because scintillation decay time of the PSF is 2.4 nsec. The spectral broadening due to (2) is also estimated to be the same order or less considering the fast response of the PMTs and the fast Pre-Amplifiers as mentioned in section II. As for (3), mode dispersion in the normal fibers (50m x 2) can be calculated to be more than 3.7 nsec from the numerical aperture of 0.2. This means that the profile broadening was dominantly due to the dispersion in the fibers. This will be why raising the discrimination level was not so effective for improving spatial resolution.

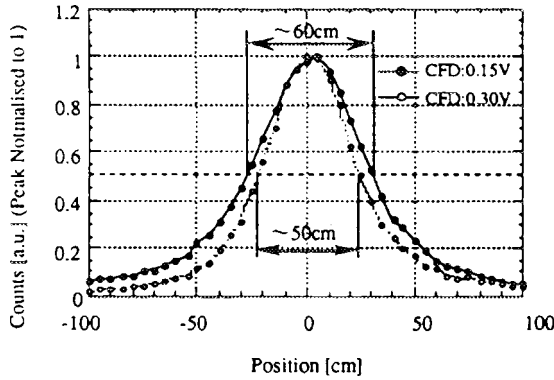


Fig. 6 Measured profile with different discrimination levels (The discrimination level was set to 0.15 V or 0.30 V).

B. Linearity

To confirm the availability of this detection system composed of PSF and normal silica fibers for a radiation distribution measurement, we checked the linearity (1) between neutron flux and peak area of the profile and (2) between neutron incident position and the peak position. As shown in Fig. 7 and Fig. 8, this system showed good linearity for the position and the intensity of incident neutrons.

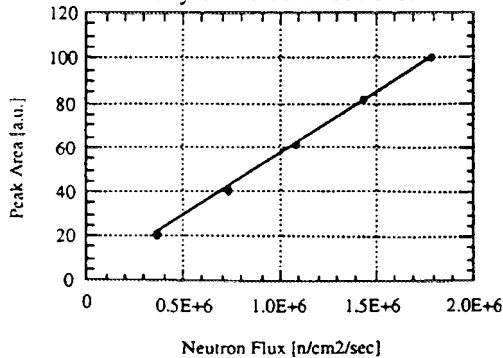


Fig. 7 Relation between neutron flux and peak area.

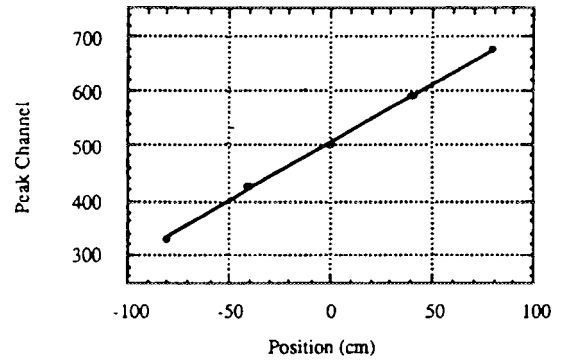


Fig. 8 Relation between neutron incident position and output peak channel.

V. UNFOLDING OF THE SPECTRA

As mentioned in section II, the spatial resolution of the long fiber system is much lower than that of the case without normal fiber optics. For enhancing the applicability of this system, an unfolding technique was applied to improve the spatial resolution.

A. Response Matrices

In order to get the response matrices of this system, we carried out numerical fitting of the measured data using the least square method. The following function was used as a fitting equation:

$$f(x) = A \left\{ \exp(-Bx^2) + C \exp(-D|x|) \right\} \quad (1)$$

where A, B, C, D were the fitting parameters and x denotes the distance along PSF. The time resolution in the electrical signal processing, in PMT, CFD and so on, was assumed Gaussian distribution corresponding to the first term of eq. 1. The second term comes from the exponential decay of scintillation in the PSF. The time dispersion in the fibers was, though it was the most dominant factor, not reflected in the functional formula, because it was supposed to broaden the spectra uniformly and not to change the response function itself. The result of fitting is shown in Fig. 9. It is found that eq.1 can express the spectra fairly well.

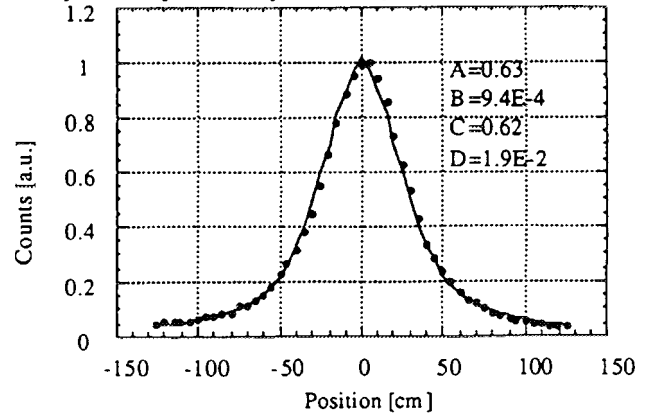


Fig. 9 Result of Fitting (Neutron beam was incident on the middle of the PSF).

B. Result of the unfolding

The measured data were unfolded using the SAND-II algorithm [6] that had been widely used for spectral unfolding for the activated foil method, etc. The unfolding formulae are based on numerical iterations as follows:

$$\ln \left(\frac{\phi_g^{k+1}}{\phi_g^k} \right) = \frac{\sum_i w_{ig}^k \ln \left(\frac{S_i^k}{S_i^{k+1}} \right)}{\sum_i w_{ig}^k} \quad (2)$$

where,

$$S_i^k = \sum_g R_{ig} \phi_g^k$$

$$w_{ig}^k = \frac{R_{ig} \phi_g^k}{S_i^k}$$

i, g : Spatial Bin Number

S_i : Measured Spectra

ϕ_g^k : Unfolded Spectra

k : Number of iteration

R_{ig} : Response Matrix

The result is shown in Fig. 10. After unfolding, the spatial resolution of this long fiber system is almost as good as the case without normal fiber optics that is shown in Fig. 4. Since the calculation used here is so simple, the result will be improved by other more refined techniques.

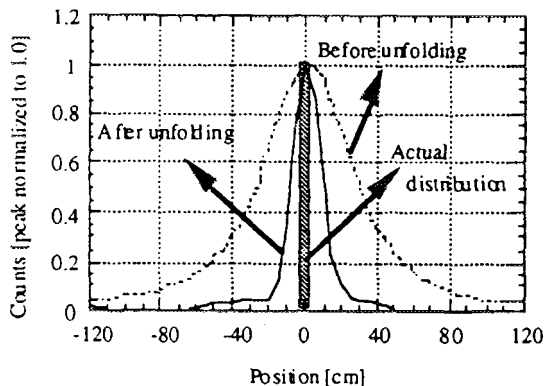


Fig. 10 Comparison of spectra before and after unfolding (Neutron beam was incident on the middle of the PSF).

VI. RADIATION DISTRIBUTION MEASUREMENT USING THE LONG FIBER SYSTEM

The long fiber system consisting of PSF and two normal fiber optics was applied to practical measurements of neutron radiation distribution. A typical neutron test field along the PSF was produced by a Cf-252 source in the arrangement of Fig. 11, where three neutron flux peaks were generated.

Figure 12 shows the measured results. The results by the fiber system (white bars) were compared to those by a conventional neutron Sv counter (Fuji Electric NSN10001). Though the results showed to be in good agreement for the positions of the neutron peaks, the contrast of peak to bottom

by the fiber system was not so clear as that by a Sv counter. However, it can also be seen in Fig. 12 that our system detects radiation distribution peaks as clearly as the Sv counter using the unfolding technique. These results suggest the feasibility of this long fiber system as a neutron dose distribution monitor instead of measuring at many monitoring points with a single neutron counter.

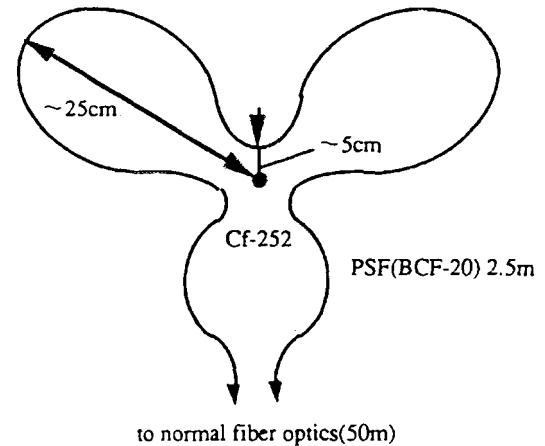


Fig. 11 Experimental arrangement for radiation distribution measurement.

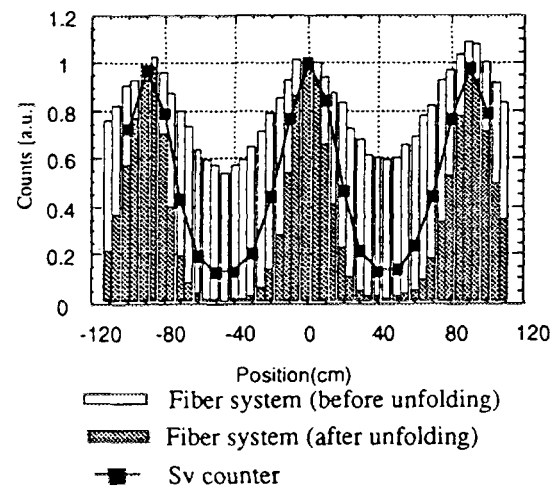


Fig. 12 Comparison between the results by the fiber system and a neutron Sv counter.

VII. CONCLUSIONS

In this study, the basic properties of the long fiber system using the TOF method were investigated as a promising neutron radiation distribution sensor. Spatial resolution of the long fiber system was about 1/3 of the PSF spectra without normal fiber optics, mainly due to the large time dispersion in the fibers. The neutron radiation distribution measured with this system was compared with that by a conventional neutron Sv counter. The peak to bottom ratio of the measured profile in the raw data was not so clear, however, it was shown that the profile could be improved by simple unfolding techniques and its results showed good agreement with that by the Sv counter. These results demonstrate the feasibility of this

system as a long radiation distribution monitor for narrow and complicated facilities such as nuclear power plants.

VIII. REFERENCES

- [1] G.B. Spector, T. McCollum and A. R. Spowart, Scintillator Fiber Optic Long Counter Response to Neutrons, Nuclear Instruments and Methods in Physical Research, A346, pp. 273-278, 1994
- [2] P. Ottonello, G. A. Rottigni, G. Zanella and R. Zannoni, Slow Neutron Imaging Using Scintillating Glass Optical Fibers, Nuclear Instruments and Methods in Physical Research, A349, pp. 526-531, 1994
- [3] S. Imai, S. Soramoto, K. Mochiki, T. Iguchi and M. Nakazawa, New Radiation Detector of Plastic Scintillation Fiber, Review of Scientific Instruments, Vol.62, No.4, pp.1093-1097, 1991.
- [4] B. Baumbaugh et al., Performance of Multiclad Scintillating and Clear Waveguide Fibers Read Out with Visible Light Photon Counters, Nuclear Instruments and Methods in Physical Research, A345, pp. 271-278, 1994
- [5] Scintillation Roundtable Update Report, BICRON Corporation, Sept. 1989.
- [6] W.N. MacElroy et al., A Computer-Automated Iterative Method for Neutron Flux Spectra Determination by Foil Activation, AFWL-TR-67-41, vol.-IV, 1967.



ELSEVIER

Correction of fast neutron scattered components from fast neutron radiography images

Koji Yoshii^{a,*}, Hisao Kobayashi^b

^a*Nuclear Engineering Research Laboratory, University of Tokyo, 2-22 Shirakata, Tokai, Naka, Ibaraki 319-11, Japan*

^b*Institute for Atomic Energy, Rikkyo University, 2-5-1 Nagasaka, Yokosuka, Kanagawa 240-01, Japan*

Abstract

Fast Neutron Radiography (FNR) results have been successfully obtained by the use of the fast neutron source reactor YAYOI of the University of Tokyo. However, an effect of contrast distortion in the FNR images was observed. The intensity of scattered fast neutrons at the center of an object image was analyzed with a simple model of an iron cylindrical sample. Analytical results agreed well with experimental results.

Keywords: Fast neutron radiography; Contrast distortion; Scattered fast neutrons

1. Introduction

Fast neutron radiography (FNR) has been expected to be a useful imaging technique for an object for which it is difficult to obtain an image with thermal neutron radiography (TNR), for instance, a hydrogen-rich material thicker than a few centimeters [1–3]. An electronic imaging system for the FNR (FNR-TV) has been used to inspect several materials as a function of thickness up to 10 cm [4]. It was also useful for inspection of an inhomogeneous material with low atomic number (Z) in a higher Z material, which is difficult to image with X-radiography.

An effect of contrast distortion in the image was observed for many objects, especially around sharp edges. The distortion is frequently called the *edge enhancement effect* [5]. However, the distortion is observed not only on the edge region, but also for the whole FNR image, because the source of distortion could be explained due to scattered neutrons originating in the object and the environment. The estimation of the scattering intensity and its spatial distribution is imperative to the quantitative analysis related to transmittance determinations.

In the TNR, Kobayashi et al. [6] proposed a method to estimate the contribution of scattered neutrons using an umbra shadow of a neutron opaque material. Unfortunately, the method cannot be applied for the FNR, since an effective neutron opaque material is difficult to realize. Hrdlicka and Peterka [7] have proposed a qualitative

method to minimize scattering effects for a thermal neutron beam.

The intensity generated in an object was discussed in this paper. A simplified method similar to the Hrdlicka and Peterka's model was applied quantitatively to the FNR. The intensity of the scattered fast neutron component was analyzed using the model of an iron cylindrical sample. The intensity was discussed as the scattered fast neutron component corresponding to only the center of the object image. Results will be compared with experiments using an iron cylindrical sample.

2. Analysis

The simplified model is assumed to estimate intensities of scattered neutrons from an object, and related parameters are shown in Fig. 1. The model is based on the following assumptions: (a) The object is a cylindrical iron sample. (b) Incident fast neutron beams are parallel beams. (c) The incident fast neutrons are attenuated in the iron sample. (d) The attenuation factor is estimated from the macroscopic total cross section for the 1 MeV neutron. (e) Neutrons are isotropically scattered in the object. (f) Multiple scattered neutrons are not considered due to that the mean free path of 1 MeV neutron for iron is about 10 cm. (g) Scattered neutrons are attenuated in the iron sample with the same attenuation factor as the incident fast neutrons, since the single scattered neutrons have 4% decrease energy from the result of the calculation.

The total intensity (I) on origin O shown in Fig. 1 of the scattered component from the object is obtained by:

* Corresponding author. Tel. +81 29 287 8457, fax +81 29 282 8242, e-mail yoshii@utnl.gen.u-tokyo.ac.jp.

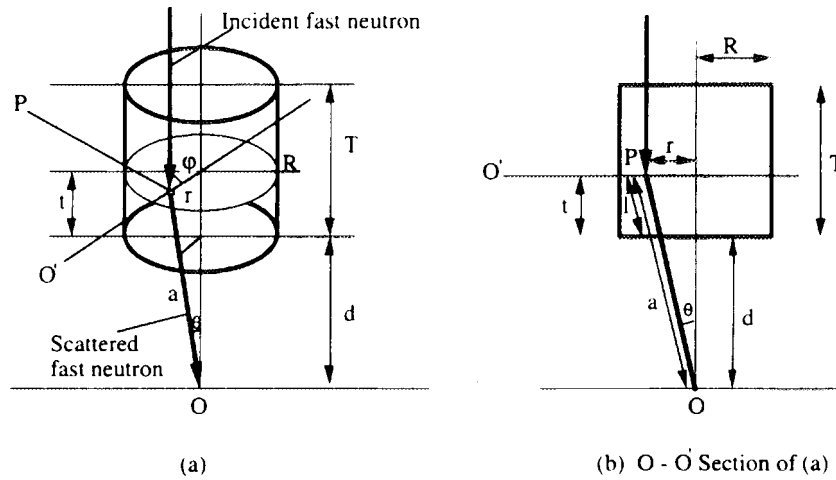


Fig. 1. A model for estimating the scattered fast neutron component.

$$I = \int_0^T \int_0^R \int_0^{2\pi} \frac{r \cos(\theta)}{4\pi a^2} \exp(-\Sigma_t(T-t)) \times \exp(-\Sigma_t l) d\varphi dr dt. \quad (1)$$

The origin O is set on the imaging device and on the centre line of the sample. The distance between the scattered point and the origin O is shown as " a ". Σ_t is the macroscopic total cross section. $(T-t)$ shows the distance between the upper surface of the sample and the scattered point. The thickness of the sample is shown as " T ". The separation " d " shows the distance between the bottom of the sample to the FNR-TV converter (or imaging device). The distance of the scattered neutron passing in the sample is shown as " l " and is expressed as:

$$l = a \frac{t}{d+t}. \quad (2)$$

3. Experiment

FNR images of objects were obtained by means of an electronic imaging technique for the FNR (FNR-TV) [4]. The FNR-TV is basically the same as the television imaging system for the TNR [8] except for the converter and the imaging tube. A specially designed luminescent converter was used with the FNR-TV and was made of a mixture of polypropylene resin and ZnS(Ag) [9]. The FNR-TV was equipped with a high sensitivity TV camera (Hamamatsu C2741-08) with a silicon intensifier target (SIT) tube and a digital image processing system (DPS; Nippon Avionics Image-sigma) with a video frame memory. The output image of the FNR-TV were integrated over 900 frames on the DPS. The integrated images (512×512 pixels with 8 bit) were fed to a personal computer for further data processing. The integrated images were cor-

rected with dark current and shading images. It is shown that the FNR-TV system has an excellent linearity between fluence and signal output, and that no correction for non-linearity effect was required. The integrated image included the effect of gamma-rays; however, the effect was not considered in this study. The gamma sensitivity of the PP converter was 13% of the total luminescence at the FNR-TV field [9].

The experimental object was a cylindrical iron sample. To estimate the scattered component as a function of the sample radius, five kinds of samples were prepared whose sizes were 3 cm thick and the radius of 1, 2, 3, 4 and 5 cm. To estimate the scattered component as a function of the sample thickness, six kinds of samples were prepared with a 3 cm radius and thicknesses of 1, 2, 3, 4, 6, 8 and 10 cm.

Intensities of the scattered component were obtained as a function of the separation distance " d ". The distance was changed from 0 to 25 cm by using a two dimensional position controller.

4. Results and discussions

4.1. Estimation of the scattered neutron component

The profiles along the radial line of circular images of the sample as a function of d were measured and are shown in Fig. 2. The highest gray scale peak at the center (270 channels in Fig. 2) is observed inside the sample (channel 220–channel 330) at $d=0$ cm. The peak height steeply decreases and the profile is spread out with increasing d . Finally the profile becomes almost independent of d at $d > 10$ cm. Therefore the intensity of the scattered neutron component generated in the object was thought to be decreased. Then the intensity of scattered neutrons was assumed to be the difference of the counts of

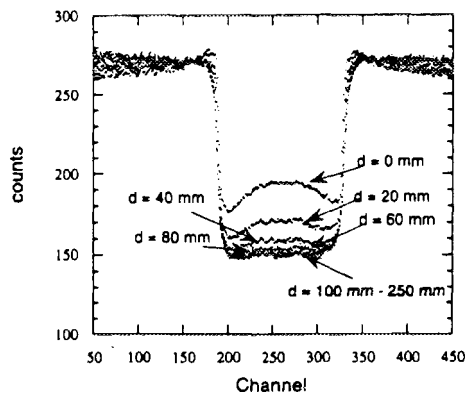


Fig. 2. Profiles of a cylindrical iron sample along the radial line of the FNR images for various distances d .

the gray scale at the centre between $d = 0$ cm and $d = 10$ cm.

4.2. Scattered neutron component as a function of the radius of the sample

Fig. 3 shows the intensity of the scattered neutron component as a function of the radius of the sample at a separation of $d = 0$ cm (where the sample was in contact with the imaging device). Analytical results at a separation of $d = 0.1$ cm were obtained for the sample whose sizes were 3 cm in thickness and from 0 to 10 cm in radius. The scattered components for the objects were estimated with the same method as in Section 4.1. The experimental values agree with the analytical values shown as small dots in Fig. 3. From these results, it is concluded that the scattered neutron component saturates at a sample radius of 6 cm.

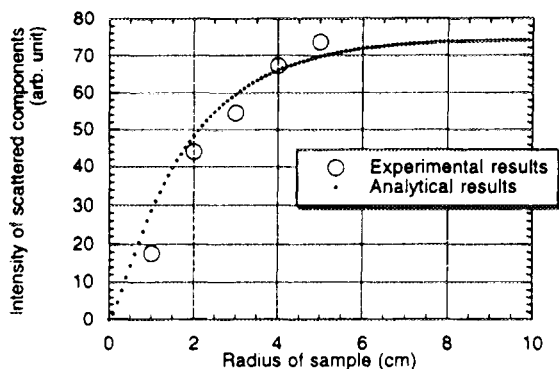


Fig. 3. Intensity of the scattered fast neutron components at the center of the FNR image as a function of the radius of an iron cylindrical sample with a thickness of 3 cm (the sample is in contact with the imaging device).

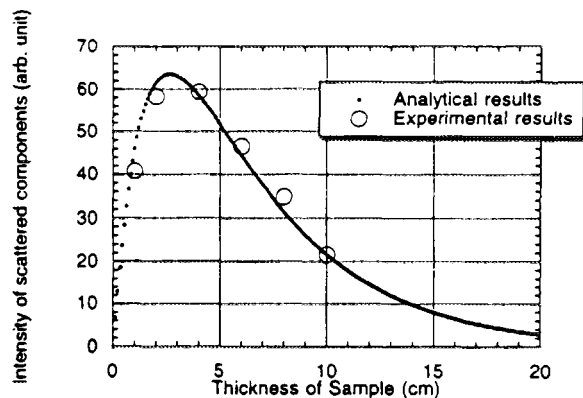


Fig. 4. Intensity of scattered fast neutron components at the center of the FNR image as a function of the thickness of an iron cylindrical sample with the radius of 3 cm (the sample is in contact with the imaging device).

4.3. Scattered neutron component as a function of the thickness of the sample

Fig. 4 shows the intensity of the scattered neutron component as a function of the sample thickness at a separation of $d = 0$ cm. Analytical results at a separation of $d = 0.1$ cm were obtained for the sample whose sizes were 3 cm in radius and from 0 to 20 cm in thickness. The experimental values agree with the analytical values shown as small dots in Fig. 4. From these results, it is concluded that the scattered component has the highest value at a sample thickness of 2.5 cm.

4.4. Estimated distance for a negligible level of scattered neutrons

The relations between the intensity of the scattered component and the separation distance " d " are shown as a

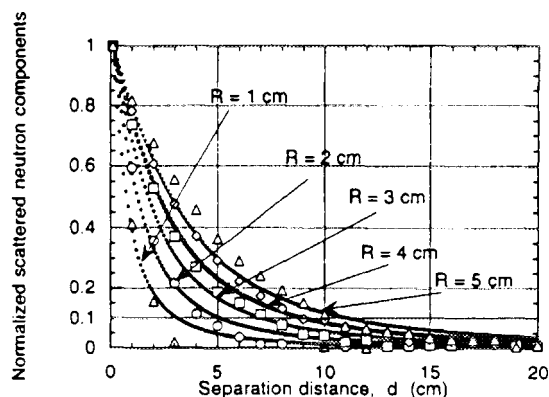


Fig. 5. Relations between the intensity and separation distance as a function of the sample radius.

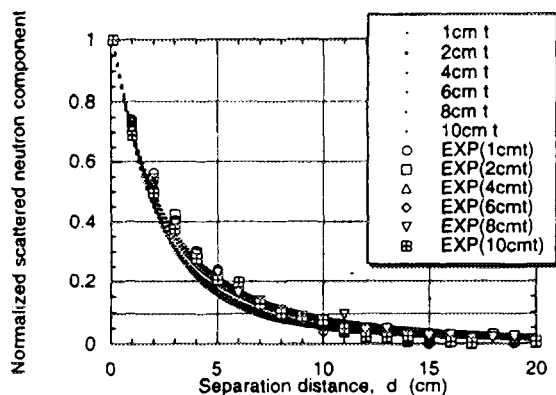


Fig. 6. Relations between the intensity and the separation distance as a function of the sample thickness.

function of the sample radius with 3 cm of thickness in Fig. 5. The intensities of the scattered neutrons were normalized by the intensities at $d = 0$ cm for five kinds of samples. As shown in Fig. 5, the intensities steeply decrease with increasing separation distance " d ". The decreasing relations for the samples depend on the radius of the samples. Results of analysis are shown as small dots in Fig. 5, and agree well with the experiments. The intensities are reduced to be negligible at the sample to imaging device distance " d " of twice the radius of the sample plus 1 cm for the 3 cm thick iron cylindrical samples, where the intensities are reduced to the 10% level in comparison with the intensity of scattered neutrons for $d = 0$ cm.

The relations between the intensity of the scattered component and the distance " d " are shown as a function of the sample thickness with 3 cm radius in Fig. 6. The intensities of the scattered neutrons were normalized by the intensities at $d = 0$ cm for six kinds of samples. As shown in Fig. 6, the intensities steeply decrease with increasing separation distance " d ". The decreasing relations for the samples do not depend on the thickness of the samples. Analytical results are shown as small dots in Fig. 6, and agree with the experimental results. The intensities are reduced to the 10% level in comparison with the intensity of scattered neutrons of $d = 0$ cm at the distance of about 8 cm for the samples of 3 cm radius.

5. Conclusion

The intensity of the scattered fast neutron component in a sample was analyzed for a fast neutron beam. The intensity of the scattered component at the centre of an object image was calculated using a simple model of the neutron behavior in an iron cylindrical sample. Results of this analysis agreed well with the experiments. The intensity of the scattered component saturated at the sample radius of 6 cm for the iron cylindrical samples of 3 cm thickness. The intensity had the highest value at a thickness of 2.5 cm for the iron cylindrical samples with 3 cm radius. The intensities steeply decreased with increasing separation distance " d " between the sample and the imaging device. The intensities of scattered neutrons were reduced to a negligible level at the separation distance of twice the radius of the sample plus 1 cm for the samples of 3 cm thickness.

Acknowledgement

The authors wish to express their gratitude to the YAYOI staff members and also to Mr. M. Satoh of the University of Tokyo for making the objects.

References

- [1] Y. Ikeda, K. Yoshii et al., Nucl. Instr. and Meth. A 279 (1989) 183.
- [2] K. Yoshii, M. Nakazawa et al., Neutron Radiography (3), eds. S. Fujine et al. (Kluwer, Dordrecht, 1990) p. 93.
- [3] K. Yoshii, Y. Ikeda et al., *ibid.* p. 365.
- [4] K. Yoshii, S. Fujine et al., Neutron Radiography (4), ed. J. Barton (Gordon and Breach, 1993) p. 527.
- [5] A.A. Harms and D.R. Wyman, Mathematics and Physics of Neutron Radiography (Reidel, Dordrecht, 1986).
- [6] H. Kobayashi et al., J. Nucl. Sci. Technol. 29 (1992) 1045.
- [7] Z. Hrdlicka and F. Peterka, eds. S. Fujine et al. (Kluwer, Dordrecht, 1990) p. 131.
- [8] S. Fujine et al., Nucl. Instr. and Meth. 215 (1983) 277.
- [9] K. Yoshii and K. Miya, Nucl. Instr. and Meth. A 335 (1993) 513.

Ⅲ. 核融合炉ブランケット設計基礎
実験装置ユーザーが主催または
後援した国際会議、
ワークショップ等一覧

核融合炉ブランケット設計基礎実験装置ユーザーが主催または後援した
国際会議、ワークショップ等 一覧（平成7年度）

	開催期間	会 議 名	開催場所	コティンメンバー (BLT関係者)	参加 者数
1	95.7.17～ 7.18	JAPAN/US Workshop on Theory and Modeling of Irradiation Effects in Materials for Fusion Energy Systems	Livermore (米国)	関村 直人 香山 晃	31
2	95.9.29～ 9.30	4th Japan-CIS Workshop on Interactions of Fuel Particles with Fusion Reactor Materials	Obnisk (ロシア)	山脇 道夫 山口 憲司	40
3	95.10.9～ 10.11	4th International Workshop on Ceramic Breeder Blanket Interactions	京都 (日本)	山脇 道夫 田中 知 山口 憲司	47
4	96.3.10～ 3.15	Engineering Foundation Conference on Turbulent Heat Transfer	San diego (米国)	笠木 伸英	80

**NEXT PAGE(S)
left BLANK**

IV. 核融合炉ブランケット設計基礎 実験装置研究参加者名簿

平成7年度 核融合炉ブランケット設計基礎実験装置研究参加者名簿

研究テーマ名	研究代表者	参加者名
1. プラズマ／固体・液体界面における不純物粒子の輸送挙動	田中 知	(システム量子工学専攻) 田中 知 (教授) 寺井 隆幸 (助教授) 米岡 俊明 (助手) 大津 繁樹 (D3) 角 泰孝 (M2) 田中 将隆 (M1) 鈴木 晶大 (M1) (原子力工学研究施設) 山口 憲司 (助教授) 松山 征嗣 (D1)
2. 核融合炉実用材料へのトリチウム付着と再放出メカニズムの解明	田中 知	(システム量子工学専攻) 田中 知 (教授) 大森 ルミ (技術官) 田中 将隆 (M1)
3. 固体表面近傍における粒子挙動の評価法の開発に関する研究	山口 憲司	(物理工学科) 伴野 達也 (講師) (原子力工学研究施設) 山脇 道夫 (教授) 山口 憲司 (助教授) 小野 双葉 (助手) Bandurko, V. (D3) 鈴木 敦士 (M2) 大越 啓志郎 (M1) 岡田 光正 (M1)
4. 水素同位体ビームによる第一壁燃料ダイナミックスの研究	山脇 道夫	(物理工学科) 伴野 達也 (講師) (原子力工学研究施設) 山脇 道夫 (教授) 山口 憲司 (助教授) 小野 双葉 (助手) Bandurko, V. (D3) 伊藤 洋 (D1) 松山 征嗣 (D1) 黄 錦濤 (D1) Swarno, H. (D1) 佐藤 力哉 (M2) 鈴木 敦士 (M2) 大越啓志郎 (M1) 岡田 光正 (M1)
5. プラズマ／壁界面における水素や水蒸気の吸着・脱離に関する量子科学的検討	長崎 晋也	(システム量子工学専攻) 長崎 晋也 (助教授) 津島 悟 (M2) 田中 将隆 (M1) 梅村 康洋 (M1)
6. ディスラプション時の第一壁の挙動	班目 春樹	(原子力工学研究施設) 班目 春樹 (教授) 岡本 孝司 (助教授) 鶴 大悟 (助手) 助川 敏男 (技術官) 石崎 泰央 (M2) 佐伯 壮一 (M2)

研究テーマ名	研究代表者	参加者名
7. 高温超電導体の核融合炉高度化の応用	宮 健三	(原子力工学研究施設) 宮 健三(教授) 上坂 充(助教授) 吉田 義勝(助手) 武田 信和(D3) 橋田 和泰(D3) 出町 和之(D2) 内一 哲哉(D1) アッティラ・ギラニ(D1) 陳 振茂(D1) 羅 雲(D1) 会田美紀子(M2) 井勝 信彦(M2) 竹下 明(M1) 福崎 康博(M1) 品川 亮介(M1)
8. 核融合炉第一壁の電磁的非破壊検査	宮 健三	(原子力工学研究施設) 宮 健三(教授) 上坂 充(助教授) 吉田 義勝(助手) 武田 信和(D3) 橋田 和泰(D3) 出町 和之(D2) 内一 哲哉(D1) アッティラ・ギラニ(D1) 陳 振茂(D1) 羅 雲(D1) 会田美紀子(M2) 井勝 信彦(M2) 竹下 明(M1) 福崎 康博(M1) 品川 亮介(M1)
9. 照射による材料組織・強度特性変化の研究	幸野 豊	(材料学科) 幸野 豊(助手) 朝倉 健太郎(助手) 佐東 信司(助手) 芹澤 久(D2) 谷川 博康(D1) 坂田 祐司(M2) 渡辺健一郎(M1)
10. 第一壁の画像解析に関する研究	岡本 孝司	(原子力工学研究施設) 班目 春樹(教授) 岡本 孝司(助教授) 鶴 大悟(助手) 馮 堅(D2) 松山 敬介(M1) 池田 耕(M1)
11. レーザー共鳴イオン化分光を用いた核融合炉材料界面特性の評価手法の開発	井口 哲夫	(システム量子工学専攻) 高橋 浩之(講師) 長谷川秀一(講師) 河原林 順(D3) 倉橋 智彦(M2) 山中 信弘(M2) 佐藤 泰(M1) 貝塚 洋志(M1) 福田 大治(M1) (原子力工学研究施設) 井口 哲夫(助教授)

研究テーマ名	研究代表者	参加者名
12. 複雑形状流路内乱流の熱・運動量輸送の数値予測	空木 伸英	(機械工学専攻) 空木 伸英(教授) 鈴木 雄二(講師) 三戸 陽一(D3) 塚原 渉(M2) 西村 賢(M2) 遠藤 誉英(M1)
13. 熱音響型冷凍機の基礎的研究	斎藤 孝基	(機械工学専攻) 斎藤 孝基(教授) 飛原 英治(助教授) 斎藤 静雄(助手) 諸山 稔員(技官)
14. 固体増殖材料表面における水素同位体の挙動	田中 知	(システム量子工学専攻) 田中 知(教授) 寺井 隆幸(助教授) 米岡 俊明(助手) 谷口 正樹(M2)
15. ウラン合金の水素同位体吸収特性	山脇 道夫	(原子力工学研究施設) 山脇 道夫(教授) 山口 憲司(助教授) 小野 双葉(助手) 伊藤 洋(D1) Suwarno, Hadi(D1) (共同研究員) 奥野 秀樹(原燃工)
16. 液体トリチウム増殖材料の物理化学的挙動	寺井 隆幸	(システム量子工学専攻) 田中 知(教授) 寺井 隆幸(助教授) 米岡 俊明(助手) 大森 ルミ(技官) 大津 繁樹(D3) 谷口 正樹(M2) 山口 貴行(D1) 小林 知洋(D1) 伊藤 康行(M2) 角 泰孝(M2) 谷口 正樹(M2) 細矢 雄司(M2) 鈴木 晶大(M1) 田中 将隆(M1) 野木 直行(M1)
17. 核融合炉用機能性セラミックス材料の放射線照射効果	寺井 隆幸	(システム量子工学専攻) 田中 知(教授) 寺井 隆幸(助教授) 米岡 俊明(助手) 大森 ルミ(技官) 大津 繁樹(D3) 谷口 正樹(M2) 山口 貴行(D1) 小林 知洋(D1) 伊藤 康行(M2) 角 泰孝(M2) 谷口 正樹(M2) 細矢 雄司(M2) 鈴木 晶大(M1) 田中 将隆(M1) 野木 直行(M1)

研究テーマ名	研究代表者	参加者名
18. トリチウム-材料相互作用におけるトラップメカニズム	小野 双葉	(システム量子工学専攻) 田中 知 (教授) (原子力工学研究施設) 山脇 道夫 (教授) 山口 憲司 (助教授) 小野 双葉 (助手) 伊藤 洋 (D1) 佐藤 力哉 (M2)
19. イオン照射下その場観察法による高エネルギーPKAカスケード損傷	関村 直人	(システム量子工学専攻) 関村 直人 (助教授) 河西 寛 (助手) 荒井 良夫 (技官) 森下和功 (特別研究員) 白尾 泰之 (M2) 相原 純 (M2) 今村 隆宏 (M1) 与那嶺 真一 (M1) (原子力総合研究センター) 岩井 岳夫 (助手) (人工物工学研究センター) 岩田 修一 (教授)
20. 核融合炉材料の照射下評価に関する研究	関村 直人	(システム量子工学専攻) 関村 直人 (助教授) 河西 寛 (助手) 荒井 良夫 (技官) 森下和功 (特別研究員) 白尾 泰之 (M2) 相原 純 (M2) 今村 隆宏 (M1) 与那嶺 真一 (M1) (原子力総合研究センター) 岩井 岳夫 (助手) (人工物工学研究センター) 岩田 修一 (教授)
21. 非金属材料のイオン照射効果の研究	石樽 顕吉	(システム量子工学専攻) 石樽 顕吉 (教授) 勝村 庸介 (教授) 松浦 千尋 (助手) 広石 大介 (助手) 浅井 圭介 (助手) 関 修平 (D3) 堂前 雅史 (D3) 半澤有希子 (D2) 渡辺 崇 (D1) 太田 隆 (M2) 千歳 範壽 (M2) 八巻 徹也 (M2) 高田 貴生 (M1) 土肥 宏一 (M1) 山田 健郎 (M1) 呉 国 忠 (研究生)

研究テーマ名	研究代表者	参加者名
22. 設計技術の体系化研究	近藤 駿介	<p>(システム量子工学専攻)</p> 近藤 駿介 (教授) 古田 一雄 (助教授) 羽島 良一 (講師) 下遠野英俊 (助手) 古浜 寛 (D3) 加藤 弘樹 (D3) 陸 道 綱 (D3) 鄭 義 相 (D2) 曹 学 武 (D1) 渡辺 正峰 (D1) 大石 隆文 (M2) 笠原 至彦 (M2) 近藤 貴夫 (M2) 佐々木秀樹 (M1) 内川 貴幸 (M1) 片岡 一朗 (M1)
23. 核融合実験炉中性子計測システムの工学設計	井口 哲夫	<p>(システム量子工学専攻)</p> 高田 英治 (助手) 原野 英樹 (D2) 浮辺 雅宏 (D1) 山中 信弘 (M2) 貝塚 洋志 (M1) 福田 大治 (M1) (原子力工学研究施設) 井口 哲夫 (助教授)
24. 光学的手法による核融合反応放射線場のキャラクターゼーション	中沢 正治	<p>(システム量子工学専攻)</p> 中沢 正治 (教授) 高橋 浩之 (講師) 高田 英治 (助手) 細野 米市 (技術官) 河原林 順 (D3) 原野 英樹 (D2) 石川 顕一 (D1) 浮辺 雅宏 (D1) イオン・フレデリキ (D1) ジェーン・ブレイ (D1) 倉橋 智彦 (M2) 山中 信弘 (M2) 貝塚 洋志 (M1) 佐藤 泰 (M1) 福田 大治 (M1) (原子力工学研究施設) 井口 哲夫 (助教授)
25. 高速中性子ラジオグラフィの散乱線補正	吉井 康司	<p>(原子力工学研究施設)</p> 宮 健三 (教授) 井口 哲夫 (助教授) 吉井 康司 (助手)

発行日 平成 8 年10月
発行所 茨城県那珂郡東海村白方白根 2-22
東京大学工学部附属原子力工学研究施設
編 集 核融合炉ブランケット設計基礎実験装置
運営委員会
委員長 井上 信幸
幹 事 田中 知 寺井 隆幸 上坂 充
関村 直人 岡本 孝司 山口 憲司
吉田 義勝
B L T管理部 吉井 康司
印刷所 茨城県那珂郡東海村村松 261
ニッセイエプロ株式会社
Tel. 029 (282) 7321
